Pattern formation and growth kinetics in eutectic systems

by

Jing Teng

A dissertation submitted to the graduate faculty

in partial fulfillment of the requirements for the degree of

DOCTOR OF PHILOSOPHY

Major: Materials Science and Engineering

Program of Study Committee:
Rohit K. Trivedi, Major Professor
Brian Gleeson
Xiaoli Tan
Balaji Narasimhan
Palaniappa A. Molian

Iowa State University

Ames, Iowa

2007

TABLE OF CONTENT

ABSTRACT

Growth patterns during liquid/solid phase transformation are governed by simultaneous effects of heat and mass transfer mechanisms, creation of new interfaces, jump of the crystallization units from liquid to solid and their rearrangement in the solid matrix. To examine how the above processes influence the scale of microstructure, two eutectic systems are chosen for the study: a polymeric system polyethylene glycol-p-dibromobenzene (PEG-DBBZ) and a simple molecular system succinonitrile (SCN)-camphor.

The scaling law for SCN-camphor system is found to follow the classical Jackson-Hunt model of circular rod eutectic, where the diffusion in the liquid and the interface energy are the main physics governing the two-phase pattern. In contrast, a significantly different scaling law is observed for the polymer system. The interface kinetics of PEG phase and its solute concentration dependence thus have been critically investigated for the first time by directional solidification technique. A model is then proposed that shows that the two-phase pattern in polymers is governed by the interface diffusion and the interface kinetics.

In SCN-camphor system, a new branch of eutectic, elliptical shape rod, is found in thin samples where only one layer of camphor rods is present. It is found that the orientation of the ellipse can change from the major axis in the direction of the thickness to the direction of the width as the velocity and/or the sample thickness is decreased. A theoretical model is developed that predicts the spacing and orientation of the elliptical rods in a thin sample.

The single phase growth patterns of SCN-camphor system were also examined with emphasis on the three-dimensional single cell and cell/dendrite transition. For the 3D single cell in a capillary tube, the entire cell shape ahead of the eutectic front can be described by

the Saffmann –Taylor finger only at extremely low growth rate. A 3D directional solidification model is developed to characterize the cell shape and tip undercooling and the experimental results are compared with the predictions of the model. From the investigation of cell/dendrite transition, a model is proposed, from which the condition for the onset of the transition can be obtained.

CHAPTER 1. GENERAL INTRODUCTION

1. Introduction

Solidification is a phase transformation process in which a volume of liquid is frozen into solid(s). It involves complex heat and mass transfer in the solid and liquid and within the interface region, the creation of new interfaces, and attachment of crystallization units from liquid to solid at the interface and their rearrangement in the solid matrix. A specific interface pattern is selected by the system through the interaction of these processes under given experimental conditions. Consequently a variety of interface patterns can be obtained by changing experimental conditions.

In different materials, the physical process governing the pattern formation can be quite different. For example, for simple atomic/molecular materials, solid/liquid interfaces are non-faceted so that the kinetic effect is usually negligible; while this effect is dominant for faceted and polymeric materials. On the other hand, the microstructure of a non-faceted material may also be controlled by the interface kinetics under extremely high growth rates. Therefore how the external processing conditions interact with internal properties to dictate the interface pattern constitutes the foremost important subject in solidification science.

Very interestingly, similar interface patterns are observed in different materials, such as the dendritic structure of a single phase shown in figures 1 [1-3] and the dual phase structure shown in figure 2 [4-6]. Though morphologically similar, the length scales in different materials can be significantly different. For instance, for the rod-eutectic microstructure in Fig. 2, the average rod spacing is on the order of 10 μm, 1 μm and 10 nm in the metallic Al-Cu (Fig. 2(a)), the ceramic alumina-zirconia (Fig. 2(b)) and the polymeric

PE-PS system (Fig. 2(c)) respectively. Thus, how a system chooses its microstructure length scale makes up the second important fields in the solidification studies. This field is even more significant since the length scale of a solidified microstructure decisively controls many properties of a material.

There are two distinct cases of microstructure evolution that depend on the direction of heat flow and the direction of the crystal growth in solidification processes, and they are called unconstrained or constrained growth. Unconstrained growth (undercooled growth)

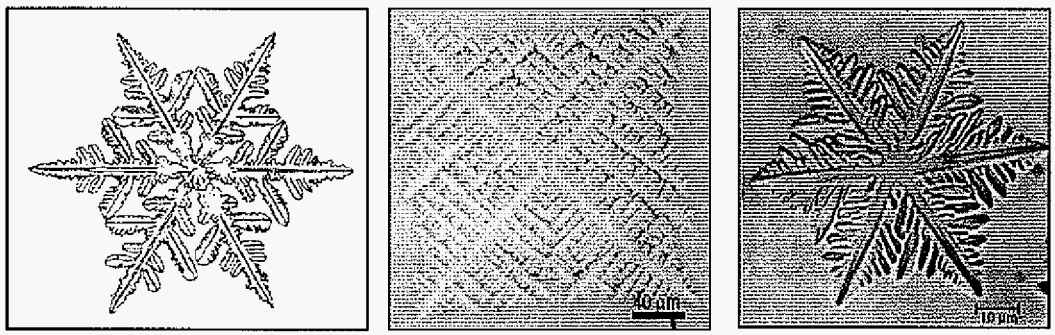

(a) (b) (c)

Figure 1. Dendritic patterns of (a) Snowflake [1]; (b) Solidified Poly(ethylene oxide) in PEO/PMMA blend [2]; and (c) Hexagonal crystal from a commercial glass [3].

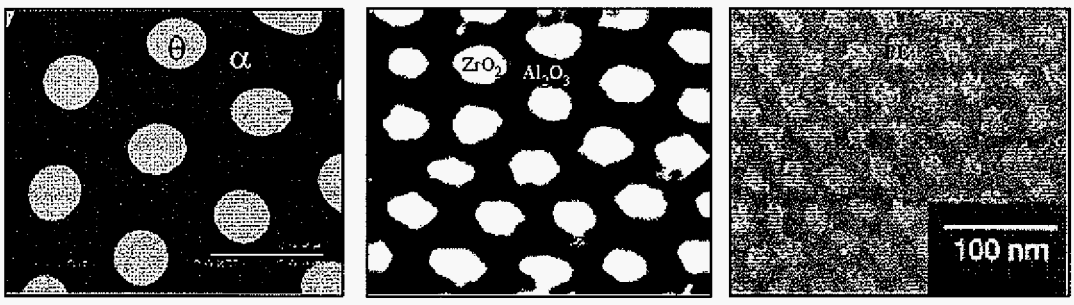

(a) (b) (c)

Figure 2. Eutectic patterns of (a) Metallic system [4]; (b) Ceramic system [5]; and (c) Polymeric system [6].

occurs in undercooled melts where the homogeneous or heterogeneous nucleation initiates the solidification process. In undercooled growth, the externally controllable parameter is the undercooling of a melt, while the growth velocity and interface temperature are selected by the solidification system together with a specific pattern and its length-scale. If the heat is dissipated in a unidirectional manner, directional solidification occurs. The great advantage of directional over undercooled growth is that this process can offer the independent and accurate control of growth velocity (V), temperature gradient (G), and the alloy composition (C_0), therefore the interface response can be quantitatively examined since these three variables are the only input parameters. This feature makes directional solidification an appropriate technique to quantitatively study pattern formation problem.

In this research, we shall investigate the formation of single-phase and two-phase patterns in eutectic systems. Two eutectic systems are examined through directional solidification experiments: one is composed of succinonitrile (SCN) and camphor, where both components are non-faceted with negligible interface kinetics; the other consists of polyethylene glycol (PEG) and 1,4-dibromobenzene (DBBZ), where both components are faceted with strong kinetic effects. The first one will serve as a model system to study single-phase patterns with two objectives: (1) to develop a theoretical model to characterize the shape selection of a cell and its tip undercooling in near-eutectic alloys; and (2) to uncover the relationship that governs the growth pattern transition from cells to dendrites in dilute alloys. It will also be employed to model the pattern evolution of rod-eutectic growth in a confined sample cell. The second eutectic system will be used to investigate the role of interface kinetics in the formation of growth patterns and to understand the fundamental physics and length scale selection of eutectic growth strongly influenced by the growth

kinetics. Specifically the scaling laws in these two eutectic systems shall be significantly different, from which the physics governing the selection of eutectic length spacing and undercooling will be investigated. The detailed study will be presented in the following chapters.

2. Dissertation Organization

This dissertation is written in an alternate format composed of two published papers, and 5 original manuscripts. References cited within each paper or manuscript are placed immediately after it. The dissertation begins with a general introduction as Chapter 1 and ends with a general conclusion as Chapter 9.

The detailed experimental results in SCN-camphor system are discussed in chapters 2 to 6. Among them, chapter 2, "Re-Determination of Succinonitrile (SCN) - Camphor Phase Diagram" and chapter 3, "Determination of the Solute Coefficient by the Droplet Migration Method", focus on the evaluation of SCN-camphor phase diagram and system parameters, including liquidus slope m, equilibrium distribution coefficient k and solute diffusion coefficient D, which are indispensable for modeling selection of growth patterns. In chapter 4, "Cellular Microstructure in Directional Solidification", the characteristics of SCN cellular pattern in capillary samples during directional solidification are investigated with near eutectic alloys in which a eutectic microstructure forms in the intercellular region. A theoretical model, based on the three-dimensional Saffmann-Taylor model is developed to characterize the shape of the cell and the undercooling at the tip. Chapter 5 is "Cell-dendrite Transition in Succinonitrile (SCN)-camphor Alloys", in which the key parameter, λ_{cd} (critical spacing), that controls the cell-dendrite transition is correlated with the alloy composition C_o,

temperature gradient G and growth velocity V through the relationship $\lambda_{cd}(GV)^{1/3}C_o^{1/4}=25.3$ $\mu m (K/s)^{1/3}$ by examining the directional solidified SCN-camphor dilute alloys. The results of two-phase structure of SCN-camphor eutectic alloy are presented in chapter 6, "Growth and Morphology of Rod Eutectics", where a model is developed for the pattern evolution of rod-eutectic growth in a confined sample cell.

Chapter 7 and 8 discuss the experimental results in PEG-DBBZ system. In chapter 7, "Crystallization Kinetics in Binary Polymer Systems", the directional crystallization technique is employed to study the crystallization kinetics of PEG, and then the interface kinetic laws of PEG-based alloys are investigated so that the effect of interface kinetics in two-phase eutectic patterns in polymeric systems can be quantitatively evaluated. Incorporating this interface kinetic law with the appropriate mass transfer mechanism in the liquid obtained from the experimental eutectic growth scaling law, an analytical model for polymeric eutectic growth is developed for polymeric eutectic growth. This work is described in chapter 8, "Crystallization Mechanism in Binary Polymeric Eutectics".

3. Literature Review

3.1. Single-phase growth patterns

A schematic eutectic binary phase diagram is shown in Fig. 3. At equilibrium condition, a liquid of composition C_E will form two solid phases simultaneously: α phase with composition $C_{s\alpha}$ and β phase of composition $C_{s\beta}$ at a unique temperature T_E.

If the alloy composition is not at C_E, the primary phase will grow first which is followed by the eutectic reaction behind the primary phase interface. The morphology of this primary phase can be planar, cellular or dendritic depending on growth conditions in a

directional solidification process. For a given alloy composition and temperature gradient, a planar interface is observed at low velocities. As the growth velocity is increased, the planar front becomes unstable and reorganizes into a periodic array of cells or dendrites, as shown in Fig. 4 [7].

The critical condition for planar front growth has been established by Mullins and Sekerka[8] and has been well verified experimentally. Significant development has also been made in the understanding of dendritic growth. The shape of a tip has been proved to be a paraboloid of revolution and its stability can be well described by the linear stability theory [9]. On the contrary, for cellular growth, because of the complicated thermal and solutal interactions between neighboring cells and the dependence of cell shape on local spacing, there remain some critical aspects unsolved in this area, such as the cell shape selection and the pattern stability, etc.

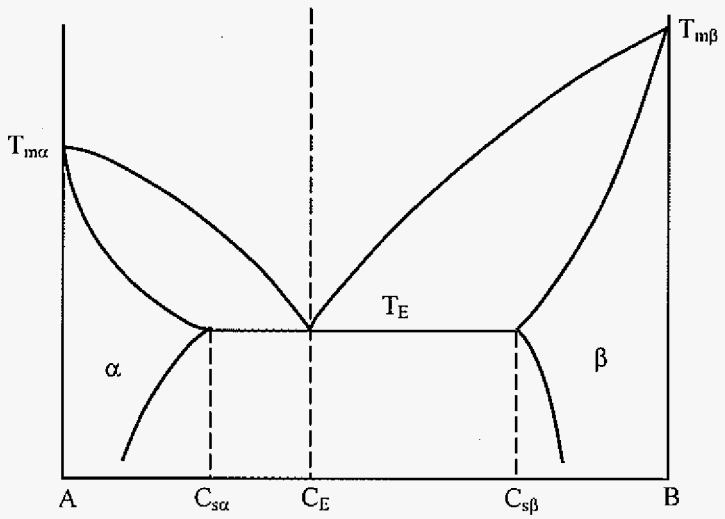

Figure 3. Schematic eutectic phase diagram.

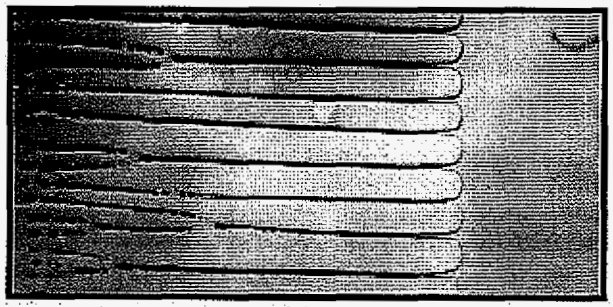

(a)

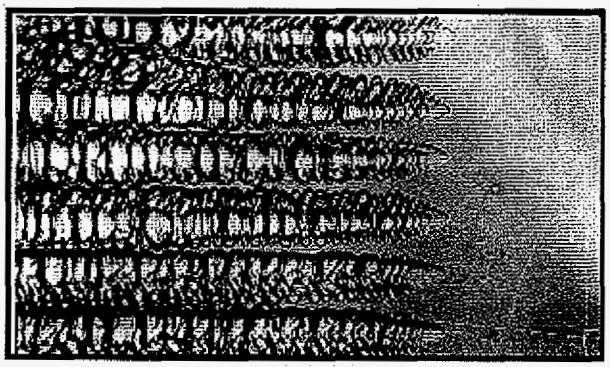

(b)

Figure 4. The effect of growth velocity on interface pattern in SCN- 4.0 wt % acetone system directionally solidified in thin rectangular samples at G = 6.7 K/mm. (a) A cellular pattern at V = 0.56 μm/s and (b) a dendritic pattern at V = 10.0 μm/s [7].

Although the general shape of the cell is complex, the experimental studies in a binary alloy of succinonitrile-salol showed that the cell shape and spacing follows some specific scaling laws. When only cells are present in a steady-state array, all apparently differing cell-shapes collapse onto a single shape when they are scaled with the local spacing [10]. The theoretical prediction from the phase-field model agreed with this experimental result and the phase-field numerical calculation of cell shape matched with the experimental shape within optical resolution. This cell shape interpolates between the asymptotic Scheil equation far from the tip and the 2D-Saffman-Taylor shape near the tip region [11]. In addition, Trivedi et al. [12] have shown that at low velocities, in the presence of intercellular

eutectic, the cell shapes ahead of the eutectic front can be described by the Saffman-Taylor finger shape. In directional solidification, the cell is three dimensional, which requires the modification of the classic 2D Saffman-Taylor model. Therefore, in this research, we will investigate the cellular structure in a thin cylindrical tube with SCN-camphor system and develop a 3D directional solidification model based on the results of the finger problem.

During directional solidification, the morphological transition from cells to dendrites is not shape but gradual. Therefore, cells and dendrites can co-exist over a range of growth conditions [7,13-14]. The cell-dendrite transition (CDT) has been studied both experimentally and theoretically and several models have been developed [15-16]. However, the criterions that been proposed in those models did not seem to agree with all the experimental studies in different alloy systems [17]. Recently, Trivedi *et. al.* [18] found a quantitative relationship for CDT transition that incorporates local spacing. We will continue to pursue this morphological transition in this research by using SCN-camphor system to determine the relationship of CDT with the critical spacing, growth condition and system parameters.

3.2. Fundamentals of eutectic growth

For the solidification of eutectic alloy, complex patterns can form at the solid-liquid interface since the eutectic reaction involves two solid phases. The eutectic morphology depends on the interface structures of two component phases. If both phases are non-faceted, regular rod or lamellar structures may form during solidification, while irregular structures may evolve if the eutectic contains at least one faceted phase. The volume fraction of the two phases, which is controlled by the alloy composition, also affects the eutectic morphology.

When the volume fraction of one phase is between 0 and 0.28, the eutectic will probably be fibrous (rod); especially if both phases are of non-faceted type. When the volume fraction is between 0.28 and 0.50, the eutectic tends to be lamellar [19]. Figure 5 [20-21] showed structures for all 3 eutectic types.

Solidifying at eutectic point is not the only way to acquire eutectic structures. Actually, the eutectic morphology can be observed in a range of compositions, and this composition range is called coupled zone. There exist two kinds of coupled zone: regular or

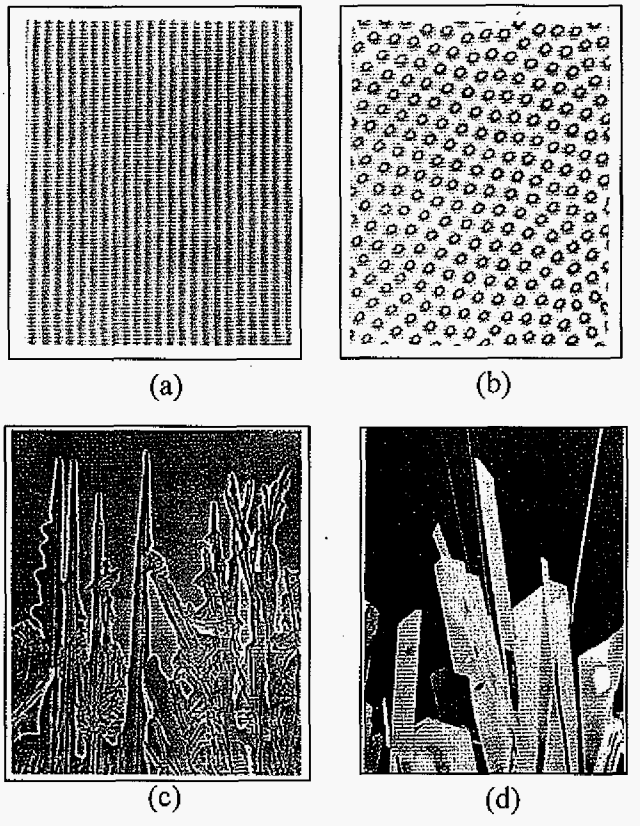

Figure 5. Examples of eutectic structures of (a) Regular eutectic, lamellar structure in Pb-17.4% Cd system [20]; (b) Regular eutectic, rod structure in Sn-18.0wt% Pb system [20]; (c) Irregular eutectics, faceted/non-faceted succinonitrile-borneol system [21]; and (d) Irregular eutectic, faceted/faceted azobenzene-benzil system [21].

skewed [20], as shown schematically in figure 6, in which coupled eutectic growth in the hatched regions is favored over primary single phase growth in a competitive manner.

Figure 7 is a schematic diagram of 2D lamellar eutectic interface in which a periodic arrangement of parallel sheets of α and β growing co-operatively in a side-by-side fashion. The definitions of spacing λ and undercooling ΔT are marked on the figure. Undercooling is the difference between eutectic melting point and the local actual temperature of the growing front, T_E-T_i, which describes the driving force for eutectic growth. This total undercooling can be separated into different terms, ΔT_C for solute diffusion, ΔT_r for surface energy, ΔT_k for interface attachment kinetics, ΔT_T for thermal diffusion, and ΔT_ε for strain energy effect. Among these terms, ΔT_T is negligible in directional solidification; ΔT_ε only exists at some certain cases. Therefore the major contributions to undercooling come from the first three terms.

The solute diffusion is caused by the concentration difference in the liquid, C_E, and solid phase, $C_{S\alpha}$ for α phase and $C_{S\beta}$ for β phase respectively (Fig. 3). The A-rich α phase rejects B-atoms in order to form α phase with composition $C_{S\alpha}$ from more concentrated composition C_E, thus the local composition of the liquid in front of α phase increases. Similarly, the B-rich β phase rejects A-atoms to increase its composition to $C_{S\beta}$ and the local composition of the liquid in front of β phase decreases. A composition gradient develops in the liquid ahead of the advancing interface with more B-rich in front of α phase and more A-rich in front of β phase. The accumulated component ahead of each phase has to diffuse away so that the interface can keep advancing. Assuming local equilibrium, then the driving force required for the solute diffusion can be calculated as $\Delta T_C = -m(C_E-C(x))$ where $C(x)$ is

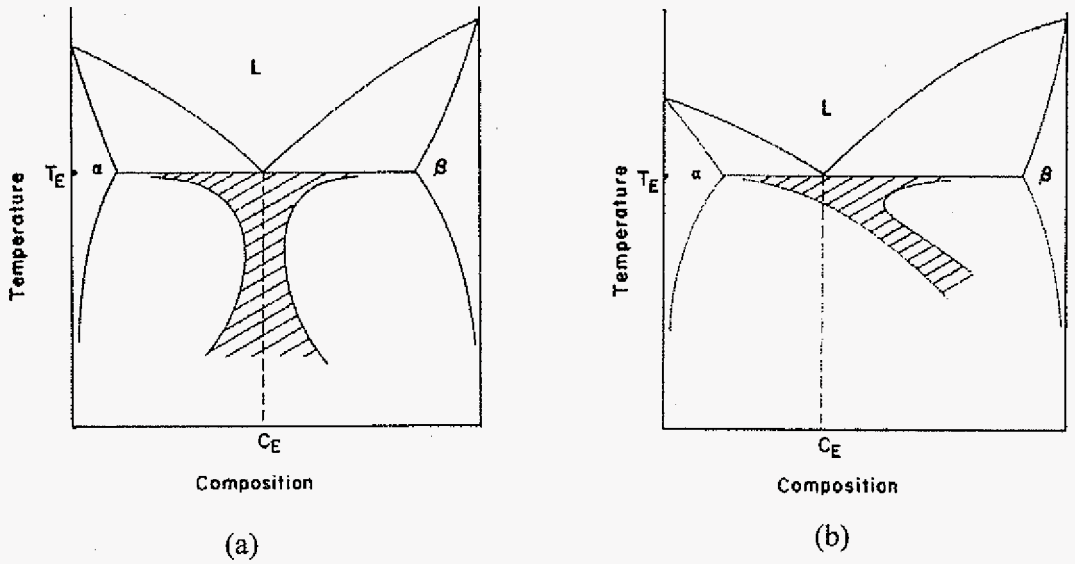

Figure 6. Schematic eutectic phase diagrams showing the temperature-composition zone (shaded regions) in which coupled eutectic growth will occur for (a) a regular coupled zone and (b) a skewed coupled zone [20].

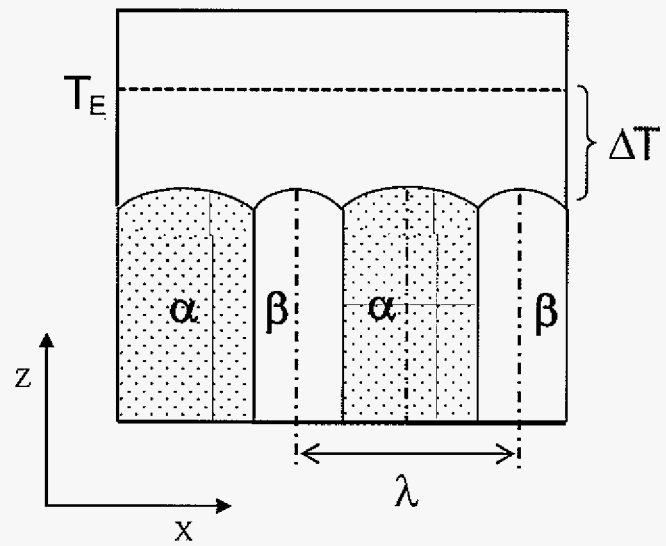

Figure 7. Schematic of 2D lamellar interface showing the undercooling ΔT and lamellar spacing λ.

the composition of the interface at x and it can be obtained from the solution of appropriate diffusion equations.

The diffusion of solute tends to minimize the scale of the morphology (eutectic spacing λ). Meantime, there is an opposing effect which arises from the increased energy associated with the increased curvature of the solid/liquid interface as λ decreases. This effect can be expressed in terms of a curvature undercooling ΔT_r, which can be calculated by Gibbs-Thomson equation as $\Delta T_r = \kappa\Gamma$ where κ is curvature and Γ is Gibbs-Thomson coefficient.

The above two terms, ΔT_C and ΔT_r correspond to changes in the local equilibrium temperature from T_E, while the third term, ΔT_k, is a specifically non-equilibrium term which provides the driving force for atomic/molecular attachment onto the solid at the interface. For metallic and other non-faceted eutectic systems, atoms/molecules can be added easily to any point of the solid surface, thus this term usually can be ignored in comparison with ΔT_C and ΔT_r. In eutectic systems which contain faceted components, ΔT_k cannot be ignored and its magnitude depends on the operative growth mechanism, e.g., uniform advance, screw dislocation or two-dimensional nucleation etc., which has been discussed by Tiller in detail [22].

Depending on nature of eutectic systems, the physics governing the eutectic growth can be quite different. Therefore the total undercooling will be the different combinations of above terms, which will lead to varied models and scaling laws.

3.3. Theoretical models of eutectic (eutectoid) growth

The theoretical modeling on eutectic growth can be traced back to Zener's work in 1946, in which the iron-carbon eutectoid reaction was examined [23]. Eutectoid reaction is similar to eutectic reaction with the only difference that the parent phase is also a solid phase. Therefore, the theoretical consideration and treatment of eutectoid or eutectic growth are more or less the same.

In Zener's phenomenal work [23], he asserted that mass transfer was by volume diffusion of carbon through austenite ahead of the interface and considered the surface energy of lamellar structure. He further derived a semi-empirical relationship between the growth rate and interface supercooling. Subsequently by assuming that the growth occurs at the maximum growth rate, he obtained the significant relationship that the product of the growth velocity and the square of the lamellar spacing should be constant. All the later developments in modeling eutectic growth are based upon Zener's model. Tiller [24] established a formal theory for eutectic alloys solidification and proposed a minimum undercooling condition which was essentially same as Zener's maximum growth rate assumption.

Jackson and Hunt [25] rigorously solved the solute diffusion field in eutectic solidification process and established the classical model for regular eutectic growth. In this model, only volume diffusion of the solute in the liquid and curvature effect were considered to contribute to undercooling, while all the other effects were neglected so that $\Delta T_i = \Delta T_C + \Delta T_r$. Convection was also considered to be negligible so that the growing front was under pure diffusive condition. Besides, a few important assumptions were also made in order to

solve the solute diffusion problem mathematically: (1) the growth velocity was sufficiently low so that the concentration field is given by the solution of the Laplace equation, i.e., $P_e = V\lambda/2D << 1$; (2) the growth front was planar so that the Laplace equation for the diffusion field could be analytically solved; (3) the total interface undercooling for each solid phase was equal, ie, $\Delta T_\alpha = \Delta T_\beta = \Delta T$. Under these assumptions, Jackson and Hunt calculated the solute undercooling ΔT_C from the solution to Laplace equation, the curvature undercooling ΔT_r from Gibbs-Thomson equation; and finally obtained the relationship between the undercooling, growth rate and eutectic spacing, as

$$\Delta T = K_1 \lambda V + K_2/\lambda \qquad (1)$$

where K_1 and K_2 are system parameters.

Equation 1 predicts that at a given growth velocity, the eutectic spacing depends on undercooling and the solutions to this equation are multiple. Then Jackson and Hunt qualitatively discussed the stability problem and concluded that of all possible spacings based on diffusional consideration for growth, only those spacings will be stable which lie in the band $\lambda_m < \lambda < \lambda_M$, as illustrated schematically in figure 8. Figure 9 schematically showed the interface responses to a local decrease in spacing. The spacing smaller than λ_m will be unstable since any depression in the interface shape will cause a lamella at depression to get narrower, which will ultimately eliminate that lamella and increase the local spacing (figure 9(a)); on the other hand, for spacing larger than λ_m, a local decrease in spacing will result in a local decrease in undercooling and the lamella will be restabilized by the change in interface shape (figure 9(b)). However, as the spacing becomes much larger than λ_m, the steady-state interface shape will develop a pocket at the center of the wide phase (figure 9(c)). At some

larger spacing λ_M, the slope of the interface becomes infinity so that all eutectic spacings above λ_M become unstable.

Then by assuming that eutectic growth occurs at the minimum undercooling, Jack and Hunt obtained:

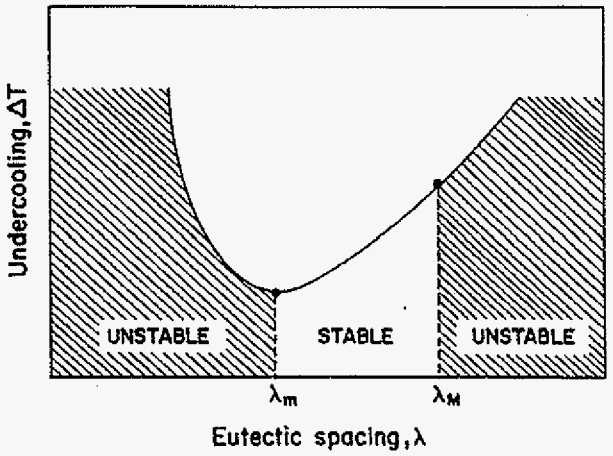

Figure 8. Relationship between the average interface undercooling and the eutectic spacing at a fixed velocity and the regions of stable and unstable spacings as predicted by JH model [20].

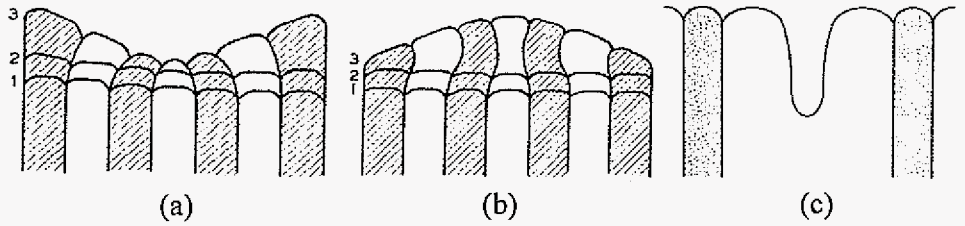

Figure 9. Schematic illustrations of (a) the instability of a lamella with $\lambda < \lambda_m$; (b) interface restabilized to a local decrease in spacing if $\lambda > \lambda_m$; and (c) a pocket developed in the center of the wider phase, leading to a shape instability [25].

$$V\lambda_m^2 = K_2/K_1 \quad (2)$$

and $$\Delta T_m = 2(K_1K_2V)^{1/2} \quad (3)$$

Ever since this classical eutectic growth model being proposed, lots of experimental studies have been carried out to verify the relationships and theoretical predictions by many eutectic alloys. Among them, the fundamental understanding in rod eutectic structure formation and spacing selection is clearly lagging behind those in lamellar eutectic structure. Recently been discovered SCN-camphor system offers a good opportunity to conduct some systematic studies in rod eutectic growth due to their transparent characteristics. In this research, we will employ this system to study the spacing selection in both steady state and dynamic processes and uncover the mechanisms responsible for spacing adjustment. We will also investigate the possible shape and arrangement changes of the minor phase rod in a confined space.

Another mass transfer mechanism, boundary diffusion, which is a short-circuit diffusion path which occurs in a thin layer ahead of the advancing interface, can also be dominant for solute transfer in the parent phase [26]. Cahn [27] developed this idea to a more fundamental theory for eutectoid growth. Based on Cahn's model, Hillert [28], Shapiro and Kirkaldy [29], and Sundquist [30] derived a relationship λ^3V=constant for eutectoid growth independently and they all assumed the local equilibrium condition at the growing front in their treatments.

Carpay and Boomgaard [31] examined the unidirectionally controlled eutectoid transformations of the compound Co_3Si, which can transformed into Co_2Si and Co, and the β-phase in the Ni-In system, which can transformed into NiIn and Ni_2In_3, and found the relationship λ^4V=constant experimentally for both systems. They explained this experimental

Table 1. Summary of the predictions of various eutectoid and eutectic growth theories [33]

Author	Relationship Predicted	Growth Criterion Selected	Volume, V_0, or Boundary Diffusion, B	Assumptions, Regarding ΔT's and D
Zener	$V\lambda^2 \exp. E/RT$ = constant $\Delta T\lambda$ = constant	Grows at maximum velocity possible	V_0	$\Delta T_k = 0$ $D \propto \exp.-E/RT$
Jackson and Hunt	$V\lambda^2$ = constant $\Delta T\lambda$ = constant	Grows at minimum T for rod growth	V_0	$\Delta T_k = 0$ D = constant
Hillert	$V\lambda^2$ = constant $\Delta T\lambda$ = constant	Grows at maximum velocity possible	V_0	$\Delta T_k = 0$ D = constant
Tiller	$V\lambda^n$ = constant, n>2 $\Delta T\lambda^m$ = constant, m>1	Grows at maximum velocity possible	V_0	$\Delta T_k \approx \Delta T$ D = constant
Bolze et al.	$V \propto \frac{\frac{1}{\lambda}(1-\frac{\lambda_c}{\lambda})}{1+\varphi/\lambda}$	Stable state λ not specified, either that which gives maximum velocity or maximum entropy production	V_0	$\Delta T_k = 0$ D = constant
Cahn	Various parameters are plotted as a function of interface mobility	Grows at a velocity $\propto \Delta G \propto \Delta T$	B	D = constant Kinetic factors determine V
Hillert	$V\lambda^3$ = constant $\Delta T\lambda$ = constant	Grows at maximum velocity possible	B	$\Delta T_k = 0$ D = constant
Sundquist	$V\lambda^3 \exp. E/RT$ = constant $\Delta T\lambda$ = constant	Grows at a velocity so that λ on verge of instability	B	$D \propto \exp.-E/RT$
Shapiro and Kirkaldy	$V\lambda^3 \exp. E/RT$ = constant $\Delta T\lambda$ = constant	Grows at a velocity corresponding to a spacing of $F\lambda_C$ where F > 1	B	$D \propto \exp.-E/RT$
Carpay and van den Boomgard	$V\lambda^4$ = constant $\Delta T\lambda^2$ = constant	Grows at a velocity $\propto \Delta T^2$	B	D = constant Kinetic factors determine V

observation by taking into account the kinetic supercooling as well as the boundary diffusion and curvature effects. Carpay [32] subsequently proposed a "lateral growth model" to describe the eutectoid growth as nucleation-controlled process in which every new atomic layer needs to nucleate on the previous layer and it presented one of the situations that interface kinetics controls the transformation. B. G. Mellor and G. A. Chadwick [33] summarized the scaling laws for eutectoid growth controlled by different physical mechanisms, as shown in Table 1.

Polymer crystal growth is controlled by two-dimensional nucleation, therefore polymer eutectic growth is expected to follow a scaling laws in which interface kinetics controlled the growth. Before discussing the polymer eutectic solidification, the crystal growth of unary polymer system will be reviewed first.

3.4 Polymer crystal growth and polymer eutectics

3.4.1. Crystallization in homopolymers

Compared with the simple atomic and molecular systems, a uniary polymer system has its distinctive natures: it consists of polymer chains of different lengths, the chains are entangled together in the liquid state and the movement of a polymer chain is through reptation process. Therefore a polymer melt usually has a high viscosity and low self-diffusivity, which leads to remarkably different crystallization features upon cooling.

1. Tendency of crystallization: Whether a polymer molecule is crystallizable or not depends on a lot of factors such as chain flexibility, side group size, stereoregularity (tacticity) and chain irregularity, etc. A large number of polymers are amorphous.

2. Degree of crystallinity: Almost all the crystallizable polymers are semicrystalline. The

crystal always contains both crystalline and amorphous regions. The fraction of amorphous region can be as large as 70%.

3. Crystallizing unit: macromolecules are in random coil conformation in concentrated solutions and in melts. High viscosity makes the mobility of whole chain very low. The molecular chain is moving by segment reptation. Thus crystallizing unit is chain segment instead of atom or molecule in non-polymeric system.

4. Crystal growth kinetics: Instead of crystallizing by the atomic jump across the growth interface in the small molecular and metallic alloys, polymer crystallization proceeds with the secondary nucleation and conformational change.

5. Length scale of the crystalline structure: small molecules are incorporated one after another into molecular crystals, producing entities of macroscopic size in three dimensions. In contrast, in a polymer crystal, one dimension is very small, usually 10nm, while another two dimensions are much larger in comparison with the third one. This means, one dimension of the polymer crystal does not grow during the crystallization, although the surface has the highest surface free energy in this dimension.

Spherulites are the most common microstructures observed for homopolymer bulk crystallization (Fig. 10(a)). A spherulite is an aggregate of crystalline plate-like lamellae that grow radially from a nucleation center. Each lamella consists of molecular chains that are folded according to some crystallographic arrangements and the direction of folding is perpendicular to the direction of growth.

Understanding the kinetics of spherulite growth has always been the focus in the study of polymer crystallization mechanism. Different experimental methods have been used to investigate the polymer crystallization kinetics. The first one is to study the crystallization

of a polymer in the non-isothermal growth process. It is usually conducted in a DSC apparatus and analyse the variation of fraction of crystalline phase [34]. The nucleation rate and growth rate are in continuous change, therefore this technique could not offer the exact information related to the growth kinetics. The second method is to study the crystallization behavior in an undercooled growth process, i.e., the polymer melt is held at some undercooling. The growth velocity can be assessed from the total crystallinity by following a property change (usually density or specific volume) or in another widely used method, by optical microscopy, in which the isothermal rate of formation and subsequent growth of spherulite can be studied separately [35]. It sub-divides into two types: one is with some crystal seeds and the other is devoid of seeds. Without seed crystals, the crystallization starts from nucleation and subsequent growth can be monitored. Usually, the growth rate is decelerating just after the nucleation and reaches a steady state at some later time. With some seeds existing, the growth rate reaches the steady state at a much shorter time and the limited number of nuclei can avoid the impingement problem so that the spherulites can grow to a larger size, making the growth rate measurement more accurate. This steady state growth rate is then correlated with the bath undercooling in order to determine the growth kinetics and to disclose the growth mechanism. The growth process can be monitored in an optical microscope with polarized illumination; however the small-angle x-ray or neutron scattering technique has also been used in the experimental study recently to discover much more details in the polymer crystal growth process, such as the size of crystalline lamellae and the crystallographic information [36-37].

Different theories have been developed to analyze polymer crystal growth kinetics. The first one was based on Avrami theory [38-40], which provides useful data on the overall

kinetics of crystallization, but little insight into the molecular process of polymer crystal growth. Keith and Padden [41-42] developed a theory to address the kinetics of spherulitic growth in crystallizing polymers. However, it was more phnomenological than mechanistic and may explain the experimental results qualitatively rather than quantitatively. A subsequent development is the secondary nucleation theory by Hoffman and co-workers [43-45], which, for the first time, provides an understanding of how a polymer chain attaches to the crystal and makes it possible to compare experiments with the theory quantitatively [46].

By secondary nucleation theory, there are three regimes to account for the polymer crystallization process from its melt.

Regime I (a single nucleation on a single growth layer): the rate of secondary nuclei ($\dot{N}_i$) is very low and is the rate controlling step for growth process. In this regime, each layer is complete before the next one nucleates This holds true at small undercoolings.

Regime II (multiple nucleations on a single growth layer): the secondary nucleation rate $\dot{N}_i$ is relatively high and there are multiple nucleation at the growing crystal plane. Multiple nucleation events in the single growth layer reduces the space for a nucleus to grow laterally. This regime occurs at higher undercoolings than Regime 1 [44, 47].

Regime III (multiple nucleations on multiple growth layers): At even higher undercooling, the rate of secondary nucleation becomes much greater, and the nucleation occurs at multiple crystal planes to facilitate a faster crystal growth. In this case, a secondary nucleus does not spread much beyond the dimensions of the nucleus.

Different regimes follow slightly different growth laws, which can be expressed as:

$$V = V_0 \exp[-U^* / R(T_c - T_\infty)] \exp[-K_g / T_c(\Delta T) f] \qquad (4)$$

where

$$K_g^I = K_g^{III} = \frac{4bT_m^0 \sigma_s \sigma_e}{k\Delta h_f}$$

$$K_g^{II} = \frac{2bT_m^0 \sigma_s \sigma_e}{k\Delta h_f}$$

In the equation, V_0 is pre-exponential term which is material related. U^* is the activation energy of transport of polymer chains across the melt/crystal interface. T_c is the crystallization temperature, T_m^0 is the equilibrium melting temperature and T_∞ is a theoretical temperature at which all motion associated with viscous flow stops. $f = 2T_c/(T_m^0 + T_c)$, which is a correction factor for temperature dependence of heat of fusion. K_g is nucleation constant.

The concept of regimes has been experimentally verified for a number of polymers such as polyethylene [48], polyoxymethylene(POM) [49] and PEO [50-51].

3.4.2. Crystallization in melt-miscible polymeric systems

For polymer alloys, the addition of second component (i.e., solute) B to the solvent A will make the crystallization process more complicated. This second component may be crystalline or non-crystalline, may be a polymer or a small molecule and may be a polymer of different structure or the same homopolymer but with different molecular weight.

The research dealing with the polymeric systems usually focuses on the morphology change. Keith and Padden [41-42, 52], for example, investigated the spherulitic textures of polypropylene and polystyrene in each isotactic / atactic blend respectively. Both of the systems showed the relatively open and coarse textures compared with corresponding pure isotactic component and the extent of openness and coarseness increased with the

concentration of the atactic component, as shown in figure 10. It was explained as the impurity (solute) segregation and redistribution in interfibrillar regions and at spherulite boundaries and a parameter $\delta=D/V$ was proposed to describe the spherulitic morphology, in which D is the diffusion coefficient for impurity in the melt and V is the radial growth rate of a spherulite. δ is the distance over which the impurity are excluded from the growth front and determines the lateral dimensions of the fibers. This treatment, initially developed to account for the cellular growth in metallic alloy, has been a convenient way to describe the morphology in a number of polymeric mixtures [53-54].

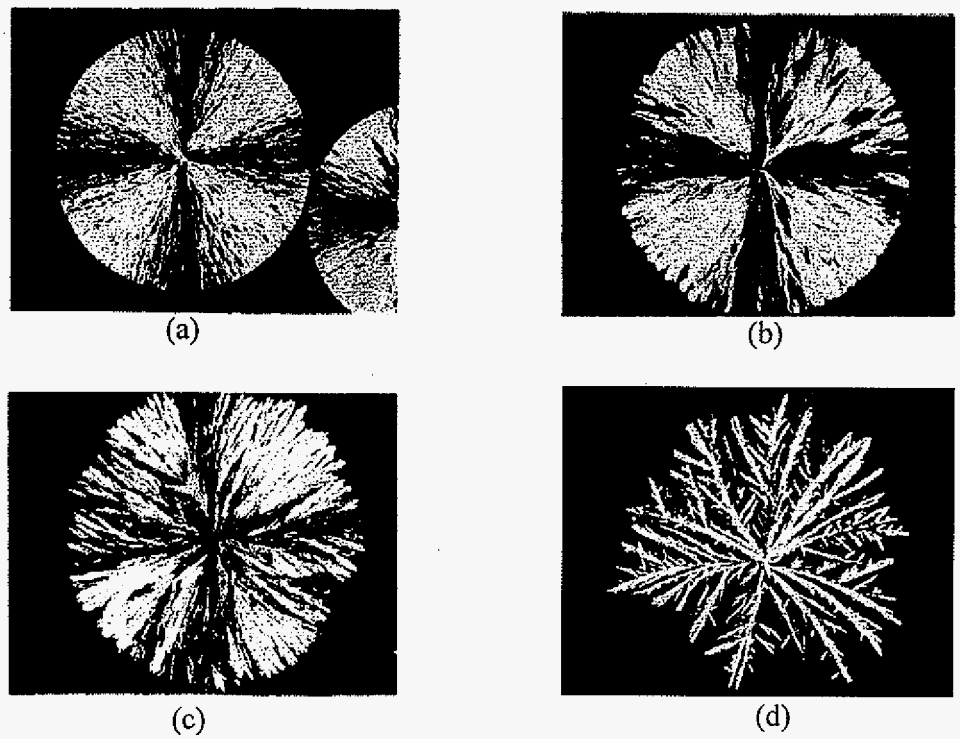

Figure 10. Spherulites grown at 125°C in isotactic polypropylene blended with the following amounts of atactic polypropylene [29]: (a) 0%, (b) 20%, (c) 40% and (d) 90%.

The crystallization kinetics in miscible blends has also been experimentally studied, and most of the investigations focus on the mixtures of crystalline/non-crystalline polymers. Generally, the crystallization rate is reduced by mixing with a non-crystalline polymer because of the dilution of the crystallizable component at the growth front and the reduction in chain mobility due to an increase of glass transition temperature (Tg) of the blends. Typical examples are seen in poly(ethylene oxide) (PEO) / poly(methyl methacrylate)(PMMA) [55], PEO / poly(n-butyl methacrylate) [56], poly(ether ether ketone) (PEEK) / poly(ether imide) (PEI) [57], poly(vinylidene fluoride) (PVDF) / PMMA[58], and poly(caprolactone)(PCL) / poly(vinyl chloride) (PVC) [59] systems except poly(3-hydroxybutyrate) (PHB) / poly(vinyle acetate) (PVAc) system[60], in which PVAc appeared to be accelerating the crystallization rate of PHB and it was attributed to an increased in the nucleation density by blending.

Due to the interplay between two crystallization processes, the microstructure formation and crystallization kinetics of crystalline/crystalline polymeric mixtures are more complex than that of crystalline/amorphous mixtures, thus the crystallization mechanism in this type of systems is far from being really understood. Actually, in the literature, the studies of crystalline/crystalline polymeric systems are very scarce because a miscible polymeric mixture in which two components are crystalline is a rare phenomenon. Up to now, the reported miscible pairs include PVDF/PBA [61], PHB/PVDF [62-63], PHB/PEO [54,64], PEO/PES [65], PEO/PBSU [66], PBSU/P(VDC-VC) [67], Nylon66/Nylon48 [68] systems and PEO blends with two quite different molecular weights[69], etc. These mixtures showed different crystalline behaviors. For example, in PVDF/PBA system, the higher-Tm PVDF component always crystallized prior to the lower-Tm component, namely, they crystallize

sequentially; While in PVDF/PHB system, two components can crystallize simultaneously and form separate phase regions.

In different systems, the changes in growth rate due to the addition of the second component are not the same. In Nylon66/Nylon48 system, the growth rate increases with the content of solute for each phase. In PHB/PEO system with PEO molecular weight 20000 [69], the presence of PEO decreases in the PHB growth rate and the depression increased with the content of PEO; While in another PHB/PEO system, where the molecular weight of PEO was 5000 [54], the growth rate of PHB increased first, then decreased with the addition of PEO. However, the reason for such a non-monotonic variation in growth rate remains unclear.

The effects of the solute (component B) on the crystallization kinetics of solvent (component A) may be summarized from the following aspects: (1) the concentration of the crystallizable component A at the growth front is decreased by an amount proportional to its volume fraction so that the kinetics of crystallization is reduced by this dilution effect. (2) For crystallization to proceed, the second component B must diffuse away from the growth front or the molecules of A must diffuse to the growth interface. This will involve a mutual diffusion process, which is different from the $G_o \exp[-U^* / R(T - T_\infty)]$ term in LH equation. (3) The transport term associated with the solid-liquid interface may be altered because of the change of T_g and thus the temperature range over which crystallization can occur is changed. (4) Most importantly, there exists the thermodynamic interaction between the A and B molecules, which may change the free energy barrier for the formation of nuclei on the crystal surface. Therefore the secondary nucleation theory has to be modified to include these aspects in order to account for the growth kinetics for alloyed polymers. The dilution effect

has been considered by directly multiplying the volume fraction of the component A in eq. 4[70]. G. C Alfonso and T. P. Russell [55] suggested a phenonenological equation describing the growth rate by considering cooperative diffusion in polymer mixtures. In their equation, they also adopted the treatment of Flory [71] and later Mandelkern [72] for free energy of critical nucleus formation in polymer/diluent system. Hiromu Saito et. Al [68] proposed a two-step diffusion mechanism to explain the crystallization kinetics in polymer blends. T. T. Wang and T. Nishi [73] modified the LH equation by taking account of the equilibrium melting point depression and glass transition temperature change upon blending. Boon and Azcue [74] included the effect of mixing entropy on the nucleation energy barrier for forming a two-dimensional critical nucleus, which was similar to the treatment by Mandelkern[72] for a cylindrical nucleus. The growth rate is given by:

$$V = \phi_1 V_0 \exp(-\frac{U^*}{R(T-T_\infty)}) \exp(-\frac{K_g}{T(\Delta T)f} + \frac{2\sigma T^0_{m(a)} Ln\phi_1}{b\Delta h_{f(a)}(\Delta T)f}) \qquad (5)$$

This equation has been widely adopted by other researchers to analyze the growth kinetics.

3.4.3. Polymer eutectic growth

In the crystallization of some polymer blends, the morphologies, in which two components alternately separate into distinct domains, either plate or rod, can be observed, although they are rare. This growth behavior is same as what we call "eutectic growth" in metal and small molecular systems.

Specific to the studies of polymeric eutectic crystal growth, the little studies are very insufficient. P. Smith and A. J. Pennings [75] examined a eutectic system composed of isotactic polypropylene and pentaerythrityl tetrabromide (organic small molecule diluent) by

pulling the alloy, which was sealed in a 4mm ID glass tube, through a 200°C oven then quenching in liquid nitrogen and subsequently fracturing to examine the transverse section. They claimed that the polymer and diluent crystallized simultaneously with a nonplanar growth front with the diluent as leading phase when the growth rate was higher than 3mm/hr. The formed eutectic microstructure was diluent rods in a polymer matrix with a quite irregular dispersion by SEM. After removal of the solid diluent phase from the polymer matrix by sublimation, the pores gave the lateral dimensions of rods, λ_1. As shown in figure 11, those pores exhibited a rather broad size distribution and λ_1 was found to depend on the growth rate R roughly according to the relation $\lambda_1^2 R=10^{-9}$ mm^3/sec, which is in agreement with JH model. Therefore, Smith and Pennings concluded that the eutectic growth of this

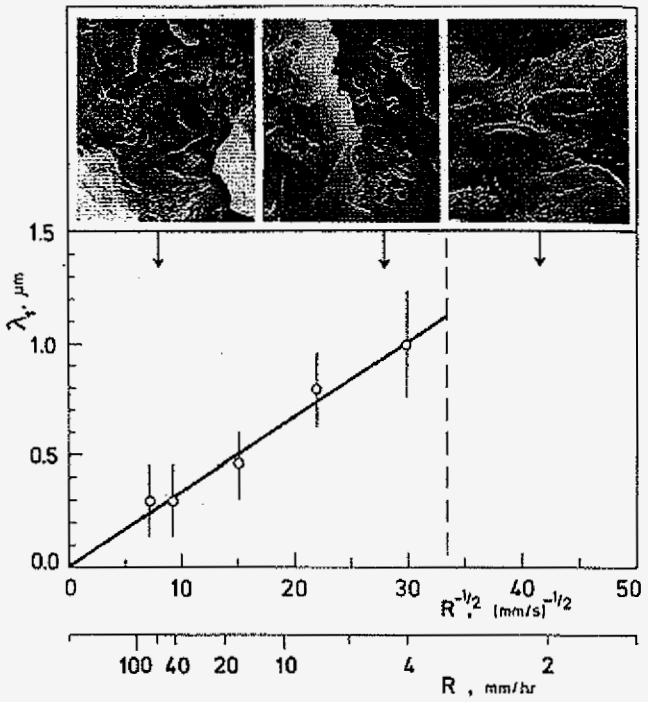

Figure 11. Measured relationship between the growth rate R and the size λ_1 of the pores from the diluent rods in the eutectic structure [75].

system exhibit a metal-like habit at solidification speeds higher than 3mm/hr although both phases are faceted. However, from our point of view, the leading of diluent phase implied that the growth is actually not coupled eutectic growth; therefore the spacing (not the pore size λ_1 but $\sqrt{5}\lambda_1$ according to the volume fraction of the two phase) measured is actually the primary spacing of the diluent phase and has nothing to do with the eutectic spacing and it cannot be compared with the eutectic growth theory. Moreover, the authors did not provide the in-situ growth morphology and the interface temperature was not measured, thus it is not possible to guarantee that coupled eutectic growth occurred in the solidification process.

The other polymeric eutectics crystal growth study was performed on a binary blend of high (270000) and low molecular (5000) weight PEO by Schultz *et.al.* [69]. Undercooled growth was adopted in this research followed by the Atomic Force Microscope (AFM) characterization after preferentially etching out the low molecular weight fraction to get the eutectic spacing λ. The researchers realized the importance of interface kinetic attachment on polymer crystal growth, therefore they adapted JH regular eutectic growth model as the basis and modified it to provide the coupling of kinetic, diffusion and curvature effects at the interface. The operation equation in their work was expressed as $V = V_0(\lambda, m, T)(1 - \bar{C}_B^{\,int})$ or $\frac{Pe}{Pe_0} = (1 - \bar{C}_B^{\,int})$ by the definition $Pe = \lambda V / D_m$. $(1 - \bar{C}_B^{\,int})$ accounted for the dilution effect in front of the growing solid. $V_0(\lambda, m, T)$ was of LH format as $V_0(\lambda, m, T) = K_0 \exp(-\frac{U^*}{R(T - T_\infty)}) \exp(-\frac{K_g}{T(T - T_m)})$, which was obtained by corrected the experimental measured pure polymer growth rate $V_0(T)$ for curvature and solute

undercooling. Thus V was simply the kinetic growth velocity altered by the solute concentration at the interface which in turn was decided by solute diffusion, the kinetic growth velocity and the spacing λ. Then $\bar{C}_B^{int}$ was determined by the same procedure as in JH treatment. In this formulation, the researchers considered the alloy melting temperature change compared with pure polymer, but they didn't mention other possible effects to polymer growth caused by blending (K_0, K_g, U^* etc. in LH equation). More importantly, an assumption of low Peclet number (Pe <1) was made in their formulation. However, the actual Peclet number calculated from their experimental results (blend with 80wt% low molecular weight fraction, 52°C, λ=1μm, and 0.31μm/s, as showed in figure 12 marked with dashed red line, which was claimed to be in good agreement with model calculation by the researchers) was 3.95>>1. Thus their model should be revised to include this high–Pe effect.

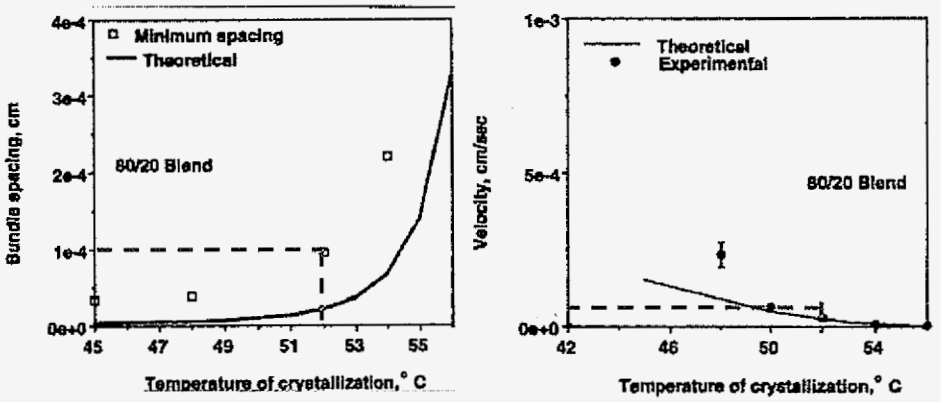

Figure 12. Computed and measured (a) eutectic spacing and (b) growth velocity verse crystallization temperature for 80/20 low/high molecular weight PEO blends [69].

3.4.4. The existing problems in polymer crystallization researches

As mentioned earlier, the undercooled growth technique has been widely used to examine the polymer growth kinetics in experimental studies, in which the nucleation and subsequent growth of a spherulite may be studied separately. In this technique, the growth velocity is calculated by measuring the crystal size as a function of time and the steady state growth rate is then correlated with the bath undercooling to determine the growth kinetics and to disclose the growth mechanism.

However, the relevant temperature and undercooling in Eq. 4 should be the values right at the growth interface, rather than the bath temperature and bath undercooling [76]. At small undercoolings, the difference between the interface temperature and the bath temperature may be negligible; nonetheless at relatively high undercoolings, the interface temperature can be higher than the bath temperature, which may pose a serious problem if the bath temperature is used to evaluate the growth kinetics. However, in directional solidification process, the growth velocity is an input parameter while the interface temperature can be measured by an embedded thermocouple so that both growth velocity and interface temperature can be obtained precisely and thus directional growth should be the appropriate technique to accurately determine the growth kinetics. Actually, this technique has been widely employed in metallic and small molecular systems and it has enhanced our understanding of growth mechanism and to the development of important concepts in solidification area although it has never been used to evaluate the relationship between interface temperature and growth rate in polymers and polymeric systems.

Another obvious drawback in polymeric alloys crystallization kinetics study is the lack of phase diagram. Due to the sluggish crystallization kinetics of a polymeric alloy, it is

rather time-consuming to accurately determine the equilibrium phase diagram experimentally. However, a phase diagram is always essential since it is the graphic representation of the thermodynamics of a system and lots of information can be obtained from phase diagram which will be very helpful to understand the solidified microstructure and evaluate the crystallization kinetics. For example, the melting temperature of an alloy is different from that of a pure solvent, and the former should be used to calculate the driving force for the crystallization of the alloy; however in literatures, the melting temperature of a pure solvent is frequently used to analyze the crystallization kinetics of a polymer blend.

Based on these facts, in this research, we shall determine the phase diagram of polyethylene glycol/ p-dibromobenzene system first to get the accurate eutectic point and liquidus line. Then the directional solidification technique will be employed to evaluate the interface kinetic effects and the composition dependences for both phases in this eutectic system. Directional growth experiments will also be carried out on alloy of eutectic composition to measure interface temperatures and spacings with velocities and thus to acquire the eutectic growth scale laws for this system. Finally, an analytical model can be developed for polymeric eutectic growth based on the appropriate mass transfer mechanism in the liquid and proper consideration of the interface kinetic attachment of polymer chains to the growing interface, which will provide understanding to polymeric eutectic growth mechanism.

References

[1] T. Kobayashi and T. Kuroda, Morphology of Crystals, Part B. ed. I, Terra Scientific Publishing, Tokyo, 1987, p.645.

[2] Laszlo Granasy, Tamas Pusztai, James A. Warren, Jack F. Douglas, Tamas Borzsonyi and Vincent Ferreiro, Nature Materials, vol. 2, 92-96, 2003.

[3] R. Trivedi and V. Laorachan, Acta Metallurgica, vol. 36, no.8, 1941-1950, 1988.

[4] Shan Liu, Je-Hyun Lee, D. Enlow and R. Trivedi, in Solidification Processes and Microstructures, TMS, 257-262, 2004.

[5] Seung Hoon Han, PhD thesis, Iowa State University, 1995.

[6] Claudio De Rosa, Cheolmin Park, Edwin L. Thomas and Bernard Lotz, Nature, vol. 405, 433-437, 2000.

[7] K. Somboonsuk, J.T. Mason and R. Trivedi, Metallurgical and Materials Transactions, vol.15A, 967-975, 1984.

[8] W. W. Mullins and R. F. Sekerka, Journal of Applied Physics, vol. 35, no. 2, 444-451, 1964.

[9] J. S. Langer, Reviews of Modern Physics, vol. 52, no. 1, 1-28, 1980.

[10] R. Trivedi, Yunxue Shen and Shan Liu, in: Proc. Int. Conf. Advanced Materials and Materials Processing, ed. by N. Chakraborty and U. Chatterjee, Tata Magraw-Hill, 42-49, 2001.

[11] R. Trivedi, Shan Liu, B. Echebarria and A. Karma, Solidification Process and Microstructure, TMS, 307-318, 2004.

[12] R. Trivedi, Shan Liu and S. Williams, Nature Materials, vol. 1, 157-159, 2002.

[13] M. A. Eshelman, V. Seetharaman and R. Trivedi, Acta Metallurgica, vol. 36, 1165-1174, 1988.

[14] M. A. Eshelman, PhD thesis, Iowa State University, 1987.

[15] W. Kurz and D. J. Fisher, Acta Metallurgica, vol. 29, 11-20, 1981.

[16] R. Trivedi, Metallurgical Transactions, vol. 15A, 1984, pp. 977-982.

[17] S. N. Tewari and V. Laxmanan, Metallurgical and Materials Transactions, vol.18A, 167-169, 1987.

[18] R. Trivedi, Yunxue Shen and Shan Liu, Metallurgical and Materials Transactions, vol. 34A, 395-401, 2003.

[19] W. Kurz and D. J. Fisher, Fundamentals of Solidification, Trans Tech Publications, Third edition, p.95.

[20] R. Trivedi and W. Kurz, in Solidification Processing of Eutectic Alloys, edited by D. M. Stefanescu, G. J. Abbaschian and R. J. Bayuzick, The Metallurgical Society, 1988.

[21] J. D. Hunt and K. A. Jackson, Transactions of the Metallurgical Society of AIME, vol. 236, 843-852, 1966.

[22] W. A. Tiller, ASM seminar, Recent Research on Cast Irons, p.129-171, 1964, New York

[23] C. Zener, AIME Trans, vol.167, 550-595, 1946.

[24] W. A. Tiller, Liquid Metals and Solidification, p.276-318, ASM, Cleveland, 1958.

[25] K. A. Jackson and J. D. Hunt, Transactions of the Metallurgical Society of AIME, vol. 236, 1129-1142, 1966.

[26] D. Turnbull, Acta Metallurgica, vol. 3, 55-63, 1955.

[27] J.W. Cahn, Acta Metallurgica, vol. 7, 18-28, 1959.

[28] M. Hillert, Inst. Met. Proc. Internat. Symp. on The Mechanism of Phase Transformations in Crystalline Solids, p.231, Manchester, 1969.

[29] J. J. Shapiro and J. S. Kirkaldy, Acta Metallurgica, vol.16, 579-585, 1968.

[30] B. E. Sundquist, Acta Metallurgica, vol.16, 1413-1427, 1968.

[31] F. M. A. Carpay and J. Van Den Boomgaard, Acta Metallurgica, vol. 19, 1279-1286,

1971.

[32] F. M. A. Carpay, Acta Metallurgica, vol. 20, 929-934, 1972.

[33] B. G. Mellor and G. A. Chadwick, Metal Science, vol.8, 65-72, 1974.

[34] Xianhua Kong, Xiaoniu Yang, Enle Zhou, and Dezhu Ma, Polymer Engineering and Science, vol.41, no.5, 786-792, 2001.

[35] Leo Mandelkern, Crystallization of Polymers, second edition, Volume 2, Chapter 9, Cambridge University Press, New York, 2004.

[36] T. P. Russell, H. Ito and G. D. Wignall, Macromolecules, vol. 21, 1703-1709, 1988.

[37] H. D. Keith, F. J. Padden, Jr., and T. P. Russell, Macromolecules, vol. 22, 666-675, 1989

[38] M. J. Avrami, Journal of Chemical Physics, vol. 7, 1103-1112, 1939.

[39] P. Meares, Polymers: Structure and Bulk Properties, Chapter 5, Van Nostrand, New York, 1965.

[40] J. N. Hay, British Polymer Journal, vol. 3, 74-82, 1971.

[41] H. D. Keith and F. J. Padden Jr., Journal of Applied Physics, vol. 35, 1270-1285, 1964.

[42] H. D. Keith and F. J. Padden Jr., Journal of Applied Physics, vol. 35, 1286-1996, 1964.

[43] J. D. Hoffman, G. T. Davis, and J. I. Lautitzen Jr., in Treatise on Solid State Chemistry, vol. 3, Chapter 7, Crystalline and Noncrystalline Solids, N. B. Hannay ed., Plenum, New York, 1976.

[44] J. D. Hoffman, Polymer, vol. 23, 656-670, 1982.

[45] J. D. Hoffman, C. M. Guttman, and E. A. Dimarzio, Faraday Discussions of the Royal Society of Chemistry, vol. 68, 177-197, 1979.

[46] L. H. Sperling, Introduction to Physical Polymer Science, third edition, Chapter 6, A John Wiley & Sons, Inc. Publication, New York, 2001.

[47] Hoffman, John D.; Frolen, Lois J.; Ross, Gaylon S.; Lauritzen, John I., Jr., Journal of Research of the National Bureau of Standards, Section A: Physics and Chemistry 79A(6), 671-99, 1975.

[48] J. D. Hoffman, Polymer, vol. 24, 3-26, 1983.

[49] S. Z. D. Cheng, B. Wunderlich, Journal of Polymer Science, Part B: Polymer Physics, vol. 24, 577-594, 1986.

[50] R. C. Allen, and L. Mandelkern, Polymer Bulletin, vol. 17, 473-480, 1987.

[51] S. Z. D. Cheng, Jianhua, Chen, James J. Janimak, Polymer, vol. 31, 1018-1024, 1990.

[52] H. D. Keith and F. J. Padden, Jr., Journal of Applied Physics, vol. 34, 2409-2421, 1964.

[53] Sossio Commino, Ezio Martuscelli and Clara Silvester, Journal of Polymer Science: Part B: Polymer Physics, vol.27, 1781-1794, 1989.

[54] Jiang-Wen You, Hsiu-Jung Chiu and Trong-Ming Don, Polymer, vol. 44, 4355-4362, 2003.

[55] G. C. Alfonso and T. P. Russell, Macromolecules, vol. 19, 1143-1152,1986.

[56] E El Shafee, Polymer International, 53, 249-253, 2004.

[57] Hsin-Lung Chen and Roger S. Porter, Journal of Polymer Research, vol. 6, no.1, 21-26, 1999.

[58] Hiromu Saito, Tetsuo Okada, Toshihiko Hamane and Takasshi Inoue, Macromolecules, vol. 24, 4446-4449, 1991.

[59] C. J. Ong and F. P. Price, Journal of Polymer Science, Polymer Symposia, 63, 59-75, 1978.

[60] J. N. Hay and L. Sharma, Polymer, vol. 41, 5749-5757, 2000.

[61] J. P. Penning, R. St. John. Manley, Macromolecules, vol. 29, 84-90, 1996.

[62] Jieping Liu, Zhaobin Qiu and Bernd-J. Jungnickel, Journal of Polymer Science, Part B: Polymer Physics, vol. 43, 287-295, 2005.

[63] H.-J. Chiu, H.-L. Chen and J. S. Lin, Polymer, vol. 42, 5749-5754, 2001.

[64] Maurizio Avella and Ezio Martuscelli, Polymer, vol. 29, 1731-1737, 1988.

[65] Zhaobin Qiu, Takayuki Ikehara and Toshio Nishi, Macromolecules, vol. 35, 8251-8254, 2002.

[66] Zhaobin Qiu, Takayuki Ikehara and Toshio Nishi, Polymer, vol. 44, 2799-2806, 2003.

[67] Jeong-Chang Lee, Hare Tazawa, Takayuki Ikehara and Toshio Nishi, Polymer Journal, vol. 30, no. 10, 780-789, 1998.

[68] G. Z Zhang, H. Yoshida and T. Kawai, Thermochimica Acta, vol. 416, 79-85, 2004.

[69] Sudhakar Balijepalli, PhD thesis, University of Delaware, 1996.

[70] Jerold M. Schultz, Polymer crystallization, Chapter 8, Oxford university press, Washington, D. C. 2001.

[71] Paul J. Flory, Journal of Chemical Physics, vol. 17, 223-240, 1949.

[72] L. Mandelkern, Journal of Applied Physics, vol. 26, 443-451, 1955.

[73] T. T. Wang and T. Nishi, Macromolecules, vol. 10, 421-425, 1977.

[74] J. Boon and J. M. Azcue, Journal of Polymer Science, Part A-2, vol. 6, 885-894, 1968.

[75] P. Smith and A. J. Pennings, Journal of Polymer Science: Polymer Physics Edition, vol. 15, 523-540, 1977.

[76] John W. Cahn, W. B. Hillig and G. W. Sear, Acta Metallurgica, vol. 12, 1421-1439, 1964.

CHAPTER 2. RE-DETERMINATION OF SUCCINONTRILE (SCN)-CAMPHOR PHASE DIAGRAM

A paper published in *Journal of Crystal Growth*[1]

Jing Teng[2] and Shan Liu[3,*]

Abstract

Low-melting temperature transparent organic materials have been extensively used to study the pattern formation and microstructure evolution. It proves to be very challenging to accurately determine the phase diagram since there is no viable way to measure the composition microscopically. In this paper, we presented the detailed experimental characterization of the phase diagram of SCN-camphor binary system. Differential scanning calorimetry (DSC), a ring-heater, and the directional solidification technique have been combined to determine the details of the phase diagram by using the purified materials. The advantages and disadvantages have been discussed for the different experimental techniques. SCN and camphor constitute a simple binary eutectic system with the eutectic composition at 23.6wt% camphor and eutectic temperature at 37.65°C. The solidus and the solubility of the

---

[1]Reprinted from *Journal of Crystal Growth*, 2006, 290, 248-257, with permission from Elsevier.

[2]Dept. Materials Science and Engineering, Iowa State University, Ames, Iowa, 50011, U.S.A.

[3]Materials and Engineering Physics Program, Ames Laboratory-USDOE, Iowa State University, Ames, Iowa, 50011, U.S.A.

*Corresponding author: e-mail: shanliu@ameslab.gov, phone: (515) 294-9319, fax: (515) 294-4291.

SCN base solid solution have been precisely determined for the first time in this binary system.

Key words: A1. Phase diagrams, A1. Eutectics, A1. Directional solidification, A3. Succinonitrile-camphor binary system

1. Introduction

Since Jackson and Hunt reported the construction of a temperature gradient stage and the use of plastically crystalline organics [1, 2], these materials have been widely used in the study of solidification microstructures. In order to understand the microstructure length-scales, properties of the experimental materials should be accurately determined, which include thermodynamic properties (phase diagram, enthalpy, entropy, interface energy and its anisotropy, growth kinetics and its anisotropy) and transport properties (mass and thermal diffusivities, viscosity, etc) [3].

A phase diagram is always essential since it is the graphical representation of the thermodynamics of an alloy system. Thermal analysis is usually used in determining the details of a phase diagram. In a metallic alloy, composition in a solid phase can be measured and much information can thus be obtained about the phase boundaries. This together with thermal analysis makes the determination of a phase diagram in a metallic system relatively easier. Moreover the melting temperature of a metallic material is generally well above the room temperature, and the freezing range of a binary metallic alloy is usually a few tens of degrees, therefore the accuracy of determining the phase transformation temperatures is not very critical. However, in the low-melting temperature organic alloys, it proves to be a challenge to accurately determine the phase diagrams. The difficulties come from a few

aspects: the purities of the available organic materials are usually lower than those in pure metallic elements; the interactions between the solute and the solvent molecules are more complex than those between the metal atoms; the relevant temperatures are low; the temperature ranges are usually small and there is no viable way to measure the composition on a microscopic scale. Therefore though Jackson and Hunt reported the use of these plastic crystals in 1960s, there are only a few binary systems with phase diagrams determined with enough confidence, such as succinonitrile (SCN) rich SCN-acetone alloy [4] and SCN-salol [5], SCN-water [6], SCN-NPG and –AMPD [7] and CBr_4-C_2Cl_6 [8].

SCN and camphor are both non-faceted, low-melting temperature plastic crystals [9, 10]. There are four versions of phase diagram of the SCN-camphor binary system [11-14]: all of them recognize that SCN-camphor is a eutectic system, but they differ in details of the phase diagram: liquidus lines, solidus lines, eutectic temperature and composition. In this paper, we re-determined this binary phase diagram experimentally by different techniques: differential scanning calorimetry (DSC), the ring-heater, steady-state dendritic and planar front growth of alloys with known compositions. We start with the preparation of experiments (section 2), present the experimental results in section 3, discuss the results and compare with the previous studies in section 4. A summary is presented in section 5.

2. Experimental

2.1. Purification of experimental materials

SCN was purified by distillation under vacuum followed by multiple passes of zone refining and the purity was characterized by the freezing range of the purified material as 3

mK [15], which corresponded to a purity of 99.9998%[1]. Camphor was purified by sublimation (twice) under vacuum from the 98% commercial product. It is not specified what impurities are present in the commercial camphor. With Nuclear-magnetic Resonance (NMR), a peak for water was clearly identified together with other peaks characteristic of the specific groups in camphor molecules; but for the sublimed camphor, the peak for water disappeared. Gas Chromatography showed a similar result. Therefore water is believed to be the main impurity in commercial camphor.

We further examined the melting point of the raw and purified camphor by DSC and found that the melting temperature of the sublimed camphor was increased from 175.5°C to 178.7°C, indicating that a higher purity of the sublimed camphor was achieved.

2.2. Preparation of alloys and DSC samples

The alloy and sample preparation was conducted in a glovebox under the protection of high-purity N_2. SCN was first weighed and placed in a ground-mouth glass bottle with a magnetic stirrer inside and was melted on a hot-plate inside the glovebox, then camphor of the required amount was subsequently added to the melt, the bottle was capped and the magnetic stirrer was turned on to enhance the camphor dissolution. After camphor was completely dissolved in SCN, five more minutes was allowed for the magnetic stirrer to mix the melt in order to ensure the compositional homogeneity. Within the composition range of (0, 50.1wt%) camphor, this extra processing time did not cause any observable camphor sublimation in the glass bottle. However further increase in camphor presented a challenge in sample preparation since the liquidus temperature increases sharply with camphor content.

[1] This purity level is estimated in the same way as Huang and Glicksman did [Acta Metall., 29 (1981) 701] since same purification processes were used.

This requires that the processing temperature for alloy mixing be correspondingly increased and it becomes difficult to accurately control the alloy composition due to the sublimation of camphor.

After the homogenization, ~10 mg liquid alloy was transferred into a DSC pan for volatile materials and the pan was sealed in the glovebox. Moreover, a thin film of gold was sputtered to the aluminum pan in order to avoid the contamination of SCN base alloy by aluminum [16].

2.3. A ring-heater setup

Figure 1 shows a schematic of the ring-heather used in the present study. It was actually a brass block with a torturous duct inside for silicon oil to flow through. The temperature of silicon oil was controlled by an oil bath to be within ±0.05°C. There was a rectangular channel (0.8×8.2mm) in the mid-height of the brass block for the sample tubing to slide through. A ϕ1.0 mm hole was drilled in the center of the bottom portion. Since the axial position of this ϕ1.0mm hole was the coolest point in the whole block, the last piece of solid was usually observed there when the sample was heated up step by step. A ϕ75μm calibrated K-type thermocouple was used to measure the sample temperature in the block. The overall uncertainty in the thermocouple and temperature recording system is ±0.05°C.

The sample used in the ring-heater setup was contained in a 0.4×8.0 mm rectangular glass tubing. A few near-eutectic alloys (SCN-15.0, 20.0, 25.0wt% camphor) were used to determine the eutectic temperature. When the temperature was below the eutectic temperature, the sample was opaque due to the scattering of light by the fine two-phase eutectic structure. When the eutectic started to melt upon heating, there were many bright

spots in the viewfield and this temperature was taken as the eutectic temperature.

For the liquidus temperature, we first referred to the DSC result and quickly increased the temperature to a value 1.0°C lower than that by DSC. Then we increased the temperature at 0.1°C increment and stayed 5~6 hours at each step to ensure the solute homogenization. The liquidus temperature was taken as the one that the solid totally disappeared. In a subsequent run, we raised the temperature directly to the value 0.2°C lower than the previously evaluated melting temperature. Then the temperature was increased by 0.1°C per step and homogenization time was extended to a day or so in order to determine the temperature the solid completely disappeared. The reproducibility was within ±0.1°C for a few runs of the same alloy composition.

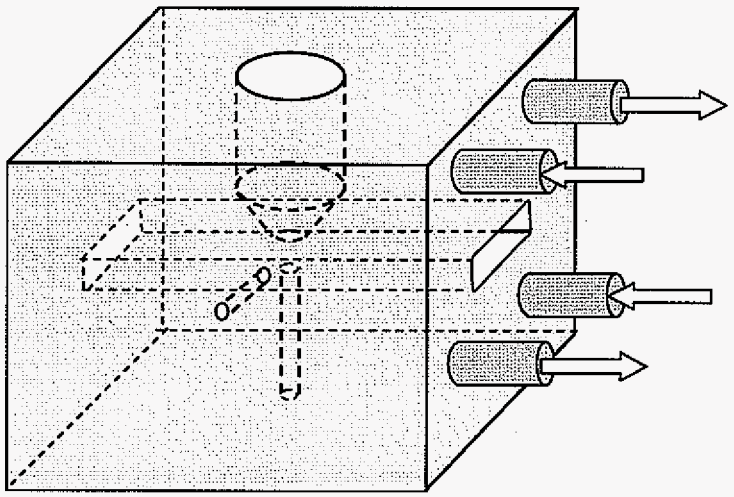

Figure 1. Schematic of the ring-heater used to determine the eutectic and liquidus temperature of an alloy. The hole in the upper half is to house a 20× objective lens, the one in the lower half (ϕ1.0 mm) is to create a slightly cooler position in the sample so that the last piece of solid will stay. The hole in the front part (ϕ0.5 mm) is for insertion of a calibrated thermocouple. The horizontal rectangular channel in the mid-height is for the sample tubing to fit in. The arrows show the flow direction of silicone oil driven by a precision oil bath.

3. Experimental Results

3.1. Calibration of DSC

Since the standard calibration of a DSC apparatus is done with pure In and Zn at a heating rate of 40 K/min, it is far from the present experimental conditions both in the relevant temperature range and the heating rates, therefore a careful calibration was first conducted with pure SCN and pure Ga. As mentioned before, the purity of SCN was 99.9998%, therefore its equilibrium melting temperature was taken as 58.08°C. Ga used was 99.9999% pure and its equilibrium melting temperature was taken as 29.72°C.

The calibration employed here was different than the routine embedded in DSC software. We first ran these two standards at heating/cooling rates in the range for our experiments: 10.0, 8.0, 6.0, 4.0, 2.0, 1.0 and 0.5°C/min. The temperature where the peak ended in a heating curve was taken as the characteristic phase transformation temperature [14]. For the peak of a pure substance melting, this temperature indicated the complete transition to liquid state.

The derived temperature depended on the heating rate. Since the same sample was used for different heating rates, the dependence of this temperature on heating rates was basically due to the thermal lag which is intrinsic to a DSC apparatus. The temperature recorded in DSC is actually the value by a control thermocouple, which is below the sample pan holder and thus away from the sample, i.e., the thermocouple does not show the actual temperature in the sample. However the heat flow recorded by DSC is for the heat absorbed by the sample in the pan, therefore the calibration procedure is crucial for DSC.

This thermal lag depends on the heating rate and the materials contained in the pan. A

faster heating rate enhances the thermal lag and pushes the peak to a higher temperature, therefore the derived melting temperature from a DSC thermograph increases with the heating rates, as shown in Figure 2 for pure SCN. On the other hand, the thermal conductivities of SCN are much lower than those for a metallic material. For example, the thermal conductivity values of liquid and solid SCN are 0.223 and 0.225 W/(m K); those values of liquid and solid aluminum are 95.0 and 210.0 W/(m K) respectively [17]. This indicates that the thermal lag is more pronounced for SCN base materials if the sample mass is the same.

From Fig. 2, a linear regression of the experimental data was applied so that extrapolation to the zero heating rate was taken as the melting temperatures of pure SCN.

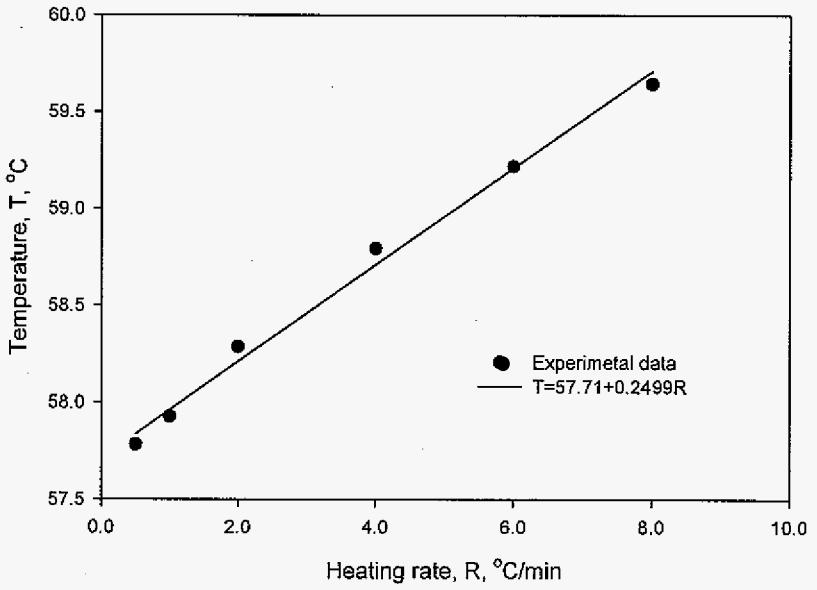

Figure 2. Dependence of the melting temperature of pure SCN on heating rates. The extrapolated value at 0°C/min is used to calibrate the DSC temperature readings within the relevant temperature range.

In comparison with the reported melting temperature of pure SCN, it was clear that there was a -0.37°C deviation (negative). Similar treatment to the case of Ga showed that there was a 0.79°C deviation (positive). Then a linearized error term within the temperature range [29.72, 58.08] °C was used to calibrate the DSC data for the samples subsequently studied.

3.2. Liquidus and eutectic temperature by DSC

Within the composition range of [0, 50.1] wt% camphor, 10 compositions (SCN-0, 0.35, 0.9, 5.1, 10.1, 15.0, 20.0, 25.0, 35.6, and 50.1wt% camphor) were chosen for the determination of both eutectic and liquidus temperature. Figure 3 showed the heating curves for a few compositions with the same heating rate 4.0°C/min. The ordinates for different compositions were intentionally shifted by some amount to avoid overlap. Only the heating curve was used for the evaluation of relevant temperatures since the nucleation undercooling for SCN base alloys can be quite a few degrees.

There was only one peak in the heating curves for very dilute compositions (≤0.9wt %, Fig.3), indicating that only one phase transformation process existed, which was the melting of primary phase. From 5.1wt% to 20.0wt% camphor alloys, two peaks were visible (Fig. 3): the one at a lower temperature was attributed to the eutectic melting and the other one at a higher temperature was for the primary phase melting. With increase in alloy composition (≤20.0wt% camphor), the peak of the primary phase melting was obviously shifted to a lower temperature. The position of the peak of eutectic melting only slightly changed on each curve, which was caused mainly by the overlap of eutectic and primary phase peak. This overlapping effect became more serious with the increase in alloy composition. For the SCN-20.0wt% camphor alloy, the primary phase peak was basically

contained within the eutectic peak and was not observable at this heating rate. For the SCN-25.0wt% camphor alloy, a small peak was just visible at 48.25°C, which was believed to be the primary phase melting peak in the hyper-eutectic region. This peak became more evident with a higher heating rate. Therefore the eutectic composition should lie between 20.0 and 25.0wt% camphor from these DSC scans.

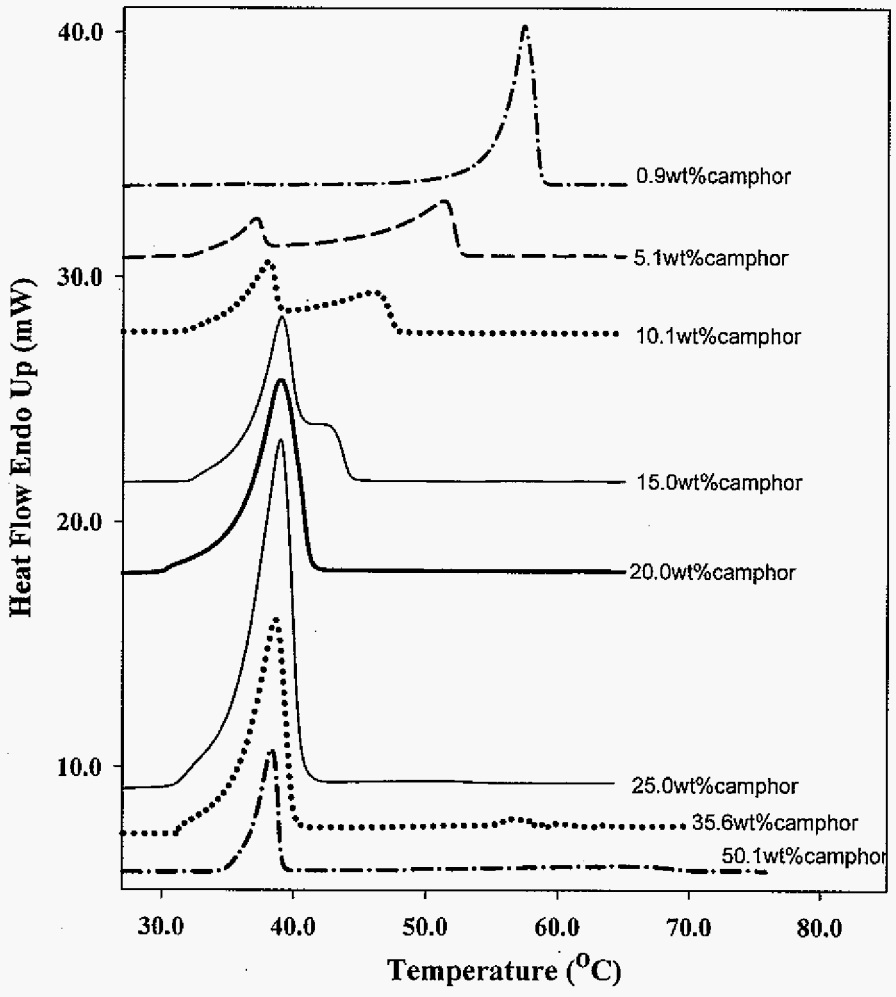

Figure 3. DSC thermographs of SCN- camphor alloys (heating rate: 4.0°C/min).

With further increase in alloy composition (SCN-35.6, 50.1wt% camphor), two peaks clearly appeared in the heating curves. The peak for the primary phase was broad and was not as sharp as the melting peak of the primary phase in the hypoeutectic range. This arose from two factors: (1) the freezing range increases much faster with composition away from the eutectic in the hyper-eutectic alloys than in the hypo-eutectic alloys, which can be seen from those previous reported phase diagrams [11-14]; (2) since the eutectic point is located between [20.0, 25.0]wt% camphor, the solid fraction of a hyper-eutectic alloy is much less than that of a hypoeutectic alloy at the same temperature (above eutectic temperature T_E) if their compositions are equally distant from the eutectic point.

For the same composition at different heating rates, the peak shape looked similar, but the position was slightly different. As the heating rate increased, the peak shifted to a higher temperature due to the thermal lag in a DSC measurement.

From the peak for the primary phase melting, the liquidus temperature was again taken as the one at which the curve became leveled, which corresponded to the transition of heat flow from being controlled by the primary phase melting to that by heat capacity of only liquid phase. Then the same procedure as in Fig. 2 was used to obtain the liquidus temperature of a given composition by extrapolating to 0°C/min heating rate (Fig. 4(a)).

The same method was applied to the eutectic peak (Fig. 4(b)). The extrapolated value at 0°C/min was used to construct the phase diagram and the extrapolated eutectic temperature at 0°C/min varied slightly within (37.51, 38.27) °C with an arithmetic mean of 37.8°C. For those near-eutectic alloys, the eutectic and primary phase melting peak seriously overlapped (Fig. 3) and the above discussion could only be applied if the overlapping peaks was mathematically separable. For those overlapping peaks, we used the Peakfit to perform the

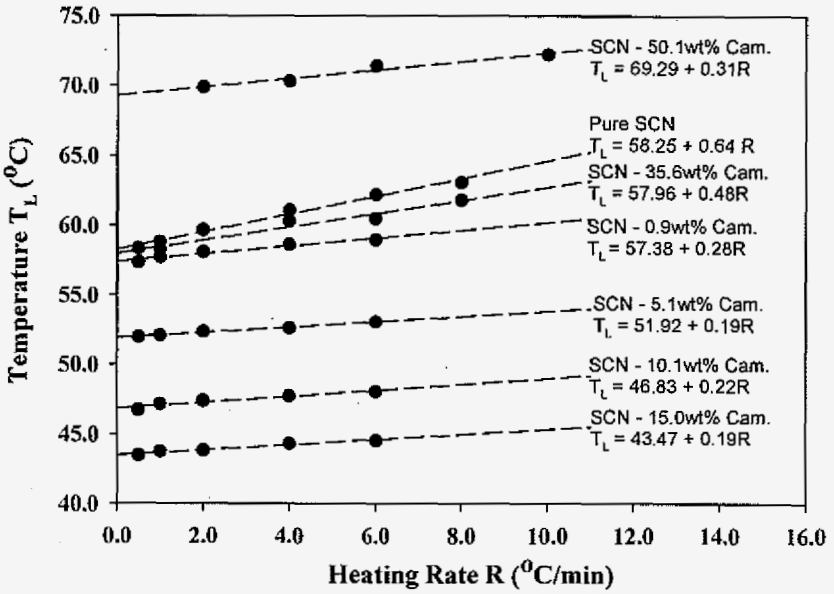

(a)

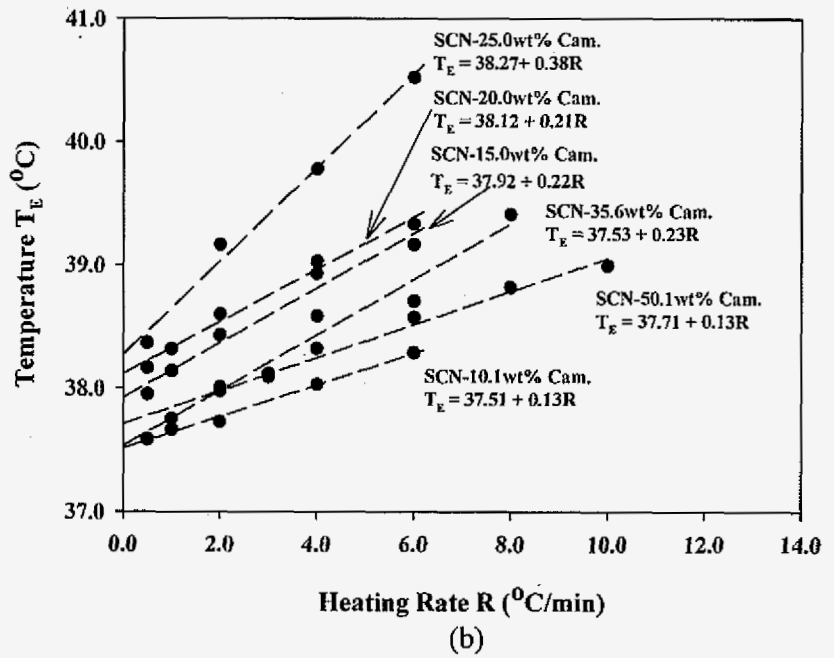

(b)

Figure 4. (a) Liquidus temperature (T_L) from different heating rates; and (b) Eutectic temperature (T_E) from different heating rates.

peak deconvolutions. Since there were many ways to deconvolute the overlapping peaks, we chose the one that gave the best fitting coefficient, which was usually higher than 0.99.

This mathematical operation applied to the case where there still were two distinct peaks in the heating curve, for example, the peaks for SCN-10.0wt% camphor and SCN-15.0wt% camphor in Fig. 3; but not to the case where there was only one peak in the thermograph, i.e., the peaks for SCN-20.0 wt% camphor alloys (Fig. 3). DSC is not applicable to this case and the ring-heater is the only way to get the liquidus and eutectic temperatures correctly.

3.3. Liquidus and eutectic temperature by the ring-heater

Liquidus and eutectic temperatures were also measured in a few near-eutectic alloys by the direct measurement of phase transformation temperatures with a ring-heater (Table 1). For convenience of comparison, the DSC measurement was also included. When the composition was lower than 5.1wt% camphor, the amount of eutectic constituent was little and it was difficult to observe the light intensity change due to the eutectic melting, therefore no measurement was attempted. The arithmetic mean of the eutectic temperature by the ring-heater is 37.65°C.

3.4. Solidus temperature in the SCN base primary phase

The solidus temperature of the primary α phase was directly measured by a calibrated thermocouple embedded in a 0.2×4.0×300 mm sample. The basic requirement for such a measurement is that the solid/liquid interface should move in a steady state planar front at a velocity, V, before the thermocouple tip touches the interface.

Since the maximum temperature gradient, G, is limited in our experimental setup to be at ~5.0 K/mm, only in the dilute alloys is it possible to obtain the steady state planar front growth. We tried three alloy compositions, SCN-0.35, -0.9 and -2.0wt% camphor and successfully measured the interface temperature for a steady state planar front, which should be the solidus temperature for each composition. Table 2 listed the experimental results and the derived equilibrium distribution coefficients at the solidus temperatures. For convenience of subsequent discussions, the liquidus slope at the solidus temperature, $m_L(T_s)$, was also included in this table.

Table 1. Liquidus and eutectic temperature from DSC and ring-heater measurement

C_o (wt% camphor)	Ring-heater		DSC	
	Liquidus (°C)	Eutectic (°C)	Liquidus (°C)	Eutectic (°C)
0.0	58.08		58.08	
0.35	57.42		57.41	
0.9	56.40		57.18	33.67*
5.1	51.82		51.57	36.16*
10.1	47.85	37.60	46.49	37.60
15.0	43.02	37.60	42.78	37.92
20.0	40.24	37.70		
25.0	42.78	37.70		
35.6	55.90	37.63	57.72	38.27
50.1	68.12		69.47	37.71
100.0			178.70	

*: the temperature is believed be to the solvus temperature for SCN base solid solution

Table 2. Solidus temperature measured by planar front growth of 3 dilute alloys					
Composition (wt% camphor)	G (K/mm)	V (μm/s)	T_s (°C)	k at T_s	$m_L(T_s)$ (K/wt% camphor)
0.35	4.46	1.0	55.70	0.20	-1.261
0.9	4.46	0.5	51.61	0.20	-1.093
2.0	5.0	0.15	48.10	0.22	-0.874

3.5. Composition determination of the terminal solid solutions ($C_{S\alpha}$) at T_E

For a binary eutectic system, compositions of two terminal solutions are also important parameters to be quantified. Previous studies indicated that there was no measurable solubility of SCN in camphor; however there were significant conflicts for the solubility of camphor in SCN and it had never been accurately determined [11-14]. For example, Kobayashi et al. [11] just assumed no solubility at eutectic temperature T_E; Taenaka et al. [12] measured the solidus temperatures for two compositions, linearly connected the measured values to the eutectic tie line and gave $C_{s\alpha}$=7.4wt% camphor; Witusiewicz et al. [14] found that the solubility of camphor in SCN at T_E was 0.3wt% camphor.

We have determined the solubility of the terminal solid solutions in the present study by carrying out coupled eutectic growth experiment on alloys with near-eutectic compositions. Since the eutectic is of rod type [14, 18], the volume fraction of the camphor phase can be easily quantified. With densities cited in literatures (Table 3), compositions of the terminal solid solutions can be found through the level rule. We have carried out experiments in SCN-13.0 and 25.0 wt% camphor alloys. For the latter, coupled eutectic growth was easily obtained at a velocity V=1.0 μm/s and the rod spacing was ~30 μm; for the former, a much lower velocity V=0.01μm/s was required and the eutectic spacing was

~100μm. By measuring the camphor rod diameters in the images taken, the volume fraction of camphor in the eutectic constituent was ~0.06 for SCN-13.0wt% camphor and 0.195 for SCN-25.0wt% camphor, which are listed in Table 3.

Table 3. Determination of terminal solid solution composition at T_E

Composition (wt% camphor)	Volume fraction from coupled growth	C_s (wt% camphor)	
13.0	0.06	7.45	present
25.0	0.195	6.87	present
22.0	0.17	6.06	[18]
23.5	0.23 (thickness 10μm) 0.177 (thickness: 13μm)	~0.3 7.08	[14]

Density of SCN base solid solution at T_E: ρ_α=1.022 g/cm^3
Density of camphor at T_E: $\rho_{camphor}$=1.020 g/cm^3

Note to the density data: for camphor, C. C. Mjojo (J. Chem Soc. Faraday Trans., 75(4)(1979)607-732) reported the lattice parameter of the hexagonal phase at 22°C: a= 0.705nm, c=1.150 nm, then the density can be calculated as $\rho_{camphor}$=1.020 g/cm^3. This value was used in the present calculation.

For SCN, the lattice parameters for the BCC phase were slightly different in two publications. Finback (Arch. Math. Naturvidenskab, B42 (1938)77) reported that *a*~0.640nm at room temperature and 2 molecules were in the unit cell. Then the calculated density is 1.015 g/cm^3. In another publication (Finbak and Henry, Tidsskrift for Kjemi og Bergvesen, 2(1942)35-36), they reported that the average value of a=0.637nm and 1.988 molecules on average were in the unit cell, then the derived density is 1.022 g/cm^3. The latter was used in the present study.

With the volume fraction known, the weight fraction can be calculated with the density data shown in Table 3 based on the assumption that the solubility of SCN in camphor is zero [11, 12, 18], therefore the solubility of camphor in SCN can be further calculated by applying level rule at the eutectic tieline. From the present experiment in SCN-13.0wt% camphor, $C_{s\alpha}$=7.45 wt% camphor; from that in SCN-25.0wt% camphor, $C_{s\alpha}$=6.87wt%

camphor.

Yao used SCN-22.0wt% camphor to conduct the coupled eutectic growth experiment and found that the volume fraction of camphor phase was 0.17 [18]. Similar calculation can be made which gave $C_{s\alpha}$=6.06wt% camphor. Witusiewicz et al. also conducted a similar experiment in SCN-23.5wt% camphor alloy and reported that the volume fraction of camphor phase was 0.23 [14], much higher than the present and Yao's study [18]. One possible reason may be related to their sample cell configuration. The authors described that their sample cell was constructed with a 10μm spacer and used this value to quantify the volume fraction of camphor phase. Actually the depth of the sample should be larger than 10 m and this conjecture was supported by the image (figure 11 in [14]) that showed that all the camphor rods were larger than 10μm in diameter. The largest rod diameter in this image was ~13μm. If this value was used to quantify the volume fraction of camphor rods instead of 10μm, then the volume fraction of camphor phase in the coupled eutectic structure was 0.177, and the derived solid solubility at T_E was 7.08wt% camphor, which is in reasonable agreement with our present study and that by Yao [18]. Considering the previous results and the present study, we set the solubility of camphor in SCN at T_E as 7.10wt% camphor and therefore the solute distribution coefficient at T_E is 0.3.

Based on our measurement (Tables 1, 2 and 3), the SCN-camphor binary alloy phase diagram can be drawn in Fig. 5. We limit the composition range to C<50.1wt% camphor, as discussed before.

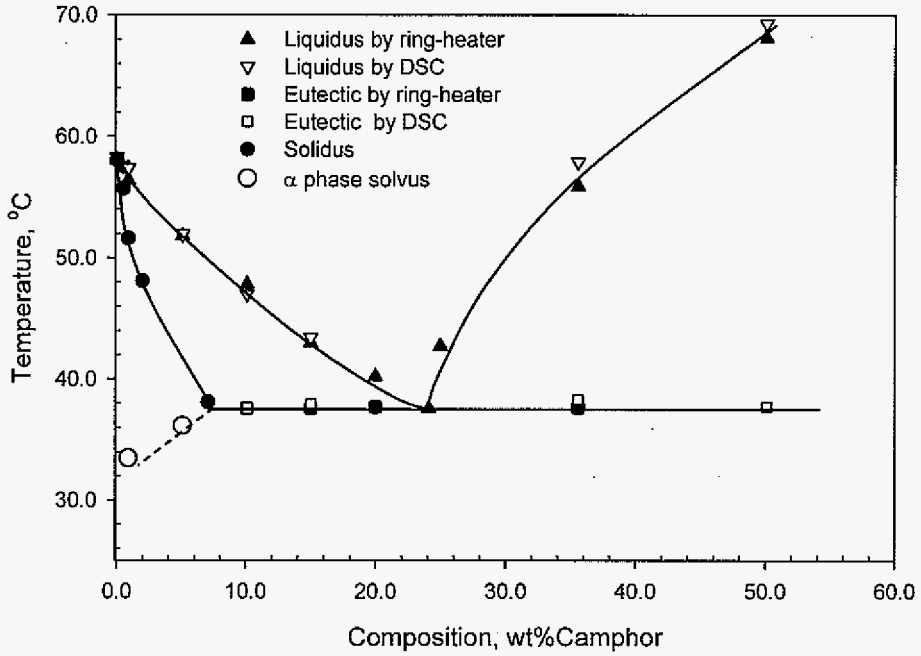

Figure 5. SCN-camphor phase diagram from the present study.

4. Discussion

4.1. Comparison among the measurement techniques

It is clear that the ring-heater and DSC method gave roughly the same result (Table 1). Since the ring-heater method gave the liquidus temperature with an accuracy of ±0.1°C, the agreement between the DSC and the ring-heater technique indicated that the calibration method used in this study was appropriate.

Though both methods are compatible, we consider that the ring-heater is more appropriate than DSC because of the peak overlap for compositions close to the eutectic point by DSC, which explains that only ring-heater data are listed in Table 1 and in Fig. 5. However, since DSC has the advantage of rapid estimate of the liquidus temperature, these

two methods are complement to make efficient and correct determination of a binary phase diagram. The liquidus line for $C<C_E$ can be expressed as:

$$T_L = 58.08 - 1.3825C + 0.0363C^2 - 6.1044 \times 10^{-4} C^3 \qquad (1)$$

For the eutectic tieline temperature, the two methods are equally important and should give the eutectic temperature very close to each other. DSC is reasonably satisfactory if the system is calibrated, as we did in the measurement. The ring-heater method is better for the near-eutectic alloys which have a large amount of eutectic constituent. Since it depends on the change in the illumination intensity in the viewfield, the variation due to the eutectic melting may not be obvious if the eutectic amount is not large, i.e., in the well off-eutectic alloys.

The exact eutectic composition is difficult to obtain. The DSC thermographs of all the near-eutectic alloys showed only a single peak since the amount of primary phase was so little and its melting peak was simply contained within the eutectic one (Fig. 3, the thermographs of SCN-(20.0, 25.0)wt% camphor). Therefore DSC measurement can only roughly determine the eutectic point to lie between 20.0 and 25.0wt% camphor. Directional solidification method is not appropriate either to accurately determine the eutectic composition since all the near eutectic alloys grow in a coupled growth manner even if the temperature gradient is very small [19]. The ring-heater measurement seems to be the most appropriate to determine the eutectic composition. However one should remember that the melting of a sample originates from a microstructure of the previous growth process and a near-eutectic alloy still grows in a coupled manner even though the composition is not exactly eutectic.

The method we used was to do a polynomial curve-fitting of the liquidus lines for

hypo-eutectic alloys (eq. 1) and to extend the curve-fitting to the eutectic temperature 37.65°C, we found that eutectic composition C_E = 23.6 wt% camphor.

From Fig. 5, we may notice that for compositions 10.1, 15.0, 20.0, 25.0, 35.6 and 50.1wt% camphor, the eutectic temperatures were the same within the experimental error. However, for SCN-0.9 and -5.1wt% camphor alloys, the temperatures were apparently lower. We assert that these temperatures may not be the eutectic temperature, but the solvus temperature for α phase, which in turn indicated that the solubility of camphor in SCN at the eutectic temperature should be higher than 5.1wt% camphor.

4.2. Equilibrium solute distribution coefficient

The equilibrium distribution coefficient is of crucial importance in understanding the solidification microstructure evolution. In order to obtain its value, we have used two different methods: measuring the solidus temperature (Table 2) and conducting the direction solidification of an alloy with known composition.

4.2.1. Solidus temperature measurement

With the measured solidus temperature, the corresponding liquid composition can be found through equation (1) and therefore the equilibrium distribution coefficient can be determined, as shown in Table 2. The value of k slightly varies with composition, indicating that both solidus and liquidus are not straight lines.

Taenaka et al. [12] used the same method to determine the solidus temperature for two hypo-eutectic alloys: SCN-2.0 and -5.0wt% camphor and gave the solute distribution coefficient k=0.33. However their results and ours were not comparable since Taenaka et al.

prepared their samples under 1×10^5 Pa argon and therefore the alloys were actually ternary.

4.2.2. Directional solidification experiment

We further conducted the directional growth experiment and verified that the value of k derived above was reasonable. Two types of growth experiments were conducted: (1) steady-state planar front growth to determine the critical growth condition $(G/V)_c$ for a planar interface to remain stable; (2) steady-state dendritic growth to determine the variation of the dendrite tip radius ρ with the growth velocity V.

The marginal stability theory on the dendrite tip radius selection indicates:

$$\rho^2 V = \frac{\Gamma D}{\sigma^* m_L(T_L) C_o (k(T_L) - 1)} \qquad (2)$$

The Mullins and Sekerka linear stability theory on planar front growth indicates:

$$\left(\frac{G}{V}\right)_C = \frac{m_L(T_s) C_o (k(T_s) - 1)}{D \cdot k(T_s)} \qquad (3)$$

Here Γ is the Gibbs-Thomson coefficient, =0.064 K μm [17]; D is the solute diffusion coefficient in liquid; $m_L(T_L)$ is the liquidus slope at the liquidus temperature T_L, =-1.36 K/wt% for an alloy composition C_o=0.35wt% camphor; $m_L(T_s)$ is the liquidus slope at the solidus temperature T_s, =-1.26 K/wt% for 0.35wt% camphor alloy (Table 2). σ* is the stability constant, =0.020 from marginal stability theory. $k(T_L)$ and $k(T_s)$ are the distribution coefficient at T_L and T_s respectively. $(G/V)_c$ is the critical ratio for a stable planar front, $=4.46\times10^{-3}$ K s/μm^2 for SCN-0.35wt% camphor. For this alloy composition, we have conducted the dendritic growth experiment and found that ρ^2V=2271.9 μm^3/s, which was the average value for dendrites under G = 1.39 K/mm within the velocity range 3.17-10.58 μm/s.

If the solute diffusion coefficient is accurately measured, either equation 2 or 3 can be used to calculate the value of k. There are two reported values of D in literatures. For example, Kobayashi et al. employed the side arm climb method to determine $D=0.3\times10^{-9}$ m^2/s based on the assumption that $k=0$ [11]. However from the present study and that by Taenaka et al [12] and Witusiewicz et al. [14], $k\neq0$, therefore the derived D value was questionable. Yao used the value $D=0.82\times10^{-9}$ m^2/s without any reference [18]. Therefore more careful study is still needed to determine the solute diffusion coefficient in SCN-camphor alloy system.

One can easily see from equations (2) and (3) that their multiplication can eliminate D and C_o. If one assumes that k may not significantly change within the freezing range of the alloy, then one obtains:

$$(\rho^2 V)\left(\frac{G}{V}\right)_C = \frac{\Gamma}{k\sigma^*}\cdot\frac{m_L(T_s)}{m_L(T_L)}\cdot\frac{k(T_s)-1}{k(T_L)-1} \approx \frac{\Gamma}{k\sigma^*}\cdot\frac{m_L(T_s)}{m_L(T_L)} \qquad (4)$$

Therefore:

$$k \approx \frac{\Gamma}{\sigma^*}\cdot\frac{1}{(\rho^2 V)}\cdot\left(\frac{V}{G}\right)_c\cdot\frac{m_L(T_s)}{m_L(T_L)} = 0.24$$

This calculated value is 20% higher than the value derived from the direct measurement of solidus temperature. Considering the errors related with the measurements of tip radius and the simplifications made in the calculation, we believe that the values of k by these two methods agree with each other.

Sato et al. [13] simply used Van't Hoff equation to calculate the solidus and reported $k=0.76$ (liquidus slope at the dilute limit: $m_L(C\rightarrow0)=-1.04$ K/wt%) , three times higher than

the value obtained in the present study. We tried the similar calculation with $m_L(C\rightarrow 0)$=-1.38 K/wt%, and obtained k=0.70, which was slightly smaller than the calculated values by Sato et al. [13], but still well away from the our experiment value k=0.20~0.30. One reason is that the magnitude of the liquidus slope at C→0 may be significantly larger than the one derived from the liquidus temperatures of the concentrated alloys. Our experimental measurement started with the alloy composition C=0.35wt% camphor, and the next one was 0.9wt% camphor. If we evaluated the slope just based on these two measurements together with the melting temperature of pure SCN, the liquidus slope is ~1.9 K/wt% camphor, nearly doubling the value by Sato et al. [13]. Another reason is the assumption of dilute ideal solution. The components here are two organic molecules with each having special groups in their molecular structures, therefore SCN and camphor cannot form ideal solutions, as the thermodynamic evaluation in this system has shown [14].

With the derived value of k, one can calculate D from either equation (2) or (3), which gives $D=0.28\times10^{-9}$ m^2/s. Then we checked the dendrite side arm climb experiment by Kobayashi et al. [11] and found that instead of $D=0.3\times10^{-9}$ m^2/s, it was actually $D/(1-k)=0.3\times10^{-9}$ m^2/s; then actual $D = 0.23\times10^{-9}$ m^2/s, which is not far from the value from the present growth experiments.

4.3. Comparison with previous studies of the phase diagram

Table 4 compares the all studies in the phase diagram for SCN-camphor and related sample preparation methods. Little was known about the details of work by Kobayashi et al. [11] except that DSC was used and that the materials were of commercial purity. They put the eutectic point at 15.5wt% camphor with eutectic temperature T_E=307.0K. The eutectic

was composed of two pure components and the liquidus lines were simply linear.

Sato et al. [13] used a ring-heater to determine the liquidus temperature in α phase region up to ~11.5wt% camphor, therefore nothing about the eutectic details was available. They used the purified SCN and as-received camphor and the samples were prepared under 1×10^5Pa Ar. Upon equilibrium with Ar, the melting temperature due to the presence of argon dropped from 331.24K to 330.0K since Ar has a finite solubility in SCN [20, 21]. The liquidus was found to be linear and the slope was determined to be -1.04K/wt%.

Taenaka et al. [12] purified both SCN and camphor. They took great care to melt/solidify their master alloys under high purity Ar to make sure that Ar dissolution in SCN reached the equilibrium state. The authors recognized the effect of Ar in their sample preparation during the subsequent measurement and acknowledged that the phase diagram they determined was actually the isopleth at a fixed Ar composition. They noticed the similar melting temperature drop for SCN and slanted tieline, clearly indicating the nature of a ternary system. They employed the directionally grown planar front interface to determine the solidus and found that the equilibrium distribution coefficient was not zero, the solidus and liquidus were linear and the maximum solubility of camphor in SCN was 7.4wt% camphor.

The most recent study in SCN-camphor phase diagram was conducted by Witusiewicz et al. [14]. They conducted the thermodynamic analysis in this alloy system, used Calphad to calculate the phase diagram and compared the calculation with their experimental determination. They used DSC to determine the liquidus temperature; however no details were given about the treatment of the peak overlap in the near eutectic alloys. The eutectic composition was 23.3wt% camphor and the temperature was 311.5K (38.3°C). There

was very limited solubility for both terminal solid solutions at eutectic temperature. The samples were prepared from purified SCN and camphor in a glovebox under Ar atmosphere, therefore some dissolution of Ar was expected, as has been shown in [12, 13, 20, 21]. Surprisingly, it seemed that Ar did not affect the alloy composition at all and the eutectic temperature was fixed within the experimental error, which was in contradiction with the observation by Taenaka et al. [12]. The reason for such a contradiction remains unclear. One possibility may be that Witusiewicz et al. [14] prepared their samples in a much shorter time so that Ar dissolution in the alloy was negligible.

Table 4. Comparison of SCN-Camphor phase diagram by different research groups

Property (unit)	Values				
	[11]	[12]	[13]	[14]	Present
$T_{m,SCN}$ (K)	327.5	329.9	330.3	331.3	331.28
T_E, (K)	307.0	306	--	311.5	310.85
C_E (wt%cam*)	15.5	26.6	--	23.3	23.6
m_{SCN}** (K/wt%)	-1.32	-0.9	-1.04	--	$-1.3825+0.0726C$ $-1.83\times10^{-3}C^2$
k_{SCN}**	0	0.33	0.76	0.013 at T_E	0.33 at T_E 0.20~0.24 at C≤2.0wt%cam.
Materials	SCN: impure Cam: impure	SCN: distillation & zone refined Cam: distilled	SCN: distillation Cam: impure	SCN: distillation & zone refining Cam: sublimed	SCN: distillation & zone refining Cam: sublimed
Atomsphere	?	10^5 Pa Ar	1 bar Ar	Ar	Dry N_2

* Cam: abbreviation for "camphor";
** m_{SCN} ad k_{SCN} are the liquidus slope and equilibrium distribution coefficient in the hypo-eutectic region.

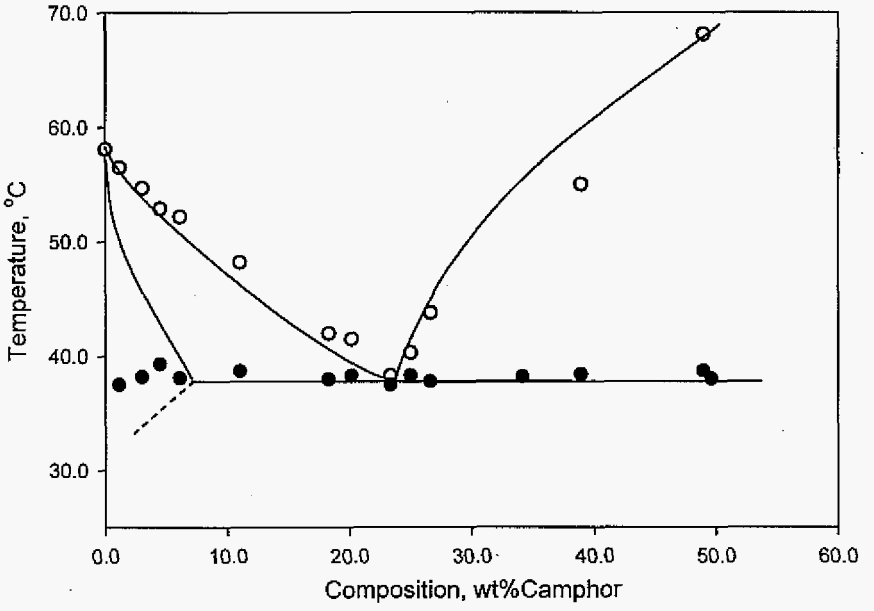

Figure 6. Comparison of the experimentally determined phase diagram in the present study (lines) and that (filled and open circles) by Witusiewicz et al. [14].

In our study, we used high-purity dry N_2 as the protective atmosphere in the glovebox where DSC and directional solidification samples were prepared. N_2 was found to be insoluble in SCN [15]. The DSC pans were sputtered with gold which is inert to SCN [16].

A comparison is made between the present study and that by Witusiewicz et al. [14] in Fig. 6. The agreement is reasonable with respect to the liquidus lines, eutectic composition and temperature, but the significant difference lies in the solidus line of the SCN base phase. We directly measured the solidus temperature by directional growth technique for a few dilute compositions and employed the coupled growth method to find $C_{s\alpha}$=7.1wt% camphor and we believe that coupled eutectic growth method employed in the present study is the most appropriate to determine $C_{s\alpha}$. Our analysis was applied to the coupled growth

experiment by Yao [18] (Table 3) and a similar value of $C_{S\alpha}$ was obtained.

5. Summary

The SCN-camphor binary phase diagram was thoroughly studied experimentally by different techniques and with the high-purity materials and the following conclusions can be reached:

1) DSC is appropriate to determine the eutectic temperature, melting temperature of a pure material and the liquidus temperature with distinctly separated peaks. DSC should be calibrated within the corresponding temperature range for these low-melting temperature organic materials.

2) A ring-heater is the most appropriate method to determine the phase transformation temperature for a pure component melting, eutectic and liquidus temperature especially when there are overlapping peaks in the DSC thermograph.

3) SCN and camphor constitute a simple binary eutectic system and the eutectic temperature is about 37.65°C and the composition is 23.6wt% camphor.

4) The liquidus line is convex in the hypo-eutectic region and is concave in the hyper-eutectic region with respect to the liquid. In the hypo-eutectic region, the liquidus line can be expressed as: $T_L = 58.08 - 1.3825C + 0.0363C^2 - 6.1044 \times 10^{-4} C^3$, therefore the liquidus slope varies with alloy composition.

5) Directional growth of a steady state planar front is the only viable way to measure the solidus temperature for these low-melting temperature organic alloys. Equilibrium distribution coefficient k=0.2~0.24 for a composition up to 2.0wt% camphor. The

maximum solubility in SCN base solid solution determined by coupled eutectic growth is equal to 7.1wt% camphor and the equilibrium distribution coefficient at T_E as 0.30.

Acknowledgement

The authors would like to thank Prof. R. Trivedi for the suggestion of using coupled growth to derive the solid solubility at eutectic temperature. This work was supported by DOE-BES and was carried out at Ames Laboratory which is operated by Iowa State University for the Office of Basic Energy Science, Division of Materials Science, U. S. Department of Energy under Contract No. W7405-Eng-82.

References

[1] K. A. Jackson and J. D. Hunt, Acta Met., 13(11) (1965) 1212.

[2] J.D.Hunt, K.A.Jackson amd H. Brown, Review Scientific Instruments., 37(6) (1966)805.

[3] R. Trivedi and W. Kurz, International Materials Reviews, 39(2) (1994) 49.

[4] M.A.Chopra and M.E.Glicksman, Metall. Trans. A, 19A (2) (1988)3087.

[5] D. Venugopalan, PhD Thesis, McMaster University, (1982).

[6] J. E. Smith Jr., D.O.Frazier and W.F.Kaukler, J. Cryst. Growth, 112 (1991) 84.

[7] V. T. Witusiewicz, L. Sturz, U. Hecht and S. Rex, Acta Mater., 53(1)(2005)173.

[8] W.F.Kaukler and J. Rutter, Mater. Sci. Engrr., 65(2)(1984)L1.

[9] E. Rubinstein, M.E.Glicksman, B.W.Mangum, Q. T. Fang and N.B.Singh, J. Cryst. Growth, 89(1) (1988)101-110.

[10] J. N. Sherwood, The Plastically Crystalline State: Orientationally Disordered Crystals, John Wiley & Sons, INC, New York, 1979, Chapter 1.

[11] K. Kobayashi, Y. Seko and P.H.Shingu, J. Jpn. Inst. Metals, 45(6)(1981)647.

[12] T. Taenaka, H.Esaka, S.Mizoguchi and H. Kajioka, J. Jpn. Inst. Metals, 52(5) (1988)491.

[13] T. Sato, W. Kurz and K. Ikawa, Trans. Jpn. Inst. Metals, 28(12) (1987)1012.

[14] V.T.Witusiewicz, L. Sturz, U. Hecht and S. Rex, Acta Mater., 52 (2004) 4561.

[15] S. Louise, PhD Dissertation, Iowa State University (Ames, Iowa, USA, 2004).

[16] E.R. Rubinstein, S.H.Tirmizi and M.E.Glicksman, J. Cryst. Growth, 106(1990) 89.

[17] W. Kurz and J.D.Fisher, Fundamentals of Solidification, Trans. Tech. Publications Switzerland, 1992, p.93 (Appendix 14).

[18] X. Yao, MS Thesis, Northwestern Polytechnical University (Xi,an, China, 1992).

[19] R. M. Jordan and J. D. Hunt, Metall. Trans., 2 (1971) 3401.

[20] M.A.Chopra, M.E. Glicksman and N.B.Singh, Metall. Trans., 19A (1988) 3087.

[21] A. Ludwig and W.Kurz, Acta. Mater., 44(9) (1996) 3643.

CHAPTER 3. DETERMINATION OF THE SOLUTE COEFFICIENT BY THE DROPLET MIGRATION METHOD

A paper published in *Metallurgical and Materials Transactions A*[1]

Shan Liu[2,*], Jing Teng[3], and Jeongyun Choi[3]

Abstract

Further analysis of droplet migration in a temperature gradient field indicates that different terms can be used to evaluate the solute diffusion coefficient in liquid (D_L) and that there exists a characteristic curve which can describe the motion of all the droplets for a given composition and temperature gradient. Critical experiments are subsequently conducted in succinonitrile (SCN)-salol and SCN-camphor transparent alloys in order to observe dynamic migration processes of a number of droplets. The derived diffusion coefficients from different terms are the same within experimental error. For SCN-salol alloys, D_L =(0.69±0.05)×10^{-3} mm^2/s and for SCN-camphor alloys, D_L =(0.24±0.02)×10^{-3} mm^2/s.

---

[1]Reprinted with permission from *Metallurgical and Materials Transactions A,* 2007, 38, 1555-1562.

[2]Materials and Engineering Physics Program, Ames Laboratory-USDOE, Iowa State University, Ames, IA, 50011, U.S.A.

[3]Dept. Materials Science and Engineering, Iowa State University, Ames, IA, 50011, U.S.A.

[*]Corresponding author: e-mail: shanliu@ameslab.gov, phone: (515) 294-9319, fax: (515) 294-4291.

I. Introduction

Liquid inclusions in a solid matrix can move in a temperature gradient field. The movement operates through the melting of the solid side in contact with the liquid inclusion with a slightly higher temperature and re-solidification of the side with a slightly lower temperature. For simplicity of the subsequent discussion, we refer to the melting side as the leading edge and the re-solidification side as the trailing edge.

The driving force for the melting/re-solidification is the composition gradient Gc, which is determined by the imposed temperature gradient G_L through the relationship $Gc=G_L/m$, m is the liquidus slope. Since melting and re-growth occur simultaneously under the diffusive solute flux, this technique has been used to evaluate the solute diffusion coefficient in the melt, melting and growth kinetics, etc [1-8]. Migration of liquid pockets also plays a significant role in the side arm climbing/coarsening in a solidification process, microsegregation, and planar front initialization [9-12].

Liquid inclusion movement in a temperature gradient field can be described by (here neglecting solute diffusion in solid):

$$V = -\frac{D_L G_L}{mC_L^*(1-k)} \qquad (1)$$

V is the droplet migration velocity, C_L^* is the liquid composition at the solidifying edge (i.e., the trailing edge), k is the equilibrium solute distribution coefficient and D_L is the solute diffusion coefficient in liquid. Since m and k can be obtained from a phase diagram and G_L is set externally, the diffusion coefficient can be calculated if V and C_L^* can be measured with confidence. However a direct measurement of C_L^* is usually not possible for a moving

droplet.

Watson and Hunt [8] applied this technique to determine the diffusion coefficient in Al-Cu alloys. They embedded two thermocouples in the sample to first determine the temperature gradient and obtained the average liquid composition within the temperature range indicated by the thermocouples. They calculated the average droplet migration velocity by measuring the distance of the leading edge of the droplet band in a few interrupted experiments. Then they used eq. (1) to derive the diffusion coefficient by incorporating the *average* velocity, *average* composition and *average* liquidus slope in the relevant temperature range. Critically speaking, this method is not appropriate since flux balance is only for the instant interface velocity and instant interface composition.

In the present study, we employed the droplet migration method to determine the solute diffusion coefficient of dilute SCN-salol and SCN-camphor alloys. The transparent nature of these materials makes it possible to observe the dynamic movement of an individual droplet in situ. The results show that a droplet moves in a slightly accelerating manner and its size increases slightly. Then we find that at each thermal gradient there exists a characteristic migration curve which is independent of the droplet size. The diffusion coefficient can be evaluated by different terms if eq. (1) is transformed to describe the change in the instant position of a droplet with time, which gives the same value within the experimental error. Experimentally derived diffusion coefficients are compared with the data available in literatures [13-16].

II. Further analysis about the droplet migration equation

Figure 1(a) schematically shows two instants of a droplet migration process. A

temperature gradient is imposed on the sample along the x direction. The origin of x axis is set at the solid/liquid interface and the axis points into the liquid. Initially, the droplet is located at the position S and has a diameter $d(t=0)$, the temperature at the trailing edge is $T(t=0)$ and the corresponding composition in the liquid is $C_L^*(t=0)$. After some time t, the droplet migrates a distance SS' to the position S' and the corresponding temperature and liquid composition are $T(t)$ and $C_L^*(t)$.

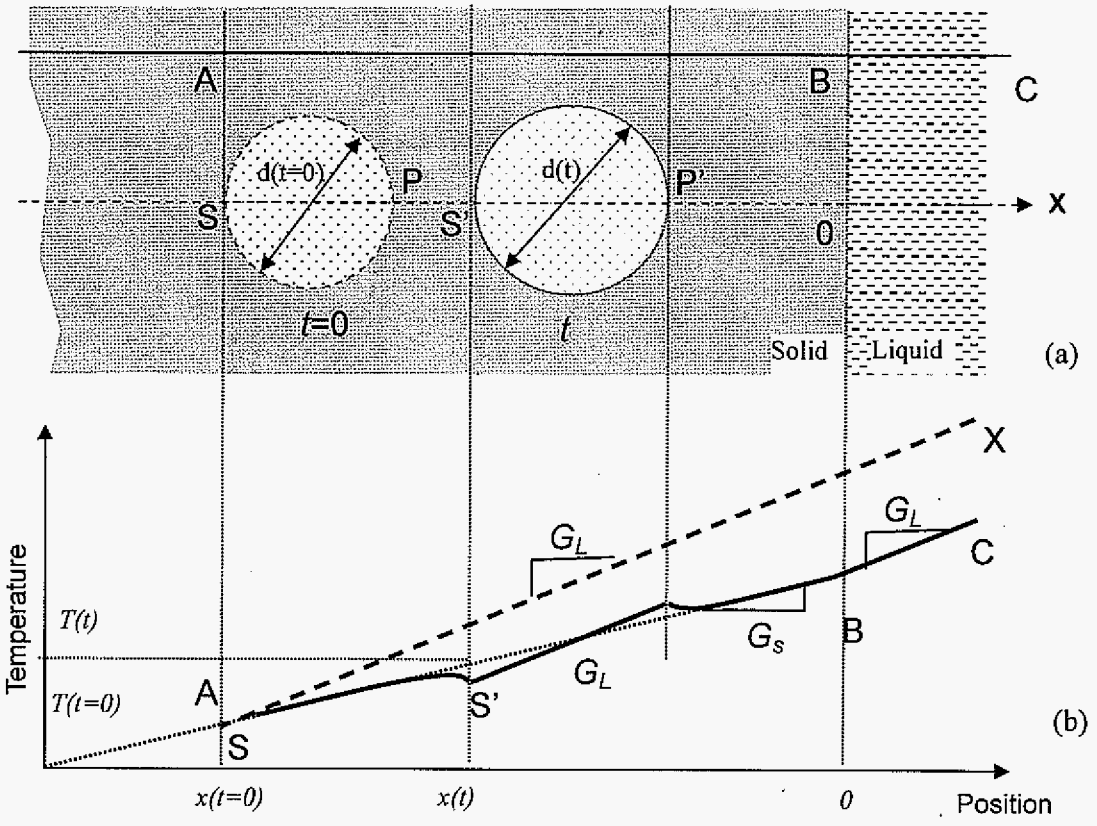

Figure 1. (a) Showing that initially a droplet of diameter $d(t=0)$ is at position S. After some time t, it moves to S' with the diameter increasing to $d(t)$. (b) Showing the possible temperature profile along the lines ABC and SS'X. ABC is located in the solid well away from the droplet; while SS'X is along the center of the droplet. The dash line is for the case assuming that there was a continuous liquid between S and X.

In Fig.1, a dashed line schematically shows the temperature profile if there was continuous liquid in the region between S and X. This line has a slope G_L, which is parallel to the temperature profile within the droplet at time t. If this was the case, the temperature T(t) could be written as:

$$T(t) = T(t=0) + G_L \cdot (x(t) - x(t=0)) \qquad (2)$$

A few assumptions needs to be made in order to relate $C_L^*(t)$ to *T(t)*: (1) the effect of curvature on liquid composition is ignored; (2) the kinetic undercooling is not taken into account since they are negligibly small for a material with a diffuse solid/liquid interface; (3) the liquidus line is straight in the relevant temperature range; and (4) the temperature gradient G_L is constant, then the liquid composition at S', $C_L^*(t)$, could be written as:

$$C_L^*(t) = C_L^*(t=0) + \frac{G_L}{m}(x(t) - x(t=0)) \qquad (3)$$

Equation (3) has been used in all the previous studies of liquid inclusion migration in a temperature gradient field. However, it is based on the assumption that there is a continuous liquid along SS'X, which is definitely not the case for a droplet or a few droplets embedded in a solid matrix. For the case of droplet migration (Fig. 2), the solid matrix is continuous except the regions occupied by droplets. From Fig. 1, it is clear that the temperature at S' should be closer to that determined by the line ABC at a position *x(t)*, rather than by the dashed line at x(t), then T(t) should be better approximated as:

$$T(t) = T(t=0) + G_s \cdot (x(t) - x(t=0)) \qquad (2')$$

Correspondingly the equilibrium liquid composition at this position is:

$$C_L^*(t) = C_L^*(t=0) + \frac{G_s}{m}(x(t) - x(t=0)) \qquad (3')$$

Clearly the only difference is that G_s replaces G_L for the determination of the temperature and composition in the droplet migration process. For SCN base dilute alloys, the solid and liquid phase have almost the same thermal conductivity, therefore $G_s \approx G_L$, and the correction is negligible. However if a material has very different thermal conductivities in the solid and liquid phase, the correction should be significant.

With the appropriate liquid composition and the flux balance at the trailing edge, eq. (1) can be re-written as:

$$V(t) = \frac{dx(t)}{dt} = -\frac{D_L G_L}{m(1-k)(C_L^*(t=0) + \frac{G_s}{m}(x(t) - x(t=0)))} \tag{4}$$

Then one can obtain:

$$t = \alpha(x(t) - x(t=0)) - \beta(x(t) - x(t=0))^2 \tag{5}$$

with $\alpha \equiv -\frac{mC_L^*(t=0)(1-k)}{D_L} \cdot \frac{1}{G_L}$ (6)

$$\beta \equiv \frac{1-k}{2D_L} \cdot \frac{G_s}{G_L} \tag{7}$$

Therefore D_L can be found through β by fitting the droplet migration process into eq. (5). On the other hand, since droplets are initially located at different positions x(t=0), $C_L^*(t=0)$ varies from droplet to droplet and can be expressed as a function of the initial position:

$C_L^*(t=0) = C_L^*(x=0) + \frac{G_s}{m} x(t=0)$, where $C_L^*(x=0)$ is the liquid composition at the solid/liquid interface. Then α can be written as:

$$\alpha = \frac{-mC_L^*(x=0)(1-k)}{D_L G_L} - \frac{G_s}{G_L} \cdot \frac{1-k}{D_L} x(t=0) \tag{8}$$

Therefore D_L can also be obtained through $d\alpha/dx(t=0)\left(=-\frac{G_s}{G_L}\cdot\frac{1-k}{D_L}\right)$ if the migration of many droplets is carefully quantified[1]. For SCN base dilute alloys, $d\alpha/dx(t=0)=-\frac{1-k}{D_L}$.

Next, we will present our experimental results on droplet migration in dilute SCN-camphor and SCN-salol alloys and analyze the experimental data based on the above derivations.

III. Experimental

We used transparent binary alloys SCN-0.7wt% salol and SCN-0.35wt% camphor for the present experimental investigation since these binary systems are widely used for studying pattern formation and microstructure evolution in a solidification process [14-20]. The phase diagram of SCN-salol was determined by Kirkaldy et al. [17], which shows that the solidus and liquidus are straight lines from 0 to 10.0wt%salol, the composition range they studied. The phase diagram of SCN-camphor was recently re-determined by Teng and Liu [19] and the solidus and liquidus are rather straight in the composition range [0, 2.0] wt%camphor. Since dilute compositions were used in this study, we consider that m and k are constant for both alloy systems. For SCN-0.35wt%camphor alloys, m = -1.32 K/wt%, and k = 0.24 [19]. For SCN-0.7wt%salol, m = -0.68 K/wt% (or -180 K/(mole fraction)) [17] and k = 0.1 (Appendix).

---

[1] The composition at the solid/liquid interface can be determined from the first term of eq. (8). If we define $\gamma \equiv \frac{-mC_L^*(x=0)(1-k)}{D_L G_L}$, then $C_L^*(x=0)=\frac{\gamma\cdot G_s}{m\cdot(d\alpha/dx(t=0))}$. It is usually higher than the alloy composition C_o, indicating that there exists a solute enriched layer ahead of a stationary solid/liquid interface. The solute enrichment in this layer is related to the Soret effect of the alloy used and may dominate the dynamics of the initial transient [12, 21]. Since it is not related to the diffusion coefficient analysis for the present work, we will not evaluate this term.

Since the compositions are very low, the freezing ranges are only a couple of degrees: for SCN-0.35wt%camphor, the freezing range is 1.5°C; and for SCN-0.7wt% salol, it is 4.3°C, therefore we will ignore the temperature dependence of the diffusion coefficient in the following analysis.

SCN was purified by distillation under vacuum followed by multiple zone refining. Camphor was purified by sublimation (twice) under vacuum and salol was purified by multiple zone refining. The alloys were prepared in a glovebox filled with dry N_2. Master alloys were infused into rectangular glass tubes (0.2H×4.0W×300L mm). The as-solidified microstructure was composed of SCN base dendrites when a sample was cooled down naturally. The orientation of the sample was chosen so that one {100} plane was parallel to the glass surface and one <100> direction was aligned with the length of the glass tube. The inter-dendritic segregation leads to formation of some liquid droplets once the sample was placed onto the temperature gradient stage. In this way, the direction of the droplet migration would be in a <100> direction since the temperature gradient was applied along the length of the sample.

The sample was placed onto a temperature gradient stage with the preset gradient. Since the rectangular glass tube had a very thin wall (200 μm thick), thermal equilibrium was reached within a couple of minutes. The droplet migration process was observed under a microscope and recorded directly into a computer after the sample was placed on the stage for ~5 minute. A series of images were continuously recorded for a fixed viewfield with fixed intervals and the migration process was digitized from these images by measuring the trailing edge of each droplet.

IV. Experimental results

We employed two different temperature gradients for each material. Salol is slightly more dense than the solvent SCN; while camphor has almost the same density as SCN, therefore the density of liquid in a droplet should be very close to the solid matrix and droplet migration can be assumed to be horizontal and parallel to the top and bottom of the sample cell. Nonetheless, we did observe that a droplet may touch the glass and disappear if its size is too large (e.g. >100 μm), therefore only the droplets of the initial size between 15 and 40 μm were selected for the study since they were almost certain to migrate to the solid/liquid interface.

4.1. Droplet migration in the SCN-0.7wt%salol sample

4.1.1. General behavior of the droplet migration

Two temperature gradients imposed were 5.2 K/mm and 2.6 K/mm. For each temperature gradient, migration of multiple droplets was carefully followed and quantified. Figure 2 shows the distribution of 22 droplets that were analyzed for G = 5.2 K/mm. They were located at different starting positions and were of different sizes. As a droplet moved towards the solid/liquid interface, the velocity tended to increase and its size became slightly larger as well. Figure 3 shows these observations quantitatively for droplet M marked in Fig. 2. Both the leading (melting) and trailing (solidifying) edge were quantified and the droplet size was taken as the difference between them. This droplet was initially located at 645 μm away from the solid/liquid interface. Its size increased from ~18.2 μm to ~25.5 μm while it moved 645 μm from its initial position to the solid/liquid interface within 580 seconds. The

slightly enlarged droplet dimension in this process indicated that the leading edge increased its velocity at a somewhat larger rate than the trailing edge. For a migration curve as shown in Fig. 3, we can now evaluate the dynamic, *in-situ* movement of an individual droplet instead of analyzing the average droplet band migration behavior, as has been done by Watson and Hunt [8].

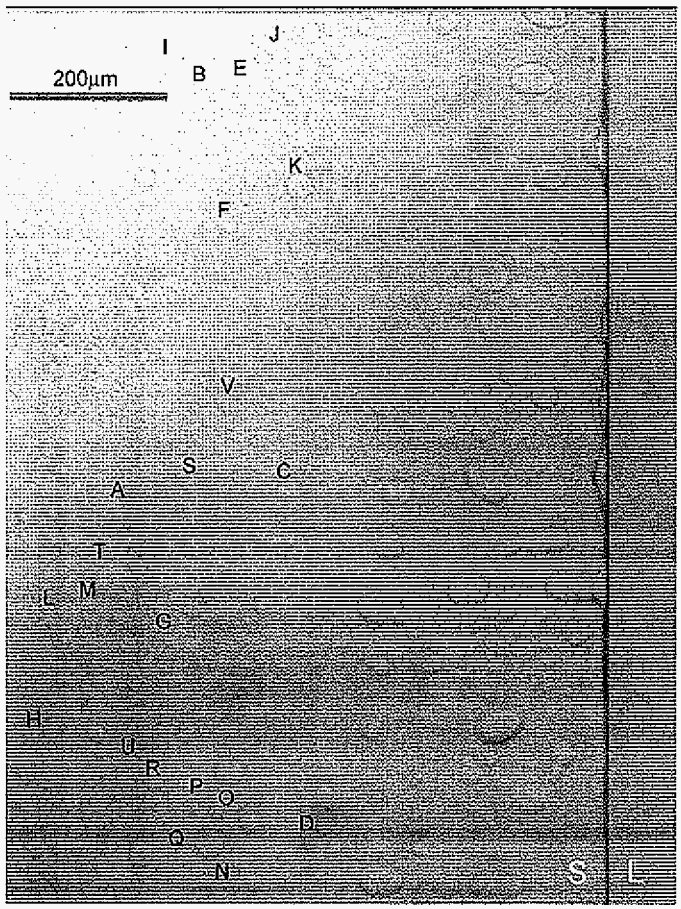

Figure 2. Overall distribution of droplets at the start of migration (SCN-0.7wt%salol, G=5.2K/mm). S stands for "solid" and L for "liquid". The 22 droplets analyzed are labeled as A, B, C, ...V.

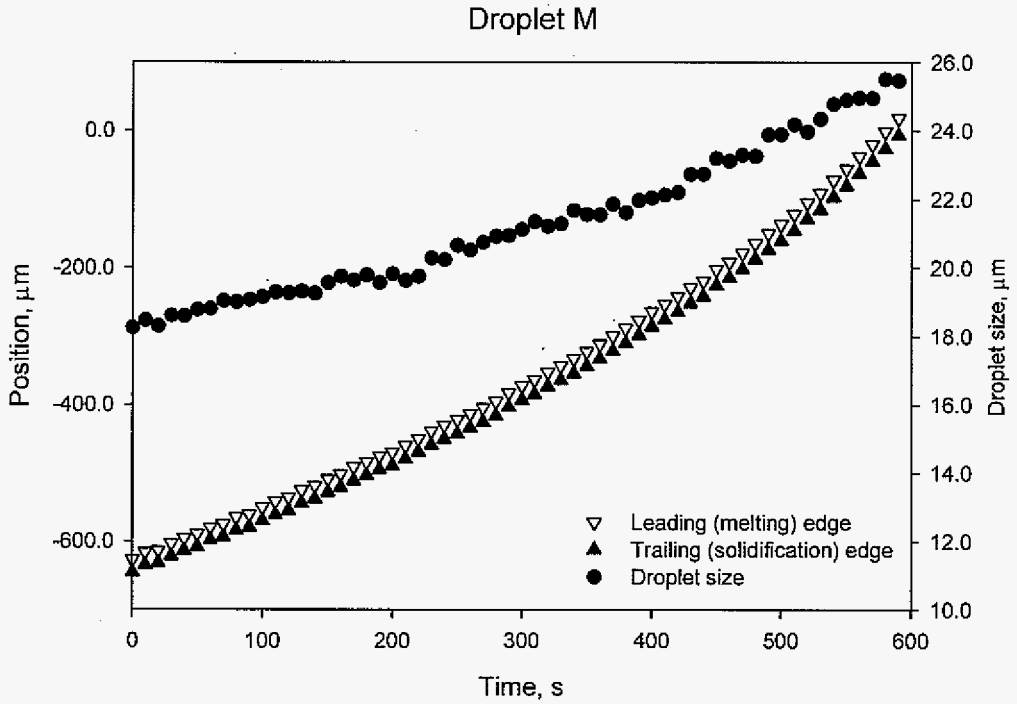

Figure 3. The variation of the position (leading and trailing edge) and the size with time for droplet M in Fig. 2.

Since the driving force imposed was aligned with the temperature gradient, the diametric circle perpendicular to the temperature gradient direction had a negligible driving force while the leading/trailing points had the maximum driving force. The difference in the driving force caused the droplets to be elongated. One may have noticed that the droplets near the solid/liquid interface were usually of elongated shape along the temperature gradient direction (Fig. 2). The shape evolution observed in the present study is same as that discussed by Jones [4-6].

Figure 4 summarizes the positions of the trailing edge of 10 droplets in the migration process. Though the initial position and the initial size may be different, all the droplets moved in a similar accelerating manner. A careful examination of Fig. 4 indicates that the

migration curves for different droplets may overlap if we shift a curve by an appropriate time interval. The result is shown in Fig. 5. The amount of shift is determined by the initial position of a droplet. For example, the droplet H in Fig. 2 is located farthest away from the solid/liquid interface. The initial position of the droplet H was -724 μm and that of the droplet M was -645 μm. The measurement showed that it took 115 seconds for the droplet H to move from -724 μm to -645 μm, therefore 115 seconds was added to the time for droplet M and this shifted the curve for M to the right-hand side and merged with the curve for H. The same operation applied to all the droplets and similar overlapping behavior was observed. For clarity, we just include ten droplet migration curves in Fig. 5.

After the appropriate shifts, the migration curves for the 22 droplets we measured collapse onto a characteristic one as shown in Fig. 5 despite the droplet size and the initial position. Therefore in addition to analyzing the individual droplet migration, we have one more option to study this characteristic curve which represents the cumulative migration behavior of all the droplets in the region of interest.

For a fixed alloy composition in this study, the characteristic curve depends only on the imposed temperature gradient. Figure 6 shows the characteristic curves in the SCN-0.7wt%salol alloy for two temperature gradients: G= 5.2 and 2.6 K/mm respectively: the one with a more shallow temperature gradient lies above the one with a steeper gradient, which agrees with the fact that a smaller thermal gradient generates a smaller driving force (composition gradient), and a slower migration velocity.

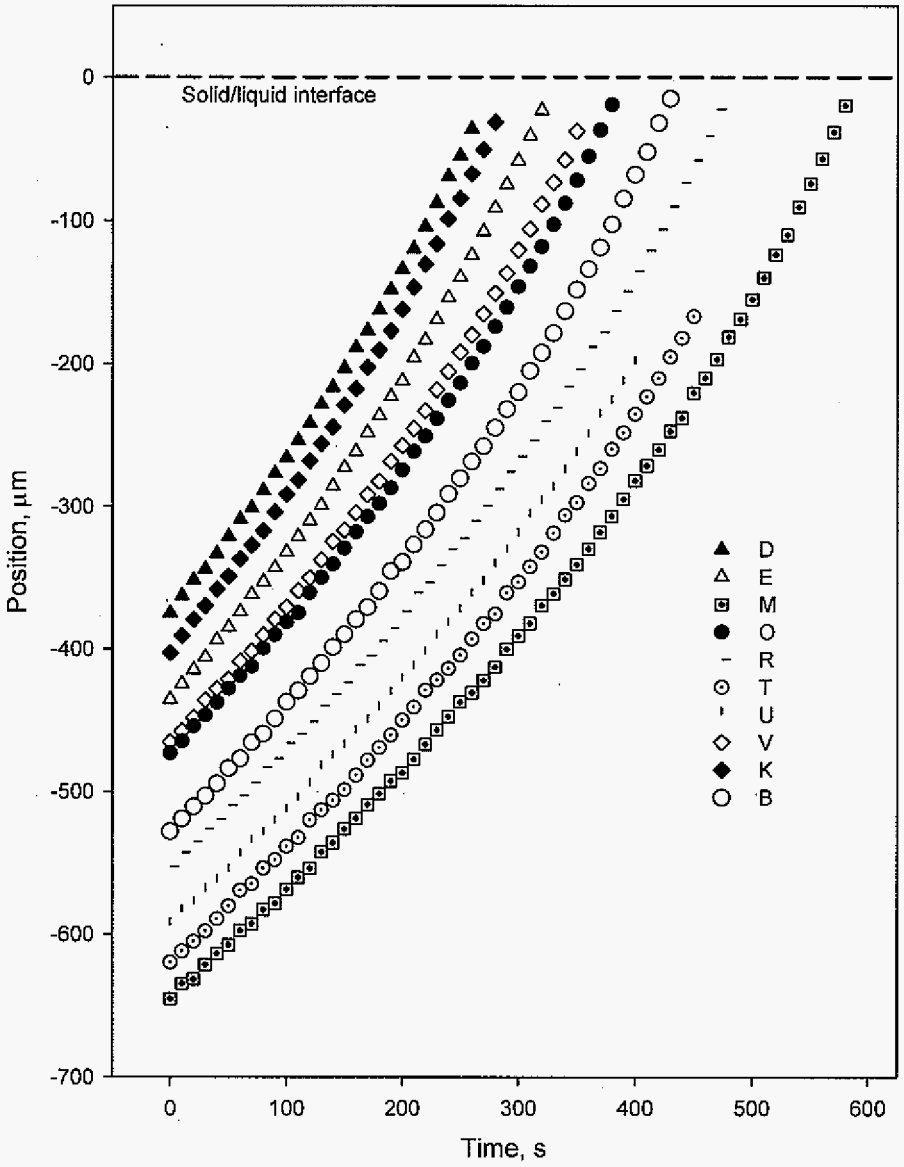

Figure 4. Summary of the quantified migration process for 10 droplets shown in Fig. 2.

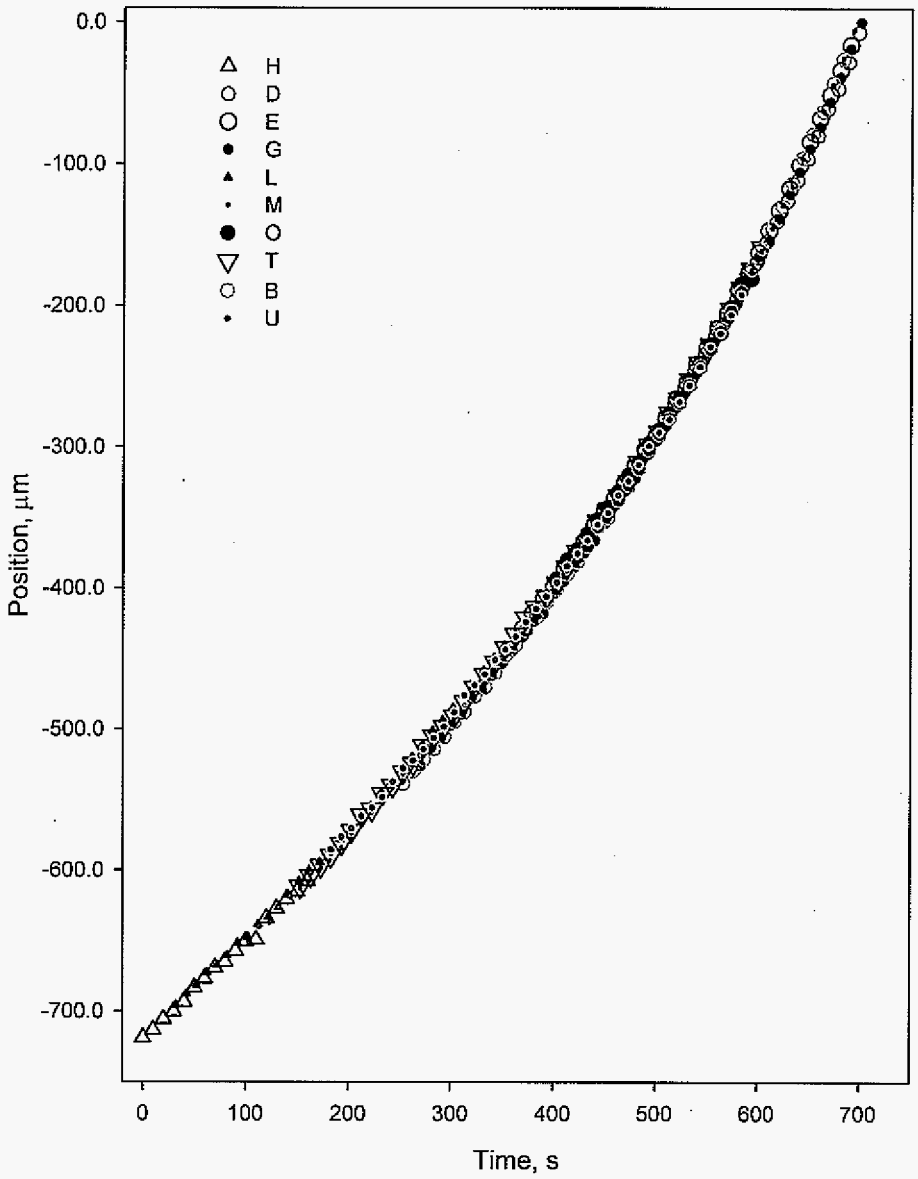

Figure 5. Overlap of the individual droplet migration path by an appropriate shift to form a characteristic migration curve (SCN-0.7wt%salol, G=5.2K/mm).

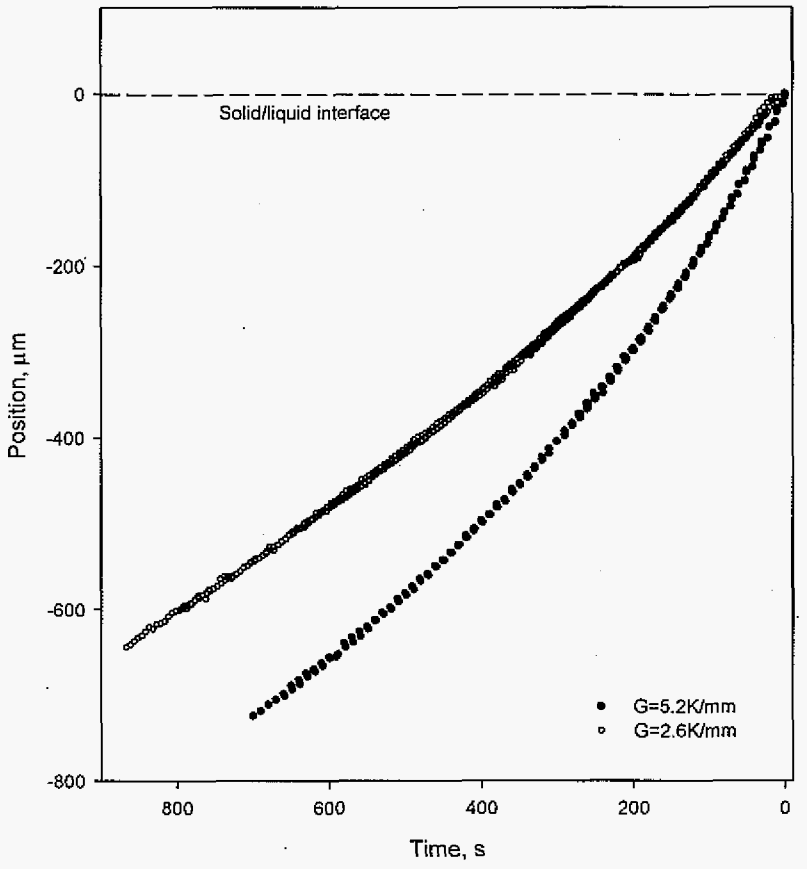

Figure 6. Characteristic migration curves for droplets of SCN-0.7wt%salol at G=2.6 and 5.2 K/mm. In order for the comparison to be made easier, we transform the time axis so that the time is zero at the solid/liquid interface.

4.1.2. Quantification of the migration curves

Table 1 lists the curve-fitting results for all 22 droplets shown in Fig. 2 into the form of eq. 5: $t = \alpha(x(t) - x(t=0)) - \beta(x(t) - x(t=0))^2$. Since x(t=0) is measured directly from the initial position of a droplet, only α and β are the parameters to be determined. The correlation coefficient for the curve-fitting is found to be always higher than 0.99. For SCN base dilute alloys, $G_s \approx G_L$, and the parameters β and α are related to D_L through:

$$\beta = \frac{1-k}{2D_L} \tag{7'}$$

$$\frac{d\alpha}{dx(t=0)} = \frac{k-1}{D_L} \tag{8'}$$

The values of β randomly change for different droplets within the range [6.044×10^{-4}, 6.985×10^{-4}] s/μm^2. From the β value of an individual droplet, the diffusion coefficient is derived by eq. (7') and the result is shown in column 5 of Table 1. The derived diffusion coefficient for G= 5.2 K/mm is (0.69±0.05) $\times10^{-3}$ mm^2/s. Under this temperature gradient, $d\alpha / dx(t=0) = -0.001414$ s/μm^2, the derived diffusion coefficient from eq. (8') is 0.64×10^{-3} mm^2/s, which is listed in the last column of Table 1.

Since all the droplets follow the same characteristic migration curve, β can also be derived from the characteristic curves (Fig. 6) and the diffusion coefficient can be calculated from this β value. For G = 5.2 K/mm, $\beta=6.77\times10^{-4}$ s/μm^2, which gives the diffusion coefficient as 0.665×10^{-3} mm^2/s.

The same procedure can be applied to the droplet migration in the SCN-0.7wt%salol alloy at G = 2.6 K/mm. Since we have observed in the previous experiments that all the droplets follow a characteristic migration curve, we quantify fewer droplets (8 instead of 22) and the results are shown in Table 2.

The diffusion coefficients from individual β values, the β value from the characteristic curve and the value from $d\alpha / dx(t=0)$ are basically the same within the experimental error and the diffusion coefficient value at the lower temperature gradient do not significantly differ from those obtained at a higher gradient. Therefore any method among the 3 evaluated here can be used to derive the diffusion coefficient, though the authors

tend to suggest using the characteristic curve since it reflects the cumulative migration behavior of many droplets and the error should be minimal.

Table 1. Summary of the droplet migration shown in Fig. 2

Droplet label	x(t=0), μm	α, s/μm	β, $\times 10^4$ s/μm^2	D_L from β, $\times 10^3$ mm^2/s	D_L from $d\alpha/dx(t=0)$, $\times 10^3$ mm^2/s
A	-624	1.317	6.65	0.677	
B	-541	1.176	6.42	0.701	
C	-400	1.018	6.866	0.655	
D	-374	0.9605	6.504	0.692	
E	-436	1.045	6.154	0.731	
F	-483	1.136	6.894	0.652	
G	-533	1.2	6.872	0.655	
H	-724	1.446	6.409	0.702	
I	-507	1.19	6.985	0.644	
J	-394	0.9653	6.044	0.744	
K	-403	0.9838	6.739	0.668	
L	-702	1.443	6.89	0.653	
M	-645	1.353	6.831	0.659	
N	-500	1.175	6.895	0.653	
O	-473	1.12	6.244	0.721	
P	-492	1.155	6.649	0.677	
Q	-506	1.18	6.82	0.660	
R	-552	1.23	6.501	0.692	
S	-491	1.138	6.429	0.700	
T	-619	1.299	6.291	0.715	
U	-593	1.29	6.955	0.647	
V	-465	1.11	6.666	0.675	0.64
	Average β		6.623	0.680	
	β from the characteristic curve		6.77	0.665	

Table 2. Quantification of the droplet migration curves for SCN-0.7wt%salol at G=2.6K/mm

Droplet label	x(t=0), μm	α, s/μm	β, $\times 10^4$ s/μm^2	D_L from β, $\times 10^3$ mm^2/s	D_L from dα/d$x(t=0)$, $\times 10^3$ mm^2/s
A	-643.7	1.763	6.166	0.729	0.63
B	-606.5	1.698	6.239	0.721	
C	-511.5	1.597	6.488	0.693	
D	-331.1	1.385	6.195	0.726	
E	-295.9	1.298	6.181	0.728	
F	-294.8	1.293	6.361	0.707	
G	-180.6	1.085	6.465	0.696	
H	-141.1	1.018	6.307	0.713	
	Average β		6.30	0.714	
	β from the characteristic curve		6.517	0.691	

4.2. Droplet migration in the SCN-0.35wt%camphor sample

Similar experiments were conducted in the SCN-0.35wt%camphor alloy at two temperature gradients, G = 3.4 and 1.3 K/mm (Fig. 7). Similar measurements of the droplet migration were made and the results are shown in Table 3. Clearly for both temperature gradients, the diffusion coefficients from three different approaches are basically the same.

V. Analysis and discussion

The derived diffusion coefficients for both SCN-salol and SCN-camphor alloys are presented in Tables 1, 2, and 3. For the SCN-0.35wt%camphor alloy at G = 3.4 K/mm, the diffusion coefficient from the β value of individual droplet measurement varies slightly within the range [0.23, 0.25]$\times 10^{-3}$ mm^2/s with an average at 0.24$\times 10^{-3}$ mm^2/s. The term

Table 3. Droplet movement in SCN-0.35wt%camphor at G=3.4 and 1.3 K/mm

Droplet label	x(t=0), μm	α, s/μm	β, $\times 10^4$ s/μm^2	D_L from β, $\times 10^3$ mm^2/s	D_L from dα/d$x(t=0)$, $\times 10^3$ mm^2/s
G=3.4K/mm					
A	-206	1.12	1.64	0.232	
B	-229	1.18	1.62	0.235	
C	-252	1.25	1.53	0.248	
D	-285	1.358	1.593	0.238	
E	-328	1.481	1.528	0.249	
F	-375	1.617	1.504	0.253	
G	-388	1.644	1.517	0.251	0.26
H	-427	1.789	1.551	0.245	
	Average β		1.562	0.243	
	β from the characteristic curve		1.633	0.233	
G=1.3K/mm					
A	-578	2.977	1.531	0.248	
B	-292	2.123	1.478	0.257	
C	-234	2.032	1.455	0.261	
D	-422	2.465	1.489	0.255	
E	-88	1.62	1.583	0.240	0.26
	Average β		1.507	0.252	
	B from the characteristic curve		1.455	0.261	

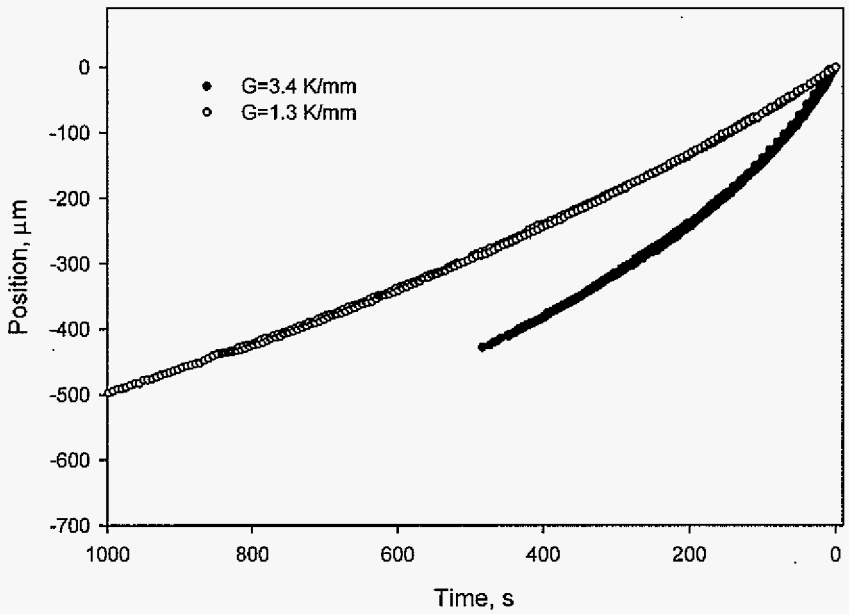

Figure 7. Characteristic migration curves for droplets of SCN-0.35wt%camphor at G=3.4 and 1.3 K/mm.

$d\alpha / dx(t=0)$ gave the diffusion coefficient as 0.26×10^{-3} mm^2/s; while the characteristic migration curve gave the diffusion coefficient as 0.23×10^{-3} mm^2/s. The diffusion coefficients at G=1.3 K/mm are similar to those at G=3.4 K/mm. We consider that all the derived values of diffusion coefficient from different terms are the same within the experimental error.

Kobayashi *et al.* measured the side arm climb distance in the constrained crystal growth process of SCN-6.0wt%camphor and obtained the solute diffusion coefficient D_L=0.3×10^{-3} mm^2/s [14]. Indeed, the term should be $D_L/(1-k)=0.3\times10^{-3}$ mm^2/s from their derivation (eq. (10) in [14]). The authors then assumed that k=0 and therefore obtained D_L =0.3×10^{-3} mm^2/s. However for the binary SCN-camphor system, k=0.24 by our recent effort to determine the phase diagram [19], and therefore D_L=0.23×10^{-3} mm^2/s, which is in

good agreement with the present study.

For the SCN-0.7wt%salol alloy at G=5.2K/mm (Table 1), the individual droplet measurement gave the diffusion coefficient slightly varying within the range [0.64, 0.74]$\times 10^{-3}$ mm^2/s with an average at 0.69×10^{-3} mm^2/s. The term $d\alpha / dx(t=0)$ gave the diffusion coefficient as 0.64×10^{-3} mm^2/s; while the characteristic migration curve gave the diffusion coefficient as 0.67×10^{-3} mm^2/s. Again, all the derived values from different terms are considered to be the same within experimental error. The derived diffusion coefficient at G=2.6 K/mm and 5.2 K/mm were found to be quite similar (Table 2).

Three different values of diffusion coefficient in the SCN-salol system have been used in literatures [13, 22,23]. Venugopalan and Kirkaldy [22] indicated that the cited value, D_L=(1~2)$\times 10^{-3}$ mm^2/s was estimated from Hildebrand's correlations; while Liu and Kirkaldy [23] did not specify the technique to determine the diffusion coefficient, but just tabulated D_L=0.8×10^{-3} mm^2/s, therefore it is difficult to compare the present study with these data. Zeidler, Albright and Kirkaldy [13], using a Gosting Diffusiometer, obtained D_L=0.4×10^{-3} mm^2/s, which is much smaller than the value obtained in this study.

Actually Zeidler, Albright and Kirkaldy re-determined the diffusion coefficient in SCN-acetone alloys and reported that D_L=0.92×10^{-3} mm^2/s [13]. This value is also much smaller than the generally accepted value D_L=1.27×10^{-3} mm^2/s, which was experimentally determined by Chopra, Glicksman and Singh [24] and has been used to explain the microstructure lengthscale selection successfully. Therefore the smaller value of diffusion coefficient by Zeidler, Albright and Kirkaldy [13] may be related to the technique employed.

In the Appendix, we presented the measurement of the solidus temperature of the

SCN-0.7wt% salol alloy. The solid/liquid interface was a stable planar front for V=1.0 μm/s and G=5.65 K/mm and a slightly larger growth rate led to the destabilization of the interface, therefore we may use the planar front stability condition to estimate the diffusion coefficient.

The linear stability theory of planar front growth [25] requires that:

$$\frac{\overline{G}}{V} = \frac{\Delta T_o}{D_L} \tag{9}$$

where $\overline{G}$ is the thermal conductivity weighted temperature gradient. Since the solid and liquid phase of dilute SCN base solutions have almost the same thermal conductivity, $\overline{G} \approx G_L$=5.65K/mm. ΔT_o is the freezing range, =4.28 K from the Appendix. Therefore D_L=0.76×10^{-3} mm^2/s. Clearly this value is very close to the data obtained through droplet migration method. This should be so since both processes (droplet migration and stable planar front growth) occur in a temperature gradient field and involve the movement of solid/liquid interface.

Watson and Hunt [8] also considered the error introduced by different densities of the solid and liquid phases. Fortunately, the density of the solid and liquid phase of SCN base dilute solutions are very close to each other [26], and this effect can be safely ignored in this study.

Another possible error in the determination of diffusion coefficient by droplet migration method is from the Soret effect. Watson and Hunt [8] pointed out that the measured diffusion coefficient (D_M) by the droplet migration method actually included both the real solute diffusion (D_L) and the Soret diffusion (D_T), and they were correlated by:

$$D_M = D_L(1 + mS \cdot C_L(1 - C_L)) \tag{10}$$

where S is the Soret coefficient, which is defined as: $S = D_T / D_L$, C_L is the liquid composition in mole fraction. Since m is negative, D_L is always larger than D_M. Though we can estimate the average liquid composition in the droplet migration process, we do not know the Soret coefficient, thus the real diffusion coefficient cannot be evaluated for both SCN-salol and SCN-camphor alloys. However, since the liquid diffusion coefficient is most frequently used to quantitatively evaluate the microstructure lengthscale selection in directional solidification processes, the values obtained in this study should be the appropriate ones to apply.

VI. Conclusion

We have revisited the equation governing the droplet migration in a solid driven by a temperature gradient and concluded that the migration process of a droplet should be fit the form $t = \alpha(x(t) - x(t=0)) - \beta(x(t) - x(t=0))^2$, from which the diffusion coefficient can be calculated from β or $d\alpha / dx(t=0)$. By carefully quantifying the droplet migration in both SCN-salol and SCN-camphor alloys, we have found that there exists a characteristic migration curve independent of droplet size and position but dependent on the temperature gradient for a given alloy. For each alloy, we have obtained consistent values of the diffusion coefficient. For the SCN-camphor alloy, D_L=(0.24±0.02)×10^{-3} mm^2/s; for SCN-salol, D_L=(0.69±0.05)×10^{-3} mm^2/s.

Acknowledgement

This work was supported by DOE-BES and was carried out at Ames Laboratory which is operated by Iowa State University for the Office of Basic Energy Science, Division

of Materials Science, U. S. Department of Energy under Contract No. W7405-Eng-82.

References

[1] W.A.Tiller, J. App. Phys. 1963;vol.34(9), pp.2757-62.

[2] W.C. Yang, H. Ade and R. J. Nemanich, Phys. Rev. 2004; vol. 69B, pp.45421/1-8.

[3] M. F. Chang, J. Electrochem.. Soc. 1981; vol.128, pp.1963-67.

[4] D. R. H. Jones, J. Cryst. Growth 1974;vol. 26, pp. 177-9.

[5] D. R.H. Jones, J. Cryst. Growth 1973;vol. 20, pp.145-51.

[6] D. R. H. Jones and G. A. Chadwick, Phil. Mag. 1971; vol 24, pp. 1327-45.

[7] H. E. Cline and T. R. Anthony, Acta Metall. 1971; vol.19, pp.175-80.

[8] M. P.Watson and J. D.Hunt, Metall. Trans. 1977; vol.8A, pp.1793-98.

[9] D. J. Allen and J. D.Hunt, Metall. Trans. 1976; vol.7A, pp.767-770.

[10] R. Riedl and H.F.Fischmeister, Metall. Trans. 1990; vol.21A, pp. 264-6.

[11] T. Kraft, O. Pompe and H. E.Exner, Metall. Mater. Trans. 1998; vol.29A, pp.359-65.

[12] H. T. Nguyen, B. Drevet, J. M. Debierre, D. Camel, Y. Dabo and B. Billia., J. Cryst. Growth 2003: vol. 253, pp. 539-48.

[13] M. Zeidler, J. G.Albright and J. S. Kirkaldy, J. Cryst. Growth, 1994; vol 142, pp.354-6.

[14] K. Kobayashi, Y. Seko and P. H. Shingu, J. Jpn. Inst. Metals 1981; vol.5(6), pp.647-51.

[15] Sato T, Kurz W and Ikawa K, Trans. Jpn. Inst. Metals 1987; vol.28(12), pp.1012-21.

[16] X.D.Yao, Z. Q.Hu, T. Huang and Y.H.Zhou, Chinese J. Mater. Research 1996; vol.10, pp.167-72.

[17] L.X.Liu and J.S.Kirkaldy, Acta Metall. 1995; vol.45, pp.2891-904.

[18] R. Trivedi, Y.X.Shen and Shan Liu Metall. Mater. Trans. 2003, vol.34A; pp.395-401.

[19] Jing Teng and Shan Liu, J. Cryst. Growth, 2006, vol.290, pp.248-257.

[20] V. T. Witusiewicz, L. Sturz, U. Hecht and S. Rex, Acta Mater. 2004; vol.52: pp.4561-71.

[21] L. Fabietti and R. Trivedi, Unpublished results on the dynamics of initial transient in SCN-water binary alloys, Iowa State University, 2003

[22] D. Venugopalan and J. S. Kirkaldy, Acta Metall., 1984, vol. 32(6), pp. 893-906.

[23] L. X. Liu and J. S. Kirkaldy, Scripta Metall., 1993, vol 29, pp. 801-6.

[24] M. A. Chopra, M. E. Glicksman and N. B. Singh, J. Cryst. Growth, 1983, vol.92, pp.543-47.

[25] W.W.Mullins and R. F. Sekerka, J. Appl. Phys., 1964, vol 35, pp.444-51.

[26] E. R. Robinstein and M. E. Glicksman, J. Cryst. Growth, 1991, vol. 112, pp.97-110.

Appendix: The equilibrium distribution coefficient in the SCN-0.7wt%salol alloy

Liu and Kirkaldy reported that k = 0.2 (based on mole fractions for the solid and liquid composition) in SCN-salol binary alloys [17]. We have done a limited number of directional solidification experiments to measure the interface temperature as a function of velocity at G=5.65K/mm. The measured interface temperature is shown in Fig. A1. For V≥10.0 μm/s, the growth morphology is dendritic, and the interface temperature approaches the liquidus temperature of the alloy (T_L=57.59°C). For V=1.0 μm/s, the growth interface at steady state is planar and therefore the measured interface temperature is equivalent to the solidus temperature of the alloy, i.e., T_s=53.29°C. For velocities in between, the morphology is cellular and the interface temperature sharply increases. For the dilute compositions, the solidus and liquidus line are linear, therefore we can obtain the equilibrium distribution coefficient from the freezing range (T_L-T_s) of this SCN-0.7wt%salol alloy, $\Delta T = T_L - T_s = mC_o(k-1)/k$, which leads to k = 0.096. Therefore we used k=0.1 in the present analysis.

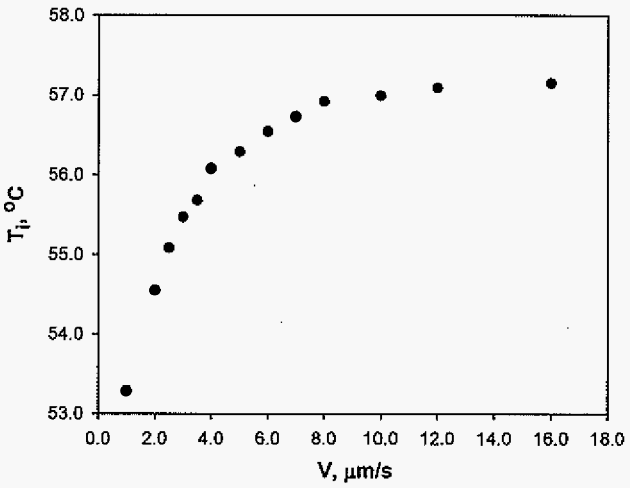

Figure A1. Variation in interface temperature with growth velocity for SCN-0.7wt%salol alloys (G=5.65K/mm).

CHAPTER 4. CELLULAR MICROSTRUCTURE IN DIRECTIONAL SOLIDIFICATION

A manuscript to be submitted to *Physical Review E*

Jing Teng[1], B. Billia[2,*] and R. Trivedi[1,3]

Abstract

The characteristics of cellular interface during directional solidification are investigated in the succinonitrile-camphor system in which a eutectic interface forms in the intercellular region. Detailed experimental studies have been carried out in capillary samples with diameters 0.1 mm to obtain a single cell that forms under purely diffusive growth conditions. Benchmark data are obtained on the shapes of the cells and on the variations in the relative width of the cell, cell tip undercooling and cell tip radius with velocity. A theoretical model, based on the three-dimensional Saffmann-Taylor model, is developed and the experimental results are compared with the predictions of the model. The results show two distinct branches of solution, with the Saffman-Taylor branch being followed only for velocities that are just above the planar interface stability threshold. At higher velocities, the results approach the parabolic tip model.

---

[1]Dept. Materials Science and Engineering, Iowa State University, Ames, IA, 50011, U.S.A.

[2]L2MP, Université d'Aix-Marseille III, Faculté Saint-Jérôme, Case 142, 13397 Marseille Cedex 20, France

[3]Materials and Engineering Physics Program, Ames Laboratory-USDOE, Iowa State University, Ames, IA, 50011, U.S.A.

*Corresponding author: e-mail: bernard.billia@l2mp.fr, phone: 33 (0) 4 91 28 81 14, fax: 33 (0) 4 91 28 87 75.

1. Introduction

During the directional solidification of alloys, a cellular array develops when the interface growth conditions exceed the threshold for the planar interface stability. The theoretical description of the cellular array is complicated due to the strong interaction of solute field between the neighboring cells which causes the interface to acquire a specific shape for steady-state growth. Consequently, the current models are based on numerical simulations [1, 2], whose results are often described by an analytical expression that is obtained by curve fitting. Several approaches have also been taken to develop an analytical model for cellular growth, but they have not been able to accurately describe the cellular array problem [3]. Analytical models, based on an analogy between the Saffmann-Taylor (ST) finger growth problems, have also been developed to describe cellular growth [4-7], and experimental studies [8] have shown that the shape of the directional solidification cells can be accurately described at low velocities by the ST finger shape over a narrow range of growth conditions if another phase such as a eutectic is present in the intercellular region, as shown in Fig. 1(b).

The ST finger problem is a classic example of the nonlinear pattern formation in nature, and has been studied extensively, both theoretically and experimentally. Most studies have been carried out for two dimensional patterns and experiments have been carried out in thin Hele-Shaw cells in which a finger shaped pattern forms when a viscous fluid is displaced by a less viscous fluid, as shown in Fig. 1(a). It is found that an infinite number of discrete branches of steady-state solutions are present in a sample of given width [9]. However, all these branches, except one, are unstable and the selection of the stable finger shape is

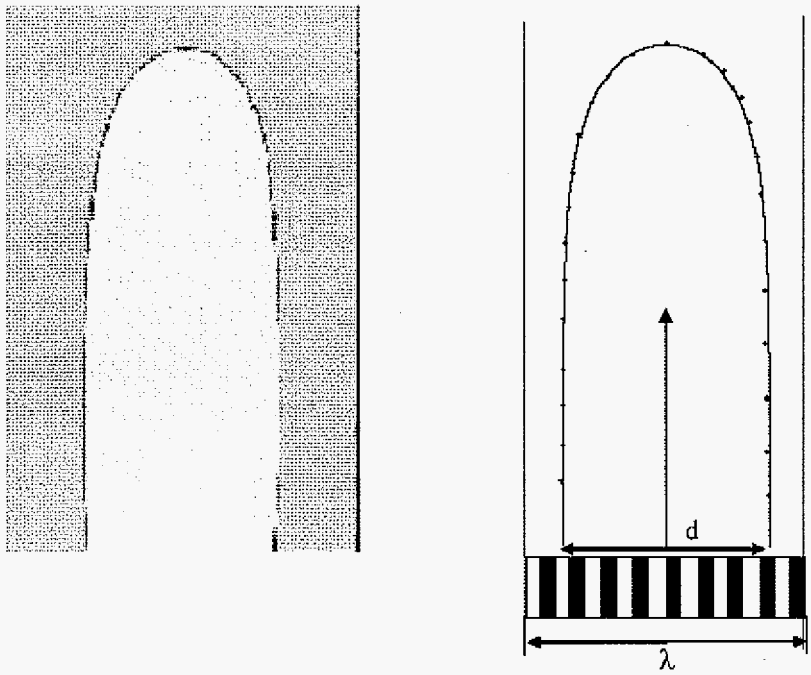

(a) (b)

Figure 1. Schematic illustrations of (a) a viscous finger, and (b) a directional solidification cell with eutectic in a cylindrical sample of diameter λ.

governed by the interface energy parameter [10].

In directional solidification, the cell is three-dimensional, and the shape of the cell is considered to have a rotational symmetry. To consider the analogy with the ST finger, a three-dimensional model of a cylindrical finger growth is required. Such a model has been developed for isotropic surface energy by Levine and Tu [11], who obtained a relationship between the relative width of the finger and the surface energy parameter, $\overline{\gamma}$, for steady-state growth. In contrast to the 2D finger problem, in which steady-state solutions are present for any non-zero surface energy parameter, Levine and Tu [11] found that no steady state finger shape exists when the interface energy parameter is below some critical value. An analogy

between the cell and finger in 3D is required.

The aim of the present work is to present the results of directional solidification experiments in the succinonitrile (SCN)-camphor system in thin cylindrical samples in which only a single three-dimensional cell forms ahead of a planar eutectic front and the growth is governed by diffusive transport only. We then investigate the following key aspects: (1) determine the shape of the cell, and establish the regime of experimental parameters for which the shape of the cell can be described by the three-dimensional Saffmann-Taylor finger shape; (2) provide benchmark data on the characteristic cell parameters (tip radius ρ, tip undercooling ΔT and cell diameter d at the eutectic front) as a function of velocity V; (3) determine the relationship between the width of the cell and the interface energy parameter for steady-state cell growth in three-dimensions, and examine the validity of the Levine-Tu relationship, which is important since ST-finger in 3D between the two fluids is unstable; and (4) determine the experimental conditions at which the shape of the cellular front deviates from the viscous finger shape, and approaches the parabolic shape. In addition to the experimental studies, a theoretical model will also be developed for the directional solidification cell with intercellular eutectic that is based on the 3D Saffmann-Taylor model. This model will define the appropriate interface energy parameter for cells, and relate it to the width of the finger for steady-state growth. Appropriate expressions for the shape of the cells and for the cell tip undercooling will also be developed, and compared with the experimental results on 3D cells.

2. Experimental Studies

Directional solidification experiments are carried out in thin cylindrical samples of a

model transparent system of SCN-camphor so that the shape of the interface and the cell tip undercooling can be measured precisely. This is a simple eutectic system with the eutectic composition as 23.6 wt% camphor and eutectic temperature 37.6 °C, as determined experimentally [12]. Relevant properties of this system are listed in Table 1. The sample was contained in a cylindrical glass tube of 100 μm ID and 550 μm OD. In order to obtain a single cell, two off-eutectic compositions were examined, 9.6 wt% and 13.0 wt% camphor. The liquidus temperatures of these alloys were measured by DSC as 47.63 °C and 44.90°C, respectively. The difference between the liquidus and the eutectic temperatures for these two alloys is 10.03 and 7.3 °C, and the freezing ranges (in absence of eutectic) were obtained as 14 °C and 16.5 °C, respectively.

Since it is not possible to place a thermocouple in a very thin tube to measure the cell tip temperature without significantly influencing the cell shape, the following procedure was used. (1) First, a calibrated thermocouple was placed in a sample to precisely measure the temperature gradient between the liquidus temperature and eutectic temperature, and (2) the cell length and cell shapes were measured in other samples free of a thermocouple, but all experimental conditions were kept identical to those for the calibration. To ensure a stable growth of cells, the cell orientation was selected such that a <100> crystallographic direction was aligned (within 5°) parallel to the axis of the capillary tube.

Experiments were carried out in SCN- 9.6 wt% camphor for two different thermal gradient values, i.e. 4.75 and 4.16 K/mm, and eight different velocities were used for each thermal gradient value. For SCN- 13.0 wt% camphor, experiments were carried out for five different velocities at a fixed thermal gradient of 2.8 K/mm. The experimental conditions are given in Table 2, and the results are listed in table 3.

Table 1. Material and Alloy Parameters for the Succinonitrile-Camphor System	
Succinonitrile	
Melting point (T_M)	331.24 K
Molar entropy of fusion (ΔH_f)	11.21 J/mol
Density of solid (ρ_S)	1.016 x 103 Kg/m^3
Density of liquid (ρ_L)	0.907 x 103 Kg/m^3
Thermal conductivity of solid (K_S)	0.224 J/msK
Thermal conductivity of liquid (K_L)	0.223 J/msK
Solid-liquid interface energy (γ)	8.95x10^{-3} J/m^2
Gibbs-Thomson coefficient (Γ)	0.64 x 10^{-7} Km
Molecular weight	80.09 g/mole
Succinonitrile-camphor	
Diffusion coefficient in the liquid (D)	2.7x10^{-10} m^2/s
Liquidus slope (m)	-1.57 K/wt%
Equilibrium partition coefficient (k)	0.3

Table 2. Experimental Conditions with Relevant Parameters				
C_0, wt% camphor	T_L Liquidus temperature, °C	ΔT_0, Freezing range, °C	G, Thermal gradient, K/mm	V_c, Critical velocity, μm/s
9.6	47.63	14.0	4.75	0.0916
9.6	47.63	14.0	4.16	0.0802
13.0	44.9	16.5	2.8	0.0458

Table 3: Summary of experimental results

C_0 = 9.6 wt % and G = 4.75 K/mm

V μm/s	T_i °C	ΔT K	ρ μm	Λ_e	Pe $=\lambda V/D$	V/V_c	kC_i/C_0	Cell shape
0.15	37.98	9.64	16.84	0.594	0.054	1.59	0.611	ST-Finger
0.20	38.82	8.80	14.0	0.654	0.073	2.16	0.584	Finger
0.30	39.75	7.87	12.8	0.664	0.110	3.25	0.554	Finger
0.40	40.83	6.80	12.1	0.676	0.148	4.36	0.519	Finger
0.50	41.55	6.08	7.5	0.680	0.186	5.47	0.496	Parabola
0.60	42.12	5.30	7.0	0.700	0.223	6.58	0.471	Parabola
0.81	42.62	5.01	5.4	0.693	0.298	8.79	0.462	Parabola
1.01	43.14	4.49	5.3	0.706	0.374	11.0	0.445	Parabola

C_0 = 9.6 wt % and G = 4.16 K/mm

V μm/s	T_i °C	ΔT K	ρ μm	Λ_e	Pe $=\lambda V/D$	V/V_c	kC_i/C_0	Cell shape
0.15	38.25	9.38	16.5	0.635	0.054	1.82	0.60	Finger
0.20	38.90	8.72	14	0.656	0.073	2.47	0.58	Finger
0.30	40.18	7.45	12.8	0.680	0.110	3.72	0.54	Finger
0.40	40.87	6.76	11.8	0.686	0.148	4.98	0.52	Finger
0.50	41.57	6.06	7.4	0.688	0.186	6.25	0.50	Parabola
0.60	41.97	5.66	6.8	0.696	0.223	7.52	0.48	Parabola
0.81	42.67	4.96	6.5	0.704	10.0	0.46	3.60	Parabola
1.01	43.05	4.57	5.4	0.710	12.6	0.45	4.67	Parabola

C_0 = 13.0 wt % and G = 2.8 K/mm

V μm/s	T_i °C	ΔT K	ρ μm	Λ_e	Pe $=\lambda V/D$	V/V_c	kC_i/C_0	Cell shape
0.125	37.90	7.00	14.95	0.590	0.046	2.73	0.52	ST-Finger
0.15	38.11	6.79	14.66	0.578	0.054	3.19	0.51	ST-Finger
0.20	39.09	6.01	13.96	0.655	0.073	4.32	0.49	Finger
0.30	39.66	5.44	8.70	0.659	0.110	6.51	0.47	Parabola
0.50	41.56	3.54	6.30	0.671	0.185	10.9	0.41	Parabola

Selected observed cell shapes are shown in Figs. 2-5. Although the general shape of the cell is complex, Trivedi et al. [8] have shown that at low velocities the cell shapes ahead of the eutectic front can be described by the 3D-Saffmann –Taylor shape given by:

$$Z = \frac{\lambda^2 \Lambda^2}{\pi^2 \rho} \ln\left(\cos\frac{\pi r}{\lambda \Lambda}\right) \qquad (1)$$

where Z is the growth direction, r is the radial direction, and ρ is the cell tip radius. The tube diameter is λ, and Λ is the relative width of the finger, i.e. $\Lambda = d_c/\lambda$, d_c being the width (or diameter) of the finger at the eutectic front, as shown in Fig. 1(b).

Figure 2(a) shows the shape of the cell in a tube of 100 μm diameter in SCN-9.6 wt% camphor, directionally solidified at V = 0.15 μm/s and G = 4.75 K/mm. The experimentally observed cell shape (shown with filled circles) is compared in Fig. 2(b) with the 3D-ST shape equation (solid line), given by equation (1), and a good match is observed for the entire shape of the cell. When the velocity was increased to 0.20 μm/s and above, or the gradient was reduced to 4.15 K/mm, deviations from theoretical shapes were observed, as noted in Table 3.

The cell shapes in a higher composition alloy of SCN-13.0 wt% camphor are shown in Figs. 3(a) and 4(a) for two different velocities of 0.125 and 0.15 μm/s at G = 2.8 K/mm. Both the shapes were found to match accurately with the theoretically predicted shape, equation (1), as shown in Figs. 3(b) and 4(b). When the velocity was increased to 0.20 μm/s and above, deviations from theoretical shapes were observed, as shown in Fig. 5. A good match is obtained only near the tip region or if the relative width is adjusted to a smaller value, as shown in Fig. 5. When the velocity was increased to 0.5 μm/s, the shape of cell tip becomes much sharper, and approached a parabolic shape, as shown in Fig. 6. The parabolic

shape matched up to about 4ρ (ρ is tip radius) distance behind the tip so that the tip undercooling could be described by the Ivantsov model.

Measurements of cell tip undercooling and cell tip radius with velocity were carried out, and the widths of the cells at the eutectic isotherm were also measured. All these data are given in Table 3. We shall discuss these results after we present an analogy between the finger and the 3D cell growth to obtain appropriate expressions.

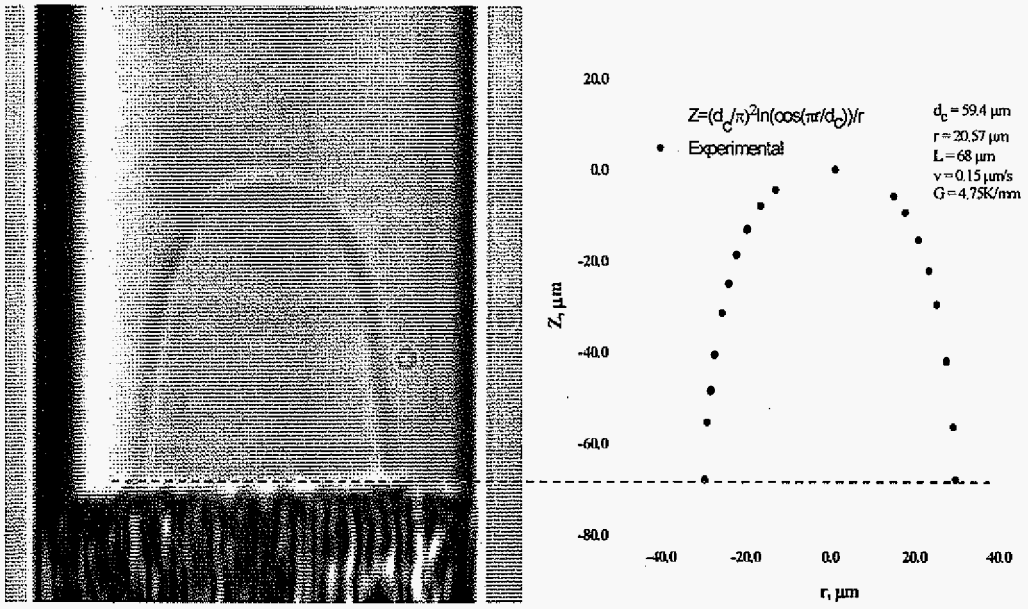

Figure 2. (a) The shape of the cell in a tube of 100 μm diameter in SCN-9.6 wt% camphor, directionally solidified at V = 0.15 μm/s with G ≃ 4.75 K/mm; (b) A comparison of the experimentally observed cell shape (shown with filled circles) with the 3D-ST shape equation (solid line).

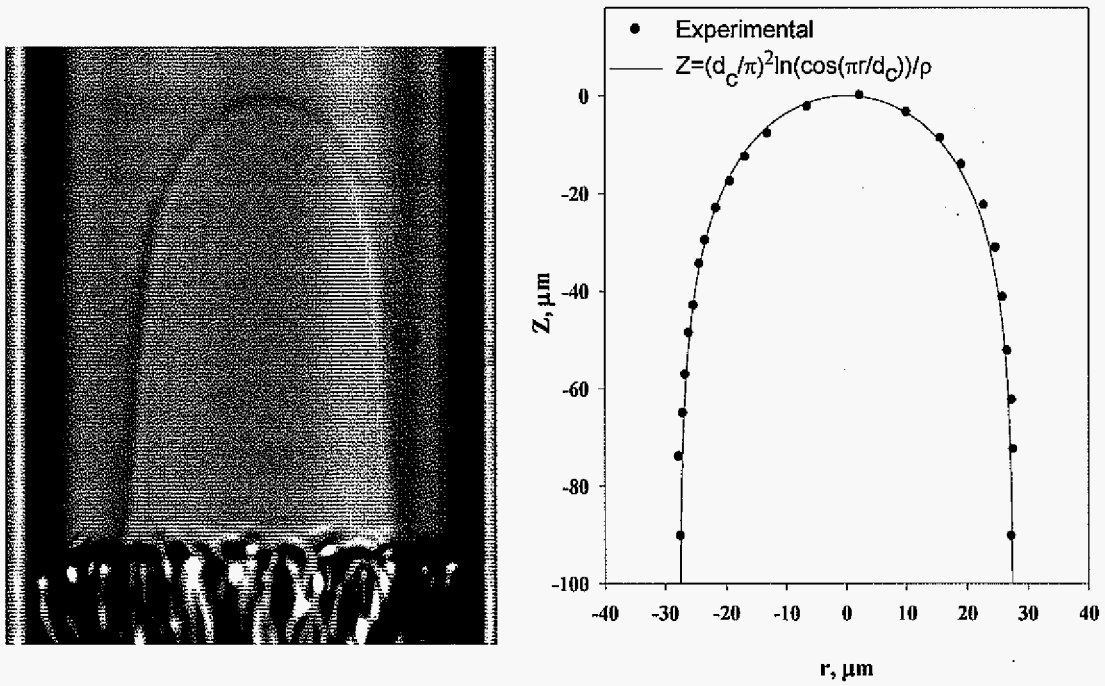

Figure 3. (a) The shape of the cell in a tube of 100 μm diameter in SCN-13.0 wt% camphor, directionally solidified at V = 0.125 μm/s with G = 2.8 K/mm; (b) A comparison of the experimentally observed cell shape (shown with filled circles) with the 3D-ST shape equation (solid line).

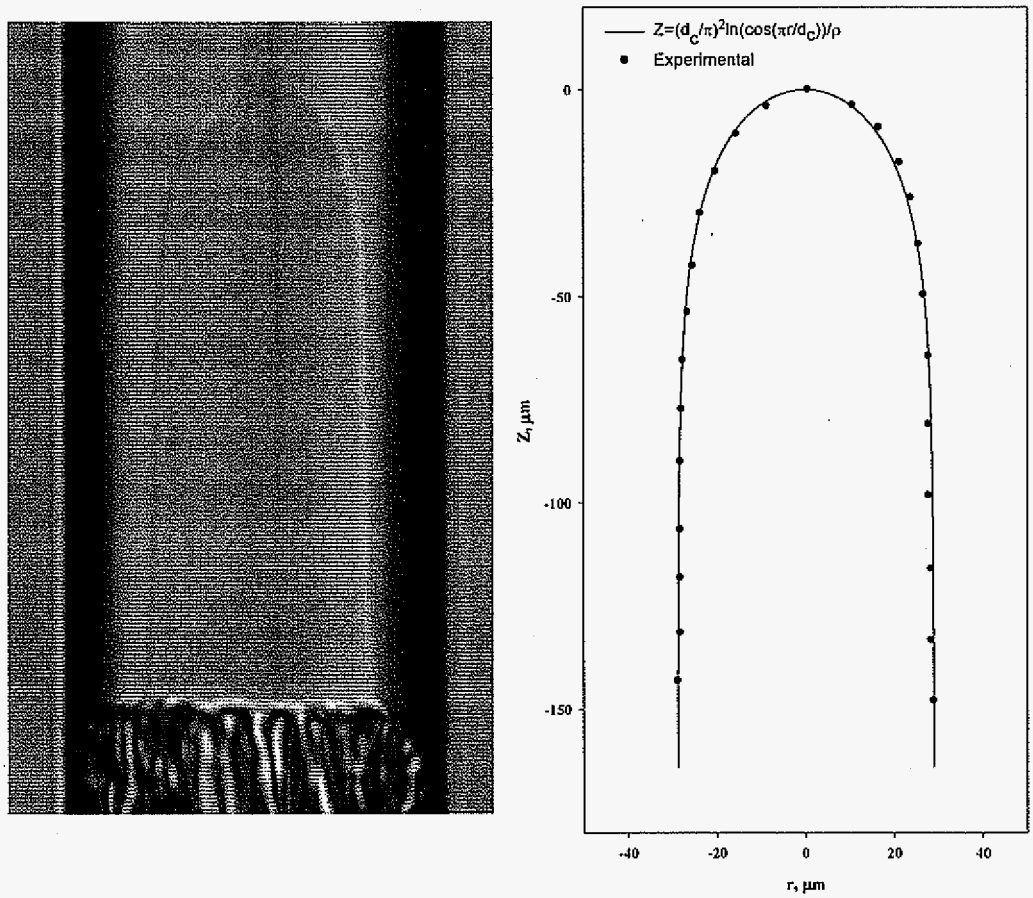

Figure 4. (a) The shape of the cell in a tube of 100 μm diameter in SCN-13.0 wt% camphor, directionally solidified at V = 0.15 μm/s with G = 2.8 K/mm; (b) A comparison of the experimentally observed cell shape (shown with filled circles) with the 3D-ST shape equation (solid line).

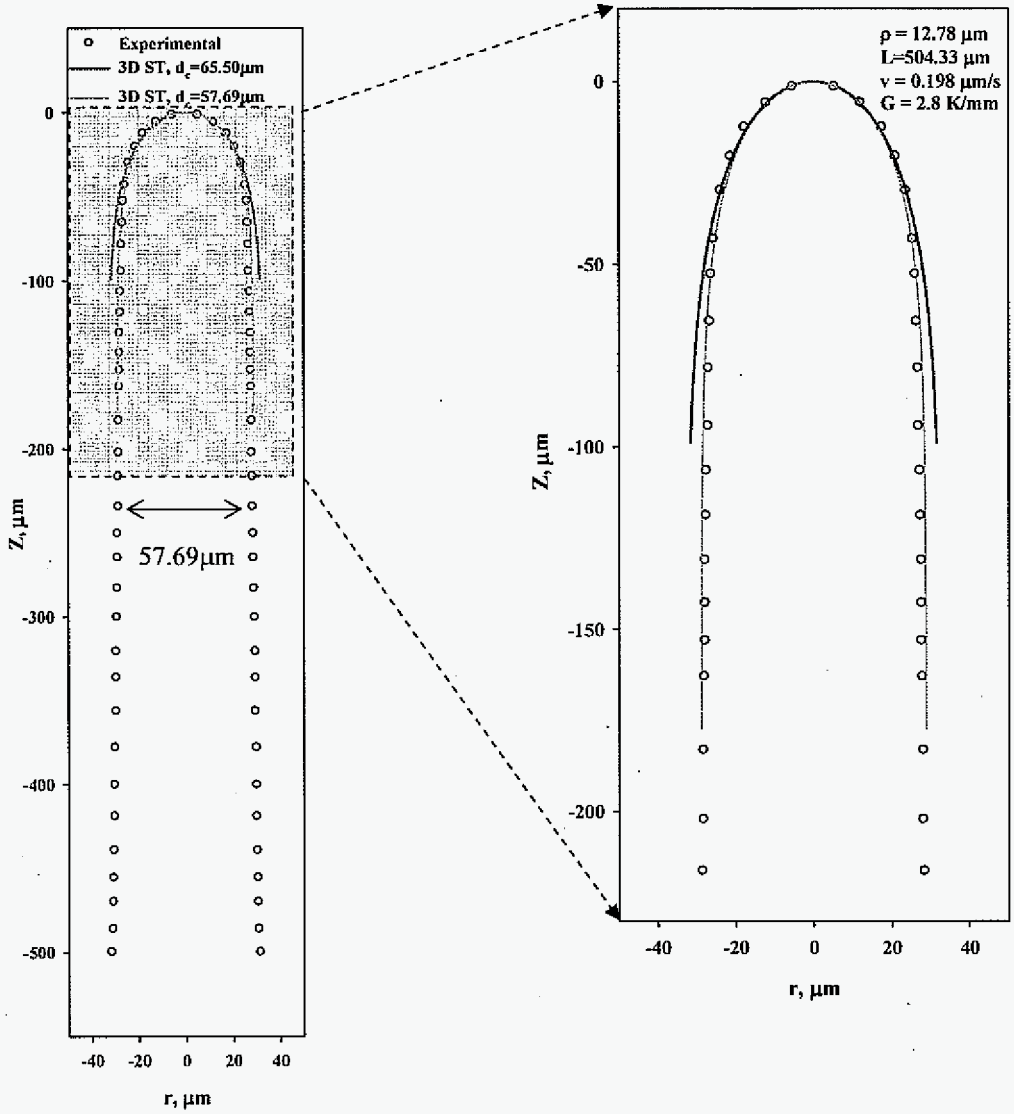

Figure 5. (a) A comparison of the experimentally observed shape (shown with filled circles) in SCN-13.0 wt% camphor, directionally solidified at V = 0.2 μm/s, at G = 2.8 K/mm; (b) A magnified view of the shape near the tip region. Experimentally observed relative width at the eutectic isotherm, which is 0.655, shows a significant deviation (solid line), and a good matching is observed only close to the cell tip region. However, a good match is observed when an effective relative width of 0.5769 is used (shown by a dotted line).

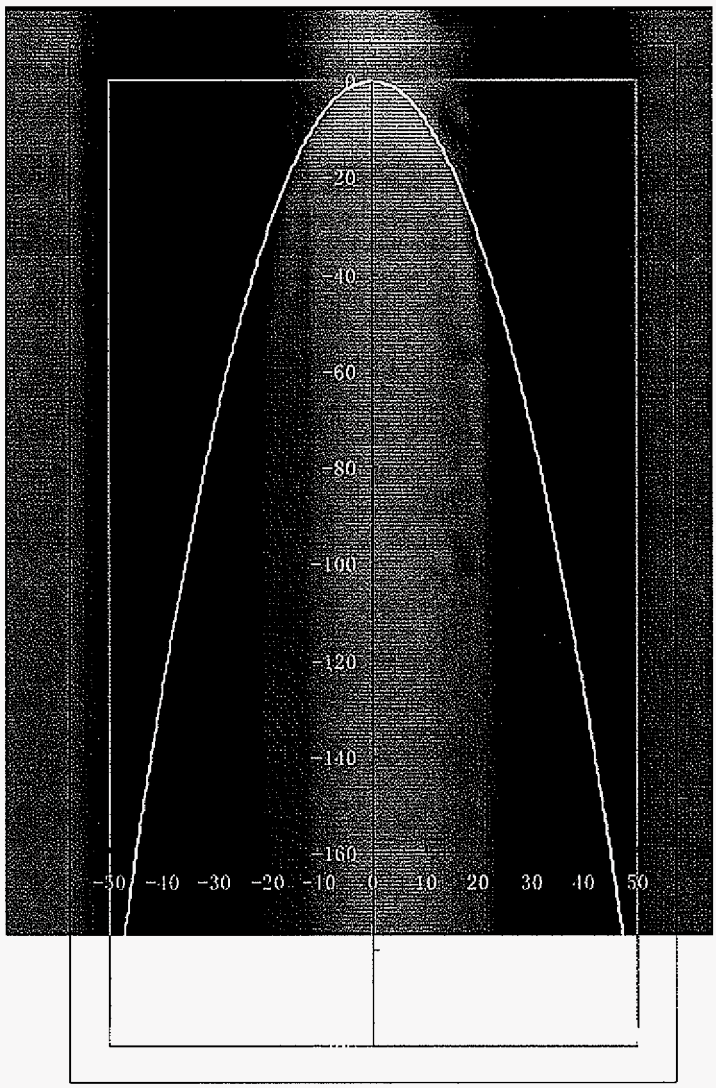

Figure 6: A comparison of parabola tip with in-situ morphology of SCN-13wt% camphor alloy at growth condition V = 0.501μm/s, G = 2.8 K/mm, ϕ100 μm.

3. Theoretical model

We first consider the analogy between the Saffmann-Taylor finger and directional solidification, and then examine the model when the results deviate from the Saffmann-Taylor branch and follow the parabolic tip shape model in presence of anisotropy in interface properties.

The analogy with the directional solidification cells and the Saffmann-Taylor finger has been discussed by Pelce and Pumir [4] and Karma and Pelce [5] for the two dimensional problem during the solidification of a single phase alloy. We shall follow their procedure, and extend the model to three-dimensional growth in presence or absence of a eutectic phase between the cells. The diffusion problem in cellular growth is considered in three regions: (i) outer solution ahead of the cell in which the concentration profile decays exponentially; (ii) the inner solution in the region of the tip; and (iii) the tail region in which the Scheil effect becomes important. The ST problem considers the velocity potential in the regions (i) and (ii) only, and the tail region causes departure from the ST finger solution. In this study, we have therefore examined the cell formation in a eutectic system in which the tail region is cut-off by the presence of a eutectic at very low growth rates. We shall thus consider the cellular growth problem in which a eutectic front is present.

A. Saffmann-Taylor model in 3D

We first consider the basic formulation of the ST-finger problem. The velocity potential, Φ, satisfies the Laplace's equation:

$$\nabla^2\Phi = 0 \qquad (2)$$

in the region outside the finger (i.e. in the viscous liquid phase). For steady-state finger

advancing at a constant velocity in the z direction, the boundary conditions at the interface and at the wall are given by:

$$\Phi_i = \overline{\lambda}\kappa \tag{3}$$

$$\mathrm{Cos}\theta = -\hat{n}.\nabla\Phi_i \tag{4}$$

$$\left.\frac{d\Phi}{dr}\right]_{r=1} = 0 \tag{5}$$

$$\left.\frac{\partial\Phi}{\partial z}\right]_{z\to\infty} = 1, \text{ and } \Phi\big]_{z\to-\infty} = \overline{\gamma}/\lambda \tag{6}$$

where κ is the curvature of the interface, γ is the interface energy parameter (often referred to as the surface tension parameter) that controls the selection of the relative width of the finger, V is the finger velocity, and θ is the angle between the local normal to the interface, n, with the growth direction z. All length scales are divided by the radius of the tube (r = a) to obtain dimensionless quantities.

B. Directional solidification

We shall first define the problem of directional solidification, and then rescale the variables to obtain equations analogous to the set of Eqs. (2) – (6). Consider directional solidification of an off-eutectic alloy of composition C_∞ under growth conditions in which steady-state cells form ahead of a eutectic front. The concentration profile in the liquid is governed by:

$$\nabla^2 C + P\frac{\partial C}{\partial z} = 0 \tag{7}$$

where the distances are normalized with the radius of the tube, a, and P=Va/D. We take the

origin at the center of the cell at the eutectic isotherm. The boundary conditions of composition and mass balance at the interface are given by:

$$C_i = C_E + \frac{Ga}{m} z_i - \frac{\Gamma}{ma}\kappa \tag{8}$$

$$P\, C_i (1-k)\cos\theta = -\hat{n}.\nabla C \tag{9}$$

The boundary condition at the wall is:

$$\left.\frac{dC}{dr}\right]_{r=l} = 0 \tag{10}$$

where C_E is the eutectic composition and κ the dimensionless curvature.

In order to remove the concentration variation at the interface due to the thermal gradient, we consider the boundary condition (Eq. (8)), and define:

$$w = C - C_E - \frac{Gaz}{m} \tag{11}$$

so that the boundary conditions for w become:

$$w_i = -\frac{\Gamma}{ma}\kappa \tag{12}$$

$$-\nabla w.n = \left[P\, C_i (1-k) + \frac{Ga}{m}\right]\cos\theta \tag{13}$$

For small Peclet number conditions, Pelce-Pumir [4] and Karma-Pelce [6] have shown that the above relationship can be approximates as:

$$-\nabla w.n = \left[P\, C_t (1-k) + \frac{Ga}{m}\right]\cos\theta \tag{14}$$

which can be written as:

$$-\nabla w.n = \left[\Delta C_E\ P\left(\frac{C_t(1-k)}{C_E - C_\infty} - \frac{1}{\nu_E}\right)\right]\cos\theta \tag{15}$$

where $\Delta C_E = C_E - C_\infty$ and $\nu_E = V\Delta T_E/GD$, in which $\Delta T_E = -m\Delta C_E$. The undercooling ΔT_E represents the maximum undercooling at which cells disappear and only eutectic forms. The physical reasoning for the approximation is that the first term in equation (13) is due to the flux normal to the interface, which is negligible for finger-shape away from the tip region. The contribution to the flux comes from the cap region at the tip where the concentration does not vary significantly for small Peclet number so that $C_i \sim C_t$.

C. Analogy with the 3D- Saffmann-Taylor model

To obtain an analogy with the Saffmann-Taylor problem, we rewrite the boundary condition, equation (14) as:

$$-\nabla\Phi.n = \cos\theta \tag{16}$$

where

$$\Phi = \frac{w}{\Delta C_E P}\left[\frac{C_t(1-k)}{C_E - C_\infty} - \frac{1}{\nu_E}\right]^{-1} \tag{17}$$

In terms of concentrations, the above function is:

$$\Phi = \frac{1}{P\,\Delta C_E}\frac{C - C_E - (Ga/m)z}{\left[\{C_t(1-k)/(C_E - C_\infty)\} - (1/\nu_E)\right]} \tag{18}$$

The value of Φ at the interface is obtained by substituting the value of w_i from equation (12) into equation (18), which gives:

$$\Phi_i = -\frac{\Gamma}{ma}\frac{1}{\Delta C_E}\frac{1}{P}\left[\frac{C_t(1-k)}{C_E - C_\infty} - \frac{1}{\nu_E}\right]^{-1}\kappa = \bar{\gamma}\kappa \tag{19}$$

The boundary condition at the tube wall, given by equation (11), becomes:

$$\left.\frac{d\Phi}{dr}\right]_{r=1} = 0 \qquad (20)$$

For small Peclet number condition, the term containing P in equation (6) can be neglected, so that the field Φ is governed by:

$$\nabla^2\Phi = 0 \qquad (21)$$

We thus note that the problem of directional cell growth, given by equations (20), (18), (15) and (19) is equivalent to the Saffmann-Taylor problem defined by equations (1-4).

The value of the dimensionless interface energy parameter, $\bar{\gamma}$, which is the control parameter for the selection of relative width, is obtained from Eq. (19) as:

$$\bar{\gamma} = \frac{4\Gamma}{G\lambda^2}\left[\frac{\nu_E C_t(1-k)}{C_E - C_\infty} - 1\right]^{-1} \qquad (22)$$

We have substituted a = $\lambda/2$, in which λ is the diameter of the tube that is equivalent to primary spacing in a cellular array. The value of $C_t(1-k)/(C_E - C_\infty) = \Delta(1-k) + C_\infty(1-k)/(C_E - C_\infty)$ can be obtained from the definition of dimensionless undercooling, $\Delta_E = (C_t - C_\infty)/[C_E - C_\infty]$, where $\Delta_E = \Delta T/\Delta T_E$. Substituting this result in Eq. (22) gives the value of γ as:

$$\bar{\gamma} = \left[\frac{4\Gamma}{G\lambda^2}\right]\left[\frac{1}{\nu_E\{(1-k)\Delta_E + C_\infty(1-k)/(C_E - C_\infty)\} - 1}\right] \qquad (23)$$

The directional solidification problem is now reformulated to be equivalent to the ST-finger problem, so that we can use the results of the 3D Saffmann-Taylor problem obtained by Levine and Tu [11]. The first result is the shape of the interface, which can be written in terms of dimensional Z and r as:

$$Z = \frac{\lambda^2 \Lambda^2}{\pi^2 \rho} \ln\left(\cos\frac{\pi r}{\lambda\Lambda}\right) \qquad (24)$$

where ρ is the principal radius of curvature at the tip, and the origin is taken at the tip of the cell.

The second important conclusion of the 3D-finger model is the existence of steady state solutions. In contrast to the 2D model for which steady-state is obtain for any finite value of $\bar{\gamma}$, the 3D model predicts four branches in the Λ-$\bar{\gamma}$ space. The upper three branches were found to be unstable with respect to tip splitting, and the lowest stable branch gave solutions only for the value of $\bar{\gamma}$ larger than 0.0067, as shown in Fig. 7. This stable branch predicts the relative width, Λ, as a function of the interface energy parameter which

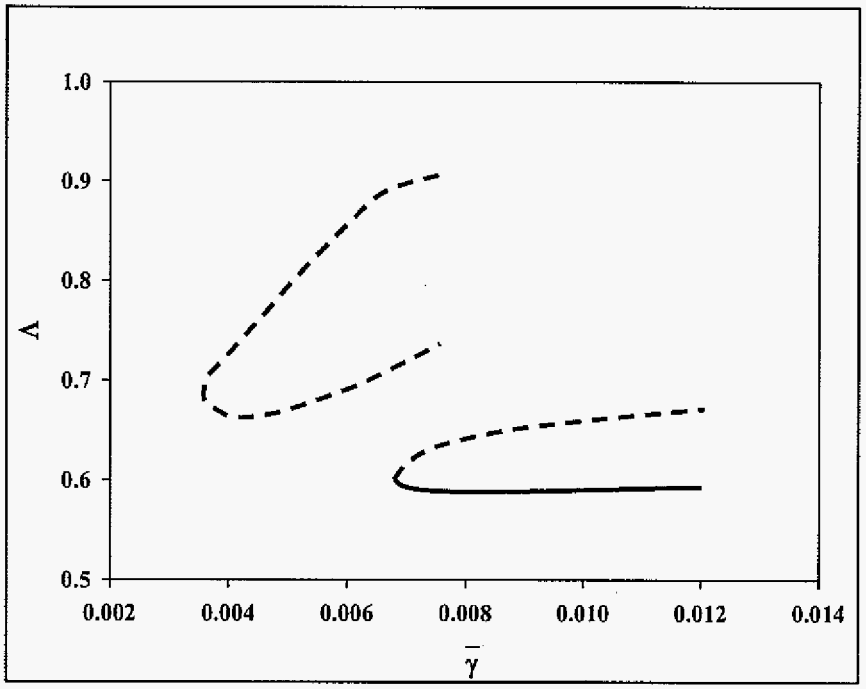

Figure 7. Relative width of ST finger vs the surface-tension parameter [11].

contains the experimental parameter ν. The smallest value of $\bar{\gamma} = \bar{\gamma}_0 = 0.0067$ corresponds to the largest relative width of $\Lambda = \Lambda_{Max} = 0.591$. The result can be written as $\bar{\gamma} = F(\Lambda)$. Although $\bar{\gamma}$ can vary over a large range, the variation in the relative width is very small when the analogy with the Saffmann-Taylor finger is valid.

Once the value of $\bar{\gamma}$ is determined from equation (23), a unique value of the relative cell width is predicted. The value of $\bar{\gamma}$, however, depends on cell tip undercooling, so that a relationship between the cell tip undercooling and the relative width is required.

D. Cell tip undercooling

We shall now develop an expression for the tip undercooling as a function of the relative width by using the procedure given by Karma and Pelce [6] for the 2D case. We first consider the concentration field in the liquid far ahead of the interface, i.e. for $z > z_t$, which decays exponentially as:

$$C - C_\infty = (C_t - C_\infty) e^{-P(z-z_t)} \qquad (25)$$

We now consider mass balance in which the rate at which solute enters the region ahead of the cell in the tube is equal to the rate at which solute is rejected from the sides of the cell and that from the curved tip region, which gives

$$-D\left(\frac{\partial C}{\partial z}\right) = \Lambda^2 \left[VC_t(1-k) + \frac{DG}{m} \right] - \frac{DG}{m} \qquad (26)$$

where the interface composition near the tip region is assumed to be constant at low P values. Matching the concentration gradient with that from equation (25) gives:

$$\Lambda^2\left[VC_t(1-k)+\frac{DG}{m}\right]-\frac{DG}{m}=V(C_t-C_\infty) \tag{27}$$

The above result can be rearranged to give the dimensionless tip undercooling as:

$$\Delta_E=\frac{\Lambda^2[C_\infty(1-k)/(C_E-C_\infty)]+(1/\nu_E)\left(1-\Lambda^2\right)}{1-(1-k)\Lambda^2} \tag{28}$$

Substituting the above result in Eq. (23), the control parameter, $\bar{\gamma}$ is obtained as:

$$\bar{\gamma}=\left[\frac{4\Gamma}{G\lambda^2}\right]\left[\frac{1-(1-k)\Lambda^2}{-k+\nu_E C_\infty(1-k)/(C_E-C_\infty)}\right] \tag{29}$$

The plot of the selection function, numerically calculated and plotted by Levine and Tu can be curve-fitted to give: $\bar{\gamma}=F(\Lambda)$. This gives:

$$\left[\frac{4\Gamma}{G\lambda^2}\right]\left[\frac{1-(1-k)\Lambda^2}{-k+\nu_E C_\infty(1-k)/(C_E-C_\infty)}\right]=F(\Lambda) \tag{30}$$

which gives a transcendental equation relating Λ with the experimental variables G and ν. Once the value of Λ is calculated, the tip undercooling can be obtained from Eq. (28).

In the above treatment the reference is taken at the eutectic isotherm and the undercooling is normalized with the difference between the liquidus and the eutectic temperature. We can also write the results in terms of the planar front as a reference point. In this case, Eqs. (28) and (30) can be written in terms of the planar front reference point parameters: $\nu = V\Delta T_0/GD$, and $\Delta = \Delta T/\Delta T_0$, in which $\Delta T_0 = mC_\infty(k-1)/k$. Substituting $\nu_E=\nu\left(\Delta T_E/\Delta T_0\right)$ and $\Delta_E=\Delta\left(\Delta T_0/\Delta T_E\right)$, and simplifying, we obtain the two main results as:

$$\bar{\gamma}=\left[\frac{4\Gamma}{Gk\lambda^2}\right]\left[\frac{1-(1-k)\Lambda^2}{\nu-1}\right]=F(\Lambda) \tag{31}$$

and

$$\Delta = \frac{k\Lambda^2 + (1/v)\left(1 - \Lambda^2\right)}{1 - (1-k)\Lambda^2} \qquad (32)$$

The above expressions are analogous to those for the 2D case [5], except that Λ in 2D is replaced by Λ^2 in 3D, and a factor of 4 in Eq. (31) comes from the radius of the sample. These equations, along with Eq. (24) for the shape of the cell, will be used for comparison with the experimental results.

4. Discussion

Experimental results are presented for the growth of a single cell ahead of the eutectic interface for directional solidification in capillary tube of 50 μm radius. A theoretical model, based on the analogy with the 3D Saffmann-Taylor finger was developed. The following aspects were investigated: (1) shape of the cell; (2) experimental conditions for which the shape matched with the predicted shape; (3) cell tip undercooling; and (4) an examination of the data with the steady-state finger growth, as predicted by the Levine-Tu model. Of the total of 21 experiments, only three experiments at very low velocities showed excellent match with the Saffmann-Taylor finger. This discrepancy will be examined and the modification in the model will be given.

A. Shape of the cell

The shapes of the experimental cells were compared with the prediction of the model based on the analogy with the 3D Saffmann-Taylor fingers. Figures 2-4 show that for experimental conditions just above the critical velocity for planar front instability, a very good agreement is obtained with the theoretically predicted Saffmann-Taylor shape. However,

the shape begins to deviate as the velocity is increased or the gradient is reduced. At higher velocities, the tip region becomes parabolic so that the cell growth solution changes from the ST branch to a parabolic branch.

B. Tip undercooling

We first examine the tip undercooling expression given by the 3D-ST model, given by Eq. (32), which can be written as:

$$\Delta = \frac{1}{\nu}\left[\frac{1-(1-k\nu)\Lambda^2}{1-(1-k)\Lambda^2}\right] \qquad (33)$$

The relationship, $\Delta = (1/\nu)$, was predicted by Bower et al. (BBF) [13]. Since $\nu = V/V_c$, the term in the large bracket is positive, a larger undercooling value is predicted compared to the BBF model. Equation (33) shows that the BBF model is the limiting case when k approaches zero or n approaches unity, i.e. close to the planar front instability condition. A significant deviation would be present for larger values of k. The experimental measurements of the interface undercooling as a function of velocity is plotted in Figs. 8(a) and 8(b) for SCN-9.6 wt% camphor, directionally solidified at G = 4.75 and 4.16 K/mm. The experimental undercooling values for both these conditions are significantly larger than those predicted by the BBF model, and this is due to a larger value of k, k=0.3, in this system. The experimental values are also a little higher than those predicted by the 3D-ST model. Note that only at one condition, which corresponds to that at the lowest velocity in Fig. 8(a), the shape of the cell matches with the ST shape, as shown in Fig. 2. The experimental data are also plotted in Fig. 9 against $1/\nu$ to see the difference with the BBF model.

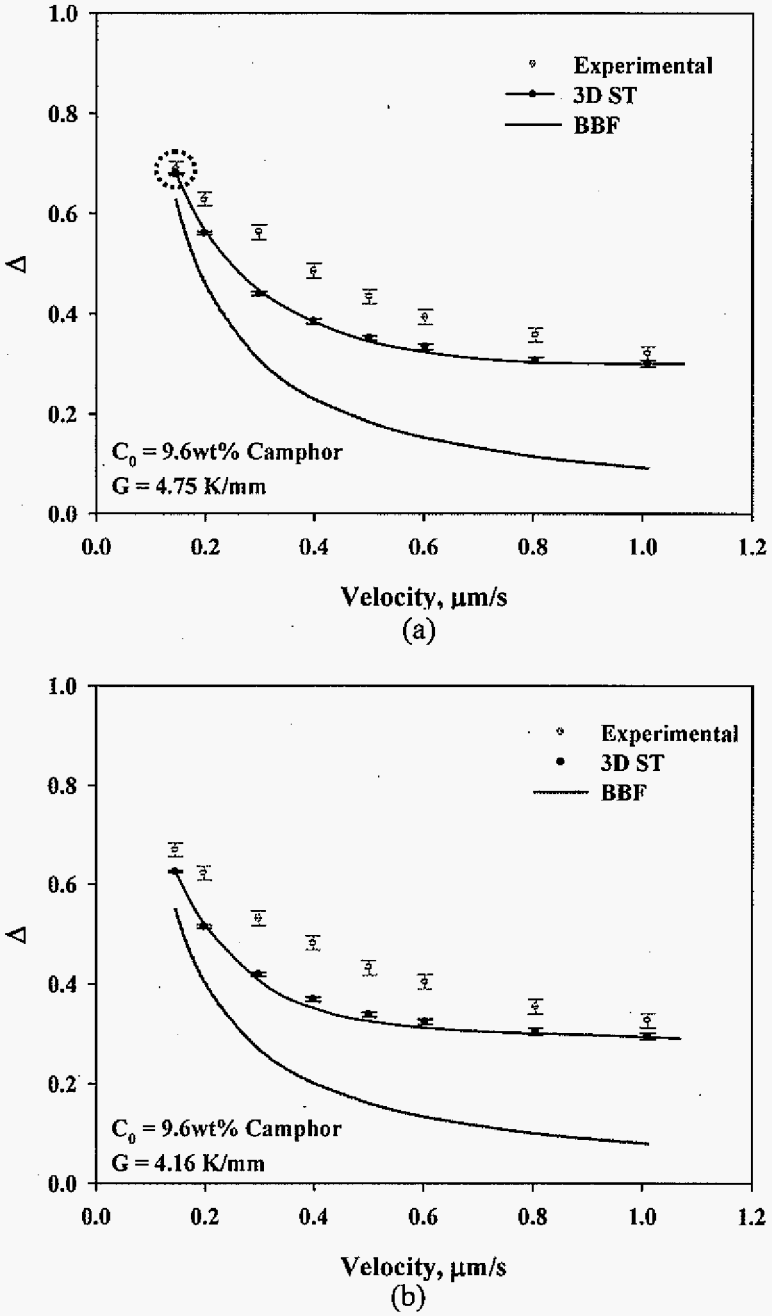

Figure 8: Experimentally measured undercooling as a function of velocity, and theoretically predicted undercooling using the 3D Saffmann-Taylor analogy. The undercooling predicted by Bower et al. [12] are also shown as BBF. SCN-9.6 wt% camphor with (a) G = 4.75 K/mm, and (b) G = 4.16 K/mm.

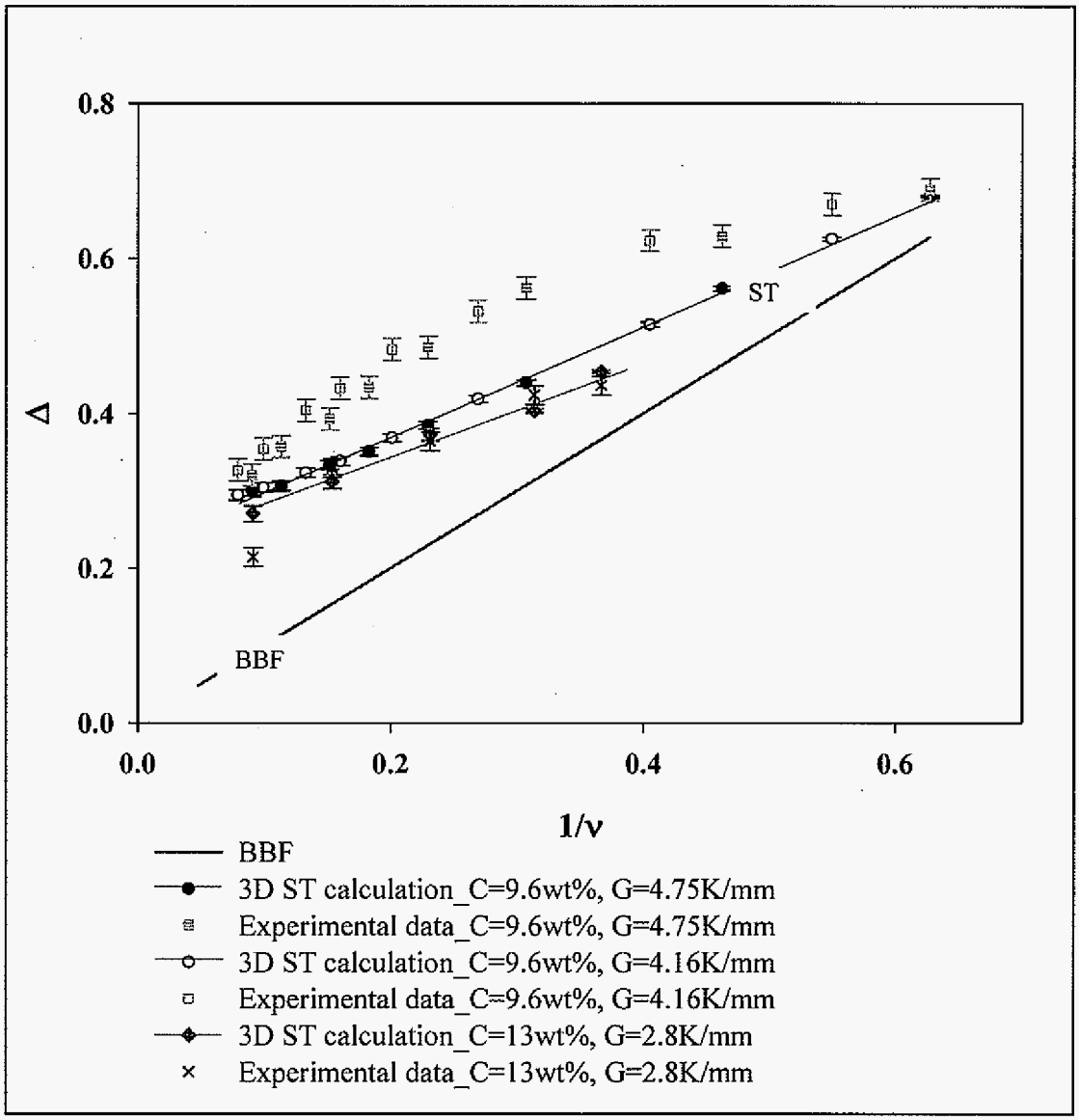

Figure 9: The variation in non-dimensional tip undercooling, Δ, with the dimensionless parameter, 1/ν, for SCN-9.6 and SCN-13.0 wt% camphor. Theoretical results for the 3D-ST model and the BBF models are also shown for comparison.

C. Relative Width

When the cell shape fits the ST shape, the cells are considered to belong to the Saffman-Taylor (finger) branch and we can directly obtain the relative width as a function of

the interface energy parameter by using equation (31). The experimentally measured relative width is plotted against $\bar{\gamma}$ in Fig. 10. The solid line is the relationship predicted by Levine and Tu [11], which may be slightly shifted due to the presence of interface energy anisotropy [14]. It is seen that only three data points show a good match, and these three points correspond to the conditions for which the cell shapes were observed to fit the ST shape, as indicated by the shape ST-finger in Table 3.

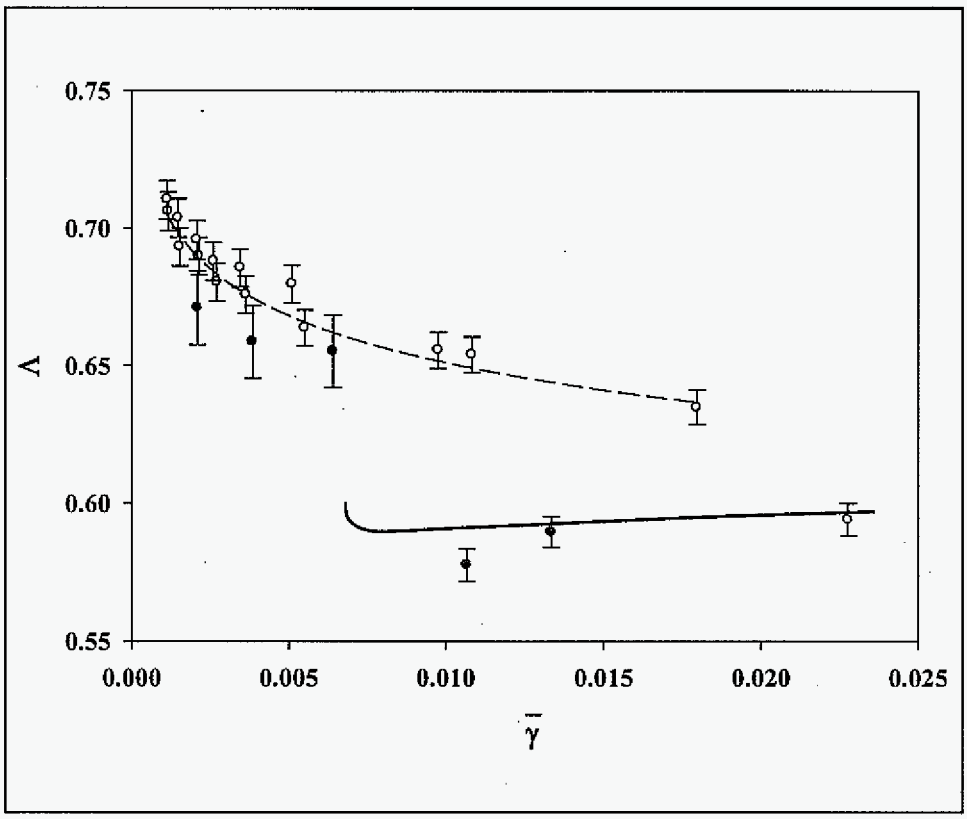

Figure 10. A comparison of the experimental results on the relative width with the results of the Levine-Tu model (solid line). The relative widths are calculated at the eutectic front. Filled and open circles are data points for SCN-13.0wt% and -9.6wt% camphor respectively. Red symbols represent the obtained cellular shapes that comply with the 3D ST equation and blue symbols are for the cellular structures that do not fit with the 3D ST equation.

For the most of the experiments, the finger shape does not match with the ST shape, as shown in Fig. 5. In these cases the lengths of the cells were larger, and the Scheil effect behind the cell was not negligible. The width of the cell at the eutectic front was larger than that predicted by the ST finger shape. As the velocity was increased, the shape of the tip became parabolic, as seen in Fig. 6. One thus considers the cells to belong to a "dendrite" branch [14]. In this case there is no longer a direct access to Λ, which becomes an effective or "hidden" parameter. In the 2D case, the relative width depends on the ratio of tip radius and spacing, (ρ/λ) as [15, 16]:

$$\Lambda = 2 / [(1 + 4\lambda/\pi\rho)^{1/2} + 1] \qquad (34)$$

and the value of Λ is calculated from the experimental measurements of ρ and λ. In 3D, we may use a similar approach by examining the 3D shape equation given by Levine and Tu [11] in the dimensional form:

$$Z = \frac{1}{c}\ln\left(\cos\frac{\pi r}{\lambda\Lambda}\right) \qquad (35)$$

The value of c can be related to the tip radius by taking the second derivative of z [8], which gives $c = (\pi^2 \rho)/(2\lambda\Lambda^2)$ or $c\Lambda = (\pi^2 \rho)/(2\lambda\Lambda)$. The relative width thus depends on c and (ρ/λ) as:

$$\Lambda = (\pi^2 / 2c)^{1/2} (\rho/\lambda)^{1/2} \qquad (36)$$

This equation gives relative width Λ as a function of (ρ/λ) and the parameter c. Levine and Tu [11] have derived a relationship between the parameter c and Λ which, for zero surface tension condition, is given by:

$$J_0(c\Lambda) - [J_1(c) / Y_1(c)]\, Y_0(c\Lambda) = 0 \qquad (37)$$

The value of c as a function of Λ is calculated numerically and substituted in Eq. 36 to obtain a relationship between Λ and ρ/λ, and the results are shown in Fig. 11. Since λ is fixed by the diameter of the sample in our experiments, Λ is related to the tip radius, ρ. For practical use, this relationship can be approximated by using the curve fit, as:

$$\frac{\rho}{\lambda} = \frac{\Lambda}{\pi(1-\Lambda)} - 0.3762\,\Lambda \qquad (38)$$

Using the experimental values of ρ and λ, the corresponding values Λ are calculated, which are in turn substituted in Eq. (31) to obtain the corresponding values of the interface energy parameter. The calculated values are listed in Table 4 and 5, and the results of the experiments are plotted as Λ_c versus $\bar{\gamma}_c$ in Fig. 12. The value of the relative width is constant at high $\bar{\gamma}_c$ values, which correspond to the Saffmann-Taylor branch, while it decreases as $\bar{\gamma}_c$ is decreased. This is predicted by Ben Amar [14], who showed that the as is $\bar{\gamma}_c$ is decreased, a transition from the Saffmann-Taylor branch to a parabolic branch occurs when anisotropy in interface energy is taken into account in the model.

The expression for the tip undercooling, developed for the condition of the validity of the ST model in Eq. (31), can be modified by using the effective relative width. Using the relationship between the effective width and the spacing/tip radius ratio, one can relate the tip undercooling with spacing, tip radius and experimental parameter. v. This is done by eliminating Λ between the following two equations.

$$\Delta = \frac{k\Lambda^2 + (1/v)\left(1-\Lambda^2\right)}{1-(1-k)\Lambda^2} \qquad (39)$$

$$\frac{\rho}{\lambda} = \frac{\Lambda}{\pi(1-\Lambda)} - 0.3762\,\Lambda \qquad (40)$$

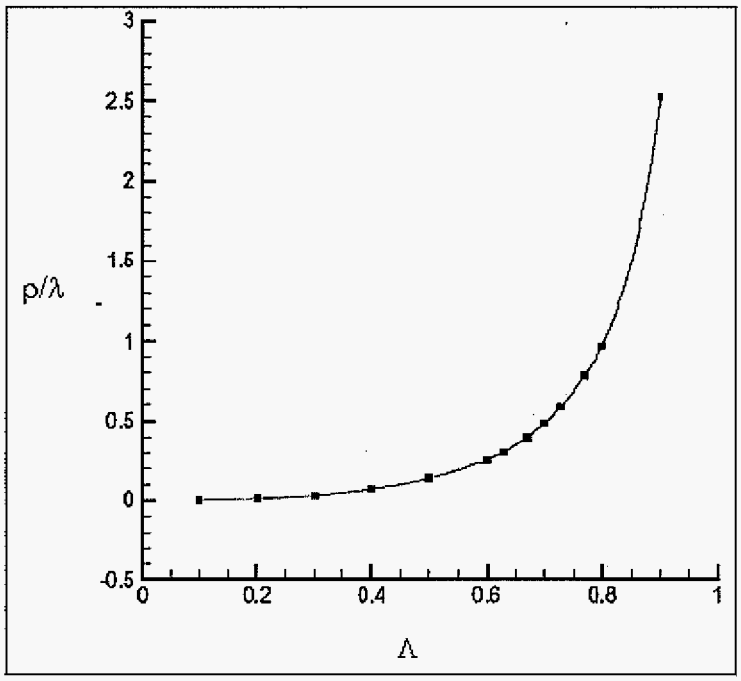

Figure 11. The variation in the relative width, Λ, with (ρ/λ).

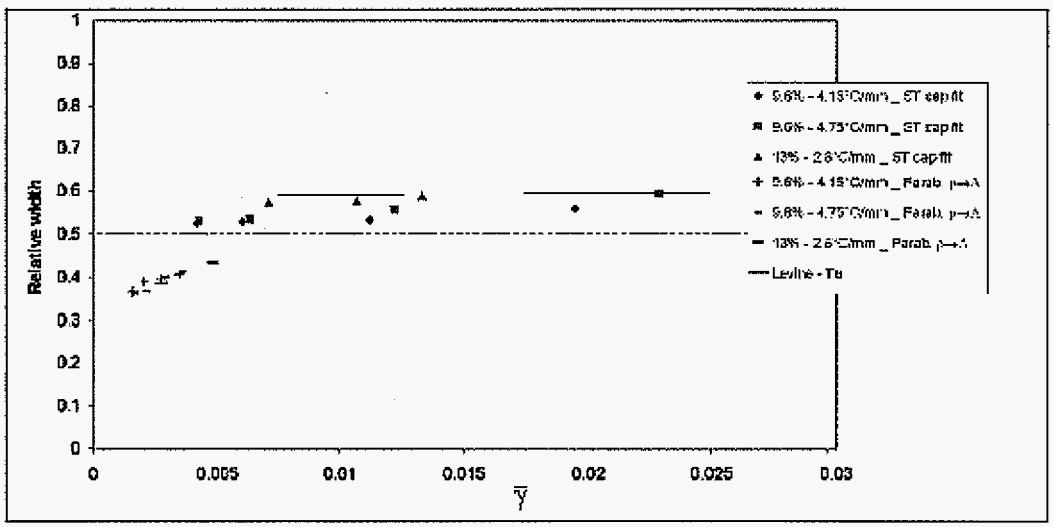

Figure 12. The variation in relative width with the interface energy parameter. The relative width is calculated by using the cell cap shape.

Table 4: Summary of relevant parameters

C_0 = 9.6 wt % and G = 4.75 K/mm

V μm/s	C_S at tip $(V/V_c)(kC_i/C_0) - 1$	γ_{LT} with Λ_e	Λ_c	γ_{LT} with Λ_c	Cell shape
0.15	0.029	0.0229	0.594	0.0229	Finger
0.20	0.261	0.0109	0.555	0.0122	Finger
0.30	0.801	0.00552	0.532	0.0064	Finger
0.40	1.26	0.00364	0.528	0.0043	Finger
0.50	1.71	0.00272	0.409	0.00355	Parabola
0.60	2.10	0.00212	0.400	0.00286	Parabola
0.805	3.06	0.00153	0.365	0.00209	Parabola
1.01	3.90	0.00117	0.362	0.00163	Parabola

C_0 = 9.6 wt % and G = 4.16 K/mm

V μm/s	C_S at tip $(V/V_c)(kC_i/C_0) - 1$	γ_{LT} with Λ_e	Λ_c	γ_{LT} with Λ_c	Cell shape
0.15	0.09	0.0180	0.56	0.0195	Finger
0.20	0.43	0.00975	0.535	0.0112	Finger
0.30	1.01	0.00510	0.53	0.00606	Finger
0.40	1.59	0.00346	0.525	0.00416	Finger
0.50	2.13	0.00261	0.407	0.00345	Parabola
0.60	2.61	0.00208	0.396	0.00280	Parabola
0.81	3.60	0.00149	0.389	0.00204	Parabola
1.01	4.67	0.00114	0.365	0.00160	Parabola

C_0 = 13.0 wt % and G = 2.8 K/mm

V μm/s	C_S at tip $(V/V_c)(kC_i/C_0) - 1$	γ_{LT} with Λ_e	Λ_c	γ_{LT} with Λ_c	Cell shape
0.125	0.42	0.0133	0.59	0.0133	Finger
0.15	0.63	0.0107	0.578	0.0107	Finger
0.20	1.12	0.00642	0.574	0.00706	Finger
0.30	2.06	0.00385	0.431	0.00481	Parabola
0.50	3.47	0.00211	0.385	0.00276	Parabola

Table 5. Relative width and tip radius to spacing ratio for cell cap model	
Λ	ρ/λ
2.0000E-01	1.1445E-02
3.0000E-01	3.1898E-02
4.0000E-01	7.0195E-02
5.0000E-01	1.3790E-01
6.0000E-01	2.5781E-01
6.3000E-01	3.1037E-01
6.7000E-01	3.9870E-01
7.0000E-01	4.8317E-01
7.3000E-01	5.8897E-01
7.7000E-01	7.7771E-01
8.0000E-01	9.7307E-01
9.0000E-01	2.5228E+00

5. Conclusions

Benchmark experimental studies are carried out to examine the shape and selection of relative width and tip temperature of directional solidification cells. A critical experimental set-up is designed to achieve the following: (i) a single three-dimensional cell is produced in a capillary sample; (ii) in situ observations of the cell shape; (iii) the growth of cells under diffusive conditions in capillary samples; and (iv) the presence of eutectic behind the cell to reduce the Scheil effect. A theoretical model, based on the analogy between the cells and 3D-ST finger was developed. Experimental results show a good agreement only within a very narrow regime of growth conditions. When the shape of the cell deviates from the ST-shape, the analysis was modified. An effective relative width was defined and calculated. The results were shown to change systematically from the ST branch to the parabolic branch as the interface energy parameter was decreased.

The tip temperature variation with velocity and thermal gradient was predicted from the model. It was shown to be significantly different from the model of Bower et al. (BBF)

[13]. The BBF model gives the results only in the limiting case when the solute distribution coefficient, k, approaches zero. Experimental results in the SCN-camphor system showed significantly larger tip undercooling that that predicted by the BBF model, but were closer to the model based on the three-dimensional ST analogy.

Acknowledgement

This work was supported by NASA and DOE-BES. A part of the work was carried out at Ames Laboratory which is operated by Iowa State University for the Office of Basic Energy Science, Division of Materials Science, U. S. Department of Energy under Contract No. W7405-Eng-82.

References

[1] G. B. McFadden and S. R. Coriell, Physica D, 12, 253 (1984).

[2] J. D. Hunt and S-Z. Lu, Metall. Mater. Trans. *Metall. Mater. Trans.*, 27A, 611, (1996).

[3] J. D. Weeks and W. Van Sarloos, Phys. Rev., A 39, 2772 (1989).

[4] P. Pelce and A. Pumir, J. Cryst. Growth, 73, 337 (1985).

[5] A. Karma, Phys. Rev., A 34, 4353 (1986).

[6] A. Karma and P. Pelce, Phys. Rev., A 41, 6741 (1990).

[7] T. Dombre and V. Hakim, Phys. Rev., A 36, 2811 (1987).

[8] R. Trivedi, Shan Liu and S. Williams, Nature Mater., 1, 157 (2002).

[9] P. G. Saffmann and G. I. Taylor, Proc. Roy. Soc. (London), A245, 312 (1958).

[10] J. W. McLean and P. G. Saffmann, J. Fluid Mech., 102, 445 (1981).

[11] H. Levine and Y. Tu, Phys. Rev., A 45, 1044 (1992).

[12] Jing Teng and Shan Liu, J. Cryst. Growth, 290, 248 (2006).

[13] T. F. Bower, H. D. Brody and M.C. Flemings , *Trans TMS-AIME*, 236, 624 (1966).

[14] Ben Amar, EuroPhys. Lett., 16, 367 (1991).

[15] B. Billia, H. Jamgotchian and R. Trivedi, J. Crystal Growth, 123, 399 (1992).

[16] M. Hennenberg and B. Billia, J. Physique, 1, 79 (1991).

CHAPTER 5. CELL-DENDRITE TRANSITION IN SUCCINONTRILE (SCN)-CAMPHOR ALLOYS

A manuscript to be submitted to *Metallurgical and Materials Transactions A*

Jing Teng[1], Shan Liu[2] and R. Trivedi[1, 2, *]

Abstract

Systematic experimental studies have been carried out to investigate the transition from cells to dendrites during the directional solidification of succinonitrile (SCN) -camphor alloys. This transition is not sharp, but occurs over a range of velocity or thermal gradient, and the diffuseness of the transition is closely related to the existence of a range of primary spacings. Within the transition zone a critical spacing, λ_{cd}, is present where a cell changes to a dendrite, and this critical spacing is shown to depended on alloy composition C_o, temperature gradient G and growth velocity V as $\lambda_{cd}\ (GV)^{1/3}C_o^{1/4}=9.92(D\Gamma)^{1/3}$ μm $(K/s)^{1/3}$, where D is the solute diffusion coefficient in the liquid and Γ is the Gibbs-Thomson coefficient. The results of the present study are then synthesized with those in the SCN-salol and SCN-acetone systems to assess the effect of system properties on the cell-dendrite transition. The shape of the tip region shows three distinct regimes: a deep cell regime in which the tip radius scales linearly with the local primary spacing; a well-developed dendrite

---

[1]Dept. Materials Science and Engineering, Iowa State University, Ames, IA, 50011, U.S.A.

[2]Materials and Engineering Physics Program, Ames Laboratory-USDOE, Iowa State University, Ames, IA, 50011, U.S.A.

[*]Corresponding author: e-mail: trivedi@ameslab.gov, phone: (515) 294-5869, fax: (515) 294-4291.

regime in which the tip radius is independent of the local spacing; and a transition regime in which the tip radius increases nonlinearly with the local spacing. For a cellular dendrite, a long wavelength instability is found and explained on the basis of noise-induced instability at a dendrite tip.

(**Keywords**: Directional solidification, dendritic growth, interface instability, succinonitrile)

I. Introduction

Fundamental studies on the cell-dendrite transition (CDT) during directional solidification are still lacking though the initial studies on this morphological transition were published more than 50 years [1, 2, 3]. A precise characterization of the transition condition has been difficult because of several complexities: (1) convection is always present in the solidification process of a bulk sample which causes the composition inhomogeneity macroscopically; (2) cells and dendrites co-exist over a wide range of growth conditions so that no well-defined boundary can be easily delineated; (3) system parameters are generally not known, which complicates the verification of modeling with experimental observations.

The transitions from a planar to non-planar interface and that from a non-planar to planar at high velocity have been well-established since these transitions have been found to be sharp so that specific relationships between the velocity, V, thermal gradient, G, and alloy composition, C_0, are observed for these two transitions. In contrast, the transition from cellular to dendritic microstructure at low velocity and the reverse transition from dendrites to cells at high velocity have not been properly characterized. Early attempts assumed the transitions to be sharp and proposed a criterion for cell to dendrite transition in terms of experimental variables G, V and C_0. For example, the cell to dendrite transition was

predicted at $V = GD/mC_0(k-1)$ in which D is the solute diffusion coefficient in the liquid, k is the equilibrium distribution coefficient of the solute and m is the slope of the liquidus. Tewari and Laxmanan [4] compared all published experimental results with different theoretical models based on a sharp transition, and concluded that no model could explain all experimental result.

An important contribution to the cell-dendrite transition (CDT) was made by Georgelin and Pocheau [5] and Trivedi et al. [6], who examined this transition in thin samples of transparent materials in which details of the transition can be visualized in situ. They showed that the transition is not sharp, but occurs over a range of experimental conditions such as velocity or thermal gradient, and both cells and dendrites coexist in this transition regime. It was shown that CDT is not a collective behavior for array growth; rather it occurs locally such that a specific cell in an array develops sidebranches when its local spacing exceeds some critical value. From detailed experimental studies in the succinonitrile (SCN) – salol system, Trivedi et al. [6] made the following conclusions. (1) The diffuse transition can be described by two limits; the start of the transition $(G/V)_{start}$ and the end of the transition, $(G/V)_{end}$. For $(G/V) < (G/V)_{start}$, only cellular structure is present, whereas for $(G/V) > (G/V)_{end}$, only dendritic structures are present. Between these two limits, both cellular and dendritic structures are found to coexist. The range of (G/V) where the two structures coexist was found to depend on composition. (2) Within the transition zone, the instability occurs when the local spacing approaches a critical cellular spacing, λ_c, which was shown to be related to the growth parameters as: $\lambda_c \propto (GV)^{-1/3}$.

The aim of the present study is three-fold. (1) To establish if the scaling law between

the critical spacing and cooling rate is not specific to a given alloy system. The experimental study of CDT is extended to the SCN-camphor alloy system, along with the analysis of the results available in the literature in other binary alloy systems. (2) To examine the effect of system parameters on the CDT. (3) To establish the mechanisms in the cell-dendrite coexistence region by the quantitative study of the changes in morphologies such as the primary spacing, the tip shape and tip radius in the transition zone. Based on the experimental results in several systems and on the mechanism in the transition zone, a more definite criterion for the cell-dendrite transition will be developed.

II. Experimental

SCN-camphor alloys were selected for this study since the dynamics of pattern formation can be observed in-situ and the relevant thermo-physical properties of this system have been determined fairly accurately. SCN was purified by distillation under vacuum and multi-stage zone refining. Camphor was purified by sublimation under vacuum. Alloys containing 0.035, 0.35, 0.65 and 0.9wt% camphor have been used since a dilute alloy offers a wider range of growth conditions where cell/dendrite coexisting microstructure may evolve. An alloy of specified composition was prepared in a glovebox filled with dry N_2 and infused into rectangular glass tubing for directional solidification. The inside dimension of the tubing was 300 mm (length)×4.0 mm (width)×0.2 mm (thickness). The thickness of the sample was taken to be the same as in the earlier studies in SCN-salol system [6] to minimize the effect of thickness on the transition.

The crystallographic orientation of the solid was pre-selected such that a (100) plane was parallel to the top surface of the glass tubing and one <100> direction was aligned along

its length. The orientation is crucial for this study since the instability developing near the tip region needs to be clearly observed, and to ensure that the effect of anisotropy in interface energy that could influence CDT is kept the same.

Due to the limited width of the sample, a dummy glass tubing of the same dimension was placed on each side of the sample to minimize the lateral heat flow. The three-tubing bundle was sandwiched between two glass plates so as to minimize the effect of possible air flow in the experimental setup.

A temperature gradient stage (TGS) was used for the directional solidification process. The sample was moved through a linear translation system driven by a computer-modulated step motor and the velocity was varied from 1.0 to 25.0 μm/s, though some higher velocities were also used for SCN-0.035wt%camphor alloys. The temperature gradient (G) can be varied by adjusting the gap between the hot and cold block and/or adjusting the temperature settings. The values of temperature gradient for this study were in the range of 1.28 to 6.03 K/mm. The TGS was mounted on a stage of an optical microscope and the experimental process was monitored through an imaging system and recorded by a high-resolution digital camera. The whole setup was placed inside a glovebox with feed-throughs for electrical connections, liquid and dry N_2.

III. Experimental Results

We start with the general observation of microstructures developed in alloys of different compositions and then focus on the transition region where cells and dendrites coexist in an array.

3.1. Microstructural observations

In order to find the parameter space where cells/dendrites may coexist, directional solidification experiments were conducted over a wide range of compositions, growth velocities and temperature gradients. The observed morphologies are summarized in Fig. 1 as microstructure maps. For SCN-0.035wt% camphor, planar front growth could be easily achieved and no dendrites were observed for the experimental conditions shown in Fig. 1(a). The morphologies observed in SCN-0.35, 0.65 and 0.9wt%camphor alloys are summarized in Figures 1(b) - 1(d). The highest velocity was set at 21.2 μm/s since the well-developed dendritic morphologies were observed in all the alloys at all temperature gradient conditions used in this study. As expected, an increase in growth velocity at a fixed thermal gradient changed the interface pattern from cellular to dendritic, and this change occurred over a range of velocity or thermal gradient, as seen in Fig. 1.

Consider now the interface morphology as a function of velocity for fixed values of the thermal gradient and alloy composition. When the interface velocity is just above the planar interface instability condition, low-amplitude cells are formed along the interface. Continual increase in velocity gives rise to complex cellular patterns consisting of doublets, multiplets and deep cells [7, 8], which finally transform to deep cells only, as shown in Fig. 2(a). In this paper, we shall focus on the deep cell to dendrite transition only, and the multiplet formation in SCN-camphor alloys will be presented separately.

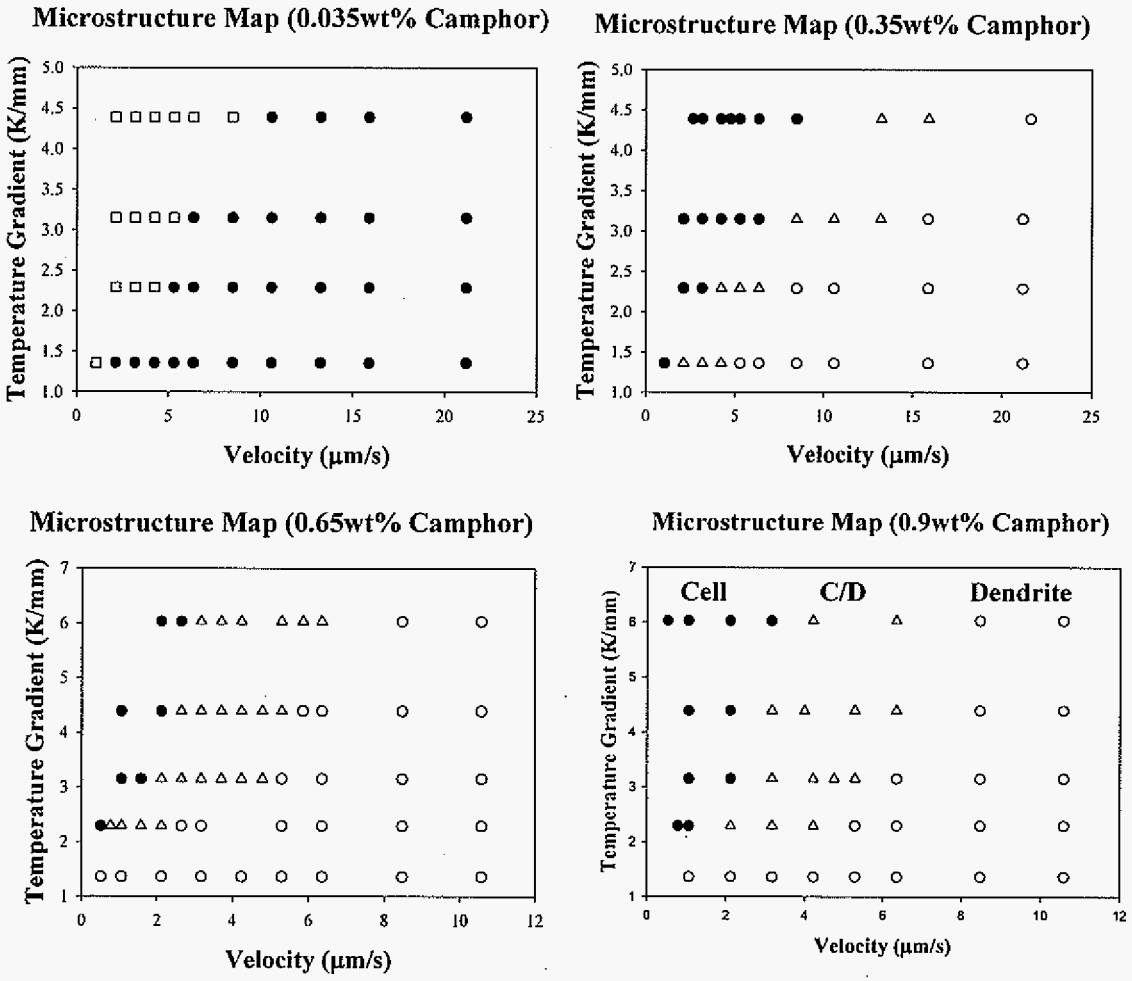

Figure 1. Microstructure map for four alloy compositions grown at different temperature gradients and velocities. Open squares □, filled dots •, open triangles Δ and open dots o represent the planar front growth, purely cellular morphology, cell/dendrite coexistence, and purely dendritic morphology respectively.

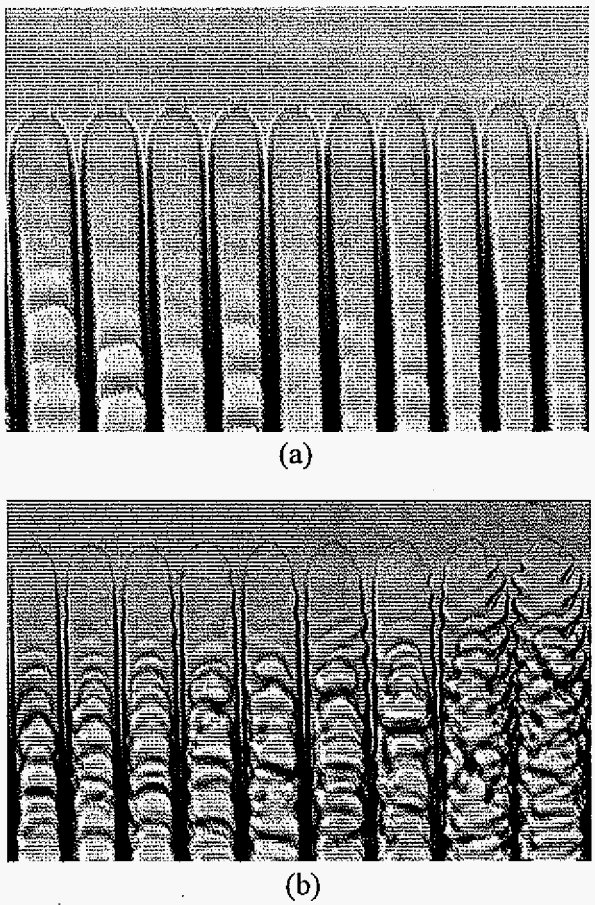

(a)

(b)

Figure 2. Cell/dendrite patterns in SCN-0.35wt%camphor (G=4.39K/mm) (a) V=7.41 μm/s; and (b) V=13.23 μm/s.

When the velocity is increased further, cell to dendrite transition is observed, as shown in Fig. 2(b). This transition will be characterized as the onset of sidebranches. In order to properly characterize the CDT in a thin sample, it is critical to control experimental parameters such that the primary spacing is compatible with the thickness of the sample. Three different cases may arise depending on the relative magnitudes of the sample thickness, d, and the primary spacing, λ_1, and they are: (i) $d>>\lambda_1$; (ii) $d\sim\lambda_1$; and (iii) $d<<\lambda_1$. The sample thickness is generally fixed, 200 μm in the present experiments, while the primary spacing λ_1

varies with growth conditions, which restricts the range of experimental parameters for which desirable ratio can be maintained.

First consider the case where $d >> \lambda_1$, where two or more layers of crystals form in the sample, which may not be appropriate for the present study. Two layers were observed in the SCN-0.035 wt% camphor, as shown in Fig. 3(a), in which the top layer is slightly dendritic but the bottom layer clearly consists of deep cells. Multi-layer growth makes it difficult to observe the dynamic transition from cells to dendrites so that higher compositions of camphor, viz. 0.35, 0.65 and 0.9wt% camphor, were selected for this study, and the temperature gradient was set at 1.36, 2.38, 3.36, 4.39 and 6.03 K/mm.

The desired case for the present study is $d \sim \lambda_1$, where a cell/dendrite grows in a three dimensional manner for both the tip shape and for spacing selection. A single layer will generally form when $d < 2\lambda_1$. When $\lambda_1 < d < 2\lambda_1$, a single layer of crystal growth may occur but the instability may develop in the vertical direction rather than in the lateral direction, such as shown in Fig. 2(b). In this case the critical spacing for the CDT is d instead of λ_1. Since instabilities in the vertical and horizontal direction are governed by the same physics, we only consider those in the horizontal plane in this study since these instabilities are much easier to resolve and can be measured accurately. The microstructure map in Fig. 1 is constructed from the observation on the lateral instability in the horizontal plane.

For the third case, $d<<\lambda_1$, instability may develop in the horizontal plane only, as shown in Fig. 3(b). The average spacing here is ~645 μm, but the sample is only 200 μm thick, therefore no instability forms in the vertical direction. However, it has been shown theoretically as well as experimentally that the microstructures and microstructural scales are

significantly altered when $d << \lambda_1$ [9] so that the CDT condition may also be influenced in a very thin sample. For SCN-0.65 wt% camphor and SCN-0.9 wt% camphor alloys the morphology is always dendritic for G=1.36K/mm, within the velocity range examined. These results clearly show that at this low thermal gradient value the spacing becomes much larger than the sample thickness, which changes the conditions for microstructure selection. If the primary spacing is larger than the sample thickness, the experimentally observed spacing is larger than a naturally selected one due to the spacing constraint [10, 11]. Since the thickness of the sample used in this study is 200 μm, experimental spacing data much larger than 200 μm will not be used for the analysis of the results. The effect of thickness on CDT is discussed in the Appendix.

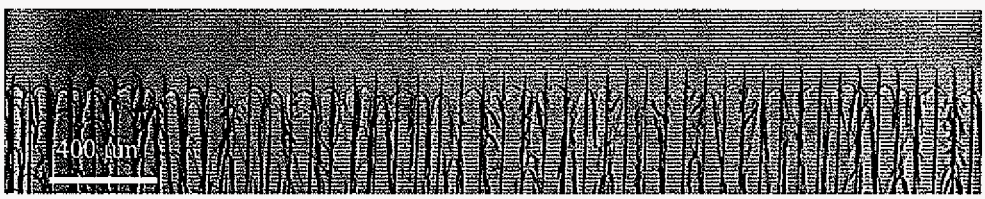

(a)

(b)

Figure 3. Interface morphology of (a) SCN-0.035wt%camphor (G=1.36K/mm, V=21.2 μm/s); and (b) SCN-0.65wt%camhpor (G=1.36K/mm, V=0.51μm/s) in a 200 μm thick sample.

3.2. Primary spacing

The variation in primary spacing with velocity is shown in Fig. 4. In this figure, the filled symbols represent the average spacing and the bars show the range of spacing observed in a given cell/dendrite array. The transition from one pattern to another is not sharp, and the diffuse nature of the transition arises from the existence of a range of primary spacing [5, 6, 12]. One can see from Fig. 4 that the maximum spacing of deep cells is almost the same as the minimum dendrite spacing, indicating that a cell with a locally large spacing has a

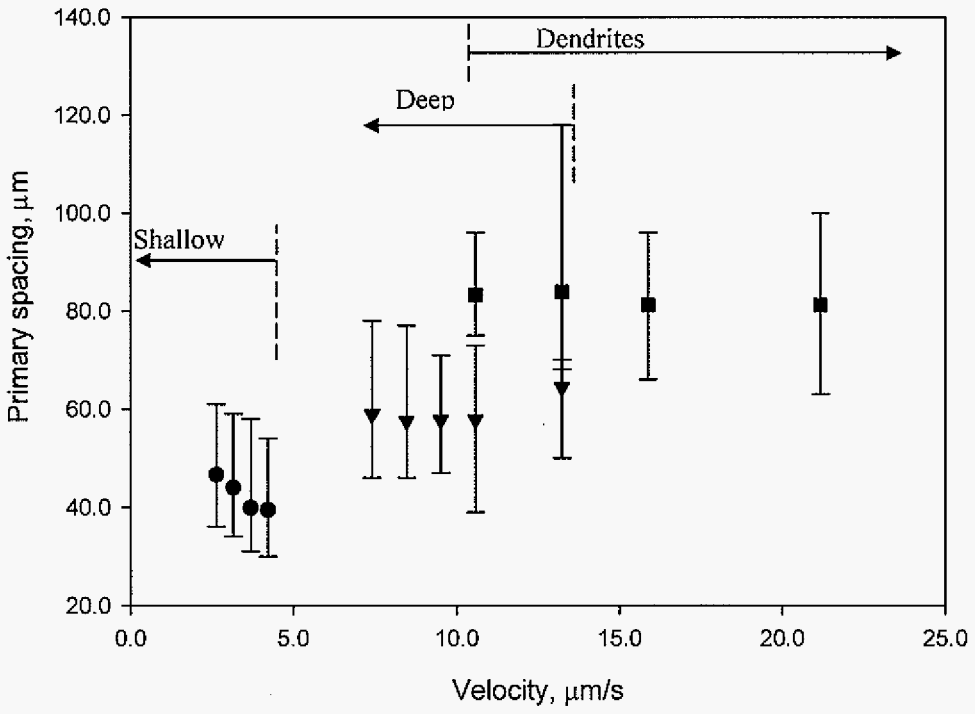

Figure 4. Variation in primary spacing with growth velocity for SCN-0.35wt%camphor (G=4.39K/mm). Filled circles are for shallow cells, inverse triangles are for deep cells and the filled squares are for dendrites.

tendency to transform to a dendrite. There are a few cases where a sharp transition from cells to dendrites may be possible [13, 14]. A thinner sample makes the growth occur in a nearly 2D configuration and the step jump of primary spacing from cells to dendrites is rather steep, which favors a sharp transition. It is also reported that if a uniform primary spacing could be obtained through some external means, CDT would be global and collective [6].

3.3. Cell-dendrite transition

Measurements in the SCN-0.65wt%camphor alloy will be presented first. Figure 1 shows the effect of composition, velocity and thermal gradient on the cell/dendrite coexistence regime. In this coexistence regime, there exists a critical primary spacing (λ_{cd}) at which a primary arm just starts to develop instabilities at the sides, so that deep cells are stable if $\lambda < \lambda_{cd}$, and dendritic growth takes over when $\lambda > \lambda_{cd}$. The critical spacing was measured experimentally, and the results are shown in Fig. 5 for different conditions of composition, thermal gradient and velocity. The critical spacing for CDT is found to decrease as the velocity or the thermal gradient is increased. Similar qualitative observations have been reported in SCN-salol, SCN-acetone, PVA-ethanol and impure SCN samples [5, 14, 15-22]. For more concentrated alloys, CDT occurs over a smaller velocity range since a higher composition shifts the velocity for morphological transition to a lower value. It should be noted that for SCN-0.35wt%camphor, cells and dendrites can still coexist even for G=1.36K/mm.

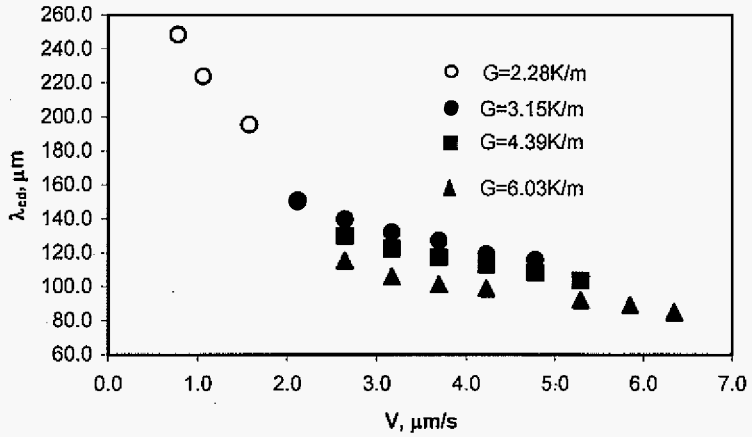

(a)

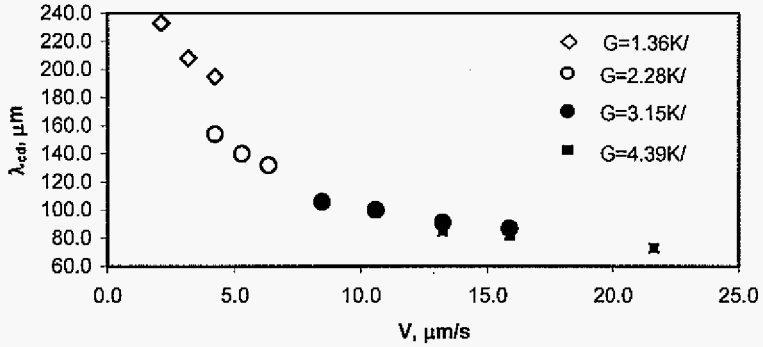

(b)

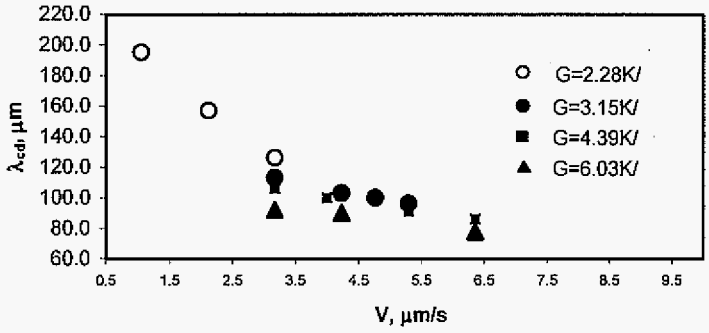

(c)

Figure 5. Variation in the critical primary spacing (λ_{cd}) for the cell to dendrite transition in: (a) SCN-0.65wt%camphor, (b) SCN-0.35wt%camphor and (c) SCN-0.9wt%camphor.

3.4. Length scale variation in the cell/dendrite coexistence regime

In a purely cellular region, it has been shown that the tip radius is closely related to the local primary spacing so that the non-dimensional shape scaled with the local spacing is invariant in a cellular array [12, 23]. On the other hand, the shape invariance breaks down once dendrites start to appear in an array [12, 24]. Therefore quantification should be carried out for each primary tip together with its side instabilities and the local primary spacing. We have thus measured the cell/dendrite tip radius (ρ), local spacing and the initial side arm spacing (λ_2^o) in the transition zone for different growth conditions.

A dendrite tip usually assumes the shape of a paraboloid of revolution so one can fit the digitized tip with a parabolic equation in order to obtain the tip radius value. However for cells, the tip shape varies from a semi-circle in the shallow cell regime to approximately parabolic in the deep cell region. Georgelin and Pocheau [25] discussed in detail how to measure the tip radius of a cell and concluded that fitting it to a parabolic equation was the most appropriate method.

In practice, two slightly different procedures were employed to fit a deep cell tip to a parabola. One is to digitally magnify a tip and match it to a standard parabola constructed with a known tip radius. This is equivalent to the traditional way of projecting a negative film to a standard parabola on a whiteboard [15]. The other method is to use image processing software to pinpoint the boundary of a tip and then to fit the data sets into a parabola equation. Both methods produce tip radius data that match closely for a dendrite tip; but for a cell tip, they may generate fairly different results since the parabolic region is not quite large and the direct magnification/projection method may become rather subjective. For a cell tip, we thus

used the linescan method to obtain the boundary of a cell tip. In order to minimize the error in determining the boundary, a radial linescan, with one end of the line fixed at ~1ρ behind the tip along the symmetry axis, was used at 1° increment counterclockwise.

Figure 6(a) shows the tip radius variation with the local spacing for SCN-0.65wt%camphor grown at V=5.29μm/s and G=4.39K/mm. In the array growth, deep cells are stable for the local spacing $92<\lambda_1<103\mu m$; while perturbations *start* to appear on the primary spines with a local spacing $\lambda_{cd}=103.5\mu m$. In the deep cells regime, the invariant non-dimensional shape is found to hold (dashed line in Fig. 6(a)). If the local spacing is >150 μm, the tip radius no longer depends on the local spacing, indicating dendrite regime in which the solutal interaction between the adjacent growing tips becomes negligible and the growth of each tip becomes isolated. In the transition zone where the local spacing varies from 103 to 150 μm, the tip radius increases with the local spacing, indicating that the tip growth is constrained by a small local spacing for which some solutal interaction is present and the dendrite is not well developed. We denote a dendrite in this region as a cellular dendrite to distinguish it from a well-developed one.

Detailed measurements of the wavelength of the initial instability were also carried out since the value of the scaling constant with the tip radius depends on the anisotropy in the interface energy in the system. These results are shown in Fig. 6(b). In the well developed dendritic regime, the ratio is found to be: $\lambda_2^o/\rho = 1.95 \pm 0.15$, while in the region of cellular dendrites, this ratio decreases from ~2.70 to 1.95 as the local spacing increases from 103 to 150 μm. This type of long-wavelength instability has already been observed in the growth in a capillary sample [11, 26] and is therefore believed to be an intrinsic growth behavior when

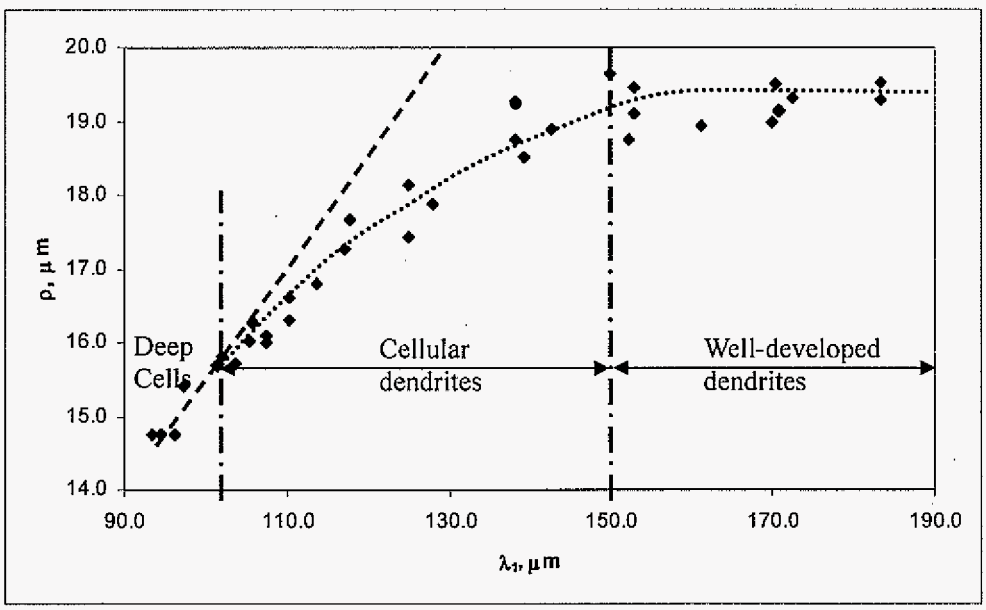

(a)

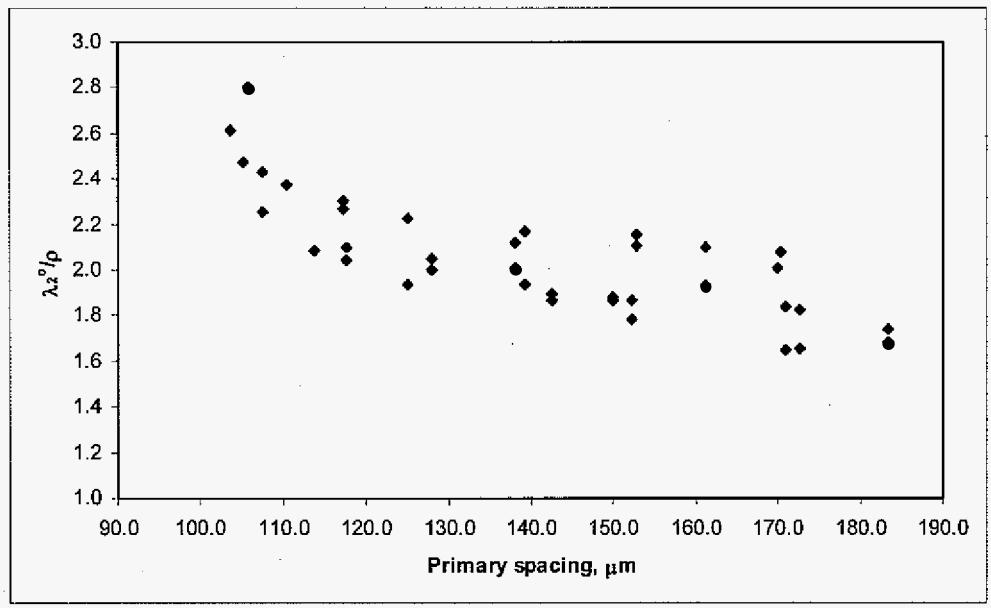

(b)

Figure 6. (a) Dependence of tip radius on local primary spacing for SCN-0.65wt%camphor alloys (G=4.39K/mm, V=5.29μm/s). The equation of the dashed line is $\rho=0.1561\lambda_1$; and (b) Variation in the ratio λ_2^{o}/ρ with the primary spacing in the same growth process.

a tip is constrained to a smaller space.

Extensive solidification studies in several transparent binary alloys have shown that λ_2^o/ρ depends on the anisotropy in interface energy and it is directly related to the anisotropy parameter, ε_4, as summarized in Table 1. The general trend is that a substance with a larger ε_4 has a larger value of λ_2^o/ρ for both the thermal and solutal dendrites. For dilute SCN-camphor alloys in the present study, nearly the same value of λ_2^o/ρ is obtained as in dilute SCN-acetone alloys that strongly indicates that these two binary systems should have a comparable value of ε_4.

Table 1. Ratio of initial side arm spacing over tip radius in transparent binary alloys

Material system	λ_2^o/ρ	ε_4, %	references
SCN thermal dendrite	3.0	0.5	1
SCN-(0.2~4.0)wt%Acetone	2.0	0.5	2
SCN-1.3wt%Acetone	2.1	0.5	3
SCN-0.65wt%camphor	1.95	?	Present study (Fig. 6(b))
SCN-0.7wt%salol	2.6	1.1	4
SCN-CBr_4	2.1		5
SCN-5.6wt%H_2O	2.8		6
CBr_4-10.5wt%C_2Cl_6	3.18		7
CBr_4-10.5wt%C_2Cl_6	3.47		7
NH_4Br-H_2O	5.2	1.6	8, 9
NH_4Cl-70wt%H_2O	4.02, 4.68		6,10
PVA thermal dendrite	4.64, 7.0	2.5, 5.0	11, 12
PVA-0.83wt%Ethanol	3.8	2.6	13

1. S.C.Huang and M.E.Glicksman, Acta Metall., 29(1981)717-734.
2. R. Trivedi and K. Somboonsuk, Materials Science and Engineering, 65(1984)65-74.
3. H. Esaka and W. Kurz, J. Crystal Growth, 72(1985)578-584.
4. L.X. Liu and J. S. Kirkaldy, J. Crystal Growth, 140(1994)115-122.
5. H. Kaya et al., J. Crystal Growth, 276(2005)583-593.
6. S. Liu, S.Z. Lu and A. Hellawell, J. Crystal Growth, 243(2002)740.
7. V. Seetharaman, L. Fabietti and R. Trivedi, Metall. Trans., 20A(1987)2567.
8. Dougherty, A. Pattern formation in dendritic solidification. NATO ASI Series, Series E: Applied Sciences (1988), 157(Random Fluctuations Pattern Growth), 133-41.
9. A. Dougherty and J. P. Gollup, Phys. Rev., 38A(6)(1988)3043.
10. H. Honjo, Y. Swada, J. Crystal Growth, 58(1982)297.
11. E. Cadirl, N. Marasli and M. Gunduz, Mater. Res. Bull., 35(2000)985.
12. M.E. Glicksman and N.B.Singh: ASTM STP 890, ASTM, Philadelphia, PA 1986, pp. 44-61.
13. R. Trivedi and J. T. Mason, Metall. Trans., 22A(1991)235.

IV. Discussion

We will first analyze the CDT data in SCN-camphor alloys of different compositions, growing under different growth conditions, to obtain the condition for the onset of the CDT. We shall then discuss the shape evolution in the coexistence regime based on the noise-induced side-arm generations. The results in the SCN-camphor system will finally be compared with those in other SCN base alloy systems, such as SCN-salol and SCN-acetone.

4.1. Cell-dendrite transition in SCN-camphor alloys

The cell-dendrite transition was shown to depend on the critical local spacing, λ_{cd}, where sidebranches become stable, and this critical spacing was found to depend on composition, velocity and thermal gradient. The characteristic length scale of the critical spacing can be expressed in terms of the following three characteristic lengths [26,27]: (i) Solute diffusion length, l_D ($\equiv D/V$), (b) thermal length, l_T ($\equiv \Delta T_o/G$), where $\Delta T_0 = mC_o(k-1)/k$ in which m is the slope of the liquidus and k is the solute distribution coefficient, and (iii) the capillary length, d_o ($\equiv \Gamma/\Delta T_o$), where Γ is the Gibbs-Thomson coefficient. The critical spacing for CDT may be expressed as [6, 26]:

$$\lambda_{cd} = f\left(l_d l_T d_0\right)^{1/3} \qquad \text{(eq.1)}$$

where f is a dimensionless pre-factor that contains the composition effect. Substituting the values of the characteristic lengths, we obtain:

$$\lambda_{cd} = f(C_o)\left[\frac{\Gamma D}{GV}\right]^{1/3} \qquad \text{(eq.2)}$$

In order to check this relationship, critical spacing is plotted against the cooling rate,

GV, in Fig. 7 for three different compositions examined in this study. For each composition, a slope of -(1/3) is obtained. Also, at the same cooling rate (GV), the critical spacing for CDT becomes smaller for a more concentrated alloy. The value of the function $f(C_0)$ for each composition can be obtained from this plot and it is found to correlate with composition by the expression:

$$f(C_o) = 9.92C_o^{-1/4} \qquad \text{(eq.3)}$$

The critical spacing for CDT in SCN-camphor system can thus be expressed as:

$$\lambda_{cd} = 9.92C_o^{-1/4}\left(\frac{D\Gamma}{GV}\right)^{1/3} \qquad \text{(eq.4)}$$

The units of spacing, temperature gradient, velocity and composition in the above equations are μm, K/μm, μm/s and wt%, respectively. If other units are to be used, the value of the constant needs to be adjusted.

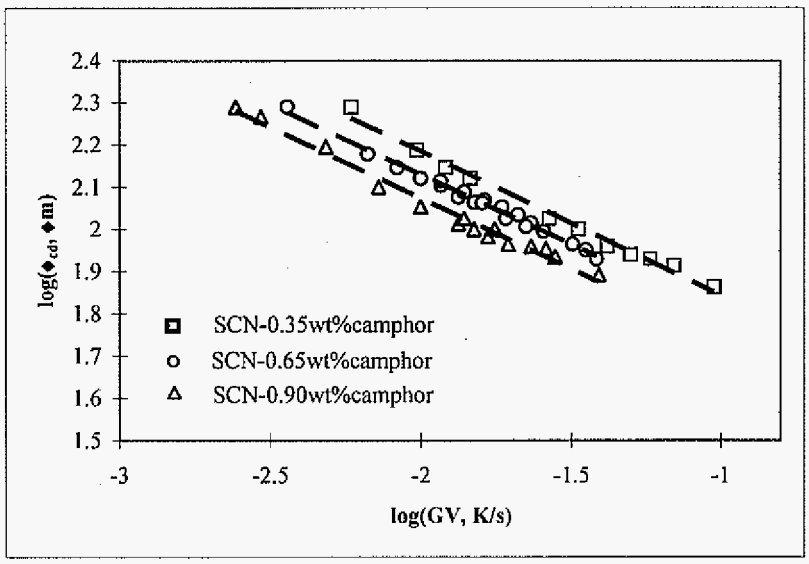

Figure 7. Relationship of the critical spacing for CDT with the cooling rate (GV) for three alloy compositions.

The expression for the critical spacing in the SCN-acetone system has also been found to be the same as eq. 4 [14, 16], except for the value of the constant that is 7.63 rather than 9.92. The relationship between the critical spacing and the controllable parameters (G and V) is also found to be the same in the SCN-salol system [6], except for the function $f(C_0)$, which is found as: $f(C_0) = 10.8\ C_0^{-1}$. These differences will be examined in a later section.

4.2. Cell-dendrite transition condition

One of the key aspects of the transition is that cells and dendrites coexist over a range of velocity or thermal gradient. Within this transition zone two important changes occur: (1) the fraction of cells in an array goes from one to zero, and the fraction of dendrites goes from zero to one. (2) The shape of the tip region changes from a somewhat broader tip to a sharp parabolic tip as cells transforms to dendrites.

The transition zone occurs due to the presence of a range of stable spacing for cells and dendrites. For steady state growth of purely cellular or dendritic arrays, there exists a stable range of primary spacing that follow a normal distribution. The maximum cell spacing ($\lambda_{c,max}$) is about 1.5 times larger than the minimum cell spacing ($\lambda_{c,min}$) [19, 28]. However, in the regime of cell/dendrite coexistence, the range of stable spacing changes for cells and dendrites since any cell spacing larger than λ_{cd} will be unstable and form dendrite. The minimum spacing in the array will correspond to that for the deep cells, the maximum spacing will correspond to that for dendrites, and the maximum cell spacing and minimum dendrite spacing will correspond to λ_{cd}.

The range of stable spacing in the transition zone will now be examined by considering the experimental results in SCN-0.35 wt% camphor alloy, solidified at

G=4.39K/mm (Fig. 4). When the velocity is increased from 10.6 μm/s to 13.0 μm/s, the maximum to minimum cell spacing ratio decreases from 1.38 to 1.31, while that for the dendrites increases from 1.28 to 1.337. These results show that the ratio of the maximum to the minimum cell spacing will vary from 1.5 at the start of the transition and decrease to one at the end of the transition. In a similar manner, the ratio for the dendrites will increase from one to 1.5 in the transition zone. Also, the fraction of cells in an array will change from one to zero in the transition zone, and the fraction of dendrites will change from zero to one. Thus, at the start of the transition region, only one dendrite has formed, while at the end of the transition all cells, except one, have transformed to dendrites. We now use these results to determine how the velocity and temperature gradient influence the spacing range for cells and dendrites, and characterize the effect of G, V and C_0 on the start of the transition regime.

Figure 8(a) schematically shows the effect of V at constant G and C_0, and Fig. 8(b) shows the effect of G at constant V and C_0. First consider the effect of velocity on the transition regime by examining the variation in spacing versus velocity in the three different regimes: cellular, dendritic and the transition regime, as shown in Fig. 8(a). The main assumption we make is that the minimum stable cell spacing in the transition zone is given by the same expression as that in the purely cellular regime, and this relationship is shown in Fig. 8(a) by the line $\lambda_{c,min}$. This assumption is reasonable near the onset of the transition, but not close to the end of the transition where only one or two cells are present, which will influence the spacing for the cell elimination and thus alter the $\lambda_{c,min}$ line. Next, the variation in λ_{cd} with V, given by eq. (4) is plotted. In the transition regime, only those cellular spacing that lie between $\lambda_{c,min}$ and λ_{ce} will be stable, and these are shown by a shaded region.

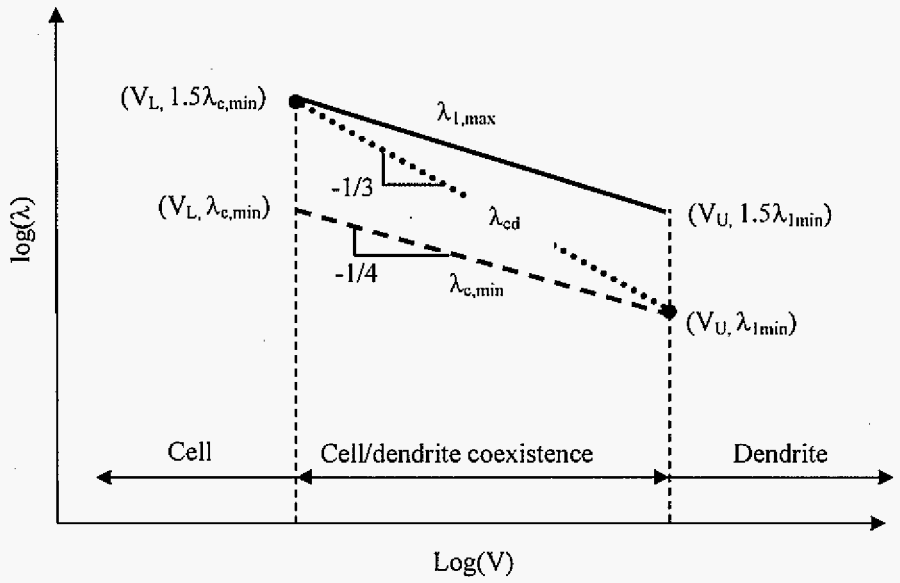

(a)

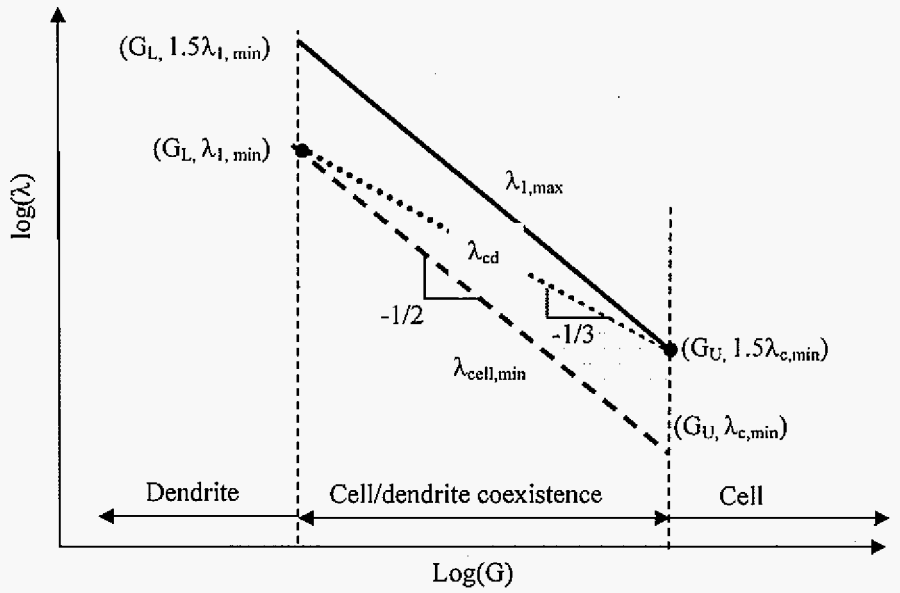

(b)

Figure 8. Schematic showing the morphological regimes and the range of spacing variation for cells and dendrites.

Under the same growth conditions, dendrite spacing is slightly larger than cell spacing [21] due to the presence of sidebranches, so that the lower limit of dendrite spacing is close to the upper limit of cell spacing. Thus, at the onset of transition the minimum dendrite spacing will be only slightly larger than $1.5\lambda_{c,min}$ and it will be close to λ_{cd} in the transition zone. Experimental results have shown that the difference in spacing between dendrites and cells is negligible for the same experimental condition. We may thus obtain the condition for the start of the transition, or the lower limit of transition, by equating $1.5\ \lambda_{c,min}$ with λ_{cd}. For $\lambda_{c,min}$, the following expression derived by Hunt [29] can be used

$$\lambda_{c,min} = (64D\Gamma)^{1/4}(m(k-1))^{1/4}\ C_o^{1/4}V^{-1/4}G^{-1/2} \qquad \text{(eq. 5)}$$

where k is the solute distribution coefficient and m is the slope of the liquidus. Equating 1.5 $\lambda_{c,min}$ with λ_{cd} equation we obtain the critical condition for the onset of the transition as:

$$\left(\frac{V}{G^2}\right)C_o^6 = \frac{(2.6677\text{x}10^4)(D\Gamma)}{[m(k-1)]^3} \qquad \text{(eq. 6)}$$

This transition condition can be written in terms of characteristic lengths as:

$$\left[\frac{l_D d_0}{l_T^2}\right] = \text{constant} \qquad \text{(eq. 7)}$$

where the value of the constant for the SCN-camphor system is $k^3C_o^3/(3.10\text{x}10^4)$

For an ideal case, the primary dendrite spacing will be close to the maximum cell spacing only at the onset of transition. The minimum spacing at the end of the transition zone will be close to the maximum cell spacing, and the maximum dendrite spacing will be 1.5 times the minimum dendrite spacing. The ideal case shown in Fig. 8 predicts that the ratio $\lambda_{1max}/\lambda_{cl,min}$ should always be 1.5 since the two bounding lines are parallel. As we discussed

earlier, the experimental observations show this ratio to be larger than 1.50 in the coexistence regime. This is due to the deviation in the shape of the dendrite tip in the transition zone, and thus one can not describe maximum spacing based on the steady-state array of dendrites. We shall now describe this shape of the dendrite in the transition zone.

4.3. Shape evolution in the transition zone

In the cell-dendrite coexistence regime, the maximum cell spacing was found to be about the same as the minimum dendrite spacing, so that the formation of side arms des not increase the spacing significantly. In order to investigate any differences between the dendrites in the coexistence zone and in the complete dendritic zone, the tip shape of primary arms was carefully examined for a fixed growth condition (SCN-0.65wt%camphor, G=4.39K/mm and V=5.29μm/s).

The quantification of tip radius, local spacing and initial side arm spacing are shown in Fig. 6, which shows clearly that the tip radius increases linearly with local spacing for cells, increases non-linearly for cellular dendrites and does not change for well-developed dendrites. Therefore we selected three primary tips in these 3 typical regions in order to assess the shape dependence on the local spacing.

Figure 9(a) shows a well-developed dendrite with a local spacing λ_1=163.0 μm, and a parabola with the measured tip radius ρ=19.58 μm is also overlapped. It is clear that the perturbations initiate at a distance ~1.5ρ behind the tip and the amplitude of the first few side disturbances increases; indicating that the concentration fields overlap with the neighboring dendrites is still negligible. Since the growth of these first few side disturbances are not influenced by the adjacent dendrites, we assert that the smooth region of the dendrite tip can

be considered to grow in an isolated manner.

Figure 9(b) shows a primary tip with a 110 μm local spacing, just slightly larger than the λ_{cd}. Instabilities develop visibly on the left side. For the sake of easy comparison, two parabolas are overlapped at the tip region: the thin- line parabola has a radius of 19.58 μm at the tip, and the thick-line parabola has a radius of 16.20 μm. The former is the value for an isolated dendrite as shown in Figure 9(a), while the latter is the measured tip radius of this primary arm. The smaller tip radius indicates that the tip region of this local spacing can feel the effect of solute field of its neighbors so that the tip cannot open up freely. If we consider the axial composition gradient does not change, then radial composition gradient is significantly reduced due to a narrow spacing, which decreases the amplification rate of the side instability. Therefore those low-amplitude noises cannot be amplified to the level where the optical system may resolve [31, 32]. Therefore only those noises with large enough amplitude can be observed to evolve into side instabilities on the surface near the tip, which leads to the formation of long-wavelength instability.

Roughly speaking, the gap between these two parabolas reflects the strength of the interaction between neighboring primary arms. One would imagine that with increase in the local spacing, the tip radius increases and the gap between these two parabolas will continually shrink, therefore the interaction among the neighboring primary arms continually weakens and more low-amplitude noise-induced instabilities will become visible, reducing the wavelength of the initial side arms (Figure 6(b)).

Further reduction in the local spacing continues to decrease the tip radius, as shown in Figure 9(c). Similarly we overlap on the tip image the parabola with no solute interaction and the actual parabola with the measured tip radius of this primary arm. Clearly the gap between

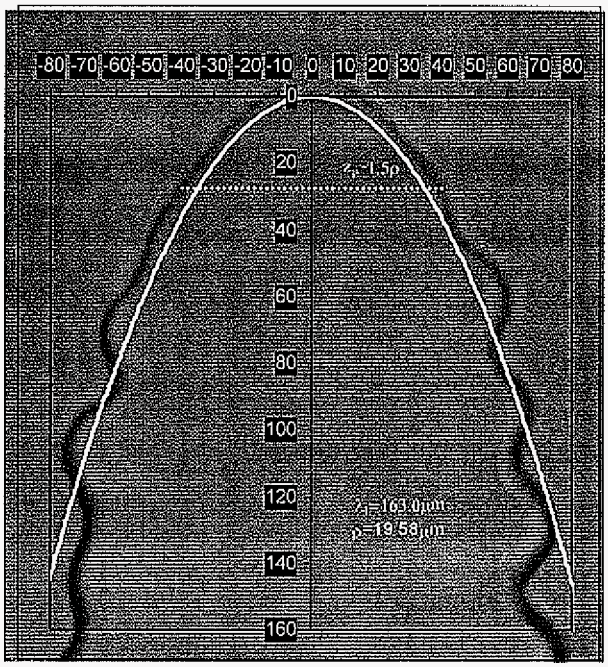

(a) well-developed dendrite, λ_1=163.0 μm, ρ=19.58μm

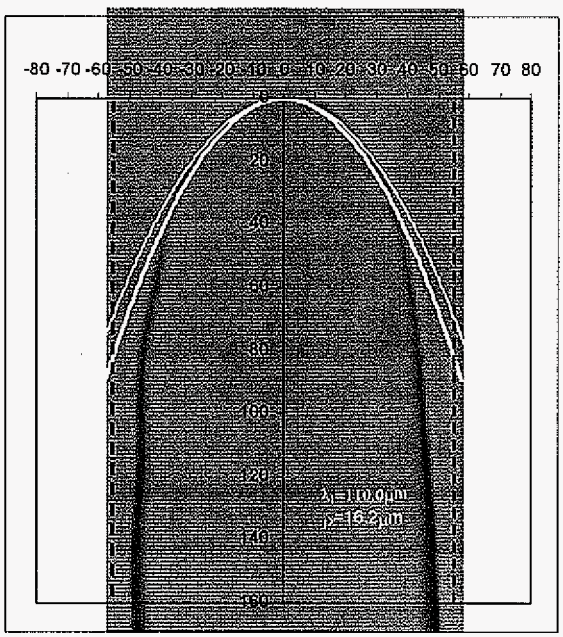

(b) cellular dendrite, λ_1=110.0 μm, ρ=16.2μm

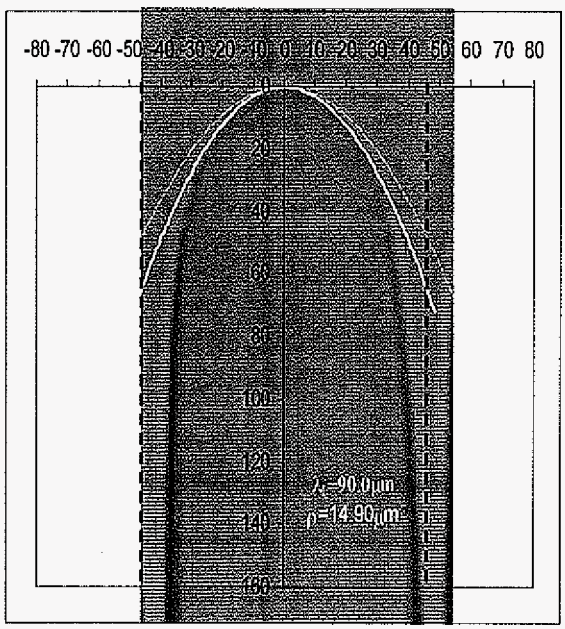

(c) Cell λ_1=90.0 μm, ρ=14.9μm

Figure 9. Dependence of the tip shape on the local spacing (SCN-0.65wt%camphor, G=4.39K/mm, V=4.23 μm/s).

them is more pronounced than that in Figure 9(b), which leads to the disappearance of perturbations from the tip surface, i.e. the formation of a deep cell.

4.4. Comparison with other SCN base systems

In order to understand how CDT depends on properties of an alloy system, we have summarized relevant studies in SCN base dilute alloys (Table 2). Experimental studies in which the system was not characterized accurately [5] have not been included in the comparison. All experimental results show that $\lambda_{cd}(GV)^{1/3} = constant$ for a given alloy composition with the differences only in its dependence on composition and the value of constant.

The expression for λ_{cd} is obtained fro the experimental observations, and it characterizes only the proper dependence of V, G and C_0. For SCN-camphor, this relationship is given by eq. (4), in which the constant 9.92 is a dimensionless parameter that may contain the values of the system parameters. The other possible dimensionless parameters relevant to the solidification microstructure formation are the solute distribution coefficient k and the anisotropy parameter, ε_4, for the solid/liquid interfacial energy. The effect of k and ε_4 can be obtained by comparing the results for SCN-camphor, SCN-acetone, and SCN-Salol, since the first two systems have the same ε_4 value but different k values, whereas the last two systems have the same k value but different ε_4 values.

We first compare the results in SCN-camphor with dilute SCN-acetone alloys. The experimental result on λ_{cd} in SCN-acetone is found to be:

$$\lambda_{cd} = 7.63\, C_o^{-1/4}\left(\frac{D\Gamma}{GV}\right)^{1/3} \qquad \text{(eq. 8)}$$

This result is analogous to that for SCN-camphor, which is given by eq, (4), with the only difference in the value of constant. Since both these systems have comparable values of ε_4, but different values of k, the difference in the constant may only be ascribed to the different values of k in these two systems: k=0.1 for SCN-acetone and k=0.21 for SCN-camphor [30]. Since the solid composition of a dendrite tip is close to kC_o, one may consider that the exponent of k should be the same as that for C_o. For this modification, the values of the constant in SCN-camphor and SCN-acetone become 14.66 and 13.57, which are quite close and within the errors in different experimental studies.

We may now compare the results in SCN-camphor (or SCN-acetone) with that in SCN-salol in order to determine the influence of the anisotropy parameter in these two systems. The data of Liu and Kirkaldy [14, 15, 20] give the following expression for the SCN-salol system:

$$\lambda_{cd} = 11.44\, C_o^{-1/6}\left(\frac{D\Gamma}{GV}\right)^{1/3} \qquad \text{(eq. 9)}$$

since the exponents of G and V are the same for both SCN-salol and SCN-acetone, and the solute distribution coefficients in both alloy systems are 0.1, the difference in the prefactor should be due to the different values of the anisotropy parameter which are: ε_4=1.1% for SCN-salol system and = 0.5% for SCN-acetone system. If we assume that there exists a universal constant that applies to all alloy systems with different ε_4 values, we the anisotropy effect should be $\varepsilon_4^{1/3}$. A general expression valid for all systems thus should have the following form:

$$\lambda_{cd} = 16.8\left(\frac{1}{kC_0}\right)^{1/n}\left(\frac{\varepsilon_4 D\Gamma}{GV}\right)^{1/3} \qquad \text{(eq. 10)}$$

This unique relationship for CDT can be applied to alloys with negligible interfacial kinetics. This modified equation can now be used to modify the condition for the onset of cell-dendrite transition, (eq. 6) and (eq. 7).

Table 2. Summary of cell-dendrite transition in SCN base dilute solutions

materials	Scaling relationship*	reference	Calculated factor before $(D\Gamma)^{1/3}$ from eq. 5
SCN-camphor	$\lambda_{cd}(GV)^{1/3}C_o^{1/4} = 9.92(D\Gamma)^{1/3}$	Present study	9.16
SCN-acetone**	$\lambda_{cd}(GV)^{1/3}C_o^{1/4} = 7.632(D\Gamma)^{1/3}$	Esaka & Kurz [16] Liu &Kirkaldy [14] Smboonsuk Eshelman et al. [17,21]	7.61
SCN-salol	$\lambda_{cd}(GV)^{1/3}C_o = 10.8(D\Gamma)^{1/3}$	Trivedi et al.[6]	1.75
SCN-ethylene	$\lambda_{cd}V^{1/2}G^{1/8}C_o^{1/2} = 445.384D\Gamma^{3/4}$	Georgelin & Pocheau [5]	
SCN-salol***	$\lambda\ (GV)^{1/3}C_o^{1/6} = 11.4373(D\Gamma)^{1/3}$	Liu & Kirkaldy [14,15]	11.95
SCN-acetone***	$\lambda\ (GV)^{1/3}C_o^{1/6} = 8.9587(D\Gamma)^{1/3}$		9.21

* Units of variables: λ_{cd}: μm; G: K/μm; V: μm/s; C_o: wt%; D: $\mu m^2/s$; Γ: K μm.

** A short summary about the experimental study in SCN-acetone alloys is given in Appendix 1.

** Using 1270 $\mu m^2/s$ and 700$\mu m^2/s$ as the diffusion coefficients in SCN-acetone and SCN-salol system respectively. The data by Liu and Kirkaldy [19] are much lower than commonly accepted values in SCN-acetone alloys. The diffusion coefficient of SCN-salol alloys was recently re-determined by the droplet migration method (Liu, Teng and Choi [33]).

V. Conclusion

Cell-dendrite transition is shown to occur over a range of velocity or thermal gradient, and detailed experimental studies have been carried out in the SCN-camphor system to obtain an expression for the critical spacing (λ_{cd}) for the cell-dendrite transition. Based on this expression, a model is proposed to obtain the condition for the onset of the cell to dendrite transition.

Experimental results on the critical spacing have been analyzed in three SCN-based systems to generalize the model so that it is not system specific. This general model includes the solute distribution coefficient and the interface energy anisotropy parameter.

The tip shape in the cell-dendrite coexistence regime strongly depends on the local spacing and a long-wavelength instability has been found through careful measurement of individual primary arms in an array. With increase in local spacing in a given array, the tip radius may linearly increase, non-linearly increase or remain unchanged. The occurrence of perturbations can be understood through the noise-induced instability theory. The maximum cell spacing is the roughly same as the minimum dendrite spacing when both morphologies coexist.

Acknowledgement

This work was supported by NASA through Marshall Flight Center and DOE-BES and was carried out at Ames Laboratory which is operated by Iowa State University for the Office of Basic Energy Science, Division of Materials Science, U. S. Department of Energy under Contract No. W7405-Eng-82.

References

[1] W. A. Tiller and J. W. Rutter, Can. J. Phys., vol. 34, 1956, pp.95-121.

[2] B. Chalmers, Principles of Solidification, John-Wiley and Sons, New York, 1964.

[3] M. Flemings, Solidification Processing, McGraw_Hill, New York, 1974.

[4] S. N. Tewari and V. Laxmanan, Metall. Trans., vol. 18A, 1987, pp.167-169.

[5] M. Georgelin and A. Pocheau, Phys. Rev. E., vol. 57E, 1998, pp.3189-3203.

[6] Trivedi, R.; Shen, Y; Liu, Shan, Metall.Mater.Trans. vol. 34A, 2003, pp.395-401.

[7] P. Kopczyniski, W. Rappel and A. Karma, Phys. Rev. E, vol. 55, 1997, pp.1282-1285.

[8] H. Jamgotchian, R. Trivedi and B. Billia, Phys. Rev. E, vol.47E, 1993, pp.4313-4322.

[9] B. P. Athreya, J. A. Dantzig, Shan Liu and R. Trivedi, Phil. Mag., vol. 86, 2006, pp.3739-3756.

[10] Shan Liu, M. Suk, L. Fabietti and R. Trivedi, The Effect of Dimensionality on Microstructures in Directionally Solidified SCN-Salol Alloys: The 133th TMS Annual Meeting, Solidification Processes and Microstructures-A Symposium in Honor of Wilfried Kurz, Ed. By M. Rappaz, C. Beckermann and R. Trivedi, pp.211-218.

[11] Liu, Shan; Trivedi, R. Materials Science Forum (2005), vol. 475-479, 2004, pp.2757-2760.

[12] P.Kurowski, C.Guthmann and S.de Cheveign, Phys. Rev. A., vol. 42A, 1990, pp.7368-7376.

[13] B. Billia, H. Jamgotchian and H. Nguyen Thi, J. Crystal Growth, vol. 167, 1996, pp.265-276.

[14] L. X. Liu and J.S.Kirkaldy, J. Crystal Growth, vol.140, 1994, pp.115-122.

[15] L. X. Liu and J. S. Kirkaldy, Acta Metall. Mater., vol. 43(8), 1995, pp.2891-1904.

[16] H. Esaka and W. Kurz, J. Crystal Growth, vol. 72, 1985, pp.578-584.

[17] K. Somboonsuk, J. Mason and R. Trivedi, Metall. Trans., vol. 15A, 1984, pp.967-975.

[18] K. Somboonsuk and R. Trivedi, Scripta Metall., vol. 18, 1984, pp.1283-1286.

[19] S. H. Han and R. Trivedi, Acta Metall. Mater., vol. 42(1), 1994, pp.25-41.

[20] L. X. Liu and J. S. Kirkaldy, Scripta Metall. Mater., vol. 28, 1993, pp.1029-1034.

[21] M. A. Eshelman, V. Seetharaman and R. Trivedi, Acta Metall., vol. 36(4), 1988, pp.1165-1184.

[22] L. X. Liu and J. S. Kirkaldy, Scripta Metall. Mater., vol. 19, 1993, pp.801-806.

[23] R. Trivedi , Shen, Y., and Liu, S. International Conference on Advances in Materials and Materials Processing, Tata McGill Hill, India, 2002, pp.42-49.

[24] Y. X. Shen, MS Thesis, Iowa State University, Ames, Iowa, 2002.

[25] M. Georgelin and A. Pocheau, J. Crystal Growth, preprint.

[26] Shuzu Lu and Shan Liu, Metall. Mater. Trans., in print.

[27] R. Trivedi and W. Kurz, Inter. Mater. Rev., vol. 39, 1994, pp.49-74.

[28] S. N. Tewari, Y.-S. Weng, G. L. Ding and R. Trivedi, Metall. Mater. Trans., vol. 33A, 2002, pp.1229-1443.

[29] J. D. Hunt, Solidification and Casting of Metals, The Metals Society, Book 192, London, 1979, p.3.

[30] J. Teng and Shan Liu, J. Crystal Growth, 2006, vol. 290, 248-257.

[31] Shan Liu, S.Z. Lu and A. Hellawell, J. Crystal Growth, vol. 234, 2001, pp.740-750.

[32] A. Pocheau and M. Georgelin, Eur. Phys.J., B21, 2001, pp.229-240.

[33] Shan Liu, J. Teng And M. Choi, Metall. Mater. Trans., 38A, 2007, pp.1555-1562.

[34] Trivedi and Eshelman, Materials Science and Engineering, 65, 1984, 65-74.

[35] K. Somboonsuk, Ph.D Thesis, Iowa State University, Ames, Iowa, 50011, 1984.

Appendix I: Summary of experimental studies in SCN-Acetone system

SCN-acetone alloys have been extensively used by different researchers either for undercooled or directional growth studies. Most of them are for the planar front breakup, primary spacing and tip radius selection, and only a few experimental studies contain limited coverage of the cell-dendrite transition, as summarized in Table A1. Apart from the alloy composition (C_o), temperature gradient (G) and growth velocity (V), the sample thickness (d) is also included in the table since it has been proved to be a control parameter for pattern selection. Actually by including this variable, an interesting results have been obtained by graphing $\log(\lambda_{cd}(GV)^{1/3}) \sim \log(C_o)$ as shown in Figure A1. Clearly there are two branches which are controlled by whether $\lambda_1 >> d$ or not. If this is the case, the primary arms are "compressed" to a 2-dimensional configuration and the spacing will be significantly increased. The tip region may still grow in 3-dimension geometry, but the primary spacing is selected due to the constraint by sample thickness, therefore we exclude these data and only consider those with tip and primary spacing both are selected in 3-dimension geometry. When we described the present experimental study in the text, we have noticed this thickness effect.

The slope of $\log(\lambda_{cd}(GV)^{1/3}) \sim \log(C_o)$ is ~-0.27 for the data from different research groups. Therefore we consider there is a dependence on $C_o^{1/4}$ in dilute SCN-acetone alloys.

Table A1. Relevant experimental results of SCN-acetone directional solidification							
Composition, wt%	G, K/μm	V, μm/s	d, μm	λ_1, μm	$\lambda_1 GV^{\frac{1}{4}}$	Pattern*	Reference
1.3	0.005	2.5	150			d	16
	0.0072	***2.5***		***260***	***57.6563107***	***dc***	
	0.0097	1.6		200	49.8877482	c	
	0.0079	8.3		110.8	44.6794846	d	
4	0.0067	0.68	150	188	31.1663364	c	17
	0.0067	***0.9***		***225***	***40.9532421***	***dc***	
	0.0067	1.17		472	93.762437	d	34
0.448	***0.00656***	***5.6***	150	***123***	***40.888615***	***cd***	35
0.09	***0.013***	***118.18***	150	***52.64***	***60.740495***	***cd***	14, 15
0.17	0.013	15.2		103	59.9928561	c	
	0.006	30.3		92.28	52.2763847	c	
	0.006	***42.5***	***55***	***84.35***	***53.4890823***	***cd***	
0.35	0.00376	2.5	150	216.3	45.6491264	cd	21
	0.00376	3		190.8	42.7905699	cd	
	0.00376	***3.6***		***180.4***	***42.9932209***	***cd***	
C: cells; d: dendrites; cd: cell/dendrite coexistence							

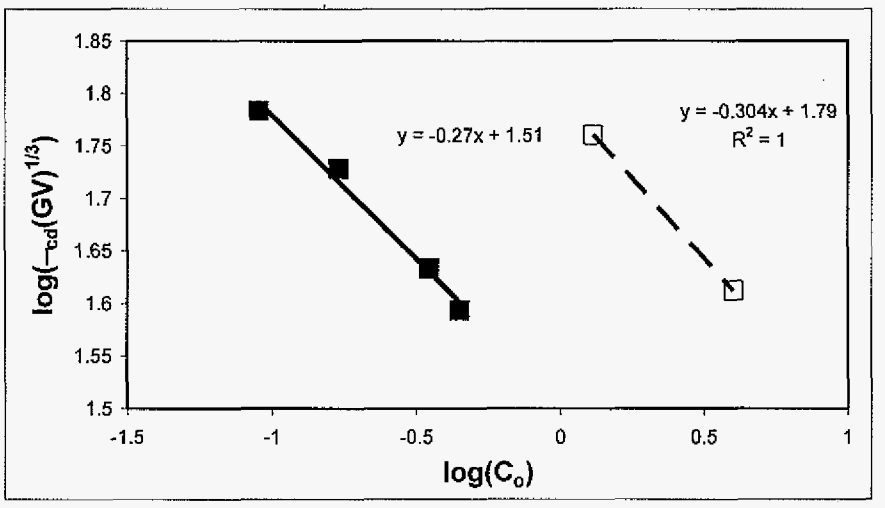

Figure A1. Plot of $\log(\lambda_{cd}(GV)^{1/3}) \sim \log(C_o)$ from the published data in literatures.

CHAPTER 6. GROWTH MORPHOLOGY OF ROD EUTECTICS

A manuscript submitted to *Acta. Mater.*

Jing Teng[1], Shan Liu[2] and R. Trivedi[1, 2,*]

Abstract

The formation of rod eutectic microstructure is investigated systematically in a succinonitrile-camphor alloy of eutectic composition by using the directional solidification technique. A new rod eutectic configuration is observed in which the rods form with elliptical cylinder shape. Two different orientations of the ellipse are observed that differ by a 90° rotation such that the major and the minor axes are interchanged. Critical experiments in thin samples, where a single layer of rods forms, shows that the spacing and orientation of the elliptic rods are governed by the growth rate and the sample thickness. In large thickness of the sample, multi-layers of rods, form with circular cylindrical rods form, and the spacing corresponds to the value predicted by the rod eutectic growth model. A theoretical model is developed for a two-dimensional array of elliptical rods that are arranged in a hexagonal or a square array, and the results are shown to be consistent with the experimental observations.

(**Keywords**: Eutectic Solidification; Microstructure; Crystallization; Directional Solidification; Modeling)

---

[1]Dept. Materials Science and Engineering, Iowa State University, Ames, IA, 50011, U.S.A.

[2]Materials and Engineering Physics Program, Ames Laboratory-USDOE, Iowa State University, Ames, IA, 50011, U.S.A.

[*]Corresponding author: e-mail: trivedi@ameslab.gov, phone: (515) 294-5869, fax: (515) 294-4291.

1. Introduction

Directional solidification of eutectic alloys offers the direct processing route to obtain in situ composite structures and has been used to produce composite turbine blades [1]. The fine eutectic spacing of the composite structure is also used in the design of optical, magnetic and superconducting materials with special physical properties [2]. Typically, the most common regular eutectics form with either a lamellar or a rod microstructure, and detailed analytical models based on diffusion in the parent phase and the interfacial energy have been proposed have been proposed by Hillert [3] and Jackson and Hunt (JH) [4] for these two eutectics. Experimental studies have also been carried out in several metallic systems to validate the models [5-6]. However, convection effects are generally present in bulk samples so that critical experiments have been carried out in thin samples of metals or transparent materials. For example, the CBr_4-C_2Cl_6 system has been used extensively to observe in situ the dynamics of lamellar eutectic evolution [7-8]. Although these experiments have provided valuable information, it has also been recognized that the microstructural features can also be influenced by the thickness of the sample. Detailed experimental observations [9-12] and theoretical modeling [13, 14] have shown that a confined space exerts a strong influence on the formation and evolution of solidification patterns in single phase alloys. The changes in microstructures, and in their characteristic lengths, occur due to the change in the geometry of the region in which solute dissipation can occur, and also due to the constraint placed by the contact angle at the interface-wall junction. Since rod eutectic growth requires a finite thickness of the sample for the 3D arrangement of rods, it is anticipated that thickness of the sample should significantly influence the rod eutectic pattern. In addition, experimental

studies on rod eutectic have been limited and primarily confined to obtain the spacing versus velocity relationship. Even these experimental results could not be analyzed unambiguously due to the lack of precise knowledge of the relevant physical parameters, and often due to the presence of convection in alloy systems in which rod eutectic forms away from the eutectic composition [15].

The aim of this paper is to present experimental results in a well characterized system of succinonitrile (SCN)–camphor in which rod eutectic forms at the eutectic composition [16-19], and which is transparent so that detailed study of rod morphology and spatial arrangements of rods can be examined in situ. It is found that when the sample is sufficiently thick to form several layers, the relationship between the velocity and spacing becomes independent of the thickness, and the results agree with the rod eutectic model based on circular cross-section of the rods that are arranged in a hexagonal pattern. However, significantly different results are obtained in thin samples that show the presence of rods of elliptical shape, and these elliptical rods form with two different orientations that differ by a 90° rotation. The rod spacing and the orientation of the ellipse are shown to depend on the velocity and the thickness of the sample. A theoretical model to analyze these experimental results is developed by characterizing the diffusion field in the elliptical cylindrical system.

2. Experimental

Directional solidification experiments are carried out in the succinonitrile (SCN) - camphor system. Both SCN and CMP are plastic crystals above the room temperature: SCN has a simple BCC structure while camphor is HCP in the temperature range of interest. SCN and camphor constitute a simple binary eutectic system with the eutectic composition at 23.6

wt% camphor and eutectic temperature 37.6 °C (Fig. 1). At eutectic composition, the volume fraction of camphor phase (β-phase) is 0.182 [14]. Due to the low volume fraction of the camphor-enriched minor phase (β), and the non-faceted nature of the solid/liquid interface of both phases in the eutectic structure, it is expected that regular rod-like eutectic morphology should prevail in a unidirectional growth process. Table 1 lists the thermo-physical properties of this binary system necessary for the present study.

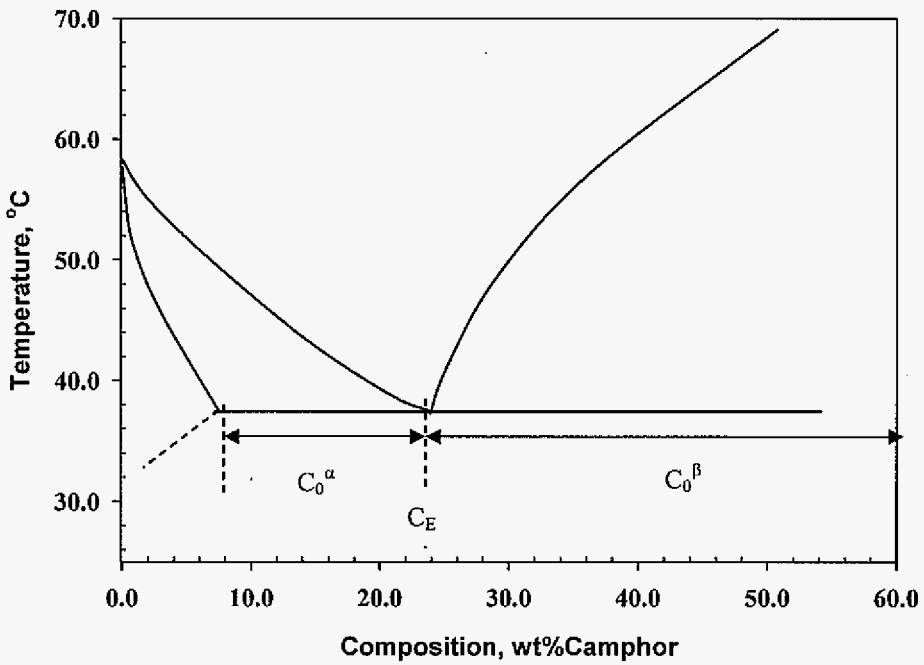

Figure 1. SCN-camphor system phase diagram [14].

Table 1. Physical Properties of SCN-Camphor Alloy		
Property	Unit	Value
Eutectic composition, C_E	wt% camphor	23.6
Maximum solubility of camphor in SCN, $C_{s\alpha}$	wt% camphor	7.10
Maximum solubility of SCN in camphor, $C_{s\beta}$	wt% camphor	~100
Density of SCN solid	g/cm^3	1.022
Density of camphor solid	g/cm^3	1.020
Volume fraction of α phase, f_α		0.818
Volume fraction of β phase, f_β		0.182
Liquidus slope of α phase, m_α	K/wt%	-0.688
Liquidus slope of β phase, m_β	K/wt%	3.664
Contact angle of α phase, θ_α	degree	38.4*
Contact angle of β phase, θ_β	degree	66*
Gibbs-Thomson coefficient of α phase, Γ_α	m K	6.4×10^{-8}
Gibbs-Thomson coefficient of α phase, Γ_β	m K	7.5×10^{-8} [11]
Solute diffusion coefficient in liquid, D	m^2/s	2.6×10^{-10} [8]
*: contact angles are measured from a few enlarged α/β/liquid triple points		

Directional solidification experiments were carried out with the SCN-24.0wt% camphor alloy. The temperature gradient was maintained at 4.5K/mm, and the velocity was varied from 0.005 to 0.51 μm/s. The sample cells were rectangular in cross-section and were about 300 mm long. Camphor can easily sublime so that sample cells of two different thicknesses (20 and 50 μm) were filled at the same time from the same batch of the alloy to obtain the same alloy composition in all samples. Since the rod morphology is governed by the thickness of the sample and the velocity, experiments were carried out at several velocities for a fixed thickness, and at the same velocity in two different thicknesses.

3. Experimental Results and Analysis

3.1. Steady-state growth patterns

Depending on the growth velocity and sample thickness, a rich variety of steady-state growth morphologies were observed. Selected microstructures that show the effect of velocity and sample thickness on the rod shape and spacing between the rods are shown in Fig. 2. For a given thickness, higher velocity gives a smaller spacing so that more layers of rods would be present, while at lower velocity fewer layers of rods would be present. The liquid-solid interface remains flat macroscopically but curved microscopically due to the force balance at α/β/liquid triple point.

First consider the effect of sample thickness at a fixed velocity. Figures 2(a) and 2(b) show the microstructures in samples of 20 and 50 μm thick samples at a velocity of 0.005 μm/s. The eutectic spacing in a thinner sample is slightly larger and the camphor phase is wider (when looked under a microscope). At this lower velocity, a single layer of rods form along the width of the sample, but the rods are not circular in cross-section; instead they become elongated in the direction of the width in Fig. 2(a), and in the direction of the thickness for the experimental conditions of Fig. 2(b), as indicated by the few β rods near the left and right edges of the sample. It is thus interesting to note that the orientation of the ellipse changes such that the major axis changes from the horizontal to the vertical direction as the thickness is increased from 20 μm to 50 μm.

The effect of velocity for a fixed thickness of 50 μm is shown in Figs. 2(b) to 2(d) for three different velocities. As the velocity increases, the growth morphologies evolve in a more complicated manner. Increase in V gradually destabilizes the single layer growth and

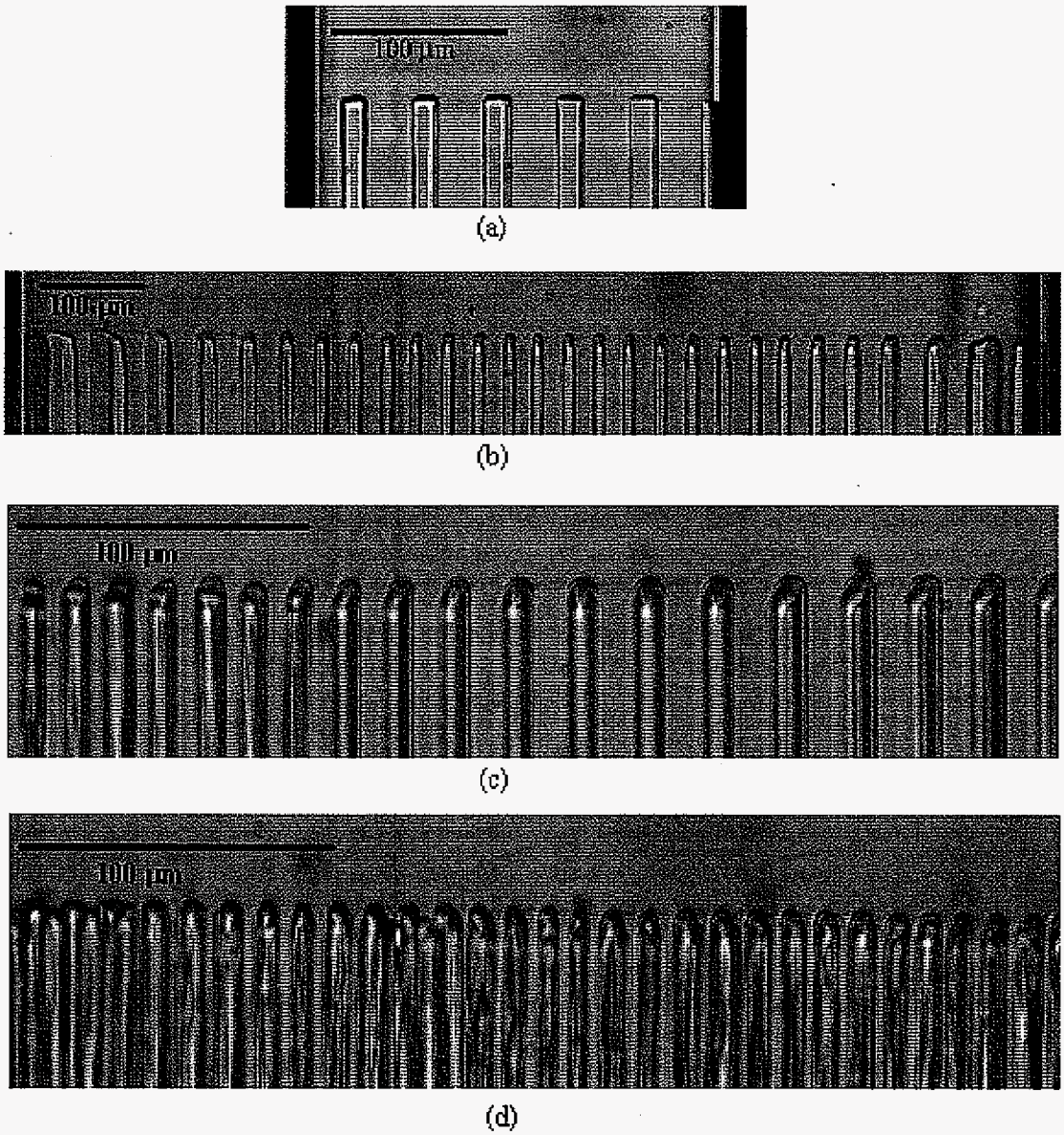

Figure 2. Typical eutectic growth morphologies of SCN-24.0wt%camphor samples
(a) V=0.005 μm/s, t=20μm, single layer of β phase rods;
(b) V=0.005 μm/s, t=50 μm, single layer of β phase rods;
(c) V=0.02 μm/s, t=50 μm, multilayer β phase rods for a smaller local spacing (left 7 rods) and single layer β rods for the larger local spacings;
(d) V=0.08 μm/s, t=50 μm, multilayer β phase rods grow.

leads to the formation of multilayer β rods in the vertical direction. Figure 2(c) shows that part of the sample with a smaller local spacing favors the multilayer growth of rods and that the part with a larger local spacing facilitates the single-layer growth of vertically elongated β rods. Further increase in V results in the growth of more layers of β rods (Fig. 2(d)). For V > 0.51 μm/s, many layers of β rods form in both the 20 and 50 μm samples so that it is not possible to observe the interface morphology clearly. The present experimental study is thus limited to V≤0.51 μm/s.

Table 2. Experimental conditions and measured eutectic spacing (G=4.5K/mm)

Sample thickness (t), μm	Growth velocity (V), μm/s	Spatial distribution	Measured Eutectic spacing, μm			β phase width (ℓ_w), μm	
			Minimum $\lambda_{e,min}$	Maximum $\lambda_{e,max}$	Average $\lambda_{e,ave}$	Minimum $\ell_{w\,min}$	Maximum $\ell_{w\,max}$
20	0.005	single layer	42.46	44.23	43.33	19.16	20.43
	0.01	single layer	30.64	36.13	34.25	13.92	14.74
	0.02	single layer	21.05	27.2	24.09	10.04	11.81
	0.08	single layer	9.7	11.84	10.52	5.05	6.81
	0.32	multilayers	4.53	6.49	5.7	3.96	4.73
	0.51	multilayers	3.35	5.48	4.62	3.51	4.27
50	0.005	single layer	30.98	39.92	33.61	14.75	15.94
	0.02[(a)]	single layer	17.83	24.39	21.36	10.28	11.3
	0.02[(b)]	two layers	15.09	16.92	15.63	7.32	9.6
	0.08	multilayers	8.54	11.43	9.88	5.48	6.86
	0.32	multilayers	4.47	5.96	5.41	3.35	4.73
	0.51	multilayers	3.51	5.34	4.56	3.2	4.12

(a) is for the elongated, single-layer growth of β rods and (b) is for the multilayer arrangement of β rods

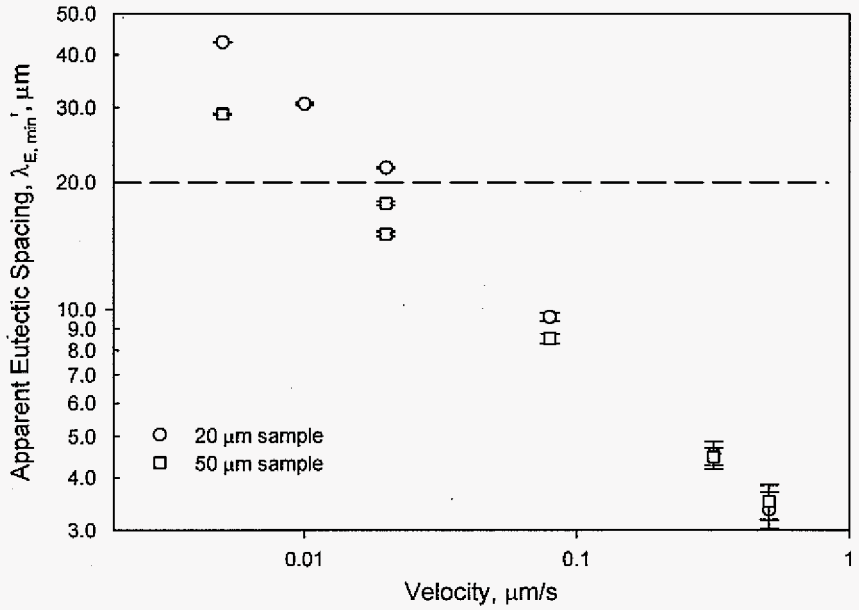

Figure 3. Variation in the measured minimum spacing with growth rate in 2 different thick samples.

Experimental conditions are listed in Table 2 together with the observed spatial distribution in terms of number of layers of rods. The experimental spacing (λ_e), which is the distance between the two adjacent β phase rods in a recorded image, and the width (ℓ_w) of the β phase rods as seen under a microscope are also measured and listed in Table 2 for different velocities. These two parameters will be used to determine the shape and orientation of the rod when a single layer of rods forms. The spacing, λ_e, is measured at different velocities for each sample. A range of spacing is present at each velocity, and the minimum observed spacing at each velocity was characterized and the results are plotted in Fig. 3. For the two highest velocities, the eutectic spacing is found to be independent of sample thickness, while at lower velocities a thinner sample gives rise to a larger spacing and this difference becomes more pronounced as the growth velocity is decreased further.

3.2. Dynamics of the spacing selection process

The transparent nature of the system is utilized in examining the dynamics of the spacing selection mechanism. Initially, the evolution of the eutectic structure is studied as a function of time by changing the track velocity from 0 to some final value V_f. Next, two sets of experiments are carried out in which the velocity is changed in two-steps, i.e. $0 \rightarrow V_i \rightarrow V_f$. At each velocity, the system is solidified until a steady-state is reached. Two sets of experiments are carried out with $V_i > V_f$ and $V_i < V_f$ so that the mechanisms operating for the increase and decrease in the spacing can be characterized.

The spacing adjustment process when the velocity is reduced from $V_i = 0.02$ to $V_f = 0.005$ μm/s is shown in Fig. 4. As the velocity is decreased, the spacing increases through the elimination of some whole columns of rods and the merging of the rods in the remaining columns. At V_i=0.02 μm/s, at least 4 layers of rods are present (Fig. 4(a)). This vertically multi-rod growth becomes more discernable in Fig. 4(b), where the velocity is decelerated. The arrows in Figure 4(b) mark those columns of rods which will soon be overgrown. In this viewfield, except the 2nd and the 3rd rod columns from left, every other β rod column is eliminated from the original interface stabilized at V_i=0.02 μm/s. At the new steady state, a single layer of β rods grows across the solid/liquid interface (Fig. 4(c)). The increase in spacing also leads to wider rods to maintain the same volume fraction.

Figure 5 shows the morphological evolution with time as the growth rate increases from $V_i = 0.01$ to V_f=0.04 μm/s in a 20μm-thick sample. The increase in velocity decreases the rod spacing so that additional rods are created through the branching of the rods. The tips of the rods become unstable and form four perturbations (or buds), and a necking of the rod

near the tip occurs (Figs. 5(b) and 5(c)). The location of the initial instability may be related to the constrained space since, in the rectangular domain, a slightly larger concentration gradient will be present along the diagonal directions. Once the instabilities grow to certain size, the interaction of the diffusion fields between the neighboring rods would eliminate some of the rods, as seen in Fig. 6.

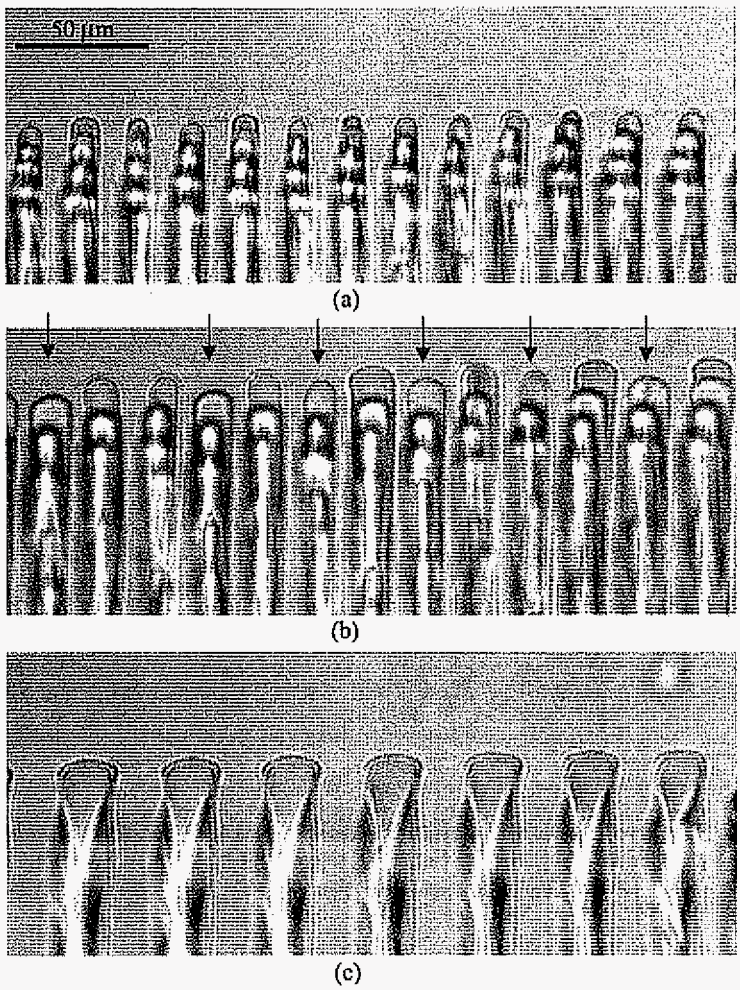

Figure 4. In-situ images of (a) Stable interface at V = 0.02 μm/s; (b) Velocity decreased 4 times from 0.02 to 0.005 μm/s and (c) Re-stabilized interface at V = 0.005 μm/s.

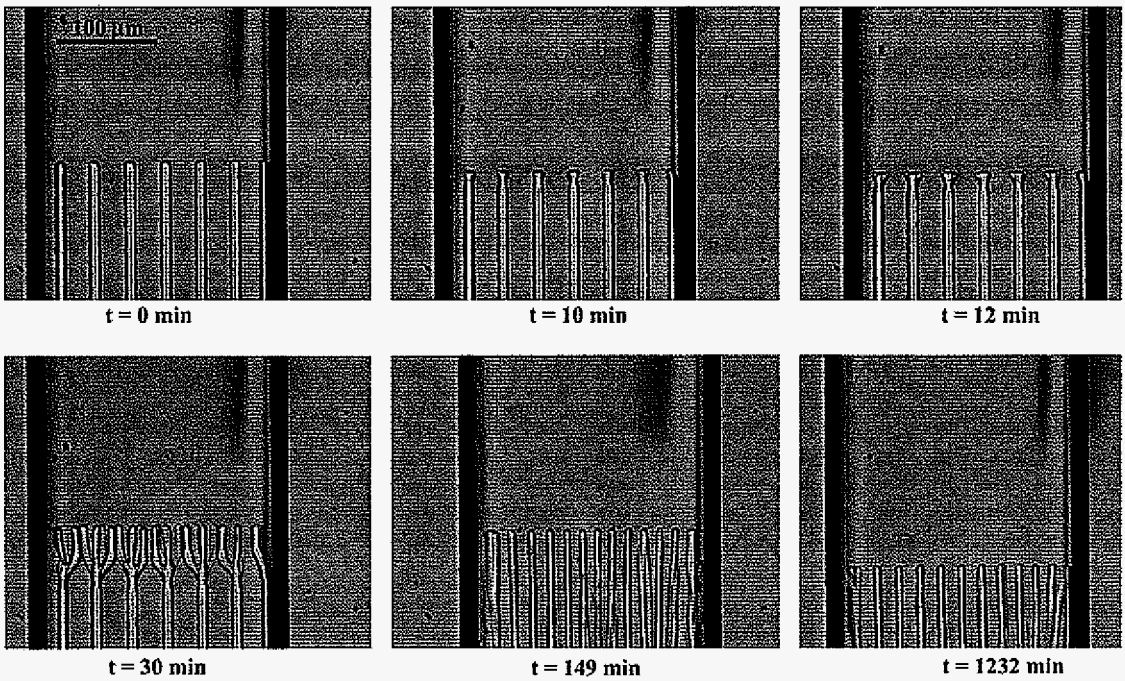

Figure 5. The eutectic in-situ morphology change with time in a velocity-increase process (SCN-24.0wt%camphor, G=4.5 K/mm, V_1=0.01 μm/s, V_2=0.04 μm/s).

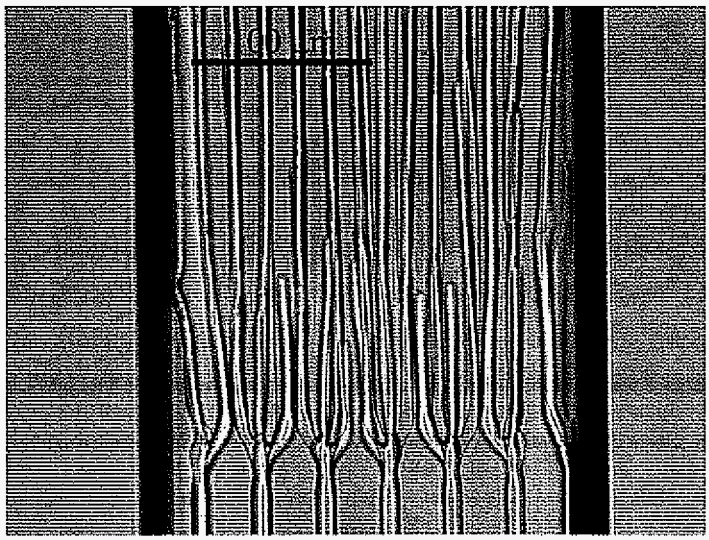

Figure 6. Interface instability and subsequent spacing adjustment in a V-increase process (SCN-24wt%camphor, G=4.5 K/mm, V_1=0.01 μm/s, V_2=0.04 μm/s).

3.3. Spatial arrangement of rods

Experimental measurements of eutectic spacing are made on the 2D projection of a 3D rod-like structure when the growth occurs in multiple layers. It is thus necessary to determine the spatial arrangement of rods, and to correlate the measured eutectic spacing, λ_e, with the actual rod eutectic spacing, λ_R, in the bulk region. For a single layer growth, $\lambda_R = \lambda_e$, but for multilayer growth of rods $\lambda_R > \lambda_e$. For an ideal hexagonal pattern of rods, there are two possible arrangements with respect to the direction of observation, as shown in Fig. 7(a) and 7(b). For the spatial arrangement shown in Fig. 7(a), $\lambda_R = \lambda_e / \cos 30$ and for the arrangement shown in Fig. 7(b), $\lambda_R = 2\lambda_e$.

In order to establish the arrangement that is present in our experiments, we first calculate the radius of the rod of the minor phase (β phase) for each arrangement by using the volume fraction f_β = 0.182 for the eutectic composition. It can be shown that for the configuration in Fig. 7(a), $r_\beta = 0.1829\,\lambda_e$ and for the configuration in Fig. 7(b), $r_\beta = 0.3168\,\lambda_e$. This simple calculation indicates that the viewfield from the top would be 63% black due to the overlap of β rods if the arrangement were like Fig. 7(b), which is contrary to the experimental observation in Figs. 2 and 4. Therefore a configuration shown in Fig. 7(a) is present in the experiments. For this multilayer configuration with ideal shape and arrangement of rods, the rod spacing is given by $\lambda_R = \lambda_e / \cos 30 = 1.155\,\lambda_e$, and the distance between the rod layers is given by: $\lambda_t = \lambda_e \tan 30 = 0.577\,\lambda_e$ or $\lambda_t = 0.50\,\lambda_R$. For this spatial arrangement of rods, the measured spacings in multilayer configurations are converted to the actual rod spacing, and the results are shown in Fig. 8 for the sample thickness of 20

and 50 μm.

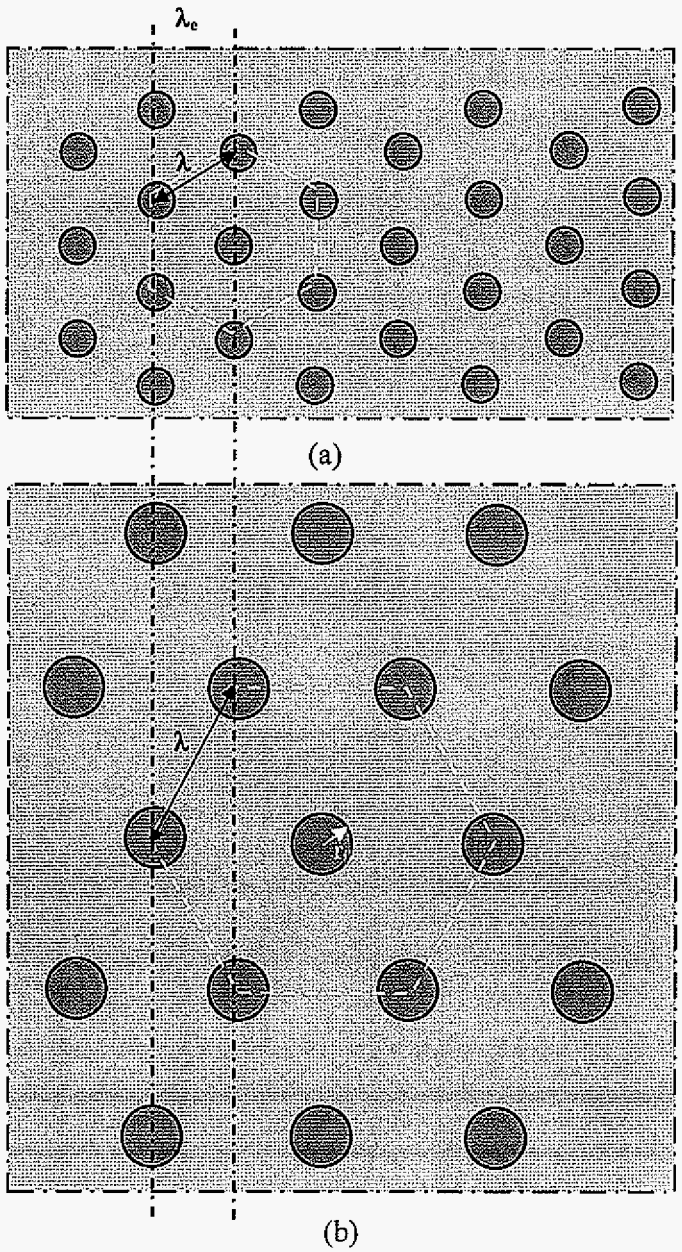

Figure 7. Two different spatial arrangements of rods with respect to the direction of observation.

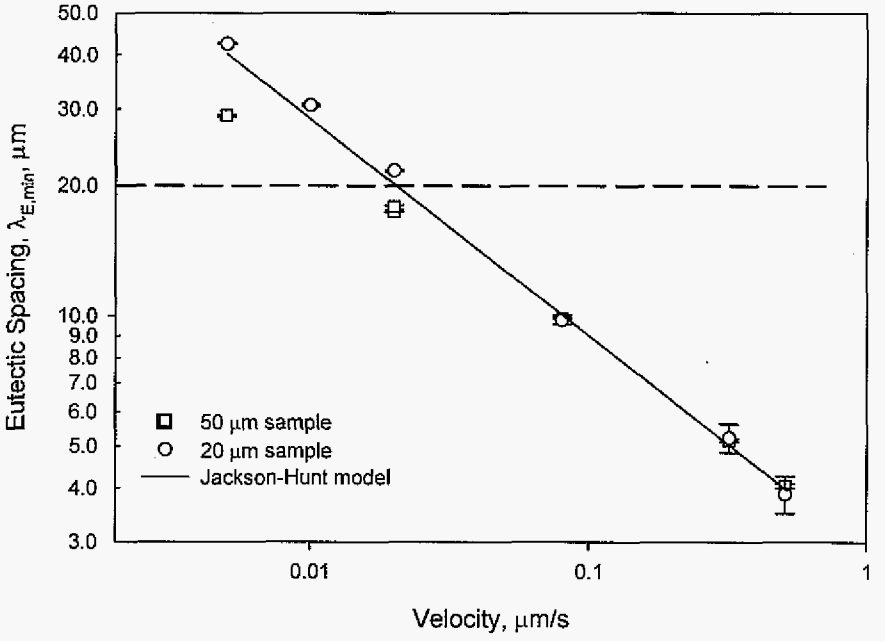

Figure 8. The measured spacing for the multiplayer growth are converted to the actual rod spacing and compared with Jackson and Hunt model (SCN-24.0wt%camphor, G = 4.5 K/mm).

3.4. Eutectic spacing selection under steady state growth

The rod spacing results for the bulk sample are now compared with the Jackson and Hunt model [4] of rod eutectic growth, which is based on rods of circular cross-section that arranged in a regular hexagonal pattern. Under the assumption that the eutectic interface grows at minimum undercooling, they obtained the scaling relationship as:

$$\lambda_{R,\min}{}^{2} V = \mathrm{K}_2 / K_1 \qquad (1)$$

where K_1 and K_2 are system-dependent parameters, which are defined as:

$$K_1 = mP\Delta C_s / f_\alpha f_\beta D \qquad (2)$$

$$K_2 = 4m\sqrt{f_\beta}\,\Sigma_i(\Gamma_i \sin\theta_i / |m_i| f_i)\,;\ \mathrm{i} = \alpha, \beta, \qquad (3)$$

where $m = |m_\alpha m_\beta| / (|m_\alpha| + |m_\beta|)$. P is related to the volume fractions of α and β phases and is defined as the summation of Bessel functions. Trivedi and Kurz [5] simplified the summation of infinite series with a power function of volume fractions that is accurate for $f_\beta \le 0.3$. A more general expression for all volume fractions is obtained as: $P = 0.2372 f_\alpha^{1.3937} f_\beta^{1.8601}$. ΔC_s is the solubility difference between β and α phase at the eutectic tie-line, $= C_{s\beta} - C_{s\alpha}$. With the values in Table 1, we find that $\lambda_{R,\min}^2 V = 7.98\ \mu m^3/s$. The theoretically predicted minimum spacing values for bulk samples are shown in Fig. 8 as a solid line. Experimental values of the rod spacing for both sample thicknesses agree quite accurately with the predicted values at higher velocities where the spacing is small so that the number of rod layers are large and approach the bulk configuration. This is the first confirmation of the validity of the rod eutectic model of Jackson and Hunt in a system in which all required system parameters have been measured accurately.

When the velocity decreases, the experimental results deviate from the theoretically predicted values in the bulk sample. This departure is due to the constraint of the sample and it can be related to the number of layers of rods. For a multilayer configuration that corresponds to the bulk configuration, the distance, between the layers in the direction of the thickness is equal to $\lambda_R/2$, as seen in Fig. 7(a). In order to determine the number of layers needed to obtain bulk configuration, we analyze the experimental spacing data in three groups. (1) The experimental data at two higher velocities (0.32 and 0.51 μm/s) show that the spacing is independent of the thickness and its value corresponds to that in the bulk sample.

The smallest number of layers for these velocities will be present in 20 μm thick sample at V = 0.32 μm/s where the number of layers is about six. (2) The second group consists of single layers of rods that form at four lower velocities in 20 μm thick sample, and at two lower velocities in 50 μm thick sample. Note that a single layer is obtained in 20 μm thick sample for velocities of 0.005 and 0.08 μm/s where the spacing between the rods differs by a factor of four. Thus it is important to note that the number of layers is not governed by the spacing between the layers in a bulk sample since the distance between the rod layers is influenced by the thickness and velocity of the sample. To examine the reason for this change in spacing, we note that the spacings at three lower velocities in 20 μm thick sample are slightly larger than the sample thickness and also larger than the predicted values in the bulk. In contrast, the spacing at V= 0.08 μm/s in 20 μm thick sample are smaller than the sample thickness and also smaller than the predicted values in the bulk. These results show that the thickness of the sample and the velocity influence both the distance between the rods in a given layer and the distance between the layers. These changes in the spacing will be determined in the next section, and they will be shown to arise from the change in shapes of the rods from circular to elliptical in cross-section and from the change in orientation of the major and minor axes of the ellipse. (3) The third case corresponds to layers of rods between two and five where thickness effect begins to influence the rod pattern. For example, the results for V=0.02 μm/s in 50 μm thick sample show one or two layers, whereas the number of layers based on the bulk spacing should be 5. It is thus important to note that the rod shape becomes elliptical when the thickness decreases to give fewer than six layers, and the distance between the layers in the direction of the thickness is influenced by the change in the diffusion field for

the elongated rods along the direction of the thickness.

3.5. Rod morphology in thin samples

The effect of sample thickness (for a fixed velocity) or velocity (for a fixed thickness) on the shape and spacing of the rods will now be established. Experimental observations in Figs. 2(a) and (b) show that the shapes of the rods deviate from a circular cross-section when the thickness of the sample is reduced. Rods in Fig. 2(a) are elongated in the lateral direction, whereas those in Fig. 2(b) are elongated in the vertical direction. To establish the shape of the rod unambiguously, we consider the results for conditions that give a single layer of rods. We consider different possible shapes of rods, as shown in Fig. 9: (a) lamellar, (b) circular cylinder, (c) elliptic cylinder with the major axis in the direction of the thickness, or (d) elliptic cylinder with the major axis in the direction of the width of the sample. The shape of the rod in a single layer formation can be determined from the experimental values of the local spacing λ_e and the measured width (ℓ_w) of the rod given in Table 2. The shape should confirm the volume fraction of the rods to be 0.182 for the eutectic composition used in this study.

First consider the possibility of the minor phase to be lamellar or rods of circular cross-section. For the lamellar shape, the local volume fraction of each "β-plate" is given by the ratio ℓ_w / λ_e and the results for experimental conditions of V = 0.02 μm/s in a 50 μm thick sample are shown in Fig. 10 as open square symbols. The calculated volume fractions are larger than the theoretical value of 0.182, which indicates that lamellar shape assumption is not valid, and the minor phase does not go across the thickness of the sample. We now examine the possibility of a circular cross section of the rod, which would give the volume

fraction as $\pi \ell_w^2 / \lambda_e \delta$, where δ is the thickness of the sample. The results are shown in Fig. 10 as filled squares. The volume fractions for assumed circular cross-section are smaller than the theoretical value, so that the experimental shape must have depth that is larger than ℓ_w, or the rods are elliptical in shape with the major axis in the direction of the thickness, ℓ_t, larger than ℓ_w.

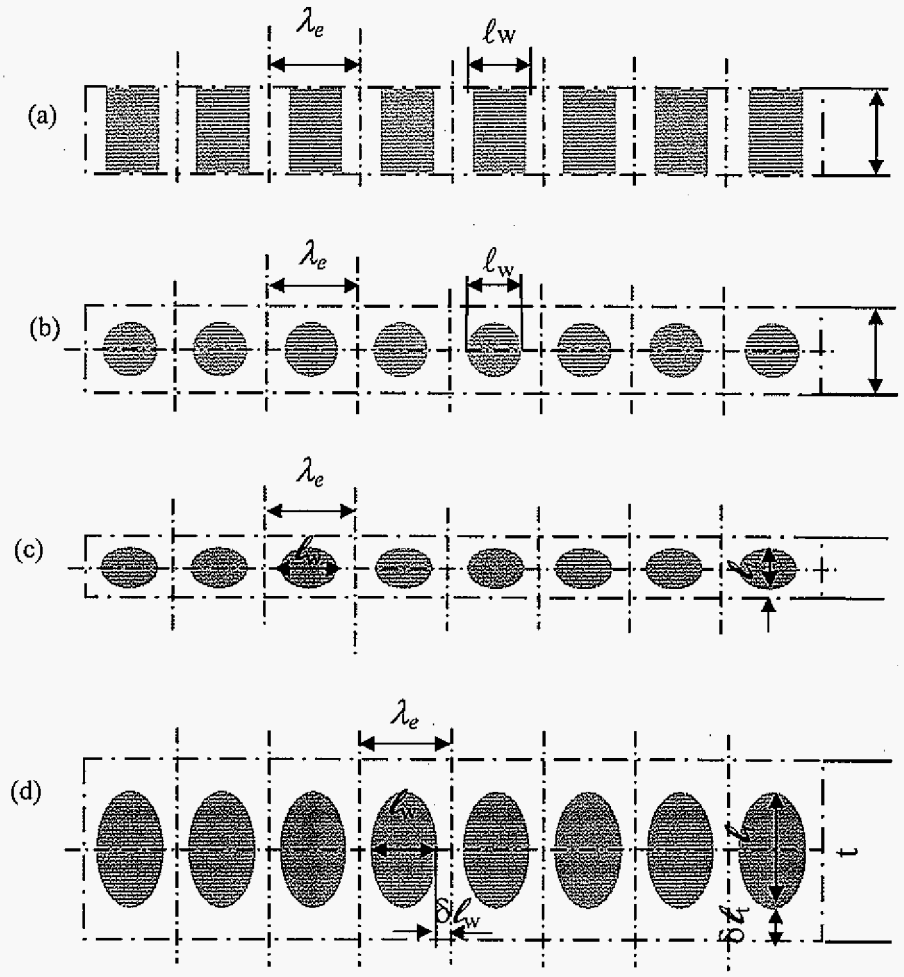

Figure 9. Schematic illustrations of the possible shapes of rods in reorganized patterns of a single layer of rods. (a) lamellar shape, (b) circular cylinder, (c) elliptical cylinder with the major axis in the direction of sample width, and (d) elliptical shape with the major axis along the sample thickness.

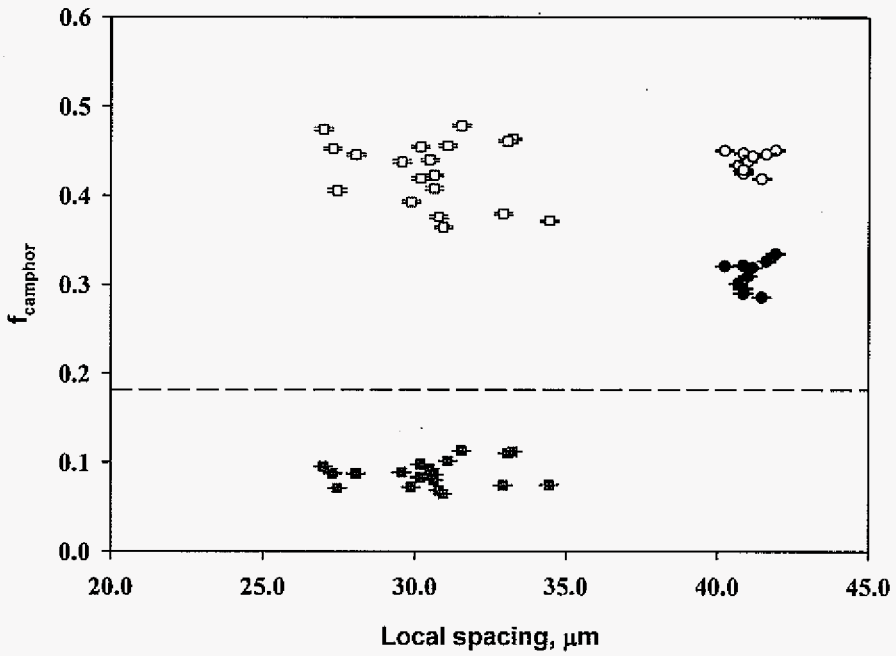

Figure 10. Calculated volume fractions of β phase. The circles are for V=0.005 μm/s in a 20 μm sample and the squares are for V=0.02 μm/s in a 50 μm sample. The open symbols are for the calculation by assuming lamellar growth and the filled ones are for the assumption of circular rod growth.

We now examine the volume fractions for experimental conditions of δ = 20 μm and V = 0.005 μm/s for assumed lamellar and circular cylindrical shape of the rods, and the results are shown in Fig. 10 as open and filled circles, respectively. Since both these volume fraction results are higher than the theoretical value, the depth of the rods must be smaller than the width of the rods, i.e. $\ell_t < \ell_w$, or the rods are elliptical in shape with the major axis along the width of the sample. This conclusion is rather obvious for the 20 μm sample since $\delta = 20\mu m$ while the measured minimum spacing $\lambda_c = 42.46\mu m$, it is impossible for a rod to assume a circular cross section and it must be elongated along the width of the sample. Thus, when the thickness of the sample becomes small enough to form a single layer of rods, the

rods assume an elliptical shape with two possible orientations of the major axis of the ellipse.

We now examine the conditions that determine the orientation of the elliptical rods. The experimental measurement of ℓ_w gives one of the axes of the ellipse, and the other axis, ℓ_t, along the thickness of the sample can be obtained by matching with the theoretical volume fraction, f_R, which is given by:

$$\ell_t = \frac{4 f_R \lambda_e t}{\pi \ell_w} \qquad (4)$$

From the experimental values of ℓ_w, λ_e *and* δ, and using f_R = 0.182 for the eutectic composition, the value of ℓ_t can be calculated. For the experimental conditions given in Fig. 2, the rods in 50 μm thick samples give the values of the two axes as $\ell_w = 10.28\,\mu m, \ell_t = 20.07\,\mu m$ that show that the rods are elongated in the direction of the thickness. In contrast, the results for 20 μm thick sample give $\ell_w = 19.16\,\mu m, \ell_t = 10.3\,\mu m$ that shows that the rod is elongated in the direction of the width of the sample.

The orientation of the ellipse under different experimental conditions, which give rise to a single layer, can be examined by defining the shape factor, ε, of a rod, as

$$\varepsilon = (\ell_w - \ell_t)/(\ell_w + \ell_t) \qquad (5)$$

When $\varepsilon > 0$, the major axis of the ellipse is along the width of the sample, and when $\varepsilon < 0$, the major axis of the ellipse is vertical in the direction of the thickness of the sample. Experimental results for a single layer of rods are now used to calculate the shape factor for different values of the relative spacing λ_e/δ, and the results are shown in Fig. 11.

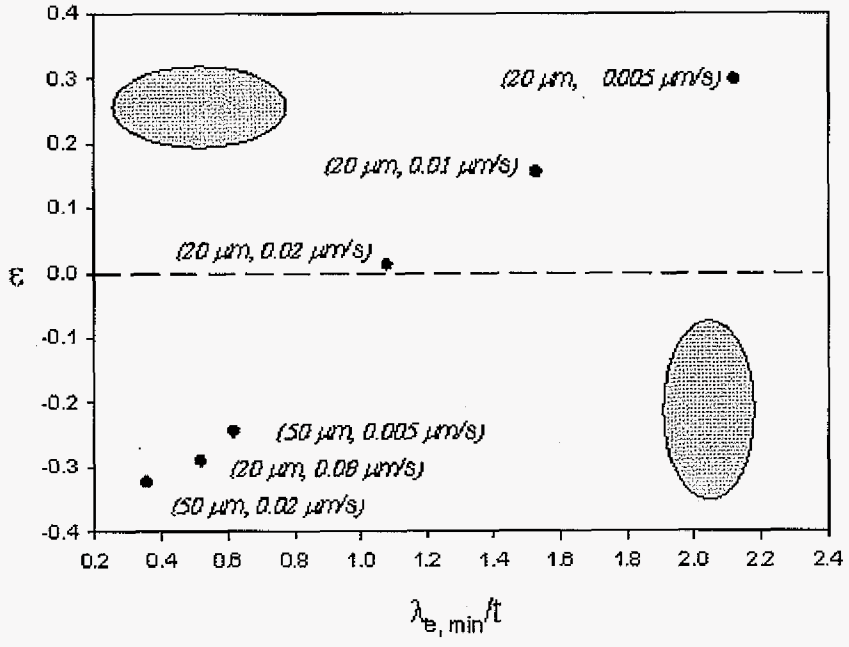

Figure 11. Summary of the experiments with a single layer of β rod growth. The numbers near each data point is for the sample thickness and the growth velocity.

Several important observations can be made in Fig. 11. (1) The major axis of the ellipse changes from vertical to horizontal direction as λ_e/δ varies from less than one to greater than one. (2) For a given thickness (20 μm), the orientation of the ellipse has a major axis in the direction of the width at low velocities (i.e. V = 0.005 μm/s), and the shape changes towards a circular cylinder as the velocity is increased to 0.02 μm/s. The major axis of the ellipse then changes from horizontal to vertical direction when the velocity is increased further to 0.08 μm/s. Thus, for a given thickness, the transition in the orientation of the ellipse occurs with increase in velocity. (3) For a given velocity of 0.005 μm/s, the orientation of the ellipse changes from horizontal to vertical as the thickness is increased from 20 to 50 μm. (4) The results in 20 μm thick sample show that the spacing between the

rods is larger than that for cylindrical rods when the major axis is in the direction of the width, and it becomes smaller when the major axis is in the direction of the thickness. These differences in the spacing are consistent with the experimental data for a single layer growth shown in Fig. 8. (5) It is sometimes assumed that the rods will become lamellae if the thickness is very small. The present results show that rods will not become lamella, but will elongate more in the direction of the width when the thickness is reduced.

The effect of the rod shape on the spacing can be visualized by considering an array of elliptical rods, as shown in Fig. 12. Two different configurations are shown that are identical in a bulk sample since they are obtained by 90^{o} rotation of the sample. However, they show distinctly different configurations when a single layer is formed or when they are viewed from a fixed direction under a microscope. The configuration of the single layer of rods can be identified in the figures, which show that when the major axis of the ellipse is along the thickness of the sample, the spacing between the rods is decreased, and the characteristic thickness of the layer of rods is increased. Similarly, when the major axis is along the width of the sample, the spacing between the rods is increased and the characteristic thickness of the layer of rods is decreased.

A theoretical model of eutectic growth for a two-dimensional array of elliptically-shaped rods will now be developed to explain the experimental observations on the spacing and orientation of the rods as a function of sample thickness and velocity.

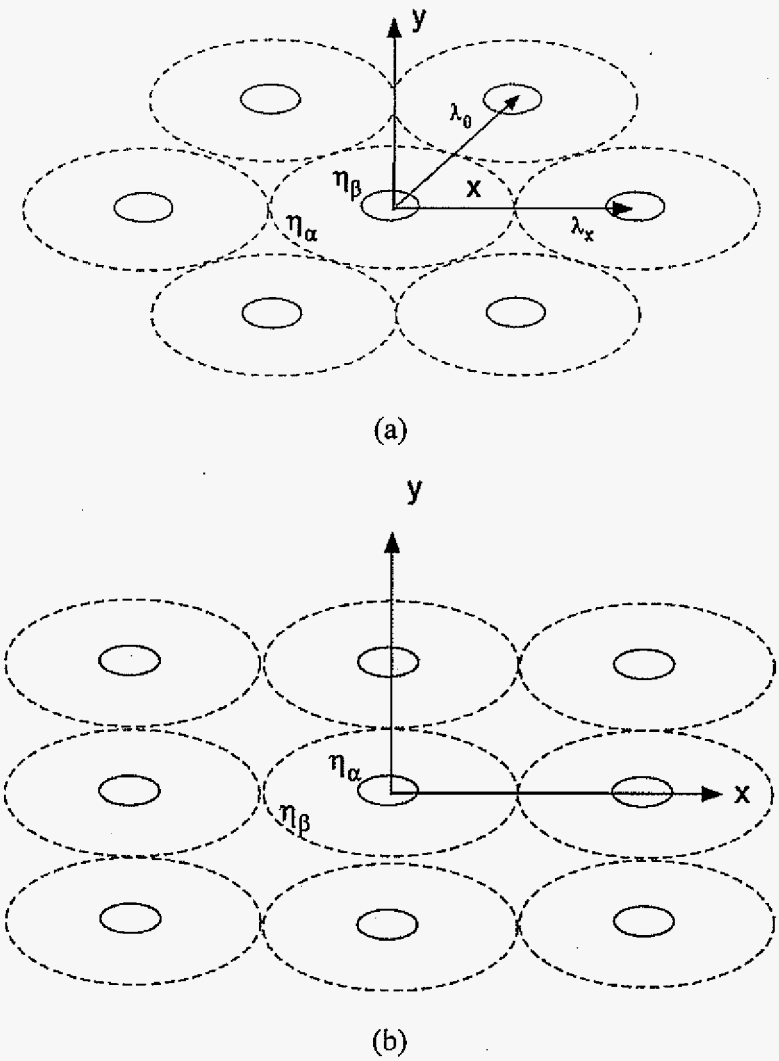

Figure 12. Two different spatial arrangements of elliptical rods viewed normal to the interface. (a) An irregular hexagonal arrangement of rods with six neighbors. (b) A rectangular arrangement with four neighbors. The dotted ellipses are the outer boundaries determined to have the same area as the controlled area for each rod.

4. Theoretical Model

4.1. Basic model

Consider a eutectic phase diagram with eutectic composition, C_E, and the initial alloy composition, C_0, as shown in Fig. 1. The composition differences between the eutectic and

the two solid phases are shown in the figure as C_0^{α} and C_0^{β}, and the total composition range is $\Delta C_0 = C_0^{\alpha} + C_0^{\beta}$. Consider a two-dimensional array of rods of elliptical cross-section, as shown in Fig. 12. A general model will now be developed by following the Jackson-Hunt [4] approach. We consider two spatial distributions: (1) an irregular hexagonal array whose results can be compared with the hexagonal array of circular rods, and (2) a square array which is more appropriate to analyze the results of a single layer of rods in thin samples.

The interface configuration is shown in Fig. 12 with the growth direction (z-direction) being normal to the plane of paper. For determining the solute profile in the liquid, we assume that the interface is planar at z = 0. The diffusion in the liquid is governed by the following steady-state diffusion equation in a coordinate system that is moving in the z-direction at velocity V.

$$\frac{d^2C}{dx^2} + \frac{d^2C}{dy^2} + \frac{d^2Z}{dz^2} + \frac{V}{D_l}\frac{dZ}{dz} = 0 \qquad (6)$$

The diffusion in the two solid phases is assumed to be negligible.

To obtain the solute profile in the liquid, consider an elliptical cylindrical coordinate system (η,ψ, z), in which the coordinates η and ψ represent a family of confocal ellipses and confocal hyperbolas, respectively [20-22]. Transformations between the Cartesian and the elliptical cylindrical coordinates are given by:

$$x = h\cosh\eta\cos\psi, \qquad (7)$$

$$y = h\sinh\eta\sin\psi, \qquad (8)$$

$$z = z, \qquad (9)$$

where x and y coordinates are shown in Fig. 12, and h is half the distance between the two foci. The axes of the ellipse along the x and y directions are given by $h\cosh\eta$ and $h\sinh\eta$, respectively. Let $\eta = \eta_\beta$ represent the rod:matrix interface and $\eta=\eta_\alpha$ be the far-field boundary of the α-phase, as shown in Fig.12.

To obtain the outside ellipse, $\eta = \eta_\alpha$ for the α phase boundary, we follow the simplification used by Jackson and Hunt [4] that the area of the ellipse is equal to the area A of the original hexagonal domain or square domain. The steady state diffusion equation in a moving elliptical cylindrical coordinate system (η, ψ, z) can be written as [22]:

$$\frac{1}{h^2(\cosh^2\eta-\cos^2\psi)}\left(\frac{\partial^2 C}{\partial\eta^2}+\frac{\partial^2 C}{\partial\psi^2}\right)+\frac{\partial^2 C}{\partial z^2}+\frac{V}{D_l}\frac{\partial C}{\partial z}=0 \qquad (10)$$

The boundary conditions can be expresses as:

$$C = C_o \quad \text{at } z\rightarrow\infty; \qquad (11)$$

$$\frac{\partial C}{\partial \eta}=0 \quad \text{at } \eta=0 \text{ and} \qquad (12a)$$

$$\frac{\partial C}{\partial \eta}=0 \quad \text{at } \eta=\eta_\alpha \qquad (12b)$$

$$\frac{\partial C}{\partial \psi}=0 \quad \text{at } \psi = 0,\ \pi/2,\ \pi \text{ and } 3\pi/2 \qquad (12c)$$

$$C(\psi+\pi)=C(\psi) \qquad (12d)$$

$$\frac{\partial C}{\partial z}=\frac{V}{D_l}C_o^{\beta} \quad \text{for } 0\le\eta<\eta_\beta \qquad (13a)$$

$$\frac{\partial C}{\partial z}=-\frac{V}{D_l}C_o^{\alpha} \quad \text{for } \eta_\beta\le\eta<\eta_\alpha \qquad (13b)$$

C_o^{α} and C_o^{β} are shown in Fig. 1.

4.2. Solution of the diffusion problem

The differential equation (10) is solved through the separation of variables method [21] and the coefficients are determined from the above boundary conditions. The equations for ψ and η are obtained as Mathieu's equations, with the solutions given by the angular Mathieu functions, $ce_{2n}(\psi,q)$ and the radial Mathieu function, $Ce_{2n}(\eta, q)$. The solution for the concentration field in the liquid is thus given by

$$C(\eta,\psi,z) = C_o + Y_0 \exp(-Vz/D) + \sum_{n=0}^{\infty}\sum_{m=1}^{\infty} Y_{2n,m}\, Ce_{2n}(\eta, q_{2n,m})\, ce_{2n}(\psi, q_{2n,m}) \exp^{-2\sqrt{q_{2n,m}}/h)z} \qquad (14)$$

It is assumed that, for m>0, $2\sqrt{q_{2n,m}}/h >> V/D$ is at low velocity. The coefficient Y_0 is obtained as:

$$Y_0 = \frac{\sinh 2\eta_\beta}{\sinh 2\eta_\alpha} C_0 - C_0^{\alpha} = f_\beta C_0 - C_0^{\alpha}. \qquad (15a)$$

$$Y_{2n,m} = \frac{4h}{\sqrt{q_{2n,m}}} \frac{V\Delta C_o}{D} \frac{\left(A_o^{(2n)} \sum_{r=1}^{\infty} 2rA_{2r}^{(2n)} \sinh 2r\eta_\beta\right)}{\Omega_{2n,m}}; \qquad (15b)$$

where $\bar{\lambda} = 2\sqrt{a_{x\alpha} a_{y\alpha}}$, in which $a_{x\alpha}$ and $a_{y\alpha}$ are the semi-axes of the outer ellipse that will be related to the rod spacing for an irregular hexagon and a square array.

The boundary condition $\left.\frac{\partial C}{\partial \eta}\right|_{\eta=\eta a} = 0$ (Eq. 7b) determines eigenvalues q that are required for the solution to be stable, and they are obtained from the following equation:

$$\left.\frac{d(Ce_{2n}(\eta,q))}{d\eta}\right|_{\eta=\eta_\alpha} = \sum_{r=0}^{\infty}(2r)A_{2r}^{(2n)}(q_{2n,m})\sinh 2r\eta_\alpha = 0 \qquad (16)$$

in which 2n is the order of the Mathieu function, and $q_{2n,m}$ is the mth positive parametric zeros satisfying Eq. (16). From equations (14) – (16), the average composition in the β-rod and the α-matrix are obtained as:

$$\overline{C}_\beta = \frac{2V}{D}\Delta C_o\overline{\lambda}\ L + C_0 + Y_0 \qquad (17)$$

$$\overline{C}_\alpha = -\left(\frac{2V}{D}\Delta C_o\overline{\lambda}\ L\ \right)\frac{A_\beta}{A_\alpha} + + Y_0 + C_0 \qquad (18)$$

where the function L is defined as:

$$L = 2\left(\frac{1}{2\sinh 2\eta_\beta}\right)^{3/2}\sum_{n=0}^{\infty}\sum_{m=1}^{\infty}\left(\frac{1}{\sqrt{q_{2n,m}}}\right)^3\frac{\left(A_o^{(2n)}\sum_{r=1}^{\infty}2rA_{2r}^{(2n)}\sinh 2r\eta_\beta\right)^2}{\Omega_{2n,m}} \qquad (19)$$

Using the procedure of Jackson and Hunt the total undercooling is obtained as the sum of the solutal (ΔT_d) and capillary (ΔT_c) undercooling. The solutal undercooling is given by:

$$\Delta T_c = \overline{m}\left[\frac{2V}{D}\Delta C_o\overline{\lambda}\ L\right]\left[\frac{1}{1-f_\beta}\right] = K_1 V\overline{\lambda} \qquad (20)$$

where $K_1 = \overline{m}\left[\frac{2}{D}\Delta C_o L\right]\left[\frac{1}{1-f_\beta}\right]$ (21)

The solutal undercooling expression is similar to that for circular rods with the terms λ and M for rods being analogous to $\overline{\lambda}$ and L, respectively. We may follow the procedure of JH to calculate the interface energy contribution

We shall first examine how the diffusion field is altered as the rods become elliptical in shape, and then examine the predictions of the model for the spacing and orientation of the

ellipse as function of growth rate and sample thickness. Because of the space constraint, the details of the model and the conditions for the selection of lamellar, circular and elliptical rods will be presented in a separate publication.

A. Diffusion Field

Composition profiles in the liquid ahead of the interface were calculated as a function of orientation by using equations (14) – (16). Since Mathieu's functions are complex, they are generally evaluated numerically [22]. Calculations were carried out for one V=0.005 μm/s, and the results are shown in Fig. 13(a). Three solute distribution curves are shown in Fig. 13(a): $\psi=0$ is along the major axis of the ellipse; $\psi=90^{\circ}$ is along the minor axis and $\psi=45^{\circ}$ is in between. The tri-angles on each curve mark the β phase boundary. Figure 13(a) shows that there is a significant variation in the radial component in the composition field, with the composition being the smallest along the major axis and the largest along the minor axis for a fixed radius. The radial composition profiles are compared with the one in the circular-cylindrical coordinates by Jackson and Hunt [4] (Fig. 13(b)).

B. Spacing and orientation selection

To apply the results of the model, the parameter, $\overline{\lambda} = 2\sqrt{a_{x\alpha}a_{y\alpha}}$, needs to be evaluated in terms of the rod spacing. The value of the parameter, $\overline{\lambda}$, depends on the spatial arrangement of the rods, as shown in Fig. 12, and it can be related to the rod spacing by simple geometrical considerations. For an irregular hexagonal arrangement, we define the distances between the rods in two directions as λ_x and λ_θ, as shown in Fig. 12(a). These spacing are related to the axes of the outer ellipse as:

$$a_{x\alpha}a_{y\alpha} = (\lambda_x\lambda_\theta / 2\pi)[4-(\lambda_x/\lambda_\theta)^2]^{1/2} \qquad (22)$$

Since our experimental results are in thin sample, the rectangular arrangement, shown in Fig. 12b, should be used to quantitatively analyze the results obtained for the single layer of rods. The outer ellipse is considered to have the same area as the area per rod, which is $\lambda_e\delta$, so we obtain:

$$a_{x\alpha}a_{y\alpha} = (\lambda_e\delta/\pi) \qquad (23)$$

For the rectangular arrangement, $\overline{\lambda}^2 = (4\lambda_e\delta/\pi)$.

The general criterion for the selection of the orientation of the major and minor axis for the two-dimensional array of elliptical rods, and the selection of elliptic rods over circular rods and lamellar eutectic, will be presented in detail in a separate paper because of the space limitation. Here we shall briefly examine the physics to capture the essence of new results obtained in this study. The spacing can be considered to depend on the velocity as: $\overline{\lambda}_e^{\,2} \sim (1/V)$, so that the spacing will be related with velocity and thickness as: $\lambda_e \sim 1/(V\delta)$. Thus, in a thin sample, the spacing for a single array of rods varies inversely with V and δ, as found in the experiments. The change in the orientation of the ellipse with the thickness is seen by considering the ratio (λ_e/δ), which is inversely proportional to the square of the thickness. Thus, for a very thin sample, $(\lambda_e/\delta) >> 1$, and the ellipse will have an orientation with major axis in the x-direction. As the thickness increase, the ellipse becomes a circle when $(\lambda_e/\delta) = 1$, and then it changes to an ellipse with the major axis in the y-direction when $(\lambda_e/\delta) << 1$. Thus the model shows that the orientation of the ellipse changes from the horizontal ($\lambda_e > \delta$) to the vertical ($\lambda_e < \delta$), as the thickness is increased. In a similar

manner, it can be seen that the ellipse changes its orientation with velocity at a fixed spacing.

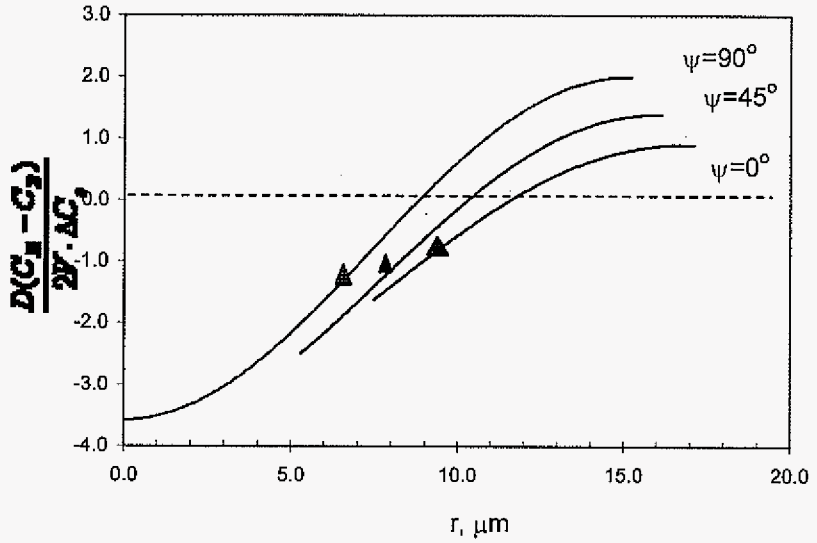

(a)

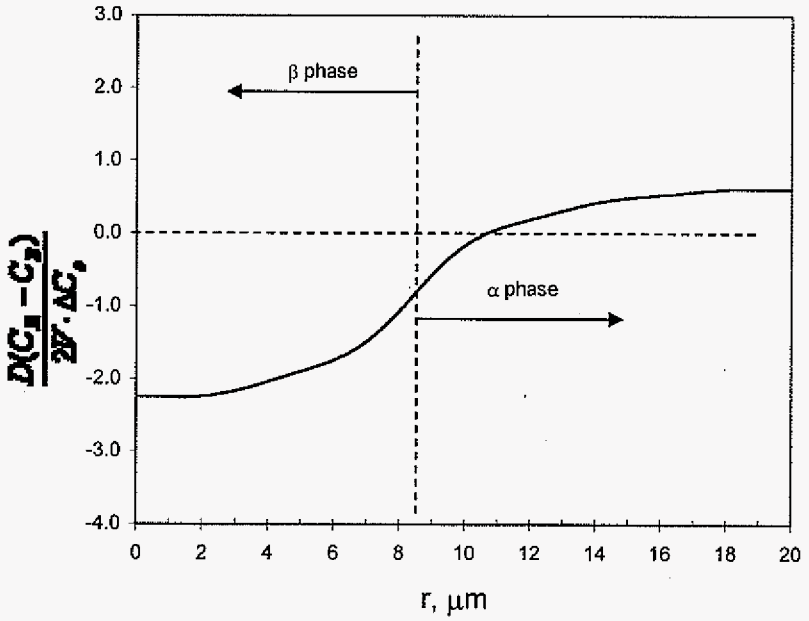

(b)

Figure 13. Comparison of the radial composition profile of the liquid at the growth interface (a) Zeroth-order Mathieu's function for a elliptical cylindrical system (b) JH model for a circular cylinder coordinate system.

5. Conclusion:

A systematic experimental study has been carried out in the well-characterized organic eutectic system (SCN-camphor) where the rod eutectic forms. Experiments are carried out in samples of finite thickness, and for conditions where multi-layers of rods form, in which case the bulk spacing variation with velocity is found to agree with the Jackson and Hunt model.

In thin samples, in which only a single layer of rods is present, a significant change in the shape and distribution of rods is discovered. A new branch of rod eutectic is found with two major differences: (i) the rod shape corresponds to an elliptic cylinder rather than a circular cylinder, and (ii) two different orientations of the ellipse that are perpendicular to each other can be present, i.e. the major axis changes from the horizontal to the vertical direction in thin samples as the sample thickness or the velocity is increased. (iii) The orientation of the ellipse also influences the spacing between the rods. The spacing increases if the major axis is in the direction of the width (or horizontal direction) and decreases if the major axis is in the direction of the thickness.

A model of rod eutectic growth with rods of elliptical cylindrical shape is developed. The diffusion field in the liquid ahead of the interface is obtained by solving the diffusion equation in an elliptical cylinder system. The solution is obtained in terms of Mathieu's functions, and the average concentration in the liquid ahead of each phase determined, from which the solutal undercooling is obtained. The results of the model are discussed for the orientation of the ellipse and the scaling law between the velocity, spacing and sample thickness for a thin sample in which only a single layer of rods is present, and the predictions

are shown to describe the experimental observations.

Acknowledgement

A part of this work was carried out at Ames Laboratory under Contract No. DE-AC02-07CH11358 with the U.S. Department of Energy. A part of this study was also supported by the Office of Microgravity Sciences, NASA.

References

[1] Mclean M, Directionally Solidified Materials for High Temperature Service, Book 296, The Metals Society, 1983, chapters 3 and 6.

[2] Weiss H, Physical Properties on In Situ Composites, in Conference on In Situ Composites II, ed. by M. R. Jackson et al., Xerox Individualized Publishing Program, 1976, pp. 377-384.

[3] Hillert M, Jernkont. Annal. 1957; 141: 757.

[4] Jackson KA and Hunt JD, Trans. Metall. AIME, 1966; 236: 1129.

[5] Trivedi R and Kurz W, Microstructure Selection in Eutectic Alloy Systems. In: Stefanescu DM, Abbaschian GJ Bayuzik RH, editors. Solidification Processing of Eutectic Alloys, Warrendale (PA) Met Soc AIME, 1988, p.3.

[6] Walker H, Liu S, Lee JH and Trivedi R, Metall. Mater. Trans., 2007; 38A: 1417.

[7] Seetharaman V, Trivedi R, Metall. Trans, 1988; 19A: 2955.

[8] Akamatsu S, Bottin-Rousseau S, Faivre G., Phys. Rev. Lett, 2004; 93: 175.

[9] Somboonsuk K, Mason JT and Trivedi R, Met. Trans. 1984; 15A: 967.

[10] De Cheveign S, Guthmann C, and Lebrun MM, J. Physique, 1986; 47: 2095.

[11] Liu S, Suk MJ, Fabietti L and Trivedi R, The Effect of Dimensionality on Microstructures in Directionally Solidified SCN-Salol Alloys. In: Rappaz M, Beckermann C,

Trivedi R, editors. Solidification Processes and Microstructures- Symposium in Honor of W. Kurz. Warrendale (PA) TMS, 2004, p.211.

[12] Trivedi R, Miyahara H, Mazumder P, Simsek E and Tewari SN, Journal Crystal Growth, 2000; 222: 365.

[13] Caroli B, Caroli C, Roulet, Journal Crystal Growth, 1986; 76:31.

[14] Athreya BP, Dantzig JA, Liu S and Trivedi R, Dimensionality, Phil. Mag., 2006; 86(24): 3739.

[15] Lee JH, Liu S and Trivedi R, Metall. Mater. Trans., 2005; 36A: 3111.

[16] Teng J and Liu S, Journal Crystal Growth, 2006; 290: 248.

[17] Witusiewicz VT, Sturz L, Hecht U and Rex S, Acta Mater., 2004; 52: 4561.

[18] Liu S, Teng J and Choi M, Metall. Mater. Trans., 2007; 38A: 1555.

[19] Keslioglu K, Boeyuek U, Erol M and Marasli N, J. Materials Science, 2006; 41: 7939.

[20] Moon P and Spencer DE, Field Theory Handbook, Springer-Verlag, New York, 1971, p.17.

[21] Chu LJ, J. Applied Physics, 1938; 9: 583.

[22] Mclachlan NW, Theory and Application of Mathieu Functions, Oxford Press, 1947, chapters II, VIII and XVII.

Appendix 1. Evaluation of the coefficient $Y_{2n,m}$.

The boundary conditions (13a) and (13b) is now used to calculate the concentration gradient at z=0, i.e.,

$$\left.\frac{\partial C}{\partial z}\right|_{z=0} = \sum_{n=0}^{\infty}\sum_{m=1}^{\infty} Y_{2n,m} Ce_{2n}(\eta, q_{2n,m}) ce_{2n}(\psi, q_{2n,m})\left(-2\sqrt{q_{2n,m}}/h\right)) \qquad \text{(A1)}$$

By using the orthogonality property of the Mathieu's functions, the value of the coefficient $Y_{2n,m}$ can be written as [22]:

$$Y_{2n,m} = -\frac{2V}{D}\frac{2h}{\sqrt{q_{2n,m}}}\Delta C_0 \frac{\left(-A_o^{(2n)}\sum_{r=1}^{\infty} 2rA_{2r}^{(2n)} \sinh 2r\eta_\beta\right)}{\left[8q_{2n,m}\left(\int_0^{\eta\alpha} Ce_{2n}^2(\eta, q_{2n,m})(\cosh 2\eta - \Theta_{2n,m})d\eta\right)\right]} \qquad \text{(A2)}$$

where $\Delta C_o = C_0^\beta + C_0^\alpha$ and the function $\Theta_{2n,m}$ is defined as:

$$\Theta_{2n,m} = (A_o^{(2n)}A_2^{(2n)} + \sum_{r=0}^{\infty} A_{2r}^{(2n)}A_{2r+2}^{(2n)})$$

Using the solution of the integral in the numerator, we obtain for the coefficient $Y_{2n,m}$.

By defining the term in the large bracket in the denominator as $\Omega_{2n,m}$, and substituting $2h = (2\overline{\lambda})(\sinh 2\eta_\alpha)^{-1/2}$, we obtain:

$$Y_{2n,m} = \frac{4V\Delta C_o}{D}(2\overline{\lambda})\left(\frac{1}{\sqrt{q_{2n,m}}}\right)\frac{\left(A_o^{(2n)}\sum_{r=1}^{\infty} 2rA_{2r}^{(2n)} \sinh 2r\eta_\beta\right)}{(\sinh 2\eta_\alpha)^{1/2}\,\Omega_{2n,m}} \qquad \text{(A3)}$$

where $\overline{\lambda} = 2\sqrt{a_{x\alpha}a_{y\alpha}}$, in which $a_{x\alpha}$ and $a_{y\alpha}$ are the semi-axes of the outer ellipse, and the function $\Omega_{2n,m}$ is given by [22]:

$$\Omega_{2n,m} = \sum_{r=1}^{\infty} A_{2r}^2 ((\xi + 4r^2 - 2q_{2n,m}\Theta_{2n,m}) \frac{\sinh 4r\eta_\alpha}{2r} +$$

$$+ 4\left(\sum_{r_i=0}^{\infty} \sum_{r_j=r_i+1}^{\infty} A_{2ri} A_{2rj} ((\xi + 4r_i r_j - 2q_{2n,m}\Theta_{2n,m}) \frac{\sinh 2(r_i + r_j)\eta_\alpha}{2(r_i + r_j)} + (\xi - 4r_i r_j - 2q_{2n,m}\Theta_{2n,m}) \frac{\sinh 2(r_j - r_i)\eta_\alpha}{2(r_j - r_i)}) \right)$$

The values of the coefficients are obtained from the recursion relations for the Mathieu's functions. The procedure for the numerical calculations of the parameter $\Omega_{2n,m}$ is described by Mclachlan [22].

CHAPTER 7. CRYSTALLIZATION KINETICS IN BINARY POLYMER SYSTEMS

A manuscript to be submitted to *Macromolecules*

Jing Teng[1] and R. Trivedi[1,2,*]

Abstract

The kinetics of crystallization of PEG phase in polyethylene glycol (PEG) and 1,4-dibromobenzene (DBBZ) binary alloys have been investigated as a function of the alloy composition by directional growth technique. A regime II/III transition can be observed and it shifts to higher velocity as the composition of DBBZ increases while the nucleation parameter K_g's remains constant in each regime. The PEG growth rate first decreases and then increases with the increasing in DBBZ composition, which can be explained by the interplay between the dilution effect as well as increased secondary nucleation energy barrier and the increase in the mobility. In addition, a comparison is made between the directional and the undercooled growth of PEG, which indicates that the driving force (i.e., undercooling) is over-estimated in an undercooled growth process.

1. Introduction

The growth kinetics of polymer bulk crystallization has been extensively studied in

---

[1]Dept. Materials Science and Engineering, Iowa State University, Ames, IA, 50011, U.S.A.

[2]Materials and Engineering Physics Program, Ames Laboratory-USDOE, Iowa State University, Ames, IA, 50011, U.S.A.

*Corresponding author: e-mail: trivedi@ameslab.gov, phone: (515) 294-5869, fax: (515) 294-4291.

the past decades and has been compared with the secondary nucleation theory [1-6]. This theory was developed by Hoffman and co-workers [7-10], who extended the classical nucleation theory by Turnbull and Fischer [11] to polymer crystallization process. Since a polymer chain can be very long and can assume complex conformations, the growth of a polymer crystal is effected by the nucleation of a new layer and subsequent spreading: the strand with a critical length and appropriate orientation is first attached to a preexisting crystalline lamellar structure (substrate) and subsequent strands are deposited by folding the chain containing the first strand. Depending on the relative magnitude of the secondary nucleation rate (i) and the spreading rate (g), three regimes have been proposed to account for the polymer crystallization process from its melt.

Regime I: $i/g \ll 1$, i.e., the rate of secondary nucleation is very low and is the rate controlling step for growth process. In this regime, each layer is complete before the next one nucleates This holds true at small undercoolings.

Regime II: $i/g \sim 1$, i.e., the secondary nucleation rate is relatively high and there are multiple nucleations at the crystal growth front. Multiple nucleation events in the single growth layer reduces the space for a nucleus to grow laterally. This regime occurs at higher undercoolings than Regime I[8,12].

Regime III: $i/g > 1$, i.e., at even higher undercoolings, the rate of secondary nucleation becomes much greater, and the nucleation occurs at multiple crystal planes to facilitate a faster crystal growth. In this case, a secondary nucleus does not spread much beyond the dimensions of the nucleus.

The growth rate in different regimes can be expressed as:

$$G = G_0 \exp[-U^* / R(T - T_\infty)] \exp[-K_g / T(\Delta T) f] \qquad (1)$$

where K_g is a nucleation parameter which is defined as:

$$K_g = Z b_0 \sigma \sigma_e T_m^0 / k \Delta h_f \qquad (2)$$

where Z equals 4 for growth regime I and III and 2 for regime II, b_0 is the crystal monomolecular layer thickness in the growth direction. σ and σ_e are the lateral and fold-surface free energies, respectively. T_m^0 is the equilibrium melting point and Δh_f is the crystal heat of fusion. The meanings of other parameters in above LH equation are as follows. G_0 is a pre-exponent factor containing all the quantities that not highly dependent on temperature, T is the crystallization temperature, U^* is the activation energy of transport of polymer chains segment across the melt/crystal interface and T_∞ is a theoretical temperature at which all motion associated with viscous flow stops and is related to the glass transition temperature of the polymer. ΔT is the degree of undercooling $(T_m^0 - T)$ and $f = 2T_c / (T_m^0 + T)$, which is a correction factor for temperature dependence of heat of fusion.

From equation (1), we can see that for homopolymer bulk crystallization, the growth rate G is governed by two quantities, the mobility term $\exp[-U^* / R(T - T_\infty)]$ and the secondary nucleation term $\exp[-K_g / T(\Delta T) f]$. Experiments in pure polymers, such as isotactic polystylene [1], polyethylene [2,4], isotactic polypropylene [3], poly(3-hydroxybutyrate) [5] and poly(ethylene oxide) [6], confirmed the existence of different growth regimes and agreed with the theory with the appropriate selection of the values of different parameters in eq. 1.

For polymer alloys, the addition of second component (i.e., solute) B to the solvent

A will make the crystallization process more complicated. This second component may be crystalline or non-crystalline, may be a polymer or a small molecule and may be a polymer of different structures or the same homopolymer but with different molecular weight. The effects of the solute on the crystallization kinetics of A may come from several aspects: (1) the concentration of the crystallizable component A at the growth front is decreased by an amount proportional to its volume fraction so that the kinetics of crystallization is reduced by this dilution effect. (2) For crystallization to proceed, the second component B must diffuse away from the growth front or the molecules of A must diffuse to the growth interface. This may involve a long-range diffusion process, which is different from the short-range diffusion, eg, the $G_o \exp[-U^* / R(T - T_\infty)]$ term in LH equation. (3) The transport term associated with the solid-liquid interface may be altered because of the change of T_g and thus the temperature range over which crystallization can occur is changed. (4) Most importantly, there exists the thermodynamic interaction between the A and B molecules, which may change the free energy barrier for the formation of nuclei on the crystal surface. Therefore the secondary nucleation theory has to be modified to include these aspects in order to account for the growth kinetics for alloyed polymers [13-17].

The crystallization kinetics in miscible blends has been experimentally studied, but most of the investigations focus on the mixtures of crystalline/non-crystalline polymers [18-25]. Generally, the crystallization rate is reduced by mixing with a non-crystalline polymer because of the dilution of the crystallizable component at the growth front and the reduction in chain mobility due to an increase of glass transition temperature (T_g) of the blends. For the miscible polymer blends composed of two crystalline polymers, only a few

studies with regard to the crystallization behavior are reported, such as poly(oxymethylene diacetate) / polyoxyethylene system [26], poly(butylenes terephthalate) / polyarylates based on bisphenol A isophthalate system(PBT/Par(I-100)) [27], Nylon 66 / Nylon 48 system [28] and Poly(3-hydroxybutyrate)/ poly (ethylene oxide) (low molecular weight) system [29]. The results are quite different on the effect of solute on the growth rate of a polymer crystal: the solute may enhance or retard the polymer crystal growth depending on the different system studied. Besides, there is no indepth discussion about the physical reason of these different effect.

Two different techniques have been widely used to examine the polymer growth kinetics for the experimental studies of the crystallization kinetics of polymers. Researchers either use DSC to study the non-isothermal growth process [30] or employ the undercooled growth to investigate the isothermal growth process. DSC can only provide useful data on the overall kinetics of crystallization (i.e., Avrami kinetics), but it cannot offer the critical information such as nucleation undercooling and in-situ growth velocity since the nucleation and growth process are entangled and are continuously changing. For undercooled growth, the nucleation and subsequent growth of a spherulite crystal may be studied separately [31]. The polymer crystal growth process is usually monitored under an optical microscope with polarized illumination, the growth velocity is calculated by measuring the crystal size as a function of time and the steady state growth rate is then correlated with the *bath undercooling* in order to determine the growth kinetics and to disclose the growth mechanism.

However, the relevant temperature and undercooling in Eq. 1 should be the values right at the growth interface, rather than the bath temperature and bath undercooling [32]. At

small undercoolings, the difference between the interface temperature and the bath temperature may be negligible; nonetheless at relatively high undercoolings, the interface temperature can be higher than the bath temperature, which may pose a serious problem if the bath temperature is used to evaluate the growth kinetics.

Another obvious drawback about the study crystallization kinetics of polymer alloys is the lack of phase diagram. Due to the sluggish crystallization kinetics of a polymeric alloy, it is rather time-consuming to accurately determine the equilibrium phase diagram experimentally. However, a phase diagram is always essential since it is the graphic representation of the thermodynamics of a system and lots of information can be obtained from phase diagram which will be very helpful to understand the solidified microstructure and evaluate the crystallization kinetics. For example, the melting temperature of an alloy is different from that of a pure solvent, and the former should be used to calculate the driving force for the crystallization of the alloy; however in literatures, the melting temperature of a pure solvent is frequently used to analyze the crystallization kinetics of a polymer blend.

The key objective of the present study is to investigate the effect of solute composition on the crystal growth kinetics of a solvent polymer. We selected poly(ethylene glycol)PEG/p-dibromobenzene (DBBZ) alloy system where PEG is the solvent and DBBZ is the solute. It has been shown [33-34] that both components are crystallizable and that PEG and DBBZ can form an intercalcate complex, which contains ~61.7wt% DBBZ. We have accurately determined the phase diagram for the composition range [0, 61.7] wt% DBBZ, within which PEG and the intercalate complex form a simple eutectic system [33], so that we can focus on the growth kinetics study in hypo-eutectic region, because in this region PEG is the primary phase crystallized from the melt first. On the other hand, we have employed the

directional growth technique to study the growth kinetics of polymer and polymer alloys. Since the growth is unidirectional, it is convenient to reach a steady state and to measure the interface temperature in situ with an embedded thermocouple. Therefore the growth rate can be directly correlated with the interface temperature and there will be no ambiguity in analyzing and interpreting the growth data.

2. Experimental

2.1. Materials

PEG (white powder, Molecular Biology Grade, Mw = 8000) and DBBZ (white crystal) were purchased from Fisher and Aldrich respectively and they were used as received. The polydispersity (PDI) of PEG was 1.035 which was obtained by GPC. The relevant properties of the materials are summarized in Table 1.

2.2. Alloy and DSC sample preparation

All the alloys were prepared by heating to 150°C under high purity nitrogen and were kept at that temperature 1hr for homogenization after the alloy was fully dissolved. 11 compositions were chosen for DSC measurements of both eutectic and liquidus temperature. They are: PEG-0, 1.2, 2.0, 3.0, 4.0, 5.0, 10.0, 25.0, 30.0, 44.6 and 61.7wt% DBBZ. Several heating rates, 1.0, 2.0, 5.0 and 10.0°C/min with the same cooling rate 2.0°C/min, were used in DSC measurements and extrapolated temperatures at 0°C/min are used to construct phase diagram. A special type of DSC aluminum pan for volatile material was used to avoid the sublimation of DBBZ. Each DSC sample weighed around 10 mg. DSC measurements were carried out under nitrogen atmosphere by a Perkin-Elmer Analysis 7 system.

Table 1. Molecular characteristics and crystallographic data			
	PEG	p-DBBZ	PEG-DBBZ compound
Chemical Structure	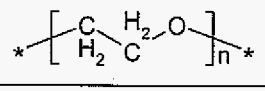	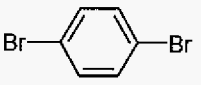	$[(-CH_2-CH_2-O)_{10} \supset (p-C_6H_4Br_2)_3]_n$
Molecular weight	8000 (PDI=1.035)	235.92	
Melting temperature (°C)	64.0	87.0	96.0
Crystal system	monoclinic	monoclinic	orthorhombic
Lattice parameters	7.95Å, 13.11Å, 19.39Å 124.6°	15.36Å, 5.75Å,4.10Å 112.5°	16.74Å, 9.68Å, 27.98Å
Chain conformation	$H_{7/2}$		$H_{10/3}$
Density (g/cm^3)	1.23		1.681

2.3. Shear viscosity measurement

The shear viscosities were measured on a cone-plate viscometer cap2000 in order to calculate the activation energy E_a by the equation $\eta=\eta_0 \exp(E/RT)$ for pure PEG and alloy. For each composition, measurements were performed at 4 different temperatures. Since molten polymers are non-Newtonian and the viscosities decrease as the shear rate increases, so that 3 different shear rates were used at each temperature, then extropolated to get zero-shear viscosity at each temperature.

2.4. Directional crystallization experiments and interface temperature measurement

The experimental setup fo directional crystallization study is shown in Figure 1. It

consists of three major parts: the temperature part including the hot and cold block and their controls, which establisheds a temperature gradient in the sample; the translation part which moves the sample back and forth for melting and solidification at a precisely controlled rate V_p and the optical imaging part including the light source, lens, a camera and an imaging recording system. The experimental material is sealed in a rectangular glass tubing with the cross-section 0.2 (thickness) × 4.0 (width) × 300 mm (length). A ϕ50 μm K-type thermocouple was inserted in the sample cell and was connected to a temperature recording system to measure interface temperature when the growth interface reached the thermocouple tip.

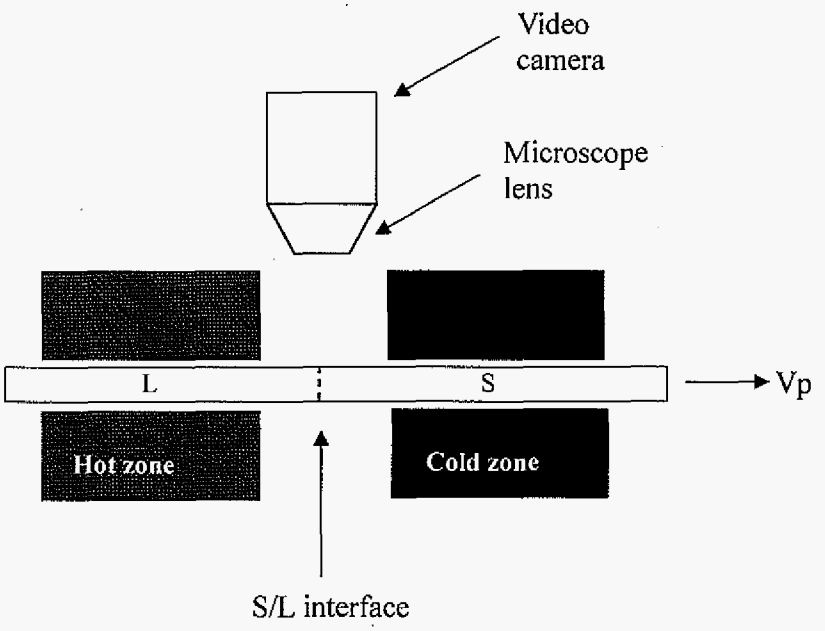

Figure 1. Schematic of a directional crystallization setup.

3. Experimental Results

We start with the determination of PEG-DBBZ phase diagram followed by the study on the growth kinetics on pure PEG and hypo-eutectic alloys.

3.1. Phase diagram determination

Figure 2 shows the DSC heating curves for 7 compositions. The ordinates for different compositions are intentionally shifted by some amount so as to avoid the overlap. For pure PEG, there are two overlapping peaks, which are for the melting of PEG crystals folded once and fully extended respectively. The fully extended conformation has a slightly higher peak temperature; therefore its peak temperature is taken as the equilibrium temperature for phase diagram construction. With addition of solute up to 5.0wt% DBBZ, we can see that the position of this peak is shifted to a lower temperature. The peak temperature reached the lowest value for the alloy of 5.0 wt% DBBZ. Then, as the DBBZ compositions increased (10.0 wt % DBBZ curve on the figure), a second peak was just visible at 69.45°C, which was believed to be the melting peak of the other primary phase melting peak. This peak became more evident and the peak position shifted to higher temperature with a more DBBZ, until the DBBZ composition reached 61.7wt%. At this composition, PEG and DBBZ form the intercalate complex, so that there was only one melting peak on the DSC heating curve. For both 10.0wt% and 30.0wt% DBBZ alloy, the first peak on the curves was at almost the same position as that for 5.0wt% DBBZ alloy, which is attributed to the eutectic melting peak.

The melting temperature that was obtained from DSC heating curve depends on the heating rate. The larger the heating rate, the higher the measured melting temperature. This

effect was basically due to the thermal lag which is intrinsic to a DSC apparatus. To correct this effect, several different heating rates were used for the same sample, so that the value extrapolated at 0°C/min can be used to construct the equilibrium phase diagram.

In order to confirm that PEG-5.0wt%DBBZ is really the eutectic alloy (Fig. 2), we used different cooling rates (2.0, 5.0 and 10.0K/min) for DSC scans and the result is shown in Fig. 3. Clearly, there is only one crystallization peak irrespective of the cooling rates. Therefore, an alloy is in the hypo-eutectic region for <5.0wt% DBBZ and the primary phase will be PEG; while it is in the hyper-eutectic region for > 5wt% DBBZ and the primary phase will be the intercalate complex.

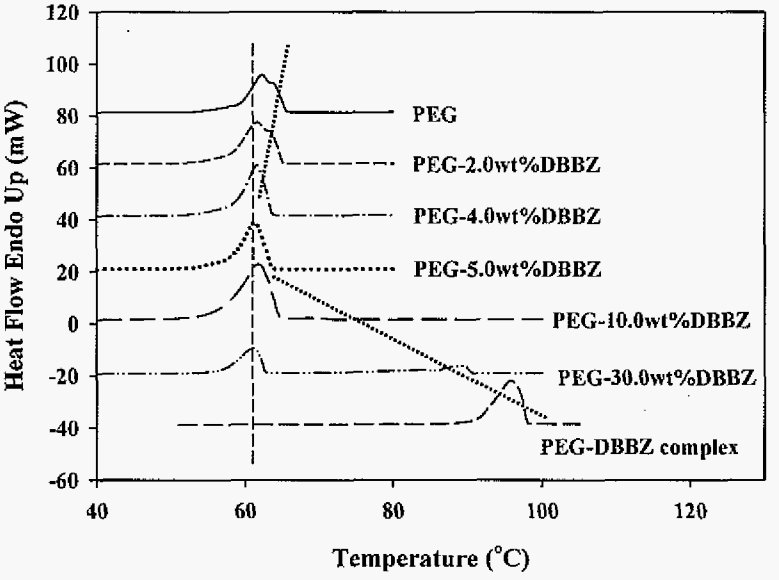

Figure 2. DSC thermographs of PEG-DBBZ alloys (heating rate: 5°C/min).

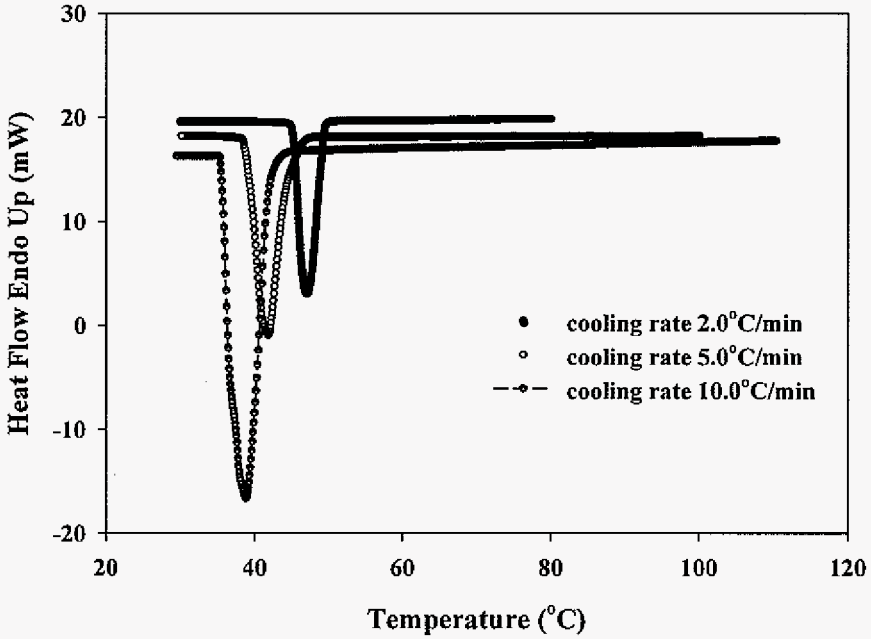

Figure 3. DSC cooling curves of PEG-5.0wt% DBBZ with different cooling rates.

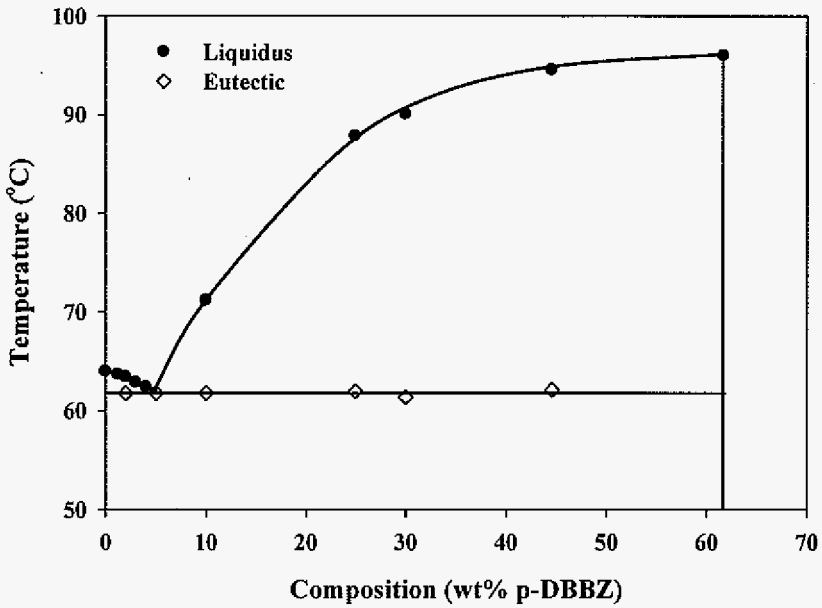

Figure 4. PEG8000–DBBZ phase diagram from DSC analysis.

The phase diagram between PEG 8000 and the intercalate complex is constructed by the extrapolated values for each composition, as shown in figure 4. The eutectic composition for our particular system is PEG-5.0wt% DBBZ, which corresponds to 8.10wt% intercalate complex, and eutectic temperature is 61.76°C.

The solidified microstructures are different for alloys in hypo- and hyper-eutectic regions since the crystalline primary phases are different. The *in situ* images for PEG-3.0wt%DBBZ and 10wt% DBBZ alloys confirmed that those two compositions belong to different regions, as shown in Fig. 5.

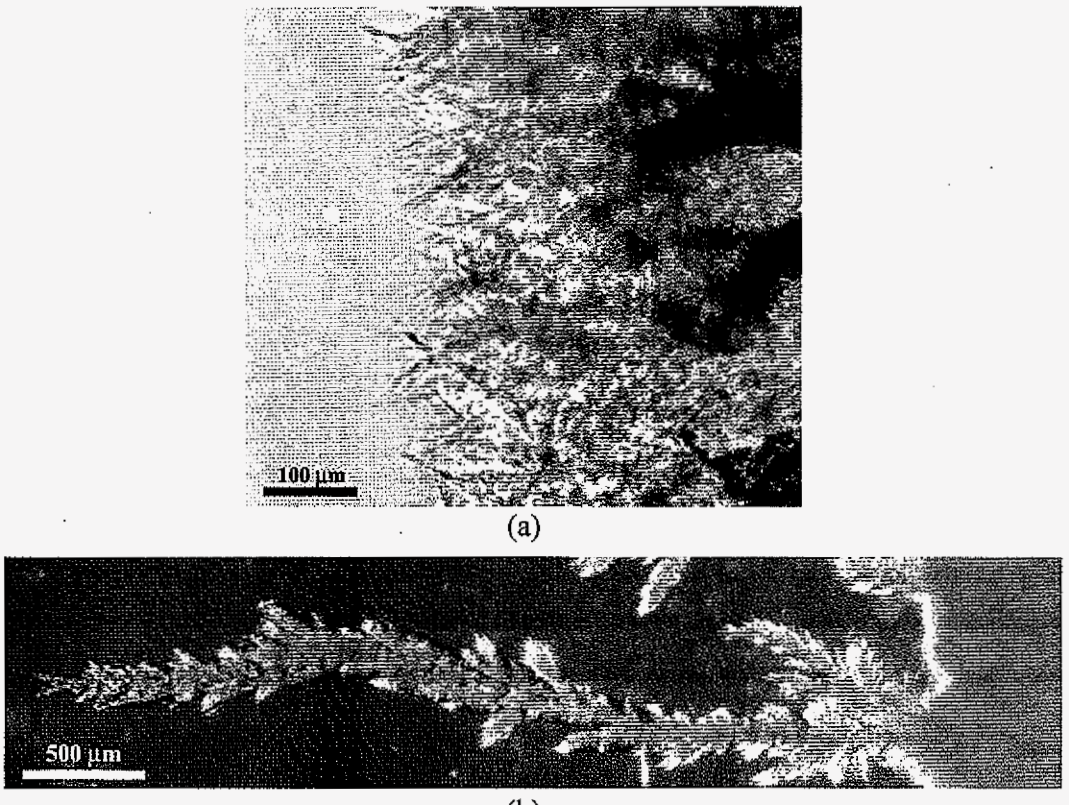

Figure 5. 2D in-situ growth images of (a) PEG-3wt% DBBZ and (b) PEG-10wt% DBBZ alloy (growth velocity = 0.25µm/s, temperature gradient = 4.5 K/mm).

3.2. Growth kinetics of pure PEG8000

Figure 6 shows the variation in the measured interface temperature of PEG 8000 with the imposed growth velocity by directional crystallization technique. The velocity varied from 0.0054 to 100.0 μm/s. The lower velocity end is limited by the translation system, while the upper velocity is limited by the multiple primary nucleation events in the liquid ahead of the growth interface, which block the directional growth and therefore no steady state can be achieved. Since we have already measured the melting point, the relationship of interface undercooling can be conveniently correlated with growth velocity, as shown in Fig. 6 (open circles). Clearly a higher growth rate requires a larger undercooling, which is in general agreement with the observations in undercooled growth.

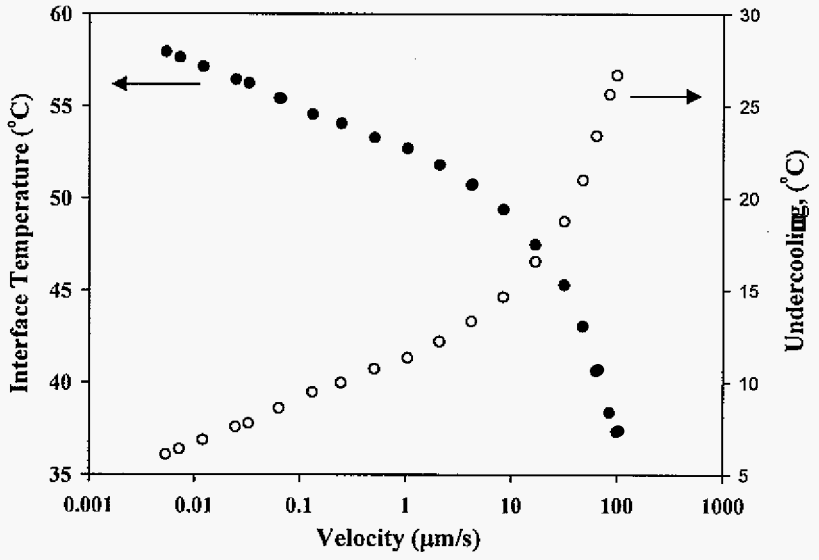

Figure 6. Variation in PEG interface temperature and undercooling with growth velocity.

In order to analyze the growth kinetics of polymer crystals, equation (1) is usually re-arranged as:

$$LnG + \frac{U^*}{R(T - T_\infty)} = LnG_0 - \frac{K_g}{T(\Delta T)f} \qquad (3)$$

Then the plot of the left-hand side of the equation (3) vs $1/T(\Delta T)f$ can provide the useful information about the value of K_g (slope) and G_0 (intercept) and this type of data presentation is usually termed as LH plot. Figure 7 shows the LH plot from our experiment data, where G and T were the input directional growth velocity and measured interface temperature. For Fig. 7, U^* = 29.3KJ/mol by Kovacs' work [35-37]. The value of T_∞ was taken, by definition, as $(T_g - 30)K$. For PEG, $T_g = 206.15K$. The equilibrium melting temperature was 337.1K, deduced from DSC measurement.

A slope change can be observed at $\Delta T \sim$ 9.5K and the ratio of the two slopes (K_g^{III} / K_g^{II}) was close to 2, indicating the transition between growth regime II and III around this undercooling. We will further discuss this in the next section and compare with reported values in PEG undercooled growth.

3.3. Effect of DBBZ content on the growth rate

From Fig. 4, we know that the eutectic composition is 5.0wt% DBBZ. At this composition, PEG and PEG-DBBZ intercalate complex crystallize from the melt together. For alloys with composition smaller than 5wt% DBBZ, PEG is the primary phase and therefore the effect of DBBZ content on the growth kinetics of PEG can be studied in this composition range. The interface temperatures were measured for some alloys in this

composition range and the results are shown in Fig. 8. With a small amount of DBBZ addition into PEG (≤2.0wt%DBBZ), a larger undercooling is needed in order to keep the same growth velocity. However if more DBBZ is added, this undercooling is decreased.

In order to see the composition effect clearly, we re-plot the variation of interface undercooling with DBBZ content for two growth velocities (Fig. 9). From Fig. 9, we can see that a maximum undercooling occurs at the composition C=1.2wt%DBBZ, i.e., in order to keep a certain growth velocity, the interface undercooling should increase with composition when C<1.2wt%DBBZ; and the undercooling should decreases with composition when C>1.2wt%DBBZ. All the other growth rates show the similar results in the low velocity range. At high velocities, all curves fall into PEG curve, which may due to solute trapping.

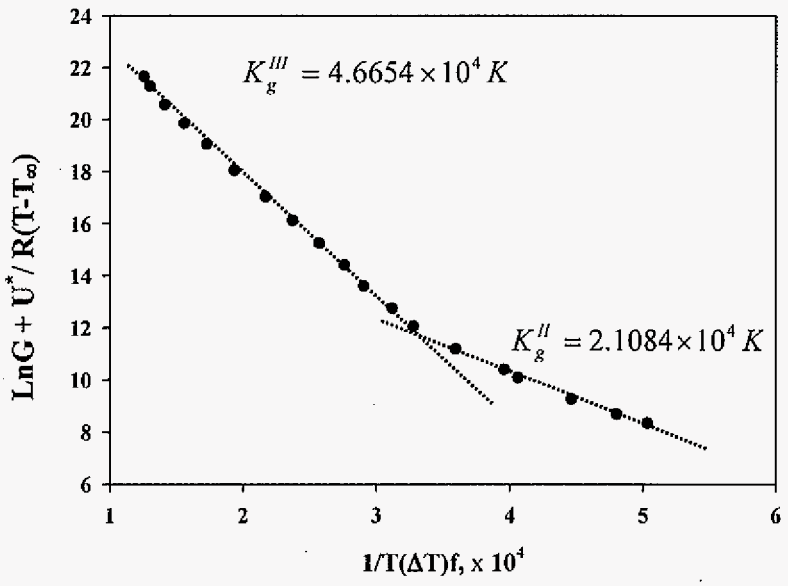

Figure 7. LH plot for PEG8000 directionally crystallized from the melt. G is in cm^3/s. The slope of the curve fitting gave the nucleation parameter K_g.

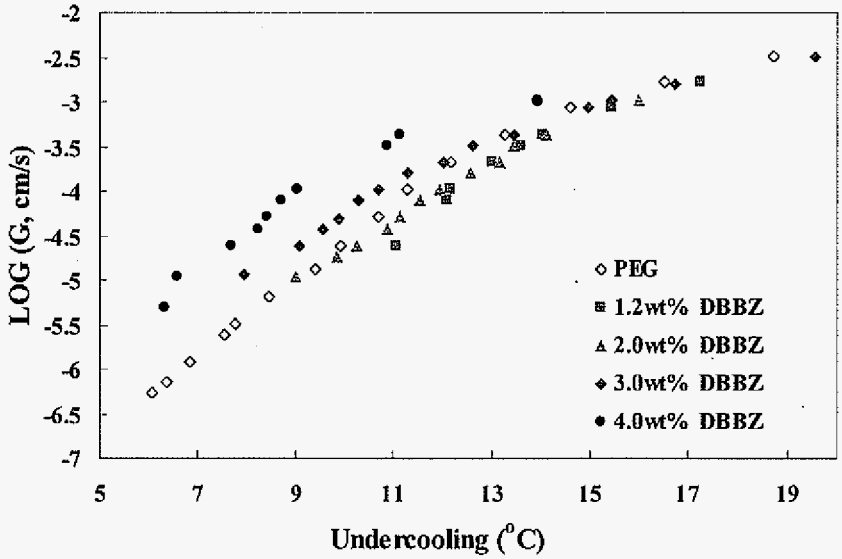

Figure 8. Dependence of growth velocity on undercooling for PEG and PEG-DBBZ hypo-eutectic alloys.

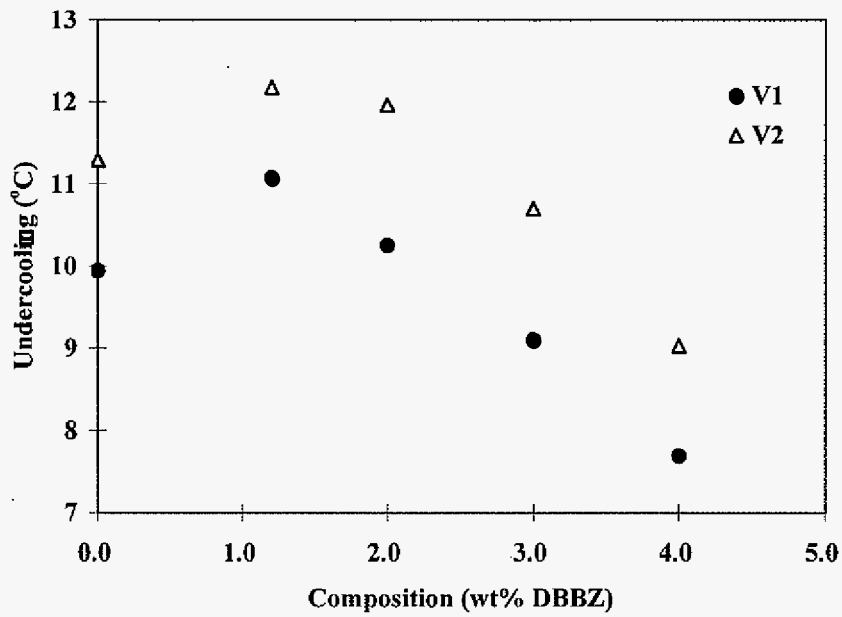

Figure 9. Effect of alloy composition on interface undercooling for growth velocities V_1=0.25 μm/s and V_2=1.05 μm/s.

4. Discussions

4.1. Quantitative comparison of PEG directional growth with undercooled growth

As mentioned previously, Kovacs *et al* [35-37] have presented a systematic study on the growth kinetics of PEO crystallized from the undercooled melt for PEO fractions in the low molecular mass range. We compare our present results with those by Kovacs et al. [35] for the same molecular weight (Fig. 10(a)). Because of the equipment limitation, the data for very small growth rates are not attainable in the present study. One can see that the data obtained in the directional growth and the undercooled growth follow the same trend; however, at high undercoolings, some differences do exist. The growth rate in a directional crystallization process is slightly larger than that in an undercooled growth process for the same undercooling.

As suggested by Cahn [32], in order to accurately disclose the growth mechanism, the growth rate V should be corrected to include the change of the self-diffusion coefficient (or viscosity) with temperature. The corrected velocity is $G(T)D(T_m^0)/D(T)$ or $G(T)\eta(T)/\eta(T_m^0)$, where D is the self-diffusion coefficient, η is the viscosity, T_m^0 and T are the melting temperature and interface temperature resepctively. This correction may be more important in polymers because the long chains of polymer molecules are in random coil comformation, therefore the viscosities of polymer melts are pretty large which makes the self-diffusion coefficient of polymers pretty small (usually 4-6 orders of magnitude samller than metal) and strongly dependant on temperature. The self-diffusion coefficient changes with temperature according to: $D(T) = D_\infty \exp\{-E_a/(kT)\}$. For PEG 8000, the activation energy E_a for self-diffusion was reported to be 26570J/mol [38]. In the present study, the activation energy

by the shear viscosity measurement is 27015.47 J/mol, which is in good agreement with literature data.

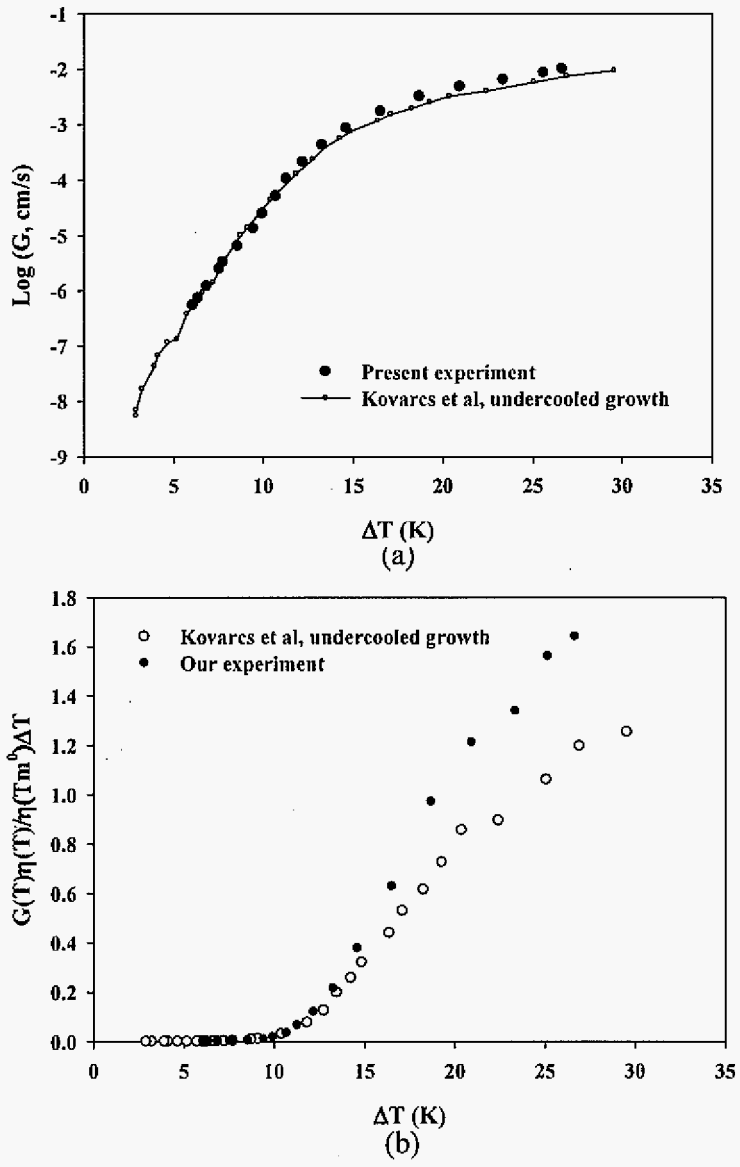

Figure 10. A comparison between undercooled and directional growth data of before and after corrected the temperature dependence of diffusivity.

We present the change in the corrected growth rate $G(T)\eta(T)/(\eta(T_m^0)\Delta T)$ with ΔT in Fig.10(b). The difference between the directional growth and the undercooled growth becomes rather clear at high undercoolings: the undercoolings obtained from the present study are consistently smaller than those for undercooled growth by Kovarcs et al. for a fixed growth velocity. We believe that in this region, the undercooling for crystal growth is overestimated in the undercooled growth since the growth rate is high, the latent heat generated at the interface can raise the temperature near the interface, therefore the actual undercooling available for growth of solid/liquid interface is less than the bath undercooling. This clearly shows the significance of the interface temperature and it should be directly measured if possible. Moreover the secondary nucleation theory of polymer crystallization considers the interface undercooling and interface temperature, rather than the bulk undercooling and bulk temperature. In the low velocity region, the two methods give the same results, indicating that heat flow does not pose any problem in the evaluation of the growth kinetics.

4.2. Growth kinetics and growth regime transition in pure PEG

Before we discuss the effect of solute addition on the kinetics of PEG crystal growth, we would like to present the baseline data for the growth kinetics and the regime transition in pure PEG case first. Figure 7 shows that there is a regime transition at $\Delta T = 9.5K$ below which the growth is in regime II and above which the growth is in regime III. In regime II, $K_g^{II} = 2.1084 \times 10^4\ K^2$ and in regime III, $K_g^{III} = 4.6654 \times 10^4\ K^2$.

According to the secondary nucleation theory (eq. 1) [7-10, 12], the relative ratio of i/g determines which growth regime it will belong to at various growth rates (or

undercoolings): i and g can be approximately expressed as:

$$\begin{aligned} i &\propto \beta \exp(-K_g /(T \cdot \Delta T \cdot f)) \\ g &\propto \beta \end{aligned} \tag{6}$$

so we have:

$$i / g \sim \exp(-K_g /(T \cdot \Delta T \cdot f)) \tag{7}$$

In above equations, the undercooling ΔT is temperature difference between the melting temperature and interface temperature during crystal growth. Since decrease in interface temperature T will increase the interface undercooling ΔT, the product T· ΔT has a maximum value at $T_m/2$ point, as shown in Fig. 11. The shaded region in Fig. 11 is the undercooling range obtained in our experiments, so T· ΔT increases as the increase of ΔT.

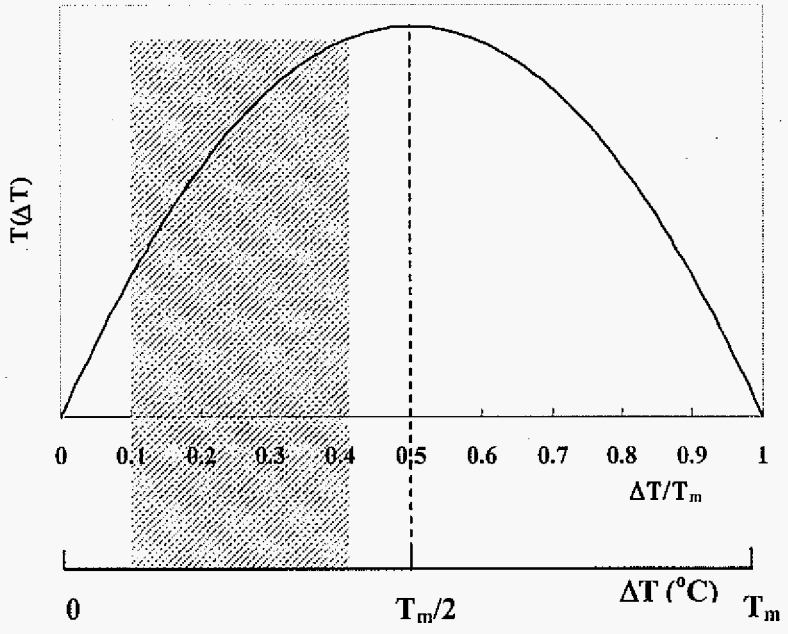

Figure 11. Variation in TΔT term with ΔT.

The correction factor f is always a number very close to 1, the change of f value with undercooling can be omitted for simplicity. Thus, in the range of present data, i/g will keep increasing with ΔT within each regime.

From PEG growth data, we already knew that the regime transition point is around ΔT = 9.5K, thus, we may set $(i/g)\big|_{\Delta T=9.5k} \sim 1$. For an undercooling larger than 9.5 K, the ratio of $(i/g)\big|_{\Delta T}$:

$$(i/g)_{\Delta T} = A\exp(-K_g/T(\Delta T)f)\big|_{\Delta T} > A\exp(-K_g/T(\Delta T)f)\big|_{9.5K}, \text{ so:}$$

when ΔT > 9.5k, $(i/g)_{\Delta T} > 1$, thus the crystal growth enters into regime III.

4.3. The growth kinetics of PEG in PEG-DBBZ hypo-eutectic alloys

As we haved mentioned earlier, the additon of solute DBBZ siginifcantly change the growth kinetics of PEG crystals in different aspects. The dilution effect has been considerd by directly multiplying the volume fraction of the solvent component in eq. (1) [39]. Boon and Azcue[15] included the effect of mixing entropy on the nucleation energy barrier for forming a two-dimensional critical nucleus. The growth rate is given by:

$$G = \phi_1 G_{0(a)} \exp(-\frac{U^*}{R(T-T_\infty)})\exp(-\frac{K_{g(a)}}{T(\Delta T)f} + \frac{2\sigma T^0_{m(a)} Ln\phi_1}{b\Delta h_{f(a)}(\Delta T)f}) \quad (4)$$

where ϕ_1 is the volume fraction of PEG phase and the subscript (a) means "alloy". Since by empirical ralation, for PEG $\sigma \approx 0.1b(\Delta h_f)$ [40], the above equation can be rearranged as:

$$G = \phi_1 G_{0(a)} \exp(-\frac{U^*}{R(T-T_\infty)})\exp(-\frac{K_{g(a)}}{T(\Delta T)f} + \frac{0.2T^0_{m(a)} Ln\phi_1}{(\Delta T)f}) \quad (5)$$

$$LnG + \frac{U^*}{R(T-T_\infty)} - Ln\phi_i - \frac{0.2T^0_{m(a)}Ln\phi_i}{(\Delta T)f} = LnG_{0(b)} - \frac{K_{g(a)}}{T(\Delta T)f} \qquad (5')$$

The plots of the left-side terms in equation (5') vs. $1/T(\Delta T)f$ can be drawn for hypo-eutectic alloys, as shown in Fig. 12. Since the actual interface temperature is much lower than the liquidus temperature $T^0_{m(a)}$, we use local liquid composition at the growth interface to calculate ϕ_i. The local concentration is obtained through the phase diagram since the measured interface temperature has been directly measured in the growth process for each alloy. We use the same values of U^* and T_g as in pure PEG case, since K_g , not like G_0, is not sensitive to their values if the growth is in the region near T^0_m [7, 18, 20,41].

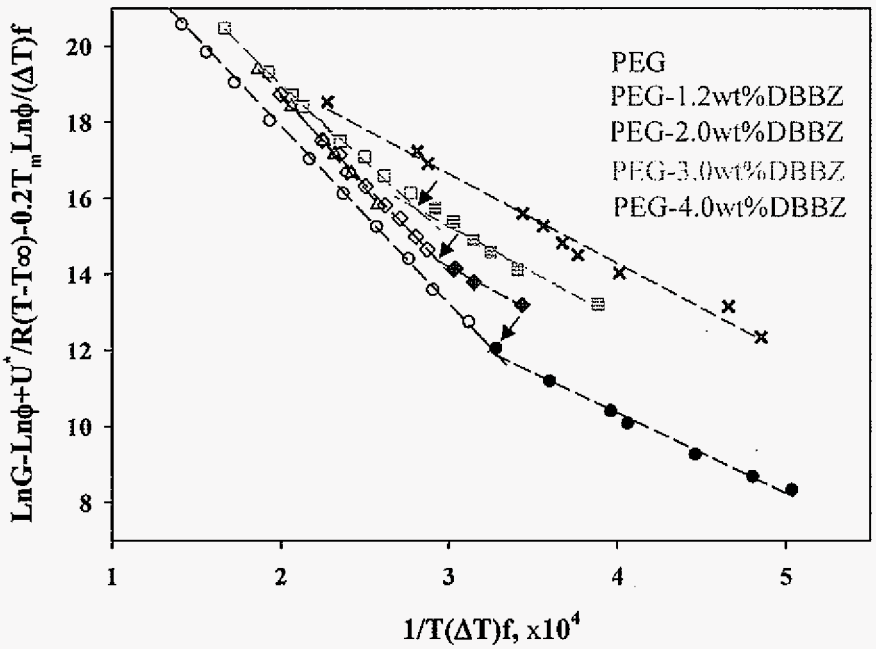

Figure 12. LH plots for pure PEG and PEG-DBBZ hypo-eutectic alloys.

Three significant observations can be made from Fig. 12: (1) it is apparent that for alloy crystallization, the transition points from growth regime II to III, which are marked as blue arrows, are systematically shifted to a higher growth rate (*e.g.*, higher undercooling) with the increase in DBBZ concentration, that is, the higher the alloy composition, the higher the growth rate needed to reach the regime transition point. (2) In each regime, the value of K_g is independent of the alloy composition (Table 3) and thus the same as that for PEG within the experimental error. (3) The G_o term increases with the alloy composition (Table 2).

Table 2. Derived values of K_g^{II}, K_g^{III} and G_o in hypo-eutectic alloys

Composition wt% DBBZ	Regime II		Regime III	
	K_g x10^{-4}, K^2	G_0 x10^9, cm/s	K_g x10^{-4}, K^2	G_0 x10^9, cm/s
0	2.018	0.343	4.665	625
1.2			4.957	1200
2	2.336	1.49	4.588	1380
3	2.454	4.25	4.331	1910
4	2.356	17.3		
In our growth rate range, alloy of 1.2wt% stays only in regime III, while 4.0wt% is in regime II only.				

The above observations are again closely related with the variation of secondary nucleation rate (i) and the lateral spreading rate of a nucleus (g) with the addition of solute molecules. For the alloy growth, the nucleation rate changes to $i \propto \beta \exp\left(-\frac{K_g}{T(\Delta T)f} + \frac{0.2T^0_{m(a)} Ln\phi_1}{(\Delta T)f}\right)$ as in equation (5), so that i/g can be expressed as:

$$(i/g)_{alloy} \sim \exp(-K_g / T(\Delta T)f + 0.2T_{m(a)} Ln\phi_t /(\Delta T)f) \qquad (10)$$

At ΔT =9.5K,

$$(i/g)\big|_{9.5K} \sim \exp(\frac{-K_g}{9.5*(T^0_{m(a)}-9.5)*f})\exp(\frac{0.2T^0_{m(a)}Ln\phi_1\big|_{(T^0_{m(a)}-9.5K)}}{9.5*f})$$

ϕ is volume fraction of PEG phase at growth interface. Since $Ln\phi_1\big|_{(T^0_{m(a)}-9.5K)} < 0$

$$(i/g)\big|_{\Delta T=9.5K} \sim \exp(\frac{-K_g}{9.5*(T^0_{m(a)}-9.5)*f})\exp(\frac{0.2T^0_{m(a)}Ln\phi_1\big|_{(T^0_{m(a)}-9.5K)}}{9.5*f}) < 1$$

Thus, for PEG crystal growth in an alloy sample, the growth still remained in regime II for ΔT =9.5K; while for pure PEG, it is the regime II/III transition point. Only with an increase in undercooling can $(i/g)_{alloy}$ approach 1, therefore, the regime transition II/III is shifted to a higher undercooling in PEG-DBBZ hypo-eutectic alloys. Clearly this shift is caused by the increased energy barrier for secondary nucleation due to the entropic contribution by adding in solute. The higher the solute composition, the larger energy barrier for secondary nucleation, and the more undercooling needed. Therefore the growth regime transition point keeps shifting to a higher growth rate (higher undercooling) with more DBBZ addition.

The crystal growth rate also depends on mobility term (β). For pure materials, the mobility is directly related with the self-diffusion coefficient, while for alloys, it is related with the mutual diffusion coefficient. The intercalate complex formed by PEG and DBBZ has a higher mobility and larger self-diffusion coefficient, since it has a much higher growth rate at the same undercooling (Fig. 13), therefore the mutual diffusion coefficient in an alloy sample should be higher than the self-diffusion coefficient of pure PEG. A higher mutual diffusion coefficient implies that PEG chains in an alloy are more flexible and PEG molecules have a higher mobility in comparison with those in a pure PEG sample at the same temperature, which leads to a higher growth rate and a higher G_o term.

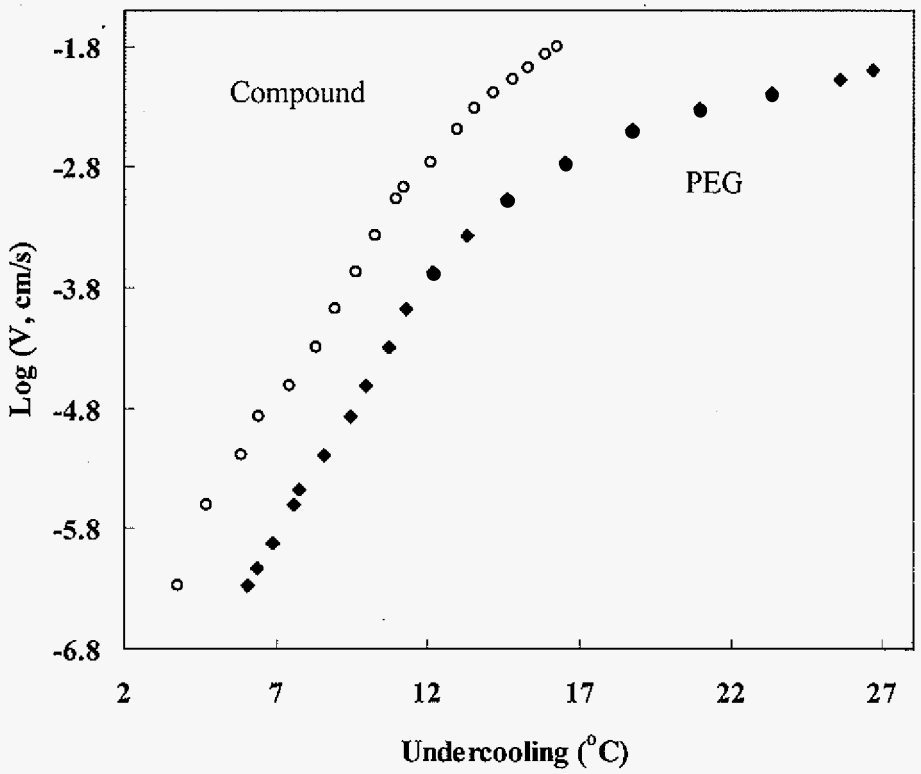

Figure 13. Comparison of the growth velocity of pure PEG with the intercalate compound.

Even in the alloy case, the value of K_g in each regime does not depend on the alloy composition (Table 2 and Fig. 12). This may be related with the fact that the crystallization material is PEG whether the sample is pure or alloyed. The solute molecules are pushed to the liquid in front of the growth interface, therefore the values of σ and σ_e may remain the same. Moreover, in the composition range of present study, the depression of the equilibrium melting temperature is less than 2°C, and the heat of fusion does not show significant change from our DSC measurement. The values of all the parameters in K_g either remain the same or

change only by a very small fraction, so we conclude that the nucleation parameter is independent of the alloy composition in the present study.

Now, we can explain the appearance of a maximum undercooling at the composition C=1.2wt%DBBZ in figure 9. When DBBZ adding into PEG melt, there were two molecular species at the growing interface, PEG and PEG-DBBZ intercalate complex. The mixing of PEG and complex increased the secondary nucleation barrier of the alloy, which will decrease the secondary nucleation rate. On the other hand, the mixing increased chain mobility, which will enhance the secondary nucleation rate and surface spreading rate. Thus, the interplay between the dilution effect as well as increased secondary nucleation energy barrier and the increase in the mobility produce a maximun value of uncercooling curve with concentration.When the composition is <1.2wt% DBBZ, the dilution effect and increased secondary nucleation energy barrier dominates, while when composition >1.2wt% DBBZ, the enhancement in species mobility dominates.

5. Conclusion

The directional crystallization technique was firstly employed to study the crystal growth kinetics of polymeric materials. The obvious advantage of this technique is that the growing interface temperature can be measured directly and accurately and that the steady-state growth is guaranteed. We chose PEG-DBBZ system for the experimental study. The phase diagram is carefully determined by DSC and we find that PEG and PEG-DBBZ intercalate complex constitute a simple binary eutectic system with the eutectic composition at 5.0wt%DBBZ and the eutectic temperature at 61.76°C. The detailed growth kinetics study of pure PEG indicates that there is a regime II/III transition at undercooling ~ 9.5K and that

the growth kinetics can be understood through the secondary nucleation theory. A comparison with the undercooled growth of PEG shows a clear difference at high growth velocities (8.5 μm/s), indicating that interface temperature of the undercooled growth is different from the bath temperature and therefore the driving force (i.e., undercooling) is over-estimated in a undercooled growth process.

The addition of DBBZ into PEG melt shifts the transition from regime II to regime III to a higher velocity, but the nucleation parameter K_g's does not change in each regime since the crystallizing material is still pure PEG. Increase in DBBZ composition first decreases (PEG-1.2 and 2.0wt% DBBZ), and then increases (PEG-3.0 and 4.0 wt% DBBZ) the PEG growth rate. Its occurrence can be explained by the interplay between the dilution effect as well as increased secondary nucleation energy barrier and the increase in the mobility.

Acknowledgement

A part of this work was carried out at Ames Laboratory under Contract No. DE-AC02-07CH11358 with the U.S. Department of Energy. A part of this study was also supported by the Office of Microgravity Sciences, NASA, under grant # NAG8-1681.

Reference

[1] Suzuki, Tadao and Kovacs, Andre J., Polymer Journal (Tokyo, Japan), 1(1), 82-100, 1970.

[2] Hoffman, John D., Frolen, Lois J., Ross, Gaylon S., and Lauritzen, John I., Jr. Journal of Research of the National Bureau of Standards, Section A: Physics and Chemistry, 79A(6), 671-699, 1975.

[3] Jiannong Xu, Srivatsan Srinivas, Hervé Marand, and Pawan Agarwal, Macromolecules, vol(31), 8230-8242, 1998.

[4] Lambert, W. Scott and Phillips, Paul J., Macromolecules, vol(27), 3537-3542, 1994.

[5] Barham, P. J., Keller, A., Otun, E. L. and Holmes, P. A., Journal of Materials Science, 19(9),2781-2794, 1984.

[6] Cheng, Stephen Z. D.; Chen, Jianhua; Janimak, James J., Polymer, vol(31), 1018-1024, 1990.

[7] J. D. Hoffman, G. T. Davis, and J. I. Lautitzen Jr., in Treatise on Solid State Chemistry, vol(3), Chapter 7, Crystalline and Noncrystalline Solids, N. B. Hannay ed., Plenum, New York, 1976.

[8] J. D. Hoffman, Polymer, vol(23), 656-670, 1982.

[9] J. D. Hoffman, C. M. Guttman, and E. A. Dimarzio, Faraday Discussions of the Royal Society of Chemistry, vol(68), 177-197, 1979.

[10] J. D. Hoffman, Polymer, vol(24), 3-26, 1983.

[11] D. Turnbull and J. C. Fisher, Journal of Chemical Physics, vol(17), no.1, 71-73, 1949.

[12] Hoffman, John D.; Frolen, Lois J.; Ross, Gaylon S.; Lauritzen, John I., Jr. Journal of Research of the National Bureau of Standards, Section A: Physics and Chemistry, 79A(6), 671-699, 1975.

[13] T. T. Wang and T. Nishi, Macromolecules, vol(10), 421-425, 1977.

[14] T. S. Chow, Macromolecules, vol(23), 333-337, 1990.

[15] J. Boon and J. M. Azcue, Journal of Polymer Science, Part A-2, vol(6), 885-894, 1968.

[16] G. C. Alfonso and T. P. Russell, Macromolecules, vol(19), 1143-1152,1986.

[17] Hiromu Saito, Tetsuo Okada, Toshihiko Hamane and Takasshi Inoue, Macromolecules, vol(24), 4446-4449, 1991.

[18] E El Shafee, Polymer International, 53, 249-253, 2004.

[19] Shiao-Wei Kuo, Wu-Jang Huang, Chih-Feng Huang, Shih-Chi Chan and Feng-Chih Chang, Macromolecules, vol(37), 4164-4173, 2004.

[20] Sossio Cimmino, Ezio Martuscelli and Clara Silvestre, Journal of Polymer Science, Part B: Polymer Physics, vol(27), 1781-1794, 1989.

[21] Hsin-Lung Chen and Roger S. Porter, Journal of Polymer Research, vol(6), no.1, 21-26, 1999.

[22] J. N. Hay and L. Sharma, Polymer, vol(41), 5749-5757, 2000.

[23] E. Dubini Paglia, P. L. Beltrame, M. Canetti, A. Seves, B. Marcandalli and E. Martuscelli, Polymer, vol(34), 996-1001, 1993.

[24] Issa A. Katime, M. S. Anasagasti, M. C. Peleteiro and R. Valenciano, European Polymer Journal, vol(23), no.11, 907-911, 1987.

[25] Zhigang Wang and Bingzheng Jiang, Macromolecules, vol(30), 6223-6229, 1997.

[26] F. Salaris, A. Turturro, U. Bianchi and E. Martuscelli, Polymer, vol(19), 1163-1170, 1978.

[27] Wen-Bin Liau, Ai S. Liu and Wen-Yen Chiu, Macromolecular Chemistry and Physics, vol(203), 294-300, 2002.

[28] G. Z Zhang, H. Yoshida and T. Kawai, Thermochimica Acta, vol(416), 79-85, 2004.

[29] Jiang-Wen You, Hsiu-Jung Chiu AND Trong-Ming Don, Polymer, vol(44), 4355-4362, 2003.

[30] Xianhua Kong, Xiaoniu Yang, Enle Zhou, and Dezhu Ma, Polymer Engineering and Science, vol(41), no.5, 786-792, 2001.

[31] Leo Mandelkern, Crystallization of Polymers, second edition, Volume 2, Chapter 9, Cambridge University Press, New York, 2004.

[32] John W. Cahn, W. B. Hillig and G. W. Sear, Acta Metallurgica, vol(12), 1421-1439, 1964.

[33] J. J. Point and C. Coutelier, Journal of Polymer Science, Polymer Physics Edition, vol(23), 231-239, 1985.

[34] J. J. Point and P. Damman, Macromolecules, vol(24), 2019-2023, 1991.

[35] Kovacs, A. J.; Straupe, C.; Gonthier, A., Journal of Polymer Science, Polymer Symposia, 59(Recent Adv. Field Cryst. Fusion Polym.), 31-54, 1977.

[36] Kovacs, A. J.; Gonthier, A.; Straupe, C., Journal of Polymer Science, Polymer Symposia, 50(Int. Symp. Macromol., Invited Lect., 1974), 283-325, 1975.

[37] Buckley, C. P.; Kovacs, A. J., Colloid and Polymer Science, vol(254), 695-715, 1976.

[38] Cheng, Stephen Z. D., Barley, Jeffrey S., and Von Meerwall, Ernst D., Journal of Polymer Science, Part B: Polymer Physics, vol(29), 515-525, 1991.

[39] Jerold M. Schultz, Polymer crystallization, Chapter 8, Oxford university press, Washington, D. C. 2001.

[40] John I. Lauritzen Jr. and John D. Hoffman, Journal of Applied Physics, vol(44), no.10, 4340-4352, 1973.

[41] Elizabeth J. Clark and John. D. Hoffman, Macromolecules, vol(17), 878-885, 1984.

CHAPTER 8. CRYSTALLIZATION MECHANISM IN BINARY POLYMERIC EUTECTICS

A manuscript to be submitted to *Macromolecules*

Jing Teng[1] and R. Trivedi[1,2,*]

Abstract

Eutectic structures are very commonly observed in many systems during solidification. The most widely used model is based on the considerations of volume diffusion in the liquid phase and the interfacial energy. However, the effects of other physical processes, such as interface kinetics, interface diffusion and interface strain energy may also be dominant in some systems. Here we examine eutectic growth in a polymeric system in which interface kinetics play a dominant role. Experimental studies show that the interface kinetics consumes a majority of the available driving force for transformation and it depends on alloy composition. The eutectic growth scaling laws are found to be different from those in metallic systems.

1. Introduction

Controlled solidification of metallic eutectics has been studied extensively since it offers the in-situ composites with unique mechanical and physical properties [1, 2].

---

[1]Dept. Materials Science and Engineering, Iowa State University, Ames, IA, 50011, U.S.A.

[2]Materials and Engineering Physics Program, Ames Laboratory-USDOE, Iowa State University, Ames, IA, 50011, U.S.A.

[*]Corresponding author: e-mail: trivedi@ameslab.gov, phone: (515) 294-5869, fax: (515) 294-4291.

Jackson/Hunt model [3] is probably the most important eutectic growth model, which provides the analysis for the coupling between the volume diffusion field of the growth phase and the curvature effect and it has been confirmed by a lot of experimental studies in metallic and small organic eutectics [4, 5]. However, in this model, the effect of interface kinetics is ignored and thus it can only illustrate the eutectic growth of non-faceted materials at low growth rate. Interface kinetics describes how the atoms/molecules attach themselves to the solid/liquid interface from the liquid. If at least one of the phases in a eutectic system is faceted (such as Al-Si, Fe-C, which are called irregular eutectics), or if a non-faceted/non-faceted eutectic grows at an extremely high velocity, the effect of interface kinetics on the eutectic growth behavior can not be ignored. There are some theoretical studies in literature about interface kinetic effect [6, 7]. However, most of them are based on JH model and just simply incorporate the interface kinetics into the expression of undercooling by assuming the continuous growth mechanism. The interface kinetic effect is far away from being well-characterized at present.

Interface kinetics is a controlling factor in polymeric materials since the crystallization is two-dimensional nucleation control. A pretty large kinetic undercooling is required during the solidification of polymers, which offers us a good opportunity to study the interface kinetic effect in eutectic growth process. However, the attention paid to polymeric eutectic growth is scarce because of the following reasons. Firstly, some characteristics of polymeric systems, such as the heterodispersity in chain length, the entanglement structure of concentrated polymer solutions and the remaining amorphous phase in the solid polymer, make the eutectic solidification in these systems much more complex than in atomic and small molecular eutectics. Secondly, the occurrence of eutectic

reaction requires that the two crystallizable components are completely miscible in the liquid. However, in polymeric systems, most pairs are immiscible due to the small gain in entropy when mixing, especially for crystalline/crystalline pairs. Therefore, it is not easy to find a polymeric eutectic system. Actually, in the reported miscible crystalline/crystalline polymeric systems in the literature, most of them consist of components that crystallize sequentially instead of simultaneously [8].

The eutectic growth of polymeric system can provide information not only on interface kinetic effect, but on rapid solidification because of the very small diffusion coefficient and strain energy effect because of the high viscoelastic melt as well. Moreover, polymeric eutectics have wide range of applications, such as producing *in situ* polymer-small molecule and polymer-polymer composites; obtaining porous polymers with controlled pore size[9]; dispersing crystalline additives in polymer homogeneously; creating regular nanopatterned surface by directional eutectic growth[10] and increasing the solubility and thus the bioavailability of a drug by using the polymer matrix as a carrier [11].

The focus of the present research is to study the directional growth of a polymeric eutectic system in which both phases have strong kinetic effect, therefore to provide understanding to its growth mechanism. With the in-depth comprehension of the interface kinetics and the appropriate mass transfer mechanism in the liquid, we will endeavor to develop an analytical model for the polymer eutectic growth. The system we selected in this research is composed of polyethylene glycol (PEG, molecular weight 8000) and p-dibromobenzene (DBBZ), with the melting points 64.0 and 87.0°C respectively. The external surface of PEG molecules presents valleys and ridges, the size and shape of which are such that they can accommodate small molecules [12], so that an intercalate complex

(compound) can form which contains 61.7wt% DBBZ and congruently melts at 96.0°C. A eutectic point exists between PEG and compound and the phase diagram is described elsewhere [13].

2. Experimental

2.1. Materials

PEG (white powder, Molecular Biology Grade, Mw = 8000, PDI = 1.035 by GPC) and DBBZ (white crystal) were purchased from Fisher and Aldrich respectively and they were used as received.

2.2. Alloy and sample cell preparation

The master alloys were prepared by heating the solid mixtures with some certain compositions to 150°C under high purity nitrogen and were kept at that temperature 1hr for homogenization after the alloy was fully dissolved.

The directional solidification experiments were carried out on a temperature gradient stage (TGS). The master alloy was sealed in a quasi 2D-rectangular glass tube (0.2mm height x 4.0mm width x 300mm length) by vacuum filling technique. A ϕ50 μm K-type thermocouple was inserted in the sample cell before filling and was connected to a temperature recording system so that interface temperatures with velocities can be measured during solidification processes. The in-situ growth morphologies were captured by optical microscope and camera connected to the TGS. For eutectic spacing measurement, a thin slab sample cell was used with the thickness about 5 μm. The growth experiments were preceded at high G/V condition so that a monolayer structure can be obtained. The images of stable

interface morphologies were recorded and the spacing data were obtained from those pictures.

3. Results

3.1. Eutectic growth morphology

Figure 1 shows the interface morphology of directionally solidified PEG-5.0wt% DBBZ (PEG-8.1wt% compound) alloy, which is the eutectic composition of PEG-compound system. The small solute diffusion coefficient of the polymeric system results in the very fine length scale, thus in order to get monolayer structure, the growth has been performed on ultra thin film (~ 5μm thickness) under high G/V ratio condition at very low growth rates.

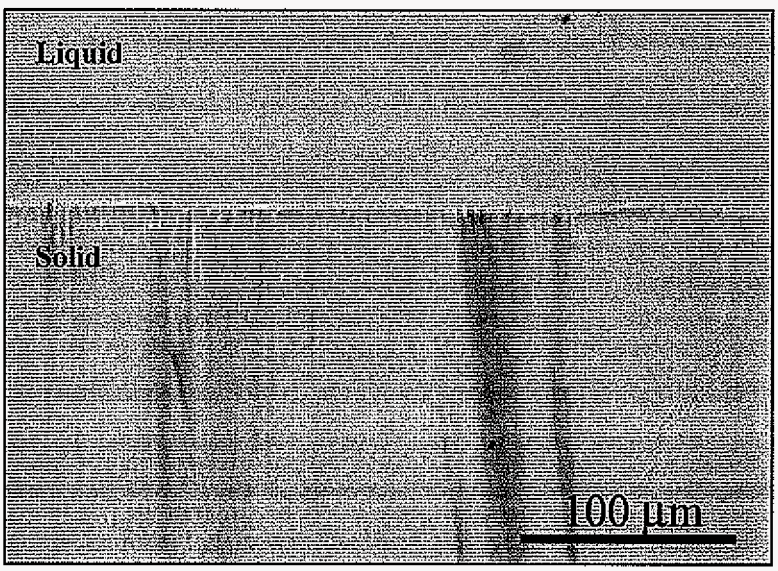

Figure 1. In-situ morphologies of directionally solidified PEG-compound eutectic (V = 0.005 μm/s).

3.2. Experimental scaling laws of eutectic growth

Variations in eutectic spacing with velocity can be obtained from the in-situ images and the results are shown in Figure 2 as Logλ versus Log V. For each growth velocity, there exists a finite range of eutectic spacings, as shown in figure 2. A straight line was obtained with the slope ~ 0.33 by curve regression of the minimum spacing data. Therefore, we obtain the relationship of eutectic spacing with velocity as $\lambda_{min}^{3}V$ = constant.

The change in interface temperature and thus the undercooling with velocity has also been measured during the directional growth. A 200 μm thick sample has been used in this experiment so that a Φ50μm thermocouple can be embedded into it. The obtained interface temperature and undercooling were shown in figure 3(a). Figure 3(b) presented the undercooling-velocity relationship in Log-Log scale and the regressed straight line has a

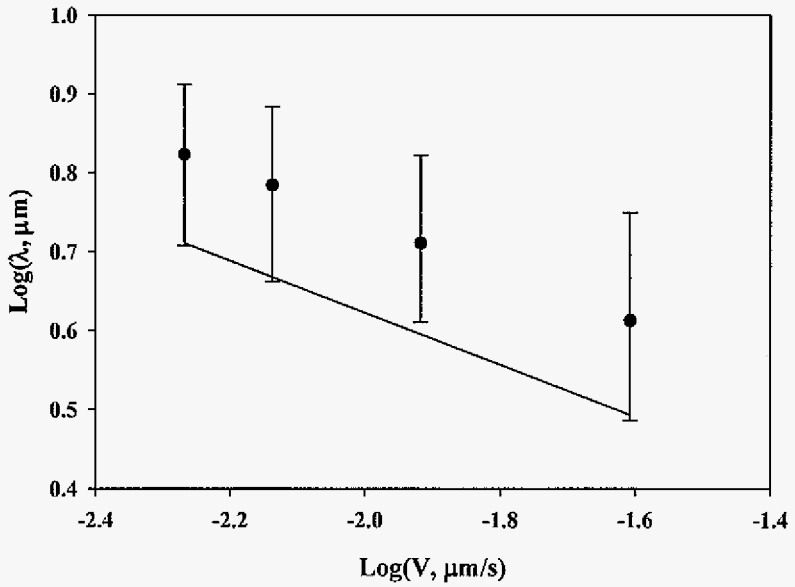

Figure 2. Spacing-velocity relationship of PEG-compound eutectic.

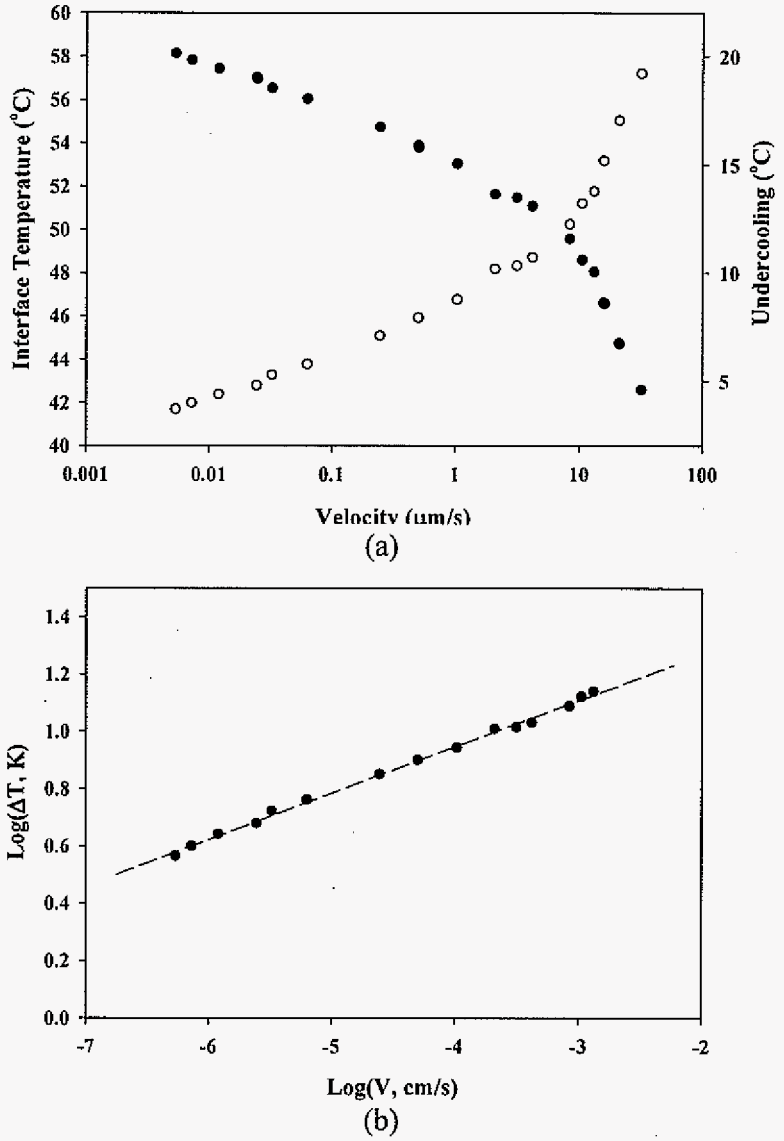

Figure 3. (a) Interface temperature and undercooling and (b) undercooling-velocity relationship of directional solidified PEG-compound eutectic.

slope of 0.16 by curve fitting, that is, $\Delta T V^{-0.16}$ = constant. Comparing with the scaling laws in JH model ($\lambda^2 V$ = constant and $\Delta T V^{-0.5}$ = constant), and one may find that there exist obvious deviations in the experimentally obtained scaling laws in PEG-compound eutectic growth,

indicating the controlling mechanism for eutectic growth in this system should be different from the one assumed by Jackson and Hunt.

3.3. Interface kinetic effect of PEG and compound

In PEG-compound eutectic, both phases have strong interface kinetics. In directional solidification of a pure material, the interface temperature will only reflect the kinetic effect. Therefore, we can quantitatively examine the kinetic effect for both PEG and compound by this technique. Figure 4 compares the normalized undercooling values ($\Delta T/T_m$) with velocities for directional solidified PEG and compound, which exhibits a few significant features:

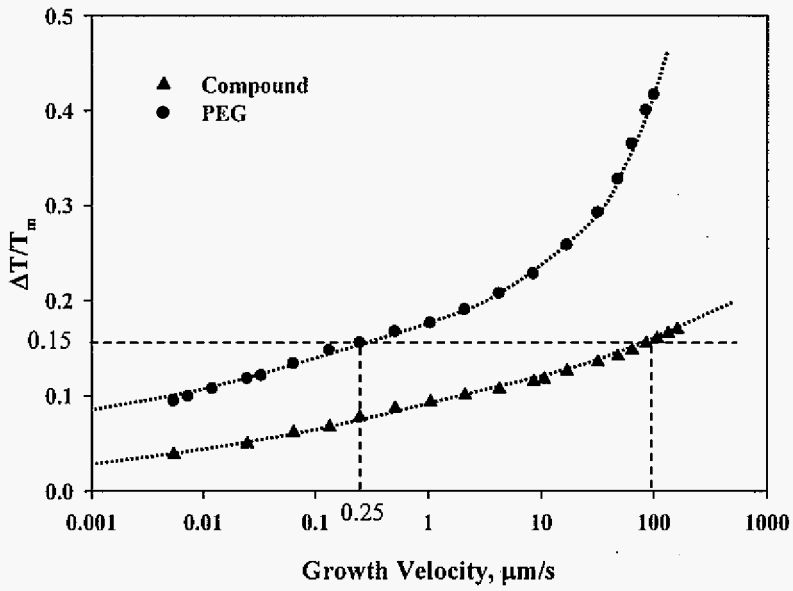

Figure 4. The comparison of normalized undercooling with velocity for directional solidified PEG and compound.

First, for both PEG and compound, the higher the growth rate, the larger the undercooling value is required, that is, the larger the kinetic effect; Second, the kinetic effect in compound growth is much smaller than that in PEG growth. For example, when growth rate is about 100μm/s for compound growth, the value of normalized driving force that required is 0.15; while for this same driving force, the growth rate of PEG can only reach 0.25μm/s, which is two orders of magnitude smaller than that of compound. This indicates that in the subsequent modeling work of eutectic growth of this system, only the kinetic effect of PEG phase need to be considered.

3.4. The composition effect of interface kinetics in hypo-eutectic alloys

Though the eutectic structure is composed of pure PEG and compound phases, the liquid immediately is not the pure component due to the solute rejection at the growth interface. Therefore the effect of composition on the growth kinetics should be thoroughly investigated. This investigation is limited in hypo-eutectic region since only the kinetic effect of PEG phase need to be considered in the modeling work, as it was mentioned earlier.

The interface temperatures with velocities at a fixed temperature gradient were measured for hypo-eutectic alloys in directional solidification processes. PEG phase was the primary phase in hypo-eutectic alloys so that the composition effect on PEG interface kinetics can be evaluated. Figure 5 gave the obtained undercooling for pure PEG and for PEG phase in hypo-eutectic alloys. We can see that with a small amount of DBBZ addition into PEG (≤2.0wt%DBBZ), a larger undercooling is needed in order to keep the same growth velocity. However if more DBBZ is added, this undercooling is decreased.

The temperature gradient effect on the interface temperature of PEG phase at fixed

growth velocities was also examined in directional solidified hypo-eutectic alloy with composition 1.93wt% DBBZ and the results were shown in figure 6. Clearly, the interface temperature and thus the undercooling are independent of temperature gradient, which indicates that the solutal undercooling was negligible in comparison with kinetic undercooling in hypo-eutectic alloy. Therefore, the total undercooling that measured during the growth of hypo-eutectic alloy can be viewed as the kinetic undercooling.

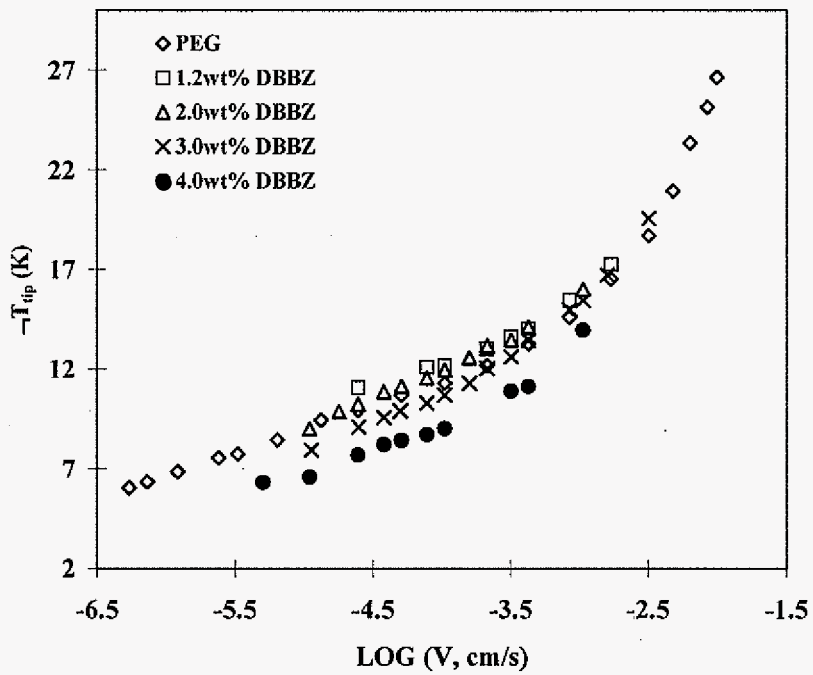

Figure 5. Dependence of undercooling on growth velocity for directional solidified PEG and PEG phase in hypo-eutectic alloys.

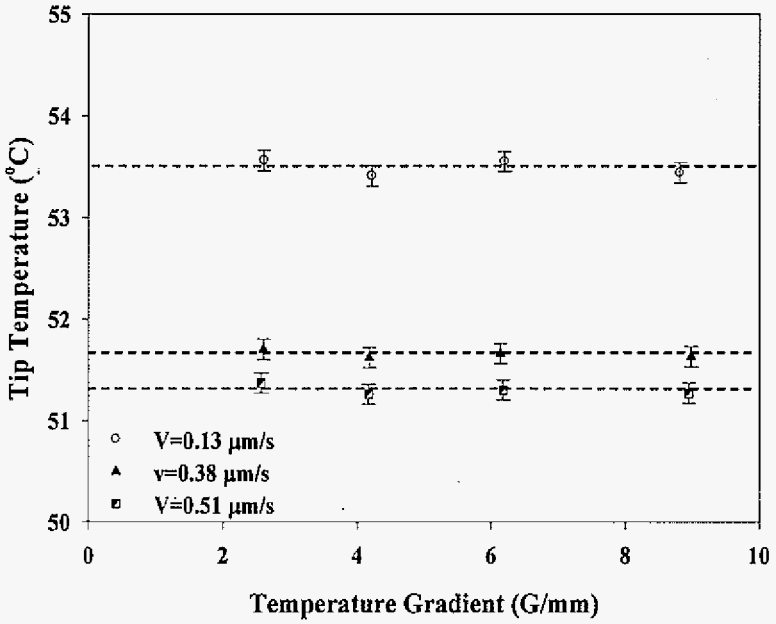

Figure 6. Dependence of tip temperature on temperature gradient for directional solidified PEG-1.93wt% DBBZ alloy.

4. Discussion

4.1. Interface kinetics of PEG in hypo-eutectic alloys

The growth kinetics of a pure crystallizable polymer is governed by the secondary nucleation theory[14-17], the growth rate can be expressed as:

$$V = G_0 \exp[-U^* / R(T - T_\infty)]\exp[-K_g / T(\Delta T) f] \qquad (1)$$

In this equation, G_0 is a pre-exponent factor containing all the quantities that not highly dependent on temperature, T is the crystallization temperature, U^* is the activation energy of transport of polymer chains segment across the melt/crystal interface and T_∞ is a theoretical temperature at which all motion associated with viscous flow stops and is related

to the glass transition temperature of the polymer. ΔT is the undercooling $(T_m^0 - T)$ and $f = 2T/(T_m^0 + T)$, which is a correction factor for temperature dependence of heat of fusion. K_g is a nucleation parameter, $\equiv Zb_0\sigma\sigma_e T_m^0 / k\Delta h_f$, where Z equals 4 for growth regime I and III and 2 for regime II, b_0 is the crystal monomolecular layer thickness in the growth direction. σ and σ_e are the lateral and fold-surface free energies, respectively. T_m^0 is the equilibrium melting point and Δh_f is the crystal heat of fusion.

Equation (1) is usually re-arranged as:

$$LnV + \frac{U^*}{R(T - T_\infty)} = LnG_0 - \frac{K_g}{T(\Delta T)f} \qquad (2)$$

Then the plot of the left-hand side of the equation (2) vs $1/T(\Delta T)f$ can provide the information about the value of K_g (slope) and G_0 (intercept) and this type of data presentation is usually termed as LH plot.

Boon and Azcue [18] modified the secondary nucleation theory in order to describe the crystallization kinetics of polymeric mixture. The growth rate is given by:

$$V = \phi_1 G_{0(a)} \exp(-\frac{U^*}{R(T - T_\infty)}) \exp(-\frac{K_{g(a)}}{T(\Delta T)f} + \frac{2\sigma T_{m(a)}^0 Ln\phi_1}{b\Delta h_{f(a)}(\Delta T)f}) \qquad (3)$$

where ϕ_1 is the volume fraction of PEG phase and the subscript (a) means "alloy". Since by empirical relation, for PEG, $\sigma \approx 0.1b(\Delta h_f)$ [19], the above equation can be rearranged as:

$$V = \phi_1 G_{0(a)} \exp(-\frac{U^*}{R(T - T_\infty)}) \exp(-\frac{K_{g(a)}}{T(\Delta T)f} + \frac{0.2T_{m(a)}^0 Ln\phi_1}{(\Delta T)f}) \qquad (4)$$

$$LnV + \frac{U^*}{R(T - T_\infty)} - Ln\phi_1 - \frac{0.2T_{m(a)}^0 Ln\phi_1}{(\Delta T)f} = LnG_{0(b)} - \frac{K_{g(a)}}{T(\Delta T)f} \qquad (4')$$

The plots of the left-side terms in equation (4') (g') vs. $1/T(\Delta T)f$ can be drawn for hypo-eutectic alloys, as shown in Figure 7. Since the actual interface temperature is much lower than the liquidus temperature $T^0_{m(a)}$, we use the local liquid composition at the growth interface to calculate ϕ_1. The local concentration is obtained through the phase diagram since the interface temperature has been directly measured in the growth process for each alloy. Both U^* and T_∞ are considered unchanged with composition and are taken the same values as PEG's since PEG is the primary phase in hypo-eutectic alloys. Specifically, U^* = 29.3KJ/mol by Kovacs' [20-22] and T_∞ is taken, by definition, as $(T_g - 30)K$ with $T_g = 206.15K$.

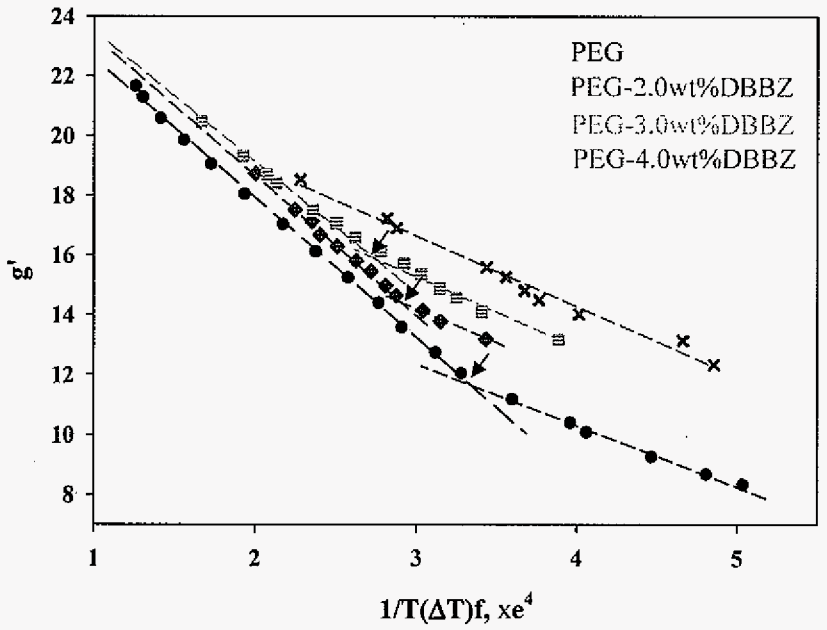

Figure 7. LH plots for directionally solidified PEG and hypo-eutectic alloys.

The LH plot of PEG growth was also shown in Figure 7. Three significant observations can be made from this figure: (1) A growth regime transition II/III can be observed for PEG growth as marked by the blue arrows on the figure. For hypo-eutectic alloy crystallization, the transitions are systematically shifted to a higher growth rate (*e.g.*, higher undercooling) with the increase in DBBZ concentration, that is, the higher the alloy composition, the higher the growth rate needed to reach the regime transition point. (2) In each regime, the value of K_g is nearly independent of the alloy composition (Table 1) and thus the same as that for PEG within the experimental error. (3) The G_o term increases with the alloy composition (Table 1). The detailed discussion of this part has been described elsewhere [13].

Table 1. Derived values of K_g^{II}, K_g^{III} and G_o in hypo-eutectic alloys

Composition wt% DBBZ	Regime II		Regime III	
	K_g x10^{-4}, K^2	G_0 x10^9, cm/s	K_g x10^{-4}, K^2	G_0 x10^9, cm/s
0	2.018	0.343	4.665	625
1.2			4.957	1200
2	2.336	1.49	4.588	1380
3	2.454	4.25	4.331	1910
4	2.356	17.3		
In our growth rate range, alloy of 1.2wt% stays only in regime III, while 4.0wt% is in regime II only.				

4.2. Kinetic undercooling in PEG-compound eutectic growth

From Figure 7, we can see that the regime II/III transition point of PEG growth shifts to a higher velocity with the composition and within our experimental velocity range, the

growth of PEG phase in PEG-4wt% DBBZ alloy is always in regime II. Therefore, for PEG-compound eutectic growth, in which the composition is PEG-5wt% DBBZ, the growth of PEG phase should also be in regime II. The kinetic undercooling in PEG-compound eutectic growth can be evaluated by examining the growth data in regime II of PEG and hypo-eutectic alloys.

We know that the growth of PEG is controlled by 2-dimensional nucleation and the interface kinetic undercooling can be expressed as[23]:

$$\Delta T_K = A / \ln(\frac{V}{B}) \qquad (5)$$

where A is a negative constant while B is a positive constant. Since our experimental velocities are within a small range [0.0054, 13.32] μm/s, for simplicity, we can fit the kinetic undercooling with the following equation:

$$\Delta T_K = K_3 V^n \qquad (6)$$

which can be rearranged as:

$$Ln\Delta T_K = LnK_3 + nLnV \qquad (6')$$

Figure 8 is the measured undercooling with velocity for PEG and hypo-eutectic alloys in growth regime II according to equation 6'. It is clear that the straight lines are obtained for all the compositions within the velocity range for this experimental study. Therefore, the corresponding values of K_3 and n can be acquired by curve fitting, which were also shown on the figure. Apparently, the value of n is independent of the alloy composition, which is reasonable since they are in the same growth regime. Thus, the composition dependence of PEG growth interface kinetics can be simply characterized by a single parameter K_3. The relationship of K_3 with composition is shown in figure 9, which can be expressed as

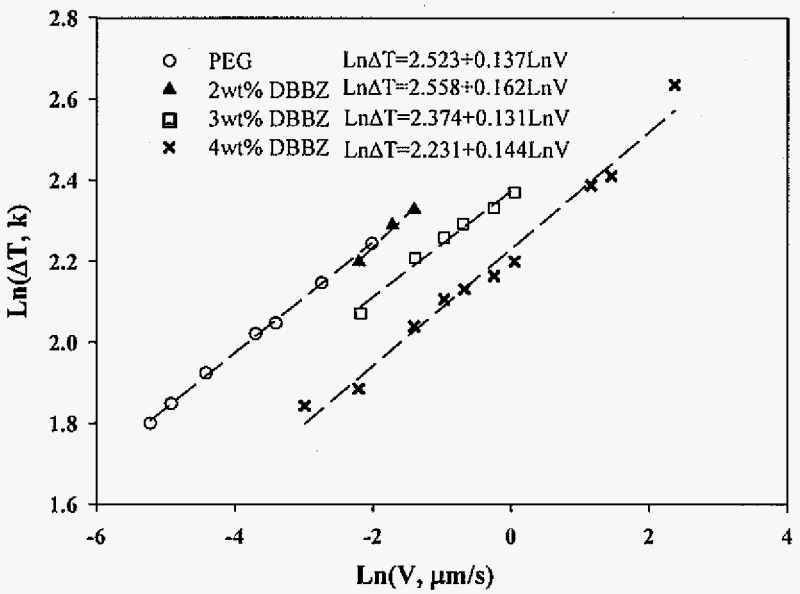

Figure 8. Variation in kinetic undercooling with velocity for PEG growth in alloys with different composition.

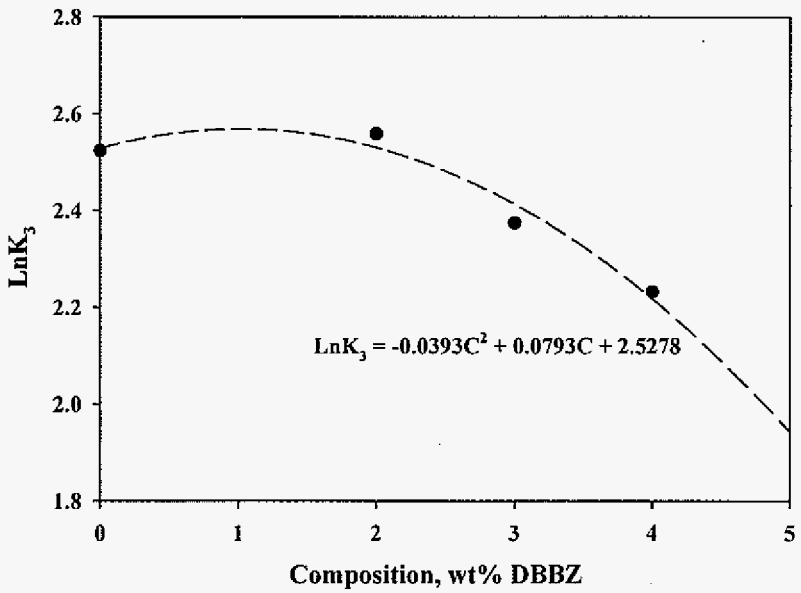

Figure 9. Composition dependence of kinetic coefficient K_3.

$LnK_3 = -0.0393C^2 + 0.0793C + 2.5278$. Therefore, we can get the K_3 value for eutectic composition, which is $e^{2.0} = 7.389$ while $n = 0.144$, which is obtained by averaging n values of PEG and hypo-eutectic alloys. Then, the kinetic undercooling can be calculated for the growth of PEG-compound eutectic alloy.

The total driving force for PEG-compound eutectic growth is consumed to drive the solute diffusion and polymer chain movement to maintain a curved interface for each phase in eutectic structure. The corresponding undercooling are denoted by ΔT_C, ΔT_r and ΔT_K, respectively. The relationship of kinetic undercooling with velocity is $\Delta T_K = 7.40V^{0.144}$, which is very close to the experiemental scaling law of total undercooling with velocity $\Delta T = 8.76V^{0.16}$. Figure 10 shows the experimental measured undercooling and calculated

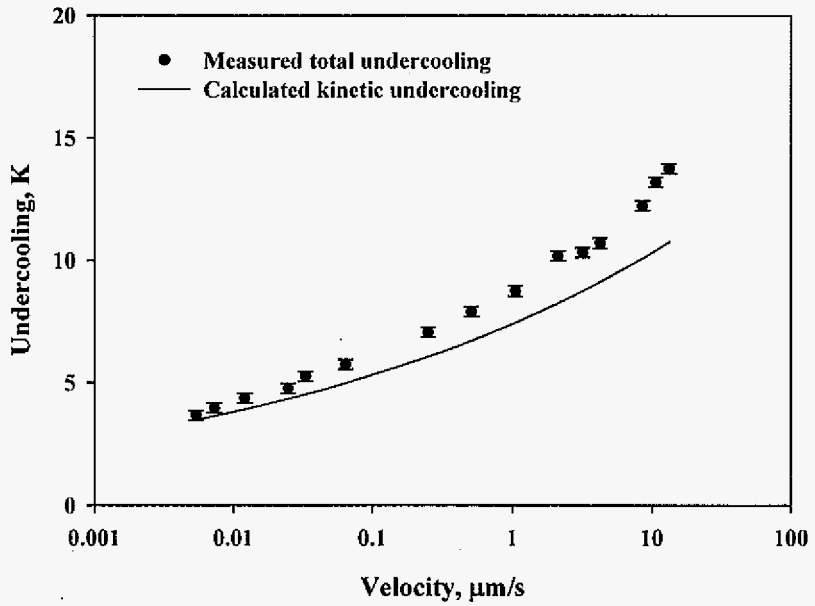

Figure 10. Comparison of calculated kinetic undercooling with measured undercooling in PEG-compound eutectic growth.

kinetic undercooling. Clearly, during the growth of PEG-compound eutectic, the kinetic undercooling should be the major part in the total undercooling measured experimentally. The difference between them is the driving force for diffusion (ΔT_C) and maintaining interface curvature (ΔT_r).

4.3. Eutectic growth at extremum condition

The experimental relationship of eutectic spacing and velocity followed the scaling law $\lambda^3 V = 0.776$. According to Carpey *et.al*[24], this scaling law indicates that in this eutectic system, the mass transfer mechanism is mainly controlled by boundary diffusion. Therefore, from boundary diffusion equation, the solutal diffusion undercooling can be written as:

$$\Delta T_C = K_1 V \lambda^2 \qquad (7)$$

where $K_1 = \frac{(C_\beta - C_e)(C_e - C_\alpha)}{12 D_B \delta_B (C_\beta - C_\alpha)}$, D_B is boundary diffusivity and δ_B is the thickness where the boundary diffusion occurs. For PEG-compound system, we can take δ_B as 7.52 nm, which is the dimension of the PEG random coil in the melt [25].

Following Jackson and Hunt, the curvature undercoolings can be expressed as:

$$\Delta T_r = K_2 / \lambda \qquad (8)$$

with $K_2 = 2m\delta \sum_i (\Gamma_i \sin\theta_i / |m_i| f_i)$ and $i = \alpha, \beta$. Here $m = |m_\alpha m_\beta| / (|m_\alpha| + |m_\beta|)$ in which m_α and m_β are the magnitudes of the PEG and the compound phase liquidus slopes at the eutectic temperature. The parameter δ is unity for lamellar growth, which is the case for PEG-compound eutectic growth due to the ultra thin sample. f_α and f_β are the volume fractions of PEG and compound phases, respectively. θ_i is the corresponding contact angle

at PEG/compound/liquid triple point. Table 2 lists some of the parameters of PEG-compound eutectic alloy that necessary for the later calculation.

Table 2. Physical Properties of PEG-compound Alloy		
Property	Unit	Value
Eutectic composition, C_e	wt% compound	8.104
Maximum solubility of compound in PEG, C_α	wt% compound	0
Maximum solubility of PEG in compound, C_β	wt% compound	100
Boundary thickness, δ_B	nm	7.52
Volume fraction of PEG phase, f_α		0.939
Volume fraction of compound phase, f_β		0.061
Liquidus slope of α phase, m_α	K/wt%	-0.415
Liquidus slope of β phase, m_β	K/wt%	1.234
Solute diffusion coefficient in liquid, D	m^2/s	10^{-13}

Now, the total undercooling can be expressed as:

$$\Delta T = K_1 V\lambda^2 + K_2/\lambda + K_3 V'' \qquad (9)$$

Adopting the same assumption as Jackson and Hunt that the solid grows at the extermum condition and the observed spacing corresponds to the minimum undercooling for a fixed velocity gives $d(\Delta T)/d\lambda = 0$. Differentiating equation (9) gives:

$$2K_1 V\lambda - K_2/\lambda^2 = 0 \qquad (10)$$

Hence:

$$V\lambda^3 = K_2/2K_1 \qquad (10a)$$

Substituting equation (10a) into equation (9) gives the relation between ΔT_C and ΔT_r at the extremum growth condition:

$\Delta T_C = \Delta T_r / 2$, therefore,

$$\Delta T - \Delta T_K = \frac{3}{2}\Delta T_r = \frac{3K_2}{2\lambda} \qquad (10b)$$

According to this equation, the sum of curvature and solutal undercooling increases with finer spacing, that is, higher velocity.

Since we already calculated the kinetic undercooling, we can calculate the curvature undercooling from equation (10b) and solutal undercooling at the extremum growth condition. Then we can estimate the value of D_B and $\Gamma\sin\theta$ from experimental velocity and spacing. For example, V=0.0054μm/s, the measured spacing and total undercooling at this velocity are 5.1μm and 3.66K, and the calculated kinetic undercooling is 3.48K. Therefore, the curvature undercooling is 0.12K from equation 10b and solutal undercooling is 0.06K.

Substituting the solutal undercooling into equation (7), D_B is estimated as a value of $1\text{x}10^{-10}$ m^2/s, which is 3 orders of magnitude higher than volume diffusion coefficient (D) [26]. Thus D_B/D is about 1000, while $\lambda/2\pi\delta_B$= 108 at this velocity. Therefore $\frac{D_B}{D} > \frac{\lambda}{2\pi\delta_B}$. According to Cahn and Hagel [27], this indicates that diffusion along the interface boundary will be the dominant transport mode, which agrees with the assumption used beforehand. Here we calculate by using the lowest experimental velocity. With the increasing velocity, the spacing decreases and the inequality relationship $\frac{D_B}{D} > \frac{\lambda}{2\pi\delta_B}$ always holds.

Substitute equation (8) into equation (10b), the value of K_2 can be calculated from the measured spacing at V=0.0054μm/s as 0.589K•μm. Therefore, total undercooling can be roughly expressed as:

$$\Delta T \approx \Delta T_K + \frac{3}{2}\Delta T_r = 7.4V^{0.144} + \frac{3\times 0.589}{2\lambda} \qquad (11)$$

Combined with experimental obtained scaling law $\lambda^3 V = 0.776$, we have:

$$\Delta T = 7.4V^{0.144} + 0.96V^{0.33} \qquad (12)$$

From equation (12), the total undercooling can be calculated with velocity for PEG-compound eutectic growth, which is shown in Figure 11. Obviously, the calculated curve fits with the experimental measured value very well. Three conclusions can be draw from Figure 11:

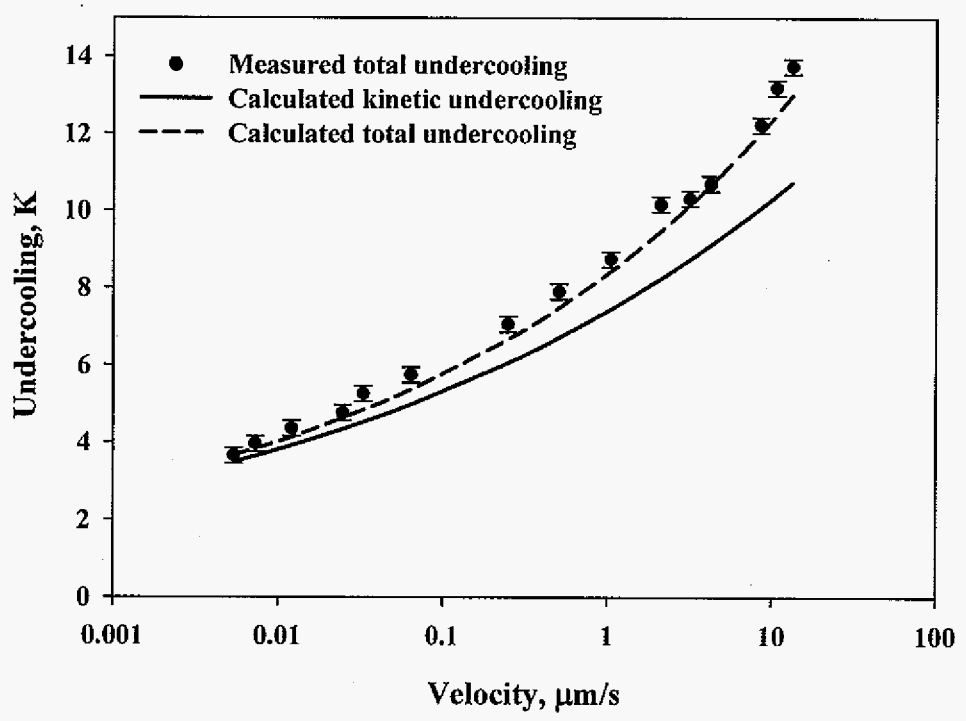

Figure 11. Calculated kinetic undercooling, total undercooling and the comparison with measured total undercooling in PEG-compound eutectic growth.

Firstly, interface kinetics of PEG phase growth consumes the vast majority of total driving force in the eutectic growth. Secondly, the sum of curvature and solutal undercooling increases with velocity, which is demonstrated by the increasing difference between the calculated values of total and kinetic undercooling. This is agrees with the prediction from equation (10b). Therefore, the third conclusion is the eutectic growth of PEG-compound alloy operates under a condition close to extremum condition, that is, minimum interface undercooling.

5. Conclusion

The growth behavior of a polymeric system, PEG-DBBZ, in which PEG and PEG-DBBZ compound can form a eutectic alloy, was studied by directional solidification technique in this research. In this system, the interface kinetics in PEG phase growth is much stronger than that in compound phase. For PEG phase, this interface kinetics is controlled by 2-dimensional nucleation and the kinetic effect depends on the alloy composition.

The experimental study in PEG-compound eutectic growth shows that interface kinetic process consumes the vast majority of total driving force for eutectic growth. For total undercooling, $\Delta T = 8.76V^{0.16}$; while the extrapolate kinetic undercooling is $\Delta T_K = 7.40V^{0.144}$. The difference between them is consumed to maintain a curvature of solid/liquid interface for both phases in eutectic structure, and to drive the solute transport in the liquid, which is controlled by boundary diffusion. Eutectic growth in this system proceeds at a condition close to minimum interface undercooling. Based on the specific mechanisms of interface kinetics and solute transport, the semi-empirical model developed in this study can describe the experimental observed scaling laws.

Acknowledgment

A part of this work was carried out at Ames Laboratory under Contract No. DE-AC02-07CH11358 with the U.S. Department of Energy. A part of this study was also supported by the Office of Microgravity Sciences, NASA, under grant # NAG8-1681.

References

[1] G. A. Chadwick, Metallography of Phase Transformation, Butterworths, London, 1972, p.107.

[2] J. D. Livingston, Journal of Crystal Growth, vol (24/25), 1974, 94.

[3] K. A. Jackson and J. D. Hunt, Lamellar and rod eutectic growth, Transactions of the Metallurgical Society of AIME, vol. 236, August, 1966, 1129-1142.

[4] Lambert R. M. Jordan and J. D. Hunt, The growth of lamellar eutectic structures in the Pb-Sn and Al-$CuAl_2$ systems, Metallurgical Transactions, vol2, December, 1971, 3401-3410.

[5] H. Walker, Growth and stability of lamellar eutectic structures, Master thesis, Iowa State University, 2005.

[6] J.F. Li and Y.H. Zhou, Eutectic growth in bulk undercooled melts, Acta Materials, 53, 2005, 2351-2359.

[7] Mingjun Li and Kazuhiko Kuribayashi, Nucleation-controlled microstructures and anomalous eutectic formation in undercooled Co-Sn and Ni-Si Eutectic Melts, Metallurgical and Materials Transactions A, vol.43A, December, 2003, 2999-3008.

[8] J. P. Penning, R. St. John. Manley, Macromolecules, vol. 29, 84-90, 1996.

[9] P. Smith and J. Pennings, Eutectic solidification of the quasi binary system of isotactic polypropylene and pentaerthrityl tetrabromide, Journal of polymer Science, Polymer Physics

Edition, vol15, 523-540, 1977.

[10] Claudio De Rosa, Cheolmin Park, Edwin L. Thomas and Bernard Lots, Microdomain patterns from directional eutectic solidification and epitaxy, Nature, vol405, 433-437, 2000.

[11] Devalina Law, Weili Wang, Eric A. Schmitt, Yihong Qiu, Steven L. Krill, and James J. Fort, Properties of rapidly dissolving eutectic mixtures of poly(ethylene glycol) and fenofibrate: the eutectic microstructure, Journal of Pharmaceutical Science, vol92, No.3, 2003, 505-515.

[12] J. J. Point and P. Damman, Poly(ethylene oxide)-p-dihalogenobenzene crystalline complex: FTIR and X-ray diffraction study of spherulitic fibers, Macromolecules, 24, 2019-2023, 1991.

[13] Jing Teng and Rohit Trivedi, Crystallization kinetics in binary polymer systems, manuscript, to be submitted.

[14] J. D. Hoffman, G. T. Davis, and J. I. Lautitzen Jr., in Treatise on Solid State Chemistry, vol(3), Chapter 7, Crystalline and Noncrystalline Solids, N. B. Hannay ed., Plenum, New York, 1976.

[15] J. D. Hoffman, Polymer, vol(23), 656-670, 1982.

[16] J. D. Hoffman, C. M. Guttman, and E. A. Dimarzio, Faraday Discussions of the Royal Society of Chemistry, vol(68), 177-197, 1979.

[17] J. D. Hoffman, Polymer, vol(24), 3-26, 1983.

[18] J. Boon and J. M. Azcue, Journal of Polymer Science, Part A-2, vol(6), 885-894, 1968.

[19] John I. Lauritzen Jr. and John D. Hoffman, Journal of Applied Physics, vol(44), no.10, 4340-4352, 1973.

[20] Kovacs, A. J.; Straupe, C.; Gonthier, A., Journal of Polymer Science, Polymer

Symposia, 59(Recent Adv. Field Cryst. Fusion Polym.), 31-54, 1977.

[21] Kovacs, A. J.; Gonthier, A.; Straupe, C., Journal of Polymer Science, Polymer Symposia, 50(Int. Symp. Macromol., Invited Lect., 1974), 283-325, 1975.

[22] Buckley, C. P.; Kovacs, A. J., Colloid and Polymer Science, vol(254), 695-715, 1976.

[23] W. A. Tiller, Isothermal solidification of Fe-C and Fe-C-Si alloys, ASM Seminar, Recent Research on Cast Iron, New York (Gordon and Breach), p129-171, 1964.

[24] F. M. A. Carpay, Growth of composites by eutectoid or other solid-state decomposition, International Metals Reviews, No.1, 1974, 1-18.

[25] G. Allen, The molecular basis of rubber elasticity, Proceedings of the Royal Society of London, Series A. vol.351, No. 1666, 381-396, 1976.

[26] Cheng, Stephen Z. D., Barley, Jeffrey S., and Von Meerwall, Ernst D., Self-diffusion of poly(ethylene oxide) fractions and its influence on the crystalline texture, Journal of Polymer Science, Part B: Polymer Physics, vol(29), 515-525, 1991.

[27] J.W. Cahn and W. C. Hagel, Theory of the pearlite reaction, in Decomposition of Austenite by Diffusional Processes, edited by V.F.Zacky and H. I. Aaronson, interscience publishers, 1962,131-192(p.187).

CHAPTER 9. GENERAL CONCLUSION

Phase diagrams of PEG-DBBZ and SCN-camphor eutectic systems are carefully determined by using a variety of experimental techniques. Detailed experimental studies are carried out comparatively in these two systems for both eutectic and primary phase growth in order to examine the physics governing the pattern formation.

The directional solidification technique is employed to investigate the growth kinetics of pure PEG for the first time, in which the interface temperature is accurately and correctly measured for a steady state growth process, i.e., the growth velocity is preset and remains constant. The growth can be understood through the secondary nucleation theory with a regime II/III transition at undercooling ~ 9.5K. A comparison with the undercooled growth of PEG shows a clear difference at high growth velocities, indicating that the driving force is over-estimated in the undercooled case.

The addition of DBBZ into PEG melt causes the regime II/III transition to shift to a higher velocity, but the nucleation parameter K_g's does not change in each regime. At the same undercooling, the PEG growth rate first decreases then increases with DBBZ composition, which can be explained by the coupling of dilution effect, increased secondary nucleation energy barrier and the improved mobility.

The experimental study of PEG-compound eutectic alloy yields the scaling laws of eutectic growth for this system, $\lambda^3 V$ = constant, $\Delta T V^{-0.16}$ = constant, which cannot be described by any existing eutectic (eutectoid) growth models. Interface kinetic undercooling is found to constitute the vast majority of total undercooling for eutectic growth in this system. The extrapolated kinetic undercooling is $\Delta T_K = 7.4 V^{0.144}$, which is close the total

undercooling $\Delta T = 8.8V^{0.16}$. The difference between them is consumed to maintain a curvature of solid/liquid interface for both phases in eutectic structure, and to drive the solute transport in the liquid through boundary diffusion. Eutectic growth in this system is found to proceed at a condition close to the minimum interface undercooling. Based on the specific mechanisms of interface kinetics and solute transport, a model has been developed to describe the experimentally observed scaling laws.

In SCN-camphor system, the experimentally obtained scaling laws follow the JH model predictions very well if the sample is thick enough to allow more than 6 layers of rods to grow, where the rods can assume the ideal shape and regular hexagonal arrangement. However, if the sample thickness is comparable to the natural eutectic spacing within a factor of 2, a single layer of rods can evolve and the cross-section of such a rod is elliptical with the major axis aligned either along the sample width or thickness direction. The diffusion field has been solved in the elliptical cylindrical coordinate system and it is found that a strong angular solute flux exists, which forces the shape of a rod to conform to the growth domain.

In the SCN-camphor system, the dynamics of eutectic spacing selection is examined. For a velocity-decrease process, elimination of arrays of rods operates to increase the spacing; while for a velocity-increase process, tip splitting controls the re-adjustment of rod spacing and the initial tip instability is controlled by the domain shape for the growth.

The growth behavior of SCN-base dilute alloys has also been examined on some interesting subjects. The single cellular structure in a thin capillary tube is grown in SCN-9.6wt% and 13wt% camphor alloys to examine the similarity of cell shape with Saffmann-Taylor (ST) finger pattern and the relationship of tip undercooling with growth condition. The results show that when d_c/λ is smaller than 0.6, the cell shape is found to

follow the 3D ST finger shape and the tip undercooling agree with 3D ST model. The cell-dendrite transition (CDT) is investigated in alloys containing 0.35, -0.65 and -0.9wt% camphor and it is found that the relationship $\lambda_{cd}\ (GV)^{1/3}C_o^{1/4}=25.3\ \mu m\ (K/s)^{1/3}$ defines the cell/dendrite transition boundary.

ACKNOWLEDGEMENT

I would like to express my sincere gratitude to my advisor, Dr. Rohit K. Trivedi, for giving me the opportunity to study and work under his supervision. His guidance, encouragement and support helped to make this research possible and my life here enjoyable.

I would like to thank all my committee members, Dr. Brian Glesson, Dr. Xiaoli Tan, Dr. Balaji Narasimhan, Dr. Palaniappa A. Molian and Dr. Surya K. Mallapragada for their suggestions on the research project and their critical readings.

My special thanks extend to Dr. Shan Liu, who has offered tremendous and continuous help in the course of research; and to other group members: Dr. Jehyun Lee, Jongho Shin, Heath Walker and Erin Sunseri for their kindhearted support.

I am much indebted to my parents, my sister and my husband. Without their support, encouragement and endurance, it would have been impossible for me to complete this study. I should especially thank my son, Haoyang, who always brings me joy, happiness and satisfaction especially at those difficult times.